MODELING OF SHAPE MEMORY ALLOY MAX PHASE COMPOSITES CONSIDERING THE INTERACTION OF MULTIPLE INELASTIC MECHANISMS

A Dissertation

by

BRIAN THOMAS LESTER

Submitted to the Office of Graduate and Professional Studies of
Texas A&M University
in partial fulfillment of the requirements for the degree of

DOCTOR OF PHILOSOPHY

Chair of Committee,	Dimitris C. Lagoudas
Committee Members,	Ibrahim K. Karaman
	Miladin Radovic
	John D. Whitcomb
	Siddiq M. Qidwai
Head of Department,	Rodney. Bowersox

August 2015

Major Subject: Aerospace Engineering

ABSTRACT

Recently, new shape memory alloy (SMA) - MAX phase composites (*e.g.* NiTi-Ti_2AlC and $NiTi - Ti_3SiC_2$) have been developed to take advantage of their unique combination of thermomechanical responses. Of particular interest are the reversible martensitic transformation of the SMA phase and the recoverable and irrecoverable deformations associated with kinking in the MAX phases. By using such behaviors in conjunction with each other, a novel composite material is produced for use in extreme environments. Specifically, the nonlinear behavior of the two constituents leads to strong mechanical damping and the possibility of developing controllable residual stress states. To take advantage of these possibilities, detailed understanding of the interactions of not just the mechansisms but also the composite microstructure is needed. Therefore, a series of models are constructed to explore the various composite behaviors.

To address this need, in this work a series of models are developed to explore the local and global responses of this system with an emphasis on the response of these composites to thermal loadings. First, the effective transformation characteristics of SMA composites with a stiff, elastic matrix are modeled using an efficient micromechanical scheme and the influence of a stress redistribution associated with transformation on the effective phase diagram is determined. The interaction of the reversible SMA phase with an elastic-plastic MAX phase through an constant stress, thermal cycle is then studied through image based finite element approaches. Specifically, two microstructure models are generated. The first being a reference two-phase system and the latter being an actual NiTi-Ti_2AlC composite. By analyzing response through such loadings it is demonstrated that martensitic transforma-

tion may be used to induce permanent deformations in the MAX phase and thereby develop residual stress states. Additional analysis of the actual composite system reveals that these residual stress states may induce an effective two-way shape memory behavior. Comparison to experimental results also shows reasonable agreement. Further simulations are used to explore the effect of the microstructure and identify the impact of different features on the effective composite response.

The previous results emphasized only permanent deformations in the MAX phase even though additional irrecoverable deformations have been experimentally observed. To incorporate these effects, an enhanced constitutive model considering both responses is needed. Currently, no such model exists in the literature. Therefore, to address this need, a constitutive model of the MAX phase behaviors is established and implemented in this work. Specifically, a three dimensional multi-mechanism model considering recoverable, irrecoverable, and damage is constructed. Both the theoretical development and numerical implementation are presented while a three dimensional material subroutine is created. The resultant model shows good agreement with experimental results and demonstrates the necessity of all three mechanisms. This enhanced constitutive routine is then used with composite models to investigate the impact of the different phases.

DEDICATION

To my family who have supported me throughout my studies

ACKNOWLEDGEMENTS

This dissertation and the work included in it would not be possible without the support and assistance of many individuals. First and foremost is my advisor, Dr. Dimitris Lagoudas, who saw something in me when encouraging me to move to Texas these past years and continue on to complete this dissertation. His support and guidance, both in technical and professional regards, have helped mold the research efforts that are manifest in this manuscript. The assistance, guidance, and opportunities that have resulted from my time under his tutelage have been enormous and efforts to that regard are greatly appreciated.

The work included here is a result of collaborations developed as part of the AFOSR MURI (FA9550-09-1-0686) and would not be possible without the assistance of the others involved in this project. Specifically, Professors Karaman and Radovic have not only served on this committee but have also providing tremendous support in terms of material specimens, experimental results, and guidance from the materials science perspective that has been essential and enabled much of what is to be presented. Their students working to this end (especially Ankush Kothalkar, Rogelio Benitez, and Liangfa Hu) also deserve mention for aiding in this effort and producing most of the experimental results that are included in this text and providing technical insight via engaging discussions. From the modeling point of view, interactions with Professor Whitcomb, both via this committee and project, have been insightful and aided in how to approach investigating the micromechanics of these unique complex materials.

Externally, I am extremely fortunate to have had the chance to collaborate with multiple research laboratories. Specifically, the efforts and techniques learned at the

US Naval Research Laboratory (via Drs. Andrew Geltmacher, Rick Everett and others) regarding microstructural characterization and modeling techniques helped form core elements of this work. The contributions of Dr. Siddiq Qidwai to this end are especially worth noting due to his service on this committee and contributions even when geographically separated. The support of Sandia National Laboratories in terms of the fellowship program which has supported the latter part of my work and collaborative internships has been crucial to my progress at Texas A&M. Such efforts have been made possible by the actions of Drs. Tom Buchheit, Jordan Massad, and Amy Sun (amongst others) and their support in this regard has been tremendous.

My development as a student has also been substantially aided by a number of members of the Department of Aerospace Engineering and the group of Dr. Lagoudas. Although there are to many to list here, the support and discussions of Drs. Darren Hartl, Yves Chemisky, Parikshith Kumar, Theocharis Baxevnais, Krishnendu Haldar, and Brent Volk has been invaluable. I would like to especially thank Darren and Brent who helped transform a "yankee" from Illinois into a reasonable approximation of an Aggie and helped guide my transition both to Texas and to the graduate student life. Many insights have also resulted from discussions with fellow students especially Majid Tabesh, Frank Gardea, Hieu Truong, and Austin Cox (amongst many others) and their support and encouragement is appreciated. The efforts of Bonnie Reid to help bring order to the sometimes confusing and complicated situations in the office were also tremendously helpful and her assistance was invaluable throughout this process.

Additionally, none of this would have been possible without the aid of my immediate (Mom, Dad, Kevin, and Susan) and extended family. The path that has brought me to this point is different from their experiences and their patience, assistance, and understanding during this endeavor have been invaluable.

Finally, I would like to acknowledge the support of the NSF IGERT fellowship which supported part of this study.

TABLE OF CONTENTS

Page

LIST OF FIGURES

LIST OF TABLES

1. INTRODUCTION

Shape Memory Alloys (SMAs) are a unique class of multifunctional materials that are currently being explored for increasingly diverse applications like actuators [29], sensors, MEMS devices [28] or vibration dampeners. Such implementations have been investigated in industries including aerospace [46, 99], civil [69, 172, 218], biomedical [71, 151, 158], and petroleum [5] and seek to take advantage of the unique reversible solid-to-solid phase transformation characteristic of this class of materials. Specifically, at high temperatures, the crystallographic configuration of SMAs is austenitic and exhibits a high-symmetry (typically cubic) structure. If the temperature (or load) is sufficiently decreased (increased) the material undergoes a martensitic transformation to a lower-symmetry (*e.g*, orthorhombic or monoclinic) martensitic structure. Because of the lower symmetry, martensitic structures may take two forms - *twinned* (or *self-accommodated*) and *detwinned*. The former is observed at lower applied loads and corresponds to martensitic variants self-arranging with no macroscopic shape change. A detwinned structure, however, corresponds to the case in which sufficient mechanical load is applied to select a preferential martensitic variant(s) yielding macroscopic shape change. This change in crystal structure from austenite to martensite leads to, amongst other things, changes in the thermoelastic properties of the material and, more importantly, (in the case of detwinned martensite) inelastic deformations of approximately 1-8%. Additionally, at the macroscale, this change further manifests as a hysteretic response in stress-strain or strain-temperature space making it attractive for use in damping or actuation

applications through specific thermomechanical loadings (for details on SMAs please see the texts of [122, 171]).

To better discuss the responses of SMAs, a stress-temperature phase diagram (an example of which is presented in Fig. 1) denoting the current crystallographic structure of the material is commonly used. The forward (austenite to martensite) and reverse (martensite to austenite) transformations producing the SMA behaviors of interest are typically defined in terms of four transformation surfaces - the martensitic start, M_s, and finish, M_f, surfaces for forward transformation and austenitic start, A_s, and finish, A_f, surfaces for reverse. The start surfaces correspond to the stress-temperature conditions in which transformation is initiated and the two finish surfaces correspond to transformation completion. These surfaces are commonly defined in terms of the zero-stress transformation temperatures (denoted M_s^0, M_f^0, A_s^0 and A_f^0) determined via calorimetry measurements. The strong thermomechanical coupling of the SMA may be seen in the phase diagram via the change in these surfaces with stress and/or temperature and may often be considered via the stress influence coefficients, C^M and C^A, for forward and reverse transformation, respectively. Two key SMA behaviors may also be described via the phase diagram - the *shape memory effect* (which gives SMAs their name) and *pseudoelasticity*. The former effect corresponds to a material which is initially in austenite being cooled into a twinned martensitic configuration. Mechanical loading then detwins the martensite leading to a pseudo-plastic type response with apparent permanent deformation. Subsequent heating, however, recovers these strains and returns the material to its remembered austenitic state. This is referred to as the *one-way shape memory effect* (OWSME) as an extra mechanical step is needed to produce the inelastic strains of interest. The *two-way shape memory effect* (TWSME), on the other hand, refers to a material which, under no applied load, produces observable macroscopic inelastic

strain corresponding to transformation via purely thermal loadings. Development of TWSME is typically associated with residual stress developed induced via various processing steps. In engineering practice, the SME is typically taken advantage of via an *actuation* loading path in which a mechanical bias load sufficient to induce detwinning is applied at a high temperature and the SMA component is subjected to a thermal cycle. Such a loading path is depicted as path (A) in Fig. 1. Pseudoelasticity, on the other hand, refers to a material which is initially austenitic undergoing a mechanical loading step that transforms the material to detwinned martensite. If the temperature is sufficiently high, above the zero-stress austentitic finish temperature, A_f^0, the corresponding inelastic deformation is recovered via unloading giving the stress-strain curve a distinctive flag shape and returning the SMA to its initial state. This path is depicted in path (B) of Fig. 1. Note, if the temperature is not above A_f^0, complete recovery does not occur leading to unrecovered inelastic strain. Such a path is sometimes referred to as pseudoplastic.

In the decades since the first observations of the shape memory characteristics in NiTi at the Naval Ordinance Laboratory in the 1960's [44] (thereby leading to the name NiTiNOL), substantial research into SMAs has lead to and continues to produce an impressive body of work with rapidly expanding use in the aforementioned commercial sectors [111]. As such, substantial research has been performed in terms of finding ways of expanding the use of these materials via either filling in the material-property space or new applications. With respect to the former, Ashby and Breéchet [9] proposed two possible avenues: creation of (i) new alloys and material systems or (ii) hybrid materials. Efforts towards the first approach have resulted in the production of shape memory polymers with larger deformations at lower stresses [136, 200], high temperature SMAs (HTSMAs) whose transformation occurs at temperatures far exceeding conventional SMAs [80,150], and magnetic

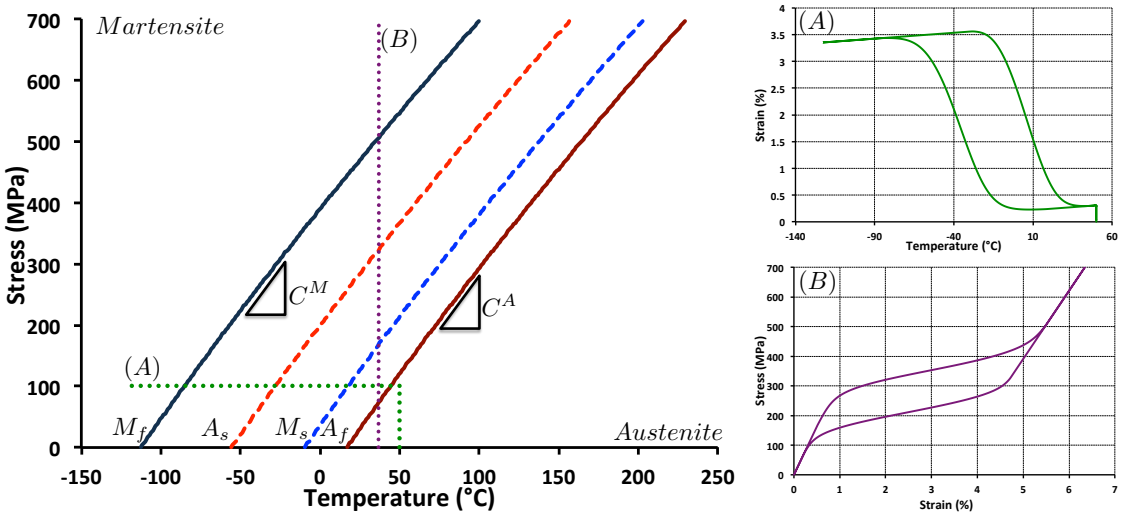

Figure 1: SMA Characteristics: (Left) Stress-temperature phase diagram of an SMA (left) with transformation surfaces M_s, M_f, A_s, and A_f indicated. (Right) Example actuation (top) and pseudoelastic (bottom) responses with loading paths denoted in phase diagram as (A) and (B), respectively. Presented results correspond to a NiTi (50.8 at% Ni) material with properties given by Table 3 of Lagoudas *et al.* [124] and responses determined via model of that same work.

SMAs (MSMAs) whose response to magnetic excitations overcomes the frequency restriction of common SMAs [116, 185]. The latter consideration, however, holds more potential and has been extensively explored. Specifically, a variety of SMA composites have been developed that seek to combine the existing properties of two unique material classes – composites and multifunctional materials.

The first SMA composite was manufactured in the late '80s by Rogers and Robertshaw [207] who embedded NiTi wires in a laminated polymer matrix composite (PMC). Initial investigations building on this effort focused on using the SME effect of the SMA wires in two ways – the so-called active property tuning (APT) and active strain energy tuning (ASET) – for sound, vibration, and damping control [26, 27, 146, 147, 203–207, 209]. The former response essentially focused on

inserting self-accommodated NiTi wires into the PMC matrix and then using temperature to induce transformation to the thermoelastically stiffer austenitic phase while the latter used detwinned wires to take advantage of both the stiffening and development of internal stresses via SMA recovery to enable even greater control. Applications and investigation considering the possibility of developing actuators soon followed by Chauhry and Rogers [52], Lagoudas and Tadjbakhsh [130, 131], and many others [16, 36, 37, 232]. Interest in using other matrix systems focused primarily on using the SME to strengthen the matrix material and increase the effective flow stress [235] – especially in aluminum matrix composites [7]. Ceramic reinforcement in NiTi (in the form of TiC particles) for similar purposes was also considered in a series of efforts by Dunand and coworkers [72,87,88,155]. Since these first pursuits, the number of applications for SMA composites has expanded greatly and gone beyond the original concepts of Roberts and coworkers. From an application standpoint, SMA composite actuators have been used to develop a number of bio-inspired robots (*e.g*, turtles [117], jellyfish [224, 225], and inchworms [229]) while morphing aerospace structures [95,175,176,217,223], and sensors [182,194] have been taken from the conceptual stage to actual development. The utilization of SMA reinforcement for strengthening and damage suppression has also been expanded into a number of new material systems and complementary self-healing methods have been extensively explored [6,45,85,118]. For a more comprehensive discussion, early reviews may be found in the work of Wei *et al.* [231] and, from the polymer matrix standpoint, Neuking *et al.* [165] while a more comprehensive (and recent) review in this area is presented by Lester and coworkers [137].

In addition to the growth of applications, the number and type matrix and reinforcing materials used in SMA composites has also greatly expanded. Examples of such variety are presented in Fig. 2 in which polymer (Fig. 2a,b), metal (2d,e), and

ceramic matrix(2c) materials have all been investigated in addition to porous media (2f). From these examples, it is evident that these composite materials encompass not only a range of matrix materials but also diverse microstructructures running from short (2b) and long fiber (2a) reinforcement to more heterogeneous distributions (2c). With respect to polymer based systems, such gains have manifest as novel architecture of the reinforcing SMA phase in the form of braided tubes [101], incorporation as warp threads [234], and ribbons with patterned holes [8]. In the metallic matrix realm, advances in manufacturing techniques (typically powder based) such as melt infiltration, pressing, and other sintering approaches have lead to the development of controlled porosity SMAs (primarily NiTi through spaceholder techniques) [14, 31, 167], Mg (both for increasing the effective yield strength [13] and damping [145]), and Al matrix systems [66, 94, 187] (including those with both NiTi and SiC reinforcement [53, 106]). Reinforcement of NiTi via additions of CNTs [79, 133] and α-Al_2O_3 [78] has also been explored. More recently, however, novel spark plasma sintering techniques (SPS) have been used to develop SMA-MAX phase ceramic composites (*e.g*, $NiTi - Ti_2AlC$, $NiTi - Ti_3SiC2$) [108,120] that leverage the inelastic responses of both the SMA and MAX phase to not only strengthen the system but also create a metal-ceramic system with an advantageous nonlinear constitutive response. An example of the latter $NiTi - Ti_3SiC_2$ case is presented in Fig. 2c.

Specifically, SMA-MAX phase composites have been proposed as an innovative and novel metal-ceramic composite for extreme environments by seeking to take advantage of the inelastic responses characteristic of each material. For the SMA, the mechanism of interest is the reversible martensitic transformation while, in the case of the MAX phases, the deformations assumed primarily to be associated with its kinking response [22, 23] are investigated. This unique behavior has experimen-

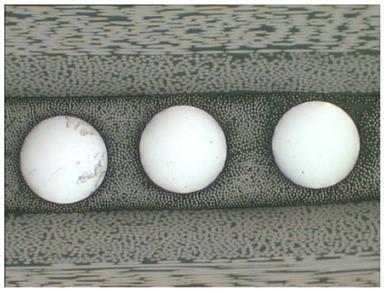

(a) Carbon/epoxy matrix reinforced with small diameter (0.25 mm) NiTi wires. Reprinted from [240] with permission from Elsevier.

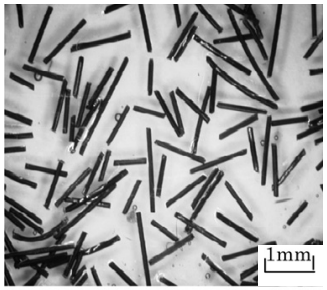

(b) ER3 epoxy resin matrix reinforced with 16.1 wt%, dispersed short (≈2 mm) NiTi fibers. Reprinted from [168] with permission from Elsevier.

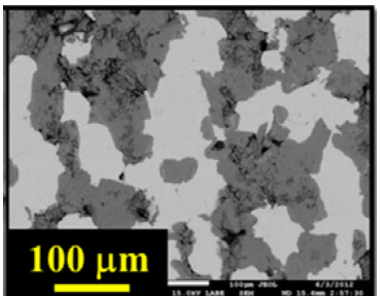

(c) $NiTi - Ti_3SiC_2$ composite produced via spark plasma sintering. Reprinted from [108] with permission from Elsevier.

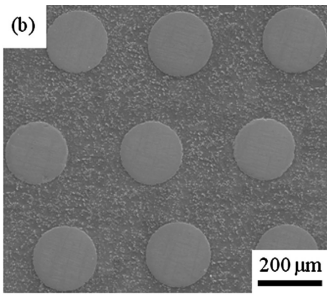

(d) Al matrix (reinforced with 5% SiC particles) composite reinforced with long NiTi fibers. Reprinted from [106] with permission from Elsevier.

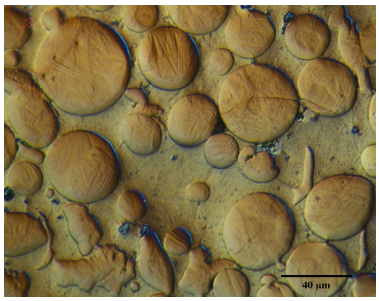

(e) Indium matrix composite with CuAlNi SMA particle reinforcement producing a high damping material. Reprinted from [208] with permission from Elsevier.

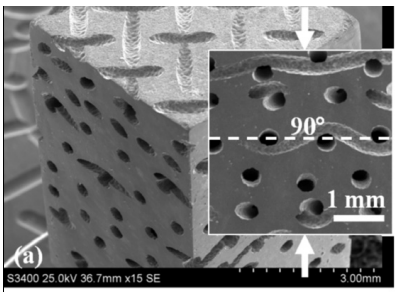

(f) Porous NiTi specimen with controlled 2D micro channels produced by via sacrificial steel meshes. Reprinted from [166] with permission from Elsevier.

Figure 2: Examples of different SMA reinforced polymer (a,b), ceramic (c), and metal (d-e) matrix composite and porous (f) systems that have recently been developed [137].

tally been observed to result in both repeatable and recoverable hysteretic loops dissipating roughly a quarter of the mechanical energy [23]. Such a response has been primarily attributed to the formation of incipient kink bands (IKBs) [24, 238] although there is still some debate in the literature about the exact cause this response [43, 113, 186]. Additionally, the development of permanent kink bands in

these materials leads to a unique damage tolerant characteristic [20,22] not often observed in ceramic materials. This combination of inelastic responses provides a novel composite with a number of unique characteristics versus traditional metal-ceramic composites. For instance, given the utilization of two inelastic constituents, the composite has a higher mechanical damping [120] of interest to hypersonic vehicles. More interestingly, the potential of the development of preferential, and controllable, residual stress states in the composite through the interaction of two characteristic response of the composite materials. One such possibility is thermally induced SMA transformation strains to impart permanent deformations in the MAX phase constituent and develop a residual stress state. Such a reference state could serve to not only train in an effective, composite two-way shape memory behavior (as has been experimentally observed [120]) but also to apply a bias load on the ceramic phase and take advantage of its superior mechanical characteristics (especially strength).

To fully consider such effects, and help explain experimental observations, a model for the thermomechanical response of SMA-MAX phase composites considering the various inelastic mechanisms operative in the system is needed. Such a model has not been previously considered, however, and will be pursued through this work. A previous model by Cheng *et al* [57]. did investigate the effective thermal properties of the $\mathrm{NiTi} - \mathrm{Ti_3SiC_2}$ system, but they did not consider the mechanical response or constituent inelasticities. Additionally, to determine the effective thermomechanical response of the composite, constitutive models of both the SMA and MAX phase materials are needed. With respect to the former, constitutive modeling of SMAs is an established field and a number of models have been developed and implemented [127, 178]. The same can not be said for the MAX phase materials as an appropriate model for use in these investigations is lacking and will also be investigate here. Therefore, to further consider the development of an SMA-MAX phase

composite model relevant topics in (*i*) MAX phase constitutive modeling and (*ii*) SMA composite modeling will be introduced.

1.1 MAX Phase Constitutive Modeling

Since the first production of dense Ti_3SiC_2 by Barsoum and El-Raghy in 1996 and corresponding observation of its unique thermomechanical characteristics [19], an increasing number of investigations (primarily experimental) have been undertaken to explore the characteristics of this and the numerous other MAX phase ceramics. This designation is used to refer to the ternary nano-layered carbides and nitrides with the general form of $M_{n+1}AX_n$ ($n = 1,\ 2$ or 3) where M is an early transition metal, A is an A-group element, and X is carbon or nitrogen [17, 22]. The most common of these are the aforementioned Ti_3SiC_2 and Ti_2AlC which will also be the specific compositions considered in this work. In general, the interest in the MAX phases arises from their high elastic stiffnesses, good electrical and thermal transport characteristics while maintaining low coefficients of thermal expansions, and thermal shock resistance while at the same time being readily machinable and damage tolerant [22].

Of particular interest is the unique thermomechanical response of these MAX phases. At low (room) temperature and slow loading conditions, repeatable and reversible cycles up to 1 GPa were observed in Ti_3SiC_2 [23]. A similar hysteretic response has also been reported in Ti_2AlC [238]. This behavior is athermal at low and moderate temperatures and remains unchanged up to $\approx$900°C. Above this temperature, the additional thermal energy aids in the dissociation of the dislocation structures responsible for the reversible cycles leading to open, rate-dependent hysteresis loops [23, 237]. For the "low" temperature response of interest, Barsoum and cowork-

ers have associated this hysteretic response with the formation of incipient kink bands (IKB) in properly aligned grains. These structures are comprised of parallel walls of dislocations with opposite signs which have not yet separated/dissociated and thus remain attracted to each other at their ends. Therefore, upon unloading, the various dislocations run back and annihilate each other [23, 24] leading to the observed reversible response. Although no direct observations of these IKB have been made, their formation is supported by high c/a ratios in the crystal structures which make twinning unlikely and the fact that dislocations are limited to motion on the basal planes [23]. Recent electron backscatter diffraction (EBSD) observations[1], however, have noted low-angle grain boundaries that occur in loop-like structures in grains of polycrystalline Ti_2AlC after mechanical loading. These dislocation structures are formed in the fashion expected of IKBs but are found in grains with moderate Schmid factors and not in grains aligned with loading as postulated by the IKB theory. With respect to the permanent deformations, and following the IKB explanation of the MAX phase response, after sufficient load has been applied, the IKB walls separate leading to the formation of permanent mobile dislocation walls which eventually coalesce to form permanent kink bands (KBs) and the corresponding delamination deformations and damage [24]. It is these kink bands which have been proposed to imbue the MAX phases with their damage tolerant characteristics [20, 21, 74]. As such, even at low temperatures and quasistatic loadings some MAX phases have been observed to exhibit a graceful failure [18]. High-strain tests at room temperature, have also demonstrated pseudoductility in Ti_2AlC [32]. At higher temperatures ($\approx$1100-1200°), however, a temperature and strain-rate dependent brittle to ductile transition has been noted in the failure response of Ti_3SiC_2 [196].

[1]Private communication of unpublished results of work by R. Benitez and Prof. M. Radovic of the MSEN department at Texas A&M University

Although the previous discussions have focused on explaining the reversible response of MAX phases through the notion of incipient kink bands, the lack of direct experimental observation has lead to some discussion with regard to the source of this behavior. Notably, some recent neutron diffraction experiments [93, 113] have been used to argue against the IKB mechanisms as the source of the observed behavior. Specifically, Jones et al. [113] attributed the macroscopically observable response to a Bauschinger like effect. Specifically, experimental *in-situ* x-ray diffraction measurements lead to observation of slip and permanent deformations occurring in soft grains (those roughly 40° from the compression axis) while hard grains (oriented along or perpendicular to the compression axis) remained elastic during loading. The macroscopic hysteresis, as postulated, is associated with residual stresses due to slip in the soft grains and repeated dislocation generation in these grains during loading that is, upon unloading, driven back due to elastic strains in the hard grains. Furthermore, the authors argue against the concept of IKB formation due to the fact that IKB formation would not in itself lead to residual strains. Their numerical predictions, which do capture some of the qualitative details of the experimental responses, do not quantitatively predict or explain all of the features observed in the mechanical tests. [113] Additionally, the formation of small permanent deformations have been previously reported in works arguing for IKB as the root cause (*e. g*, Zhen *et al.* [237]) and Barsoum and Radovic [22] explicitly state that small plastic strains are occasionally necessary to nucleate IKBs. In a similar fashion, Guitton *et al.* [93] used *in-situ* neutron diffraction to study the response of Ti_2AlN and proposed a mechanism depending on hard and soft grains interacting to generate dislocations in grains not aligned with the compression axis. Limited quantities of dislocations are nucleated such that there is no hardening in the soft, plastic grains and the dislocations either run back to the nucleation site or cross

the entire grain to the boundary during unloading [93]. Going a different direction, Poon and colleagues [186] neglect any reversible mechanism in their analysis of the response of Ti_2AlC and instead attribute all hysteretic activities to crack friction. This, however, neglects previous (and recent) experimental evidence indicating the presence of a recoverable/reversible deformation even at low and mild stress levels without obvious permanent deformations [43]. Bearing all of this in mind, the notion of the formation of IKB-like dislocation structures as the cause of the reversible deformation is adopted here (although following the EBSD observations it is not assumed that these form in grains aligned with the loading direction). This is due to the wealth of supporting observations such as the greater absolute dissipation of porous versus bulk specimens [220, 238] which support a kink-type mechanism and the recent EBSD observations. Furthermore, the fact that the IKB-like dislocation structures observed via the aforementioned EBSD investigation occur in the "soft" grains of the neutron diffraction studies shows agreement with those results.

Due to these interesting properties and responses, there has been interest in the MAX phases for a variety of engineering applications. In order to utilize the material in various applications, however, predictive models of the behavior need to be developed. To this end, Barsoum and colleagues [24] have developed a physical model based on the kinking theory of Frank and Stroh [81] for the IKB response. This model, although useful for the analysis of experimental results, is not formulated in 3D or prepared for the prediction of the MAX phase responses. Similarly, two one-dimensional models based on hysteretic unit operators [114] and the Preisach-Mayergoyz model [239] have been constructed but are limited to IKB regimes. In contrast to this, Poon and coworkers [186] focused on the permanent deformation regime and utilized a one dimensional formulation based on crack-sliding to simulation and predict the hysteresis loops in the regime they postulated as being purely

due to frictional crack-sliding. Finally, Jones *et al.* [113] utilized a elastic-plastic self consistent model (EPSC) with a number of simplifications (*e.g*, single slip system and lack of work hardening) which even the authors admit limit their results to be considered only as approximate. Bearing all this in mind, there is not currently a model which can capture all the relevant mechanisms or has been developed and implemented for use in a three dimensional finite element package.

1.2 SMA Composite Modeling

Broadly speaking, techniques for the analysis of composite and heterogeneous materials may categorized as either a *mean-field* or *full-field* approach [132]. Mean-field techniques focus on dividing the composite microstructure into a series of distinct phases and determining the average state of the different phases and composite. Such approaches are typically based on either the classical results of Eshelby [77] and his Equivalent Inclusion methods [77, 160, 195] (*e.g*, the Mori-Tanaka [30, 159, 160] and Self-Consistent [105] methods) or variation principles using linear thermoelastic comparison composites [162, 163]. Full-field approaches, on the other hand, focus on the development of a computational domain and solving for the resultant deformation fields via numerical techniques, typically the finite element method (FEM), and averaging for the effective response. These methods may be subdivided according to the computational domains used – unit cell (UC) or representative volume element (RVE) [181]. The former is used with periodic structures in which a repeating heterogeneous structure may be identified while the latter refers to the identification of a statistically representative volume of a nonuniform microstructure (see Pindera *et al.* [181] for a lengthier discussion). Both methodologies have previously been used for the study of heterogeneous media with nonlinear constituents and comparisons

between various approaches considering elastic-plastic [48, 68, 90, 132, 179, 210, 211], viscoplastic [67, 180], and damage [49] constituent responses may be found in the literature. Here, the prior application of these approaches to SMA composites is presented to motivate the models developed for the case of SMA-MAX composites of interest in this study.

Initial SMA composite modeling efforts focused on the use of analytical techniques to develop models of SMA actuators [52, 130, 131] and composite plates [112, 205]. Mean field approaches utilizing the Mori-Tanaka method soon followed to predict and analyze the response of SMA composites [33, 39, 41, 126, 235]. Specifically, Yamada *et al.* used such an approach to demonstrate the potential of the SME to increase the effective flow-stress of an SMA reinforced Al composite. The ability of micromechanical methods to capture the thermomechanical response was demonstrated by Lagoudas *et al.* [126] who analyzed the case of an SMA fiber reinforced composite and compared the results of both a UC (using the FEM) and the Mori-Tanaka method. Noting this applicability, Boyd and Lagoudas used the Mori-Tanaka method to explore the composite transformation characteristics of SMA composites and determined the effective transformation surfaces [39] and demonstrated the possibility of developing an effective TWSME even if the SMA only exhibits the OWSME [41]. The impact of material variability on the effective composite response was considered by Bhattacharyya and Lagoudas [33] who discretized the SMA fiber reinforcement into a series of distinct phases with different transformation temperatures and used the Mori-Tanaka method to investigate the impact of the probabilistic distribution of these temperatures on the effective composite response. For the analysis of SMA-based structures, finite element techniques using layer-wise laminate approaches were developed and used for the analysis of active metal-laminate composites [125, 129].

As a result of increasing utilization of SMA composites with a wide variety of

matrices and intended applications, modeling approaches have also advanced substantially. With respect to mean-field approaches, the Mori-Tanaka, Self-Consistent, and variational methods have all been utilized to study a variety of materials. A summary of these various efforts are presented in Table 1.1. First, regarding the Mori-Tanaka method, the behavior of porous SMAs has been studied by a variety of authors [75,76,164,190,236]. Zhao and Taya [236] considered an analytical approach and focused on solving for the various stages of the pseudoelastic curve while Nemat-Nasser and coworkers [164] utilized a three phase approach treating austenite and martensite separately. Qidwai *et al.* [190] and Entchev and Lagoudas [75, 76] both utilized an incremental Mori-Tanaka approach like that developed by Lagoudas *et al.* for a metal-ceramic composite [128]. The former effort of Qidwai and coworkers [190] compared their micromechanical results to those of an UC and demonstrated that the micromechanical averaging approach overpredicted the initial stress for phase transformation while the latter investigation of Entchev and Lagoudas [75] developed an explicit relation for the macroscopic inelastic strain and considered the impact of pore shape. In a follow-up work, Entchev and Lagoudas [76] also incorporated transformation induced plastic (TRIP) strains into their constitutive formulation and explored the impact of the change in SMA thermoelastic properties on the effective response. Additional efforts via mean-field approaches have focused on capturing the influence of precipitates on the macroscopic behavior. For instance, Collard and coworkers [61,62] investigated the effect of elastic Zr precipitates in a CuZnAl polycrystal through a two scale approach. At the single grain level, the Zr precipitates were embedded in an SMA matrix and the constitutive responses was determined via the Mori-Tanaka method. A self-consistent approach was then adopted to determined the averaged polycrystalline response [61,62]. For an inelastic precipitate, Piotrowski and colleagues [183,184] focused on the response of NiTiNb by treating

the Nb as elastic-plastic, ductile precipitates in a transforming NiTi matrix. In their work, the authors demonstrated that the plasticity in the Nb phase expanded the transformation hysteresis and used used the model to study the response of pipe couplers [183, 184].

Mori-Tanaka based models have also been constructed treating the SMA as

Table 1.1: Mean-field approaches used to investigate SMA-reinforced composites [137]

Methodology	**Reinforcement**	**Matrix**	**References**
Mori-Tanaka	Fiber	Elastomer	[39, 41, 148]
”	”	Metal	[134, 241]
”	Particle	”	[34, 35, 235]
”	–	Porous SMAs	[75, 76, 164, 190]
”	–	Precipitated SMAs	[56, 62, 183, 184]
Self-consistent	Particle	Metal or elastomer	[58, 219]
”	Fiber	Elastomer	[154]
Mori-Tanaka & Self-consistent	–	Precipitated SMAs	[61]
Second order variational	”	Elastomer	[42]

the reinforcement phase. Specifically, Lu and Weng [148] and Zhu and Dui [241] both constructed multi-phase models considering distinct representations of austenite, martensite, and the matrix. In the former case, an elastomer matrix material was investigated and the superiority of fibrous (vs. other) reinforcement in terms of stiffness, ease of transformation, and damping possibilities was demonstrated [148]. The latter studied elastic-plastic matrices (a metal and polymeric material) and considered the effect of reinforcement shape on the residual stresses of the constituents through mechanical loading at different (isothermal) temperatures. Expanding on

previous MMC strengthening efforts (*e.g*, [235]), Lee and Taya [134] considered the interaction of prestrains in the SMA reinforcement and plasticity in the metal matrix and predicted the increase in the effective yield strength through shape memory recovery. Birman [34, 35] developed a three-dimensional "exact inverse" method utilizing the Mori-Tanaka method to determine the effect of transformation on the effective thermomechanical properties and stress state of an SMA reinforced composite [34] and energy dissipation [35].

Although not as prevalent, other mean-field approaches have been used for the analysis of SMA composites. For instance, a self-consistent scheme was constructed by Cherkaoui and collogues [58] and used to study the stress and strain states of the phases as a function of the applied thermomechanical loading. In a subsequent effort by Song *et al.* [219], this model to study the influences of a wide set of loading and phase distribution parameters and noted a strong dependence on these parameters. A separate investigation by Marfia and Sacco [154] also developed a self-consistent formulation. In this case, however, a tension–compression asymmetric SMA constitutive routine was incorporated and the corresponding effects considered. Importantly, as a part of this effort, the authors also constructed a UC FEM to validate their model. Briggs and Ponte Catandeda [42], on the other hand, utilized a second order variational approach to explore optimization of an SMA composite in terms of maximum contraction (via recovery) and bandwidth. From their analysis, it was noted that a soft matrix with restrained fibers could lead to a better response time – albeit with an associated energy penalty.

Mean-field approaches, although potent tools for the quick, efficient analysis of inelastic composites, do have a number of complications and limitations. For instance, microstructures that may be considered are typically somewhat simple. For instance, Eshelby based approaches require an elliptical inhomogeneity shape and a clear dis-

tinct matrix should be evident (self-consistent approaches for polycrystalline materials have been developed). In some more complex microstructures, parameterizing the microstructure in such a way may be difficult if not impossible – *e.g*, two-phase interpenetrating composites with roughly equivalent volume fractions. Additionally, as only phase average responses are considered some issues driven by local stress-concentrations and concerns may not be captured. An example of this is the over-prediction of the pseudoelastic onset stress noted by Qidwai and coworkers [190]. In previous investigations with elastic-plastic materials, it has also been shown that the choice of stiffness tensor (scent, isotropized tangent, or anisotropic tangent) used in the micromechanical formulation produces substantially different inelastic responses (in the form of hardening during yielding) [48]. Such limitations have been investigated and discussed in detail for elastic-plastic materials [48, 181, 211] and are expected with other inelastic reponses (*e.g*, martensitic transformation). One way that has been considered to address many of these concerns is the utilization of computationally more expensive full-field analysis techniques.

In terms of SMA composites, both UC and RVE full-field methods have been utilized and efforts towards this end are presented in Table 1.2. With respect to the former, UC methods have been applied to study a variety of heterogeneous material systems. For instance, Qidwai *et al.* [190] considered the response of porous SMAs considering both open and closed porosity while the response of NiTi fiber reinforced metallic elastic-plastic [64, 65] and elastomer [4] matrix materials has also been explored. In the former investigations, the impact of volume fraction, cross-sectional shape, and pre-strain on both proportional and non-proportional loadings were analyzed [64, 65] while the latter focused on internal stresses induced by the fiber SME [4]. A variety of UCs for different hybrid composites with different reinforcement configurations and latent heat conditions were explored by Aurrichio

and Petrini [12]. Sepiani and Ghazavi [212] treated the problem of an SMA reinforced woven composite under biaxial loadings and noted the substantial impact of the SME on the in-plane behavior of such woven materials. Approaches using asymptotic expansion methods have also been adopted. Specifically, Chatzigeorgiou *et al.* [51] investigated periodic composites with SMA constituents and utilized a step-by-step approach to simultaneously solve the micro- and macroscale problems. The developed framework was used to analyze multilayered systems with metallic elastic-plastic and SMA layers under different combined tension-shear isothermal mechanical loadings. They noted a strong interaction between the transformation and plasticity mechanisms and a loss of convexity in the effective austenite finish yield surface under some combined loadings. The case of SMA wire reinforced composites was investigated via an asymptotic expansion approach by Herzog and Jacquet [102]. The multiscale problem was also tackled by Marfia and colleagues [152,153] by using a self-consistent technique in a computationally efficient fashion.

In a series of investigations, Freed, Aboudi and coworkers utilized the high-fidelity method of cells [2] to study a range of SMA composite materials. For instance, the role of prestressed SMA fibers in concrete materials was explored using both a damage-based [85] and a coupled damage-plastic [82] constitutive model for the concrete matrix. Through these investigations, the ability of such SMA reinforcement to improve the yield strength of the effective concrete was considered. It was shown that higher activation temperatures produced corresponding gains in the preferable prestresses [85] and decreased residual plastic strains in the damage-plastic case [82]. Further studies explored the impact of heat transfer and thermomechancial coupling on SMA reinforced aluminum and epoxy systems and was demonstrated that these effects were more pronounced in the former case [84]. Various combinations of axial and transverse loadings and their impact on the OWSME and TWSME of those

Table 1.2: Full-field approaches used to investigate SMA-reinforced composites [137]

Methodology	**Reinforcement**	**Matrix**	**References**
Unit cell	–	Porous SMAs	[190]
”	Fiber	Elastomer	[4]
”	”	Elastomer or Metal	[64, 65]
”	”	Nylon fiber/ elastomer (Woven composite)	[212]
Homogenization	”	Elastomer	[102, 153]
”	”	Polymer	[12, 83, 84]
”	”	Metal	[12, 51, 83, 84, 152]
”	”	Concrete	[82, 85]
”	–	SMA honeycombs	[86]
RVE analysis	–	Precipitated SMAs	[25]
”	–	Porous SMAs	[10, 174, 189]
”	Particulate	MAX Phase	[57, 141]
”	Fiber	Metal	[119]

same composite systems [83]. In all of these UC cases, however, the computational domains considered remain rather simple – mostly in the form of a single inhomogeneity.

To enable more detailed representations of microstructures, 3D RVEs are often constructed. Unlike UCs which are based on a repeatable microstructural unit, RVEs are invoked to study irregular microstructures in which a statistically representative volume is identified and appropriate computational domain constructed. Although a number of definitions of an RVE may be found in the literature [70,104,110,115], the fundamental premise of an RVE is that the response of the associated computational domain (i) does not depend on the macroscopic boundary conditions [104, 110] and (ii) is sufficiently large such that macroscopic response is spatially independent [70]. The necessary size to address these concerns is a function of micrstructural features and responses and ways to identify the requisite size and sampling techniques have

been presented by Kanit *et al.* [115].

Although extensively utilized in elastic-plastic materials, the adoption of 3D RVEs for the analysis of SMA composites is still somewhat limited. Until recently, most such efforts were with respect to porous SMAs [10, 174, 189]. In the earliest case, Qidwai and DeGiorgi [189] focused on the dynamic behavior of porous NiTi. Importantly, however, they constructed their computation RVE in a statistically-informed fashion using characterization results from X-ray microtomography. Subsequent efforts, however, by Panico and Brinson [174] and Ashrafi *et al.* [10] used a random RVE generation approach. The former effort explored the development of permanent strains in the SMA matrix through pseudoelastic loadings [174] while the latter investigation focused on studying the pressure dependence of the porous RVEs to motivate the development of a constitutive model [10]. A later effort by Baxevanis and coworkers [25] tackled the problem of the impact of precipitates on the effective thermomechancial response of bulk Ni-rich SMAs. To that end, they constructed a series of RVEs with different numbers, and sizes, of precipitates and simulated the response through both pseudoelastic and actuation loading paths incorporating diffusional and coherency effects. A recent extension to this work has focused on predicting the response of such SMAs considering different heat treatments by constructing appropriate RVEs and good agreement between experiments and numerical efforts was shown [63]. In a somewhat different vein, Kohlhaas and Klinkel [119] utilized an FE^2 approach to study different configurations of SMA wire reinforced structures thereby demonstrating the capability of an FE^2 approach to analyze such problems.

In the SMA-MAX phase composite case of interest to this work, a number of complications not yet addressed by the previous composite models may be identified. First, with the exception of the concrete examples, most efforts have focused

on porous, polymer matrix, or metal matrix systems. The impact of the much stiffer ceramic MAX phase on the transformation characteristics (both during elastic and inelastic loading) needs to be addressed. Additionally, although some efforts have looked at the response of these composites through SME recovery (*e.g*, [82,85]) that actuation response with multiple inelastic constituents has yet to be explored. Beyond these constitutive issues, another challenge is posed by the SMA-MAX phase composites and their microstructures. Specifically, the manufacture of the composites (via spark plasma sintering) results in the formation of porosity (up to ≈15% depending on sintering conditions) and the reduction in transformable NiTi - up to half of the initial material may be unable to transform in the worst cases of $NiTi - Ti_2AlC$ composites [108]. This latter effect is primarily associated with NiTi being consumed by interface reactions and corresponding compositional changes and can have a substantial impact on the effective composite response [108]. Therefore, the porosity and non-transforming material are essentially additional phases that must be accounted for in the microstructural model. As most efforts discussed above focus solely on two-phase systems, the incorporation and study of effects related to these phases need to be performed. The exception to this statement is a previous effort by Cheng et al. [57] who analyzed the thermal properties of the $NiTi - Ti_3SiC_2$ composite incorporating both an interphase and porosity. In this study, the interface was shown to play a strong role in lowering the heat flux through the NiTi phase. Their analysis, however, was limited to the purely thermal case.

1.3 Objectives and Specific Aims

As discussed above, recent efforts into the production and characterization of SMA-MAX phase ceramic composites have highlighted a number of interesting responses and characteristics associated with the nonlinear constituents. To further

analyze and expand on these issues, model(s) of these composite systems are needed to not only provide additional insight and aid in understanding the experimental results but also provide feedback in to material developers in terms of ways to improve specific responses. For instance, experimental results have indicated a roughly order of magnitude difference in actuation strain developed during constant stress thermal cycles between $NiTi - Ti_3SiC_2$ and $NiTi - Ti_2AlC$ composites given similar compositional concentrations [120, 141] although the source of this difference is still being explored. Additionally, the role of the microstructure (potentially associated with the previous observation) on the various responses of the composite system needs to be identified and accounted for.

Therefore, in this work, a series of models are constructed to analyze and investigate the response of these composites. Given the complexity of the composite systems (both in terms of microstructure and nonlinear constituents) involved, this is done via a multistage approach. First, in Section 2, micromechanical models of the system are developed to investigate the effective transformation characteristics of stiff, ceramic matrix system and look at the impact of martensitic transformation on load redistribution. To build upon these results, in Section 3, image-based finite element approaches are used to model the response of $NiTi - Ti_2AlC$ system and investigate the interaction of nonlinear constitutive response of the different phases. Importantly, the impact of the additional phases present in the system on the effective response are explored.. These investigations focus on the development of permanent deformations in the Ti_2AlC and neglect some of the other inelastic responses. Section 4 seeks to rectify this problem and develop a constitutive model for polycrystalline MAX phases accounting for multiple inelastic mechanisms and discusses the numerical implementation of said model. This expanded model is then used in Section 5 to consider the impact of these additional mechanisms and consider

the relative impact of the different mechanisms. Concluding remarks summarizing this work and thoughts towards future efforts in this area are give in Section 6.

2. EFFECTIVE SMA COMPOSITE TRANSFORMATION CHARACTERISTICS*

Before proceeding into analysis of specific loading paths, it is beneficial to consider and investigate the effective transformation characteristics of these composites. Specifically, given the strong contrast in thermomechanical materials and large transformation strains that may develop in the SMA phase, establishing the interaction between these deformations and the matrix remains crucial in understanding any stress redistribution or similar effects in such composites. These behaviors will play a strong role in the following analysis and understanding them ahead of time will aid in the interpretation of the results. Therefore, a micromechanical model of the composite system is constructed and used to determine the state of the material at the beginning and end of transformation and consider both the effective behavior of the composite system and the interaction between the various constituents. Therefore, in this section the model is introduced in Section 2.1 and results are then presented in Section 2.2. A summary of the important findings are then presented in Section 2.3.

2.1 Modeling Approach

In developing the model for the composite system two components are needed – constitutive models of the phases and a micromechanical model. With respect to the former, a reversible constitutive model for SMAs is introduced in Section 2.1.1 while a micromechanical approach capable of describing an appropriate composite is introduced in Section 2.1.2. The two models are then combined in Section 2.1.3 to

*Portions of this chapter are reprinted from "Transformation Characteristics of SMA Composites" by B. T. Lester, Y. Chemisky, and D. C. Lagoudas *Smart Materials and Structures*, **20**, 094002 ©IOP Publishing [138].

develop a framework capable of describing the behaviors of SMA composites.

2.1.1 Shape Memory Alloy Modeling

Constitutive modeling of SMAs has been extensively explored in the past quarter century or so. Broadly speaking, these efforts focus on two main thrusts - micromechanical [178] and phenomenological [127] approaches. The former efforts focus on modeling the result of a single crystal from a micromechanical standpoint by focusing on the kinetics of transformation and then averaging the response over a polycrystal to get an effective response [109, 142, 177]. Typically such approaches are computationally intensive and ill-suited to large scale structural simulation. Phenomenological models, on the other hand, focus on utilizing appropriate internal state variables to describe the macroscopically observable response and enable much more efficient modeling of an SMA polycrystal. A number of such models (*e.g*, [55, 124, 173]) have been constructing using a variety of ensembles of internal state variables (ISVs) (typically various combinations of martensitic variant volume fractions and transformation strain tensors) and used to model the response of SMA structures. In the following work, the recent phenomenological model of Lagoudas *et al.* [124] will be utilized as it is developed with an eye towards the efficient analysis of the actuation response of SMA composites and has been used to analyze a variety of SMA structures and components [96, 169]. Furthermore, this model is an extension of earlier forms of the model of Boyd and Lagoudas [40] and the unified model of Lagoudas *et al.* [125]. Subsequent efforts have further developed the model [123, 192]. For use in the micromechanical model development and aid in subsequent discussion, the model is briefly presented.

The work of Lagoudas *et al.* [124] develops a phenomenological model for the macroscopic behavior of SMAs. Specifically, an internal state variable approach

is adopted which utilizes continuum thermodynamics to derive constitutive relations [59, 60]. The martensitic volume fraction, ξ, and transformation strain tensor, ε_{ij}^{tr}, are used as state variables to capture the effects of the changing internal crystallographic configuration on the macroscopic material response. From the resulting analysis of the free energy, an additive strain decomposition is returned which may be written as (in an incremental, rate-independent form[2]),

$$d\varepsilon_{ij} = d\varepsilon_{ij}^{el} + d\varepsilon_{ij}^{th} + d\varepsilon_{ij}^{tr}, \tag{2.1}$$

with $d\varepsilon_{ij}$, $d\varepsilon_{ij}^{el}$, and $d\varepsilon_{ij}^{th}$ being the total, elastic, and thermal strain increments. The total strain increment, $d\varepsilon_{ij}$ is assumed to be prescribed by the boundary value problem of interest while the thermoelastic strain increments may be written as,

$$d\varepsilon_{ij}^{el} = M_{ijkl}\left(\xi\right) d\sigma_{kl} + dM_{ijkl}\left(\xi\right) \sigma_{kl}, \tag{2.2}$$

and

$$d\varepsilon_{ij}^{th} = \alpha_{ij}\left(\xi\right) dT + d\alpha_{ij}\left(\xi\right) \left(T - T_0\right), \tag{2.3}$$

where M_{ijkl} and α_{ij} are the current fourth-order compliance tensor and second-order coefficient of thermal expansion tensor, respectively. External state variables, the Cauchy stress and temperature, are denoted σ_{ij} and T with T_0 being a reference, strain free temperature. In the two preceding relations, an explicit dependence of the thermoelastic tensors on the martensitic volume fraction is shown. Previous investigations have shown that the rule of mixtures is sufficient to capture the evolution [39] and the current compliance and thermal expansion tensors may be given as $M_{ijkl} = M_{ijkl}^{A} + \xi \Delta M_{ijkl}$ and $\alpha_{ij} = \alpha_{ij}^{A} + \xi \Delta \alpha_{ij}$, respectively, and a superscript

[2]In this relation, and all that follow, typical Einstein notation convention is assumed and utilized.

A (or M) denote the austenitic (martensitic) property. The Δ is used to define the difference between the martensitic and austenitic values - *e.g*, $\Delta\alpha_{ij} = \alpha_{ij}^{M} - \alpha_{ij}^{A}$. In what follows, the explicit dependence of the thermoelastic properties on ξ will be assumed and not shown for brevity and it is assumed that each phase is thermoelastically isotropic.

Next, the evolution of the inelastic transformation strain needs to be defined. To this end, it is postulated that transformation is a volume-preserving, shear based deformation [192] and the transformation evolves with (and only with) changes in the martensitic volume fraction leading to an evolution expression of the form,

$$d\varepsilon_{ij}^{tr} = \Lambda_{ij}^{t} d\xi, \qquad \Lambda_{ij}^{t} = \begin{cases} \frac{3}{2} H^{cur}\left(\sigma^{VMeff}\right) \frac{\sigma'_{ij}}{\sigma^{VMeff}} & d\xi > 0 \\ \frac{\varepsilon_{ij}^{tr-rev}}{\xi^{rev}} & d\xi < 0 \end{cases}, \tag{2.4}$$

where σ'_{ij} is the deviatoric stress tensor defined via $\sigma'_{ij} = \sigma_{ij} - \frac{1}{3}\sigma_{kk}\delta_{ij}$ (δ_{ij} being the kronecker delta) and σ^{VMeff} is the von Mises effective stress and is defined as $\sigma^{VMeff} = \sqrt{\frac{3}{2}\sigma'_{ij}\sigma'_{ij}}$. The current transformation strain magnitude, H^{cur} is assumed to be a function of the effective stress magnitude [95, 124] and is given as,

$$H^{cur} = \begin{cases} H_{min} & \sigma^{VMeff} \leq \sigma_{crit}^{VMeff} \\ H_{min} + (H_{sat} - H_{min})\left(1 - e^{-k\left(\sigma^{VMeff} - \sigma_{crit}^{VMeff}\right)}\right) & \sigma^{VMeff} > \sigma_{crit}^{VMeff} \end{cases}, \tag{2.5}$$

with H_{min} and H_{sat} being the minimum and maximum observed transformation strain magnitude corresponding to any observed TWSME behavior and full detwinning, respectively. Fitting terms (k and σ_{crit}^{VMeff}) are used to approximate the evolution of macroscopic inelastic strain magnitude due to the stress dependence of the detwinning process without introducing an extra internal state variable and the ensuing additional complexity and computational cost. The form of the reverse transfor-

mation tensor is selected to enforce the physical constraint that when the material is fully austenitic ($\xi = 0$) no transformation strains should be present ($\varepsilon_{ij}^{tr} = 0$). Therefore, $\varepsilon_{ij}^{tr-rev}$ and ξ^{rev} correspond to the transformation strain tensor and martensitic volume fraction at reversal.

Finally, to complete the previous relations, the increment of martensitic volume fraction ($d\xi$) needs to be found. This is done by using the transformation strain evolution equation (Eqn. 2.4) and the second law of thermodynamics. Through this process, a thermodynamic driving force conjugate to transformation, π^t, is found and may be given as[3],

$$\pi^t = \sigma_{ij}\Lambda_{ij}^t + \frac{1}{2}\sigma_{ij}\Delta M_{ijkl}\sigma_{kl} + \sigma_{ij}\Delta\alpha_{ij}\left(T - T_0\right) + \rho\Delta s_0 T - \rho\Delta u_0 - f^t. \tag{2.6}$$

In Eqn 2.6, ρ, s_0, and u_0 are the material density, reference entropy, and reference entropy, respecitively, and f^t is the smooth hardening function which is solely a function of the martensitic volume fraction and material parameters. Utilizing this thermodynamic driving force, a transformation function (analogous in purpose to a yield function in plasticity) of the form,

$$\Phi^t = \begin{cases} \pi_{fwd}^t - Y_{fwd}^t\left(\sigma_{ij}\right) & d\xi > 0 \\ -\pi_{rvs}^t - Y_{rvs}^t\left(\sigma_{ij}\right) & d\xi < 0 \end{cases}, \tag{2.7}$$

is assumed in which Y^t is the critical value for forward or reverse martensitic transformation and is assumed to depend on the stress following experimental observations ($Y_\gamma^t = Y_0^t + D\sigma_{ij}\Lambda_{ij}^{t-\gamma}$) [95, 124]. The subscripts fwd and rvs are used to indicate the form of the functions for forward and reverse transformation, respectively. This

[3]Following common SMA modeling practice it is assumed that the specific heats of the two phases are the same so that $\Delta c = 0$

constitutive model has previously been numerically implemented as a user material subroutine (UMAT) [96, 124] in Abaqus [1] via an elastic-predictor, inelastic corrector approach with a convex cutting plane - return mapping correction scheme [213]. Although not unconditionally convergent, past studies have shown that for a vast majority of problems of interest the convex cutting plane approach is sufficient to achieve convergence with substantial increases in computational speed [191].

2.1.2 Micromechanical Model

A micromechanical approach capable of describing the response of an SMA composite at the beginning and end of transformation is needed. Specifically, the problem of a thermoelastic matrix with embedded SMA inhomogeneities is studied. By focusing on the state of the material at the beginning and end of transformation, effects like thermal expansion mismatch and transformation strains developed during a cycle may all be considered to be inelastic eigenstrains and the problem becomes that of an inhomogeneous inhomogeneity. Therefore, the results and methodologies of Eshelby [77] and his equivalent inclusion method [160, 195] may be leveraged.

To develop the model of interest, a composite like that presented in Fig. 3a is considered. Specifically, the general composite being investigated is comprised of N elliptically shaped inhomogeneities each comprising a volume fraction c^i (with the constraint $\sum_{i=0}^{N} c^i = 1$) embedded in a distinct matrix. In this case, it is assumed that the SMA constituents are the composite reinforcement and are treated as inhomogeneities. The elastic stiffness of the inhomogeneities and matrix are given by L^r_{ijkl} and L^0_{ijkl}, respectively. In the following, a superscript will be used to denote the phase of the variable being considered with "0" being the matrix while an overbar is used for effective, composite measures. The composite is taken to have an effective

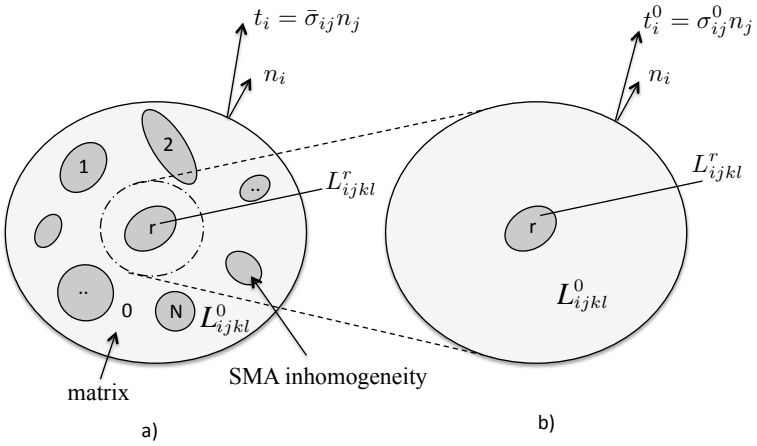

Figure 3: a) Representation of a SMA-composite, with N SMA inhomogeneities, subjected to the applied tractions t_i. b) Representation of a the r-th inhomogeneity in an infinite matrix, subjected to an applied traction $t^0_i = \sigma^0_{ij} n_j$, according to the Mori-Tanaka approximation [30, 195].

stiffness, stress, and strain represented by $\bar{L}_{ijkl}$, $\bar{\sigma}_{ij}$, and $\bar{\varepsilon}_{ij}$, respectively, where the effective stress and strain are volume averaged quantities (*e.g*, $\bar{\sigma}_{ij} = \int_V \sigma_{ij} dV$). Additionally, as the average response is of interest here, only phase average values of the various field quantities will be discussed. For instance, ε^r_{ij} is the average strain of the r-th phase and is defined via $\varepsilon^r_{ij} = \int_{V_r} \varepsilon_{ij} dV$. Furthermore, it is assumed that an homogeneous temperature field is present. Finally, the following assumptions are introduced with respect to the stress and strain of the constituents and composite materials:

1. Tractions t_i applied along the boundary S (with outward normal, n_i) of the composite are taken to be $t_i = \bar{\sigma}_{ij} n_j$ with the volume averaged stress also being the applied.

2. Transformation strains are treated as inelastic eigenstrains in the inhomogeneities. Noting Eqn. 2.5, however, these strains depend on (i) the stress level of the given SMA inhomogeneity, σ_{ij}^r, and (ii) the loading path history. With respect to the latter consideration, the analysis here will be limited to proportional loadings. The former point introduces a coupling between the constitutive and micromechanical behaviors and will be addressed later in this section.

3. The average strain in the r-th SMA inhomogeneity may be additively decomposed as:

$$\varepsilon_{ij}^r = \varepsilon_{ij}^{r-el} + \varepsilon_{ij}^{r-th} + \varepsilon_{ij}^{r-tr}, \tag{2.8}$$

where ε_{ij}^r, ε_{ij}^{r-el}, ε_{ij}^{r-th}, and ε_{ij}^{r-tr} are the total, elastic, thermal, and transformation strains, respectively. The local constitutive law of the r-th SMA phase is then written as,

$$\sigma_{ij}^r = L_{ijkl}^r \left(\varepsilon_{kl}^r - \varepsilon_{kl}^{r-th} - \varepsilon_{kl}^{r-tr}\right) \tag{2.9}$$

4. The matrix phase is taken to be thermoelastic whose total strain is written,

$$\varepsilon_{ij}^0 = \varepsilon_{ij}^{0-el} + \varepsilon_{ij}^{0-th}, \tag{2.10}$$

producing a constitutive law of the form,

$$\sigma_{ij}^0 = L_{ijkl}^0 \left(\varepsilon_{kl}^0 - \varepsilon_{kl}^{0-th}\right). \tag{2.11}$$

One essential feature of bulk SMAs that need to be incorporated in any micromechanical approach is the developed inelastic transformation strains. The evolution of such strains is typically modeled with an incremental formulation (see Section 2.1.1)

although here an alternative approach is sought so that only the total strains are considered. A solution is readily apparent by treating the transformation strains as eigenstrains in the micromechanical context. The complexity in this, however, is that transformation and its induced eigenstrains will alter the micromechancial stress partitioning. Therefore, a coupling between the global micromechanical and local constitutive behaviors is observed and must be both be satisfied.

To construct the model to that end, the Eshelby Equivalent Inclusion Method [77, 160, 195] and the Mori-Tanaka approximation [30, 195] will be utilized. First, the single inhomogeneity problem represented by Fig. 3b is considered and Eqn. 2.9 is recalled. It is noted that the total strain field, ε_{ij}^{r} may be decomposed as $\varepsilon_{ij}^{r} = \bar{\varepsilon}_{ij} + \tilde{\varepsilon}_{ij}$ where $\tilde{\varepsilon}_{ij}$ is the perturbation strain field arising from the presence of the inhomogeneity. The constitutive law may then be rewritten as,

$$\sigma_{ij}^{r} = L_{ijkl}^{r} \left(\bar{\varepsilon}_{kl} + \tilde{\varepsilon}_{kl} - \varepsilon_{kl}^{r-in} \right), \tag{2.12}$$

with ε_{ij}^{r-in} being introduced as the combined inelastic strain tensor and defined as $\varepsilon_{ij}^{r-in} = \varepsilon_{ij}^{r-th} + \varepsilon_{ij}^{r-tr}$. Following the approach of Eshelby, this constitutive law may also be rewritten by introducing an additional eigenstrain, ε_{ij}^{r-*}, associated with the difference in stiffness between matrix and inhomogeneity such that

$$\sigma_{ij}^{r} = L_{ijkl}^{0} \left(\bar{\varepsilon}_{kl} + \tilde{\varepsilon}_{kl} - \varepsilon_{kl}^{r-in} - \varepsilon_{kl}^{r-*} \right). \tag{2.13}$$

Equating Eqns. 2.12 and 2.13 yields the classical equivalence statement,

$$L_{ijkl}^{r} \left(\bar{\varepsilon}_{kl} + \tilde{\varepsilon}_{kl} - \varepsilon_{kl}^{r-in} \right) = L_{ijkl}^{0} \left(\bar{\varepsilon}_{kl} + \tilde{\varepsilon}_{kl} - \varepsilon_{kl}^{r-in} - \varepsilon_{kl}^{r-*} \right). \tag{2.14}$$

Additionally, it is observed from Eqn. 2.10 that both matrix and inhomogeneities may have inelastic strain contributions. As such, it is assumed that the effective strain tensor has elastic and inelastic components and may therefore be decomposed as $\bar{\varepsilon}_{ij} = \bar{\varepsilon}^{el}_{ij} + \bar{\varepsilon}^{in}_{ij}$ and the previous equivalent statement may be rewritten as,

$$L^r_{ijkl}\left(\bar{\varepsilon}^{el}_{kl} + \tilde{\varepsilon}_{kl} - \left(\varepsilon^{r-in}_{kl} - \bar{\varepsilon}^{in}_{kl}\right)\right) = L^0_{ijkl}\left(\bar{\varepsilon}^{el}_{kl} + \tilde{\varepsilon}_{kl} - \left(\varepsilon^{r-in}_{kl} - \bar{\varepsilon}^{in}_{kl}\right) - \varepsilon^{r-*}_{kl}\right). \quad (2.15)$$

In this way, any inelastic eigenstrains are now separated and treated in a combined fashion enabling the consideration of an inelastic matrix. A total equivalent eigenstrain is then introduced of the form $\varepsilon^{r-**}_{ij} = \varepsilon^{r-*}_{ij} + \left(\varepsilon^{r-in}_{ij} - \bar{\varepsilon}^{in}_{ij}\right)$ such that the classical solution of Eshelby relating the perturbation and eigenstrain fields,

$$\tilde{\varepsilon}^r_{ij} = S^r_{ijkl}\varepsilon^{r-**}_{kl}, \quad (2.16)$$

may be introduced. In Eqn. 2.16, S^r_{ijkl} is the Eshelby tensor that is a function of the thermoelastic properties of the matrix and inhomogeneity shape. Closed form solutions of this tensor for simple cases (*e.g*, spherical or fiber inhomogeneities in an isotropic matrix) may be found in various texts [160, 195] while a numerical scheme based on gauss integration has been developed by Gavazzi and Lagoudas [89] for the general anisotropic case. Equation 2.15 may then be solved analytically for ε^{r-**}_{ij} in terms of the applied and inelastic strains and combined with Equations 2.12 and 2.16 yields a new constitutive law of the form,

$$\sigma^r_{ij} = L^r_{ijkl}\left(T^r_{klmn}\bar{\varepsilon}^{el}_{mn} + R^r_{klmn}\left(\varepsilon^{r-in}_{mn} - \bar{\varepsilon}^{in}_{mn}\right)\right), \quad (2.17)$$

where T^r_{ijkl} and R^r_{ijkl} are the Eshelby interaction tensor and inelastic interaction tensor. These tensors take the form,

$$T^r_{ijkl} = \left[I_{ijkl} + S^r_{ijmn} \left(L^0_{mnrs} \right)^{-1} \left(L^r_{rskl} - L^0_{rskl} \right) \right]^{-1}, \tag{2.18}$$

with I_{ijkl} being the fourth order identity tensor ($I_{ijkl} = \frac{1}{2} \left(\delta_{ik}\delta_{jl} + \delta_{il}\delta_{jk} \right)$) and

$$R^r_{ijkl} = S^r_{ijmn} \left[\left(L^r_{mnrs} - L^0_{mnrs} \right) S^r_{rsqp} + L^0_{mnqp} \right]^{-1} L^r_{qpkl} - I_{ijkl}. \tag{2.19}$$

To relate the local constitutive law, Eqn. 2.17, to the global effective stress, the definition of the effective stress is recalled,

$$\bar{\sigma}_{ij} = \sum_{r=0}^{N} c^r \sigma^r_{ij} = \sum_{r=0}^{N} c^r L^r_{ijkl} \left(T^r_{klmn} \bar{\varepsilon}^{el}_{mn} + R^r_{klmn} \left(\varepsilon^{r-in}_{mn} - \bar{\varepsilon}^{in}_{mn} \right) \right). \tag{2.20}$$

The Mori-Tanaka assumption [30, 159, 160] schematically depicted in Fig. 3b is introduced. Specifically, in this limited RVE, the applied traction is assumed to correspond to the matrix value to account for interaction effects between the various precipitates. Therefore, $\bar{\varepsilon}^{el}_{ij} = M^0_{ijkl}\sigma^0_{kl}$ and $\bar{\varepsilon}^{in}_{ij} = \varepsilon^{0-in}_{ij}$ leading to a revised form of Eqn. 2.20,

$$\bar{\sigma}_{ij} = \sum_{r=0}^{N} c^r L^r_{ijkl} \left(T^r_{klmn} M^0_{mnrs} \sigma^0_{rs} + R^r_{klmn} \left(\varepsilon^{r-in}_{mn} - \varepsilon^{0-in}_{mn} \right) \right). \tag{2.21}$$

Importantly, the inelastic eigenstrain in the right-most term in now written as the different between the inhomogeneity and matrix inelastic strains. Therefore, any inelastic strains in the matrix may be incorporated in the formulation in the same fashion that inelastic responses in the inhomogeneities are being investigated here. By solving Eqn. 2.21 for σ^0_{ij}, using the Mori-Tanaka approximation and returning to

Eqn. 2.17, an expression for the stress in the r-th phase may be found,

$$\sigma_{ij}^{r} = B_{ijkl}^{r}\left(\bar{\sigma}_{kl} - \sum_{n=0}^{N} c^{n} L_{klmn}^{n} R_{mnrs}^{n}\left(\varepsilon_{rs}^{r-in} - \varepsilon_{rs}^{0-in}\right)\right) + L_{ijkl}^{r} R_{klmn}^{r}\left(\varepsilon_{mn}^{r-in} - \varepsilon_{mn}^{0-in}\right), \tag{2.22}$$

in terms of the macroscopically known applied stress, $\bar{\sigma}_{ij}$, the inelastic eigenstrains, and the stress concentration tensor, B_{ijkl}^{r}, that takes the classic form,

$$B_{ijkl}^{r} = L_{ijmn}^{r} T_{mnrs}^{r} M_{rsop}^{0}\left[\sum_{n=0}^{N} c^{n} L_{opab}^{n} T_{abcd}^{n} M_{cdkl}^{0}\right]^{-1}. \tag{2.23}$$

2.1.3 Micromechanical Model of the Effective Transformation Behavior of an SMA Composite

With the constitutive and micromechanical models established, the two models are now combined to produce a model capable of exploring the effective transformation behavior of an SMA composite. Specifically, a two-phase SMA composite is considered, where the SMA inhomogeneities are collectively treated as one phase having the same shape and orientation with volume fraction c^{SMA} and all quantities related to this phase are denoted with the superscript "SMA". The second phase is the thermoelastic MAX phase matrix, and all quantities related to this phase are denoted by the subscript 0. To determine the effective transformation surfaces of the considered composite, namely M_s, M_f, A_s and A_f, the four corresponding transformation conditions must be determined. Such surfaces are functions of the bulk SMA state and its material parameters. In the composite case, however, the SMA stress is a function of the applied macroscopic loading and microstructural parameters. With

this in mind, the four transformation conditions may be expressed as Eqns. 2.24,

$$\begin{aligned}
\Phi^t_{fwd}(\sigma^r_{ij}\left(\bar{\sigma}_{kl}\right), T, \xi = 0) = 0 \quad &\Rightarrow T = M_s, \\
\Phi^t_{fwd}(\sigma^r_{ij}\left(\bar{\sigma}_{kl}\right), T, \xi = 1) = 0 \quad &\Rightarrow T = M_f, \\
\Phi^t_{rev}(\sigma^r_{ij}\left(\bar{\sigma}_{kl}\right), T, \xi = 1) = 0 \quad &\Rightarrow T = A_s, \\
\Phi^t_{rev}(\sigma^r_{ij}\left(\bar{\sigma}_{kl}\right), T, \xi = 0) = 0 \quad &\Rightarrow T = A_f,
\end{aligned} \tag{2.24}$$

where the local dependence on the global variables is explicitly given. The determination of these surfaces in terms of macroscopic variables may be performed as follows:

1. To determine the effective transformation surface corresponding to the onset of forward transformation, M_s, it is first noted that the SMA is in the austenitic state. Thus, the transformation strain is zero ($\varepsilon^{tr}_{ij} = 0$) and the elastic stiffness is that of the SMA is that of austenite, $L^{SMA}_{ijkl} = L^{A}_{ijkl}$. The inelastic strain simply reduces to the thermal expansion strain and becomes,

$$\varepsilon^{SMA-in}_{ij} = \alpha^{SMA}_{ij}\left(T - T_{ref}\right), . \tag{2.25}$$

   In this case, the local SMA stress is written, as:

$$\sigma^{SMA}_{ij} = B^{SMA-A}_{ijkl}\bar{\sigma}_{kl} - b^{A}_{ijkl}\left(\alpha^{SMA}_{kl} - \alpha^{MAX}_{kl}\right)\left(T - T_{ref}\right), \tag{2.26}$$

   with

$$b^{A}_{ijkl} = L^{A}_{ijmn}R^{SMA-A}_{mnrs}\left(c^{SMA}B^{SMA-A}_{mnkl} - I_{mnkl}\right), \tag{2.27}$$

   where the superscript "SMA-A" refers to tensors evaluate using the thermoelas-

tic properties of an austenitic SMA. To determine the onset of transformation, the local transformation criteria $\Phi^t_{fwd}(\sigma^{SMA}_{ij}, T, \xi = 0) = 0$ needs to be satisfied with σ^{SMA}_{ij} defined via Eqn. 2.26. Hence, an effective transformation criterion for the onset of forward transformation is written as,

$$\begin{aligned}
\bar{\Phi}^r_{fwd}\left(\bar{\sigma}_{ij}, T, 0\right) &= (1-D)\left(B^{SMA-A}_{ijkl}\bar{\sigma}_{kl}\right. \\
&\quad \left. -b^A_{ijkl}\left(\alpha^{SMA}_{kl} - \alpha^{MAX}_{kl}\right)\left(T - T_{ref}\right)\right)\Lambda^{t-fwd}_{ij} \\
&\quad + \frac{1}{2}\Bigg[\left(B^{SMA-A}_{ijkl}\bar{\sigma}_{kl} - b^A_{ijkl}\left(\alpha^{SMA}_{kl} - \alpha^{MAX}_{kl}\right)\left(T - T_{ref}\right)\right) \\
&\quad \Delta M_{ijmn}\left(B^{SMA-A}_{mnrs}\bar{\sigma}_{rs} - \right. \\
&\quad \left. b^A_{mnrs}\left(\alpha^{SMA}_{rs} - \alpha^{MAX}_{rs}\right)\left(T - T_{ref}\right)\right)\Bigg] \\
&\quad + \rho\Delta s_0 T - \rho\Delta u_0 + f^t_{fwd}(0) - Y^t_0 = 0. \qquad (2.28)
\end{aligned}$$

This condition is satisfied when $T = M_s$, yielding the effective transformation surface as a function of the applied stress $\bar{\sigma}_{ij}$.

2. To find the transformation limit for the end of forward transformation, at which point the SMA is fully martensitic, the transformation strain needs to be accounted for. In this case, the inelastic strain in the SMA phase is written:

$$\varepsilon^{SMA-in}_{ij} = \alpha^{SMA}_{ij}\left(T - T_{ref}\right) + \varepsilon^{tr}_{ij}, \qquad (2.29)$$

To determine the functional form of the transformation strain, the evolution equation (Eqn. 2.4) is integrated for the case of full transformation under isobaric stress conditions. This assumption is a reasonable approximation in the case of proportional loadings. Therefore, the transformation strain is taken to

be:

$$\varepsilon_{ij}^{tr} = H^{cur}\left(\sigma^{SMA-VMeff}\right)\frac{3}{2}\frac{\sigma_{ij}^{'SMA}}{\sigma^{SMA-VMeff}}. \tag{2.30}$$

With this assumption, the expression of the local stress in the SMA phase becomes:

$$\sigma_{ij}^{SMA} = B_{ijkl}^{SMA-M}\bar{\sigma}_{kl} - b_{ijkl}^{M}\left[\left(\alpha_{kl}^{SMA} - \alpha_{kl}^{MAX}\right)(T - T_{ref}) + \varepsilon_{kl}^{tr}\right], \tag{2.31}$$

where B_{ijkl}^{SMA-M} and b_{ijkl}^{SMA-M} are determined considering the stiffness of the martensitic phase. In this case, a simple analytical expression of the local stress as a function of the applied stress and temperature does not exist due to the coupling between the local SMA stress and the transformation strain magnitude. Therefore, the local stress in the SMA for a specific applied stress and temperature has to be numerically evaluated. The effective transformation surface for the end of the forward transformation $\bar{\Phi}_{fwd}^{t}(\bar{\sigma}_{ij}, T, \xi = 1) = 0$ is met when $T = M_f$, which corresponds to the temperature to complete forward transformation at the applied stress $\bar{\sigma}_{ij}$.

3. To determine the transformation limit for the onset of reverse transformation, the relationship $\Phi_{rev}^{t}(\sigma_{ij}^{SMA}, T, \xi = 1) = 0$ needs to be satisfied. As the material is in the martensitic phase state at this point, the inelastic strain is:

$$\varepsilon_{ij}^{SMA-in} = \alpha_{ij}^{SMA}(T - T_{ref}) + \varepsilon_{ij}^{tr-rev}, \tag{2.32}$$

where the transformation strain is that at reversal, $\varepsilon_{ij}^{tr-rev}$, and is taken to be that found at the end of forward transformation for the same applied stress

level. The local stress in this case is then written:

$$\sigma_{ij}^{SMA} = B_{ijkl}^{SMA-M}\bar{\sigma}_{kl} - b_{ijkl}^{M}\left[\left(\alpha_{kl}^{SMA} - \alpha_{kl}^{MAX}\right)(T - T_{ref}) + \varepsilon_{kl}^{tr-rev}\right], \quad (2.33)$$

The transformation criteria for the onset of reverse transformation is then given as:

$$\begin{aligned}
\bar{\Phi}_{rev}^{t}(\bar{\sigma}_{ij}, T, \xi = 1) \;=\; & -(1+D)\left(B_{ijkl}^{SMA-M}\bar{\sigma}_{kl}\right. \\
& \left. -b_{ijkl}^{M}\left[\left(\alpha_{kl}^{SMA} - \alpha_{kl}^{MAX}\right)(T - T_{ref}) + \varepsilon_{kl}^{tr-rev}\right]\right) \\
& \Lambda_{ij}^{t-rev} - \frac{1}{2}\left[\left(B_{ijkl}^{SMA-M}\bar{\sigma}_{kl} - \right.\right. \\
& \left.\left. b_{ijkl}^{M}\left[\left(\alpha_{kl}^{SMA} - \alpha_{kl}^{MAX}\right)(T - T_{ref}) + \varepsilon_{ij}^{tr-rev}\right]\right)\Delta M_{ijmn} \\
& \left(B_{mnrs}^{SMA-M}\bar{\sigma}_{rs} - b_{mnrs}^{M}\left[\left(\alpha_{rs}^{SMA} - \alpha_{rs}^{MAX}\right)(T - T_{ref})\right.\right. \\
& \left.\left. + \varepsilon_{rs}^{tr-rev}\right]\right) - \rho\Delta s_0 + \rho\Delta u_0 + f_{rev}^{t}(1) = 0. \qquad (2.34)
\end{aligned}$$

The temperature satisfying this condition is A_s.

4. Finally, the end of reverse transformation temperatures, A_f, are determined when the condition $\Phi_{rev}^{t}(\sigma_{ij}^{SMA}, T, \xi = 0) = 0$ is satisfied. As the material at this point is in the austenitic phase, the local stress in the SMA phase in this last case the same as the martensitic start condition (Eqn. 2.26). The

transformation criteria is written:

$$\begin{aligned}\bar{\Phi}^{r}_{rvs}\left(\bar{\sigma}_{ij},T,0\right) &= -\left(1+D\right)\left(B^{SMA-A}_{ijkl}\bar{\sigma}_{kl}-\right.\\ &\quad \left. b^{A}_{ijkl}\left(\alpha^{SMA}_{kl}-\alpha^{MAX}_{kl}\right)\left(T-T_{ref}\right)\right)\Lambda^{t-rev}_{ij}\\ &\quad -\frac{1}{2}\Bigg[\left(B^{SMA-A}_{ijkl}\bar{\sigma}_{kl}-b^{A}_{ijkl}\left(\alpha^{SMA}_{kl}-\alpha^{MAX}_{kl}\right)\left(T-T_{ref}\right)\right)\\ &\quad \Delta M_{ijmn}\left(B^{SMA-A}_{mnrs}\bar{\sigma}_{rs}-\right.\\ &\quad \left. b^{A}_{mnrs}\left(\alpha^{SMA}_{rs}-\alpha^{MAX}_{rs}\right)\left(T-T_{ref}\right)\right)\Bigg]\\ &\quad -\rho\Delta s_0 T+\rho\Delta u_0+f^{t}_{rev}(0)-Y^{t}_{0}=0. \end{aligned} \tag{2.35}$$

2.2 Results

To explore the transformation characteristics of an SMA-MAX composite, a representative composite is analyzed using the established model. The SMA is taken to be a Ni60Ti40 (wt%) material characterized by Hartl *et al.* [95] and the resultant thermoelastic and transformation model parameters determined by the same authors in a companion work [96] are given in Table 2.1. The matrix phase is taken to be Ti_2AlC that (for the purposes of this study) is assumed to behave thermoelastically. This is done to focus on the impact of (*i*) the stiffness contrasts of the materials and (*ii*) influence of martensitic transformation. The relevant properties are given in Table 2.2 and it is noted that the Ti_2AlC is more than three times stiffer than the NiTi phase. The composite is taken to have 30% SMA inhomogeneities, and the zero thermal mismatch strain reference temperature, T_{ref}, is taken to be room temperature (20°C).

Table 2.1: Model parameters for Ni60T40 (wt%) [96].

Parameter	Value
E^A	90 GPa
E^M	63 GPa
$\nu^M = \nu^A$	0.33
$\alpha^M = \alpha^A$	10 x 10^{-6} $^\circ C^{-1}$
M_s^0	35°C
M_f^0	-31°C
A_s^0	15°C
A_f^0	69°C
$C^A\big\vert_{300\text{MPa}}$	16 MPa/°C
$C^M\big\vert_{300\text{MPa}}$	10 MPa/°C
H_{min}	0.0
H_{sat}	0.0158
σ_{crit}	12 MPa

Table 2.2: Material properties for the Ti_2AlC matrix [198].

Parameter	Value
E^{MAX}	278 GPa
ν^{MAX}	0.17
α^{MAX} (from [18])	8.20 x 10^{-6} $^\circ C^{-1}$

2.2.1 Transformation Characteristics with Spherical SMA Inhomogeneities

The effective phase diagram of the composite is determined by satisfying both the local and global conditions by using the model developed in Section 2.1.2 and is presented in Fig. 4. These results correspond to a uniaxially loaded composite ($\bar{\sigma}_{ij} = \bar{\sigma}\delta_{i1}\delta_{j1}$) subjected to a cooling–heating cycle. The phase diagram of the bulk SMA is also presented for comparison. From Fig. 4, it is observed that all the composite transformation limits require higher applied stresses to transform at a given

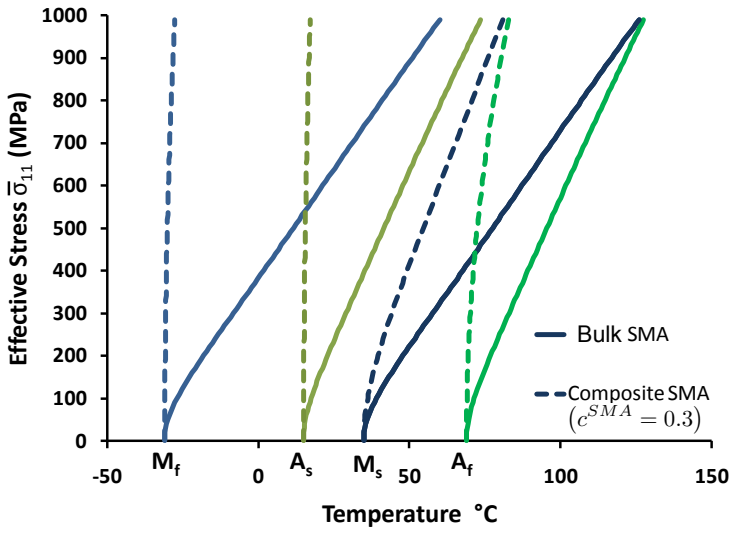

Figure 4: Effective phase diagram for a SMA composite with spherical SMA inhomogeneities ($c^{\text{SMA}} = 0.3$) and for bulk SMA. ©IOP Publishing. Reproduced with permission from [138] by permission of IOP Publishing. All rights reserved.

temperature than those corresponding to the bulk SMA. The two transformation limits in which the SMA is martensitic, M_f and A_s, both exhibit the same behavior - a near vertical limit such that the temperatures needed to trigger the end of forward transformation and the beginning of reverse transformation are almost stress invariant. On the other hand, the forward transformation initiation limit, denoted by M_s, maintains a similar, albeit steeper, behavior in comparison to the bulk case. The last transformation limit, A_f, is also strongly affected. This behavior presents an interesting deviation from bulk SMA behavior. Specifically, an important assumption of the bulk SMA constitutive model is that the forward (M_s and M_f) and reverse transformation limits (A_s and A_f) each share a common, stress-influence coefficient (slope) in the phase diagram. This commonality in not maintained in the effective response.

To under the behaviors presented in Fig. 4, two key differences between the bulk and composite case need to be considered. First, as the two materials in the composite have dissimilar elastic moduli, the constituents have different phase average stresses. Given the thermomechanically stiffer nature of the Ti_2AlC phase, it will carry a larger portion of the stress than the NiTi phase. Therefore, it is expected that the SMA reinforcement stress will be lower than the effective applied stress. The second different is the presence of the inelastic transformation strains. Such strains are only presence in the martensitic phase and it is noted that the two surfaces corresponding to a martensitic SMA (M_f and A_s) are those exhibiting the same near vertical behavior not observed with M_s and A_f. Additionally, as may be seen in Eqn. 2.4, the transformation direction tensor, Λ_{ij}^t, that appears in the expression for the transformation surface, has different forms for the forward and reverse transformation. The former case has a stress dependence while the latter is constant through reverse transformation to ensure complete recovery. Recently, Chatzigeorgiou *et al.* [51] noted that under non-proportional loadings this reverse form of the tensor may produce effective yield surfaces that are not convex in stress state. Although such loadings are not considered here, it is important to note the importance of the selection of this form. Nonetheless, with these sources in mind it can be reasonably deduced that the composite stress pertaining and transformation strains developed during loading lead to the changes in the transformation cases. Furthermore, the presence of these strains has a substantial impact on the martensitic surfaces.

As differences in the composite transformation limits are observed when the SMA is martensitic or austenitic, the effect of transformation on the local stress state of the matrix and SMA phases needs to be investigated further. To explore this effect, two cases are considered: *i*) when the SMA is austenitic, at the onset of forward

transformation, and *ii*) when the SMA is martensitic, at the end of forward transformation. The evolution of the stress in the direction of loading of each phase, σ_{11}^r, as a function of the applied stress $\bar{\sigma}_{11}$ for these cases is presented in Fig. 5. It is observed that at the end of forward transformation there is an increase in the stress in the MAX phase with a corresponding decrease in the SMA. Although the change in SMA stiffness due to phase transformation alters the stress state of the composite, the magnitude of the decrease in the SMA stress and the decreased influence of the applied load on the SMA stress state at M_f indicate that this is a secondary cause of stress reduction. Put another way, the martensitic transformation (especially its strains) induces a redistribution of stress amongst the phases. This reduction in stress in the SMA phases results in lower transformation temperatures for the completion of forward and onset of reverse transformation.

To further explore this stress reduction, it is necessary to investigate the relationship between the transformation strain and the applied stress. Therefore, the local transformation strain in the direction of applied uniaxial loading of the SMA is presented in Fig. 6 as a function of applied stress, $\bar{\sigma}_{11}$. The dense case is also presented for comparison. Note that the transformation strain presented is the strain in the SMA phase determined at the limit M_f for each applied stress level. From the results in Fig. 6, a large reduction in the local transformation strain is observed for the composite case in comparison to the bulk results. By considering this result with the decrease in stress presented in Fig. 5, it is concluded that the reduction in transformation strains generated is the result of two mechanisms - the stress concentration effect and stress redistribution due to transformation. First, without the consideration of transformation strains, the local stress in the SMA is linked to the applied stress through the stress concentration tensor B_{ijkl}^{SMA}. In the case of a stiff matrix, the stress level in the SMA phase is significantly less than in the matrix

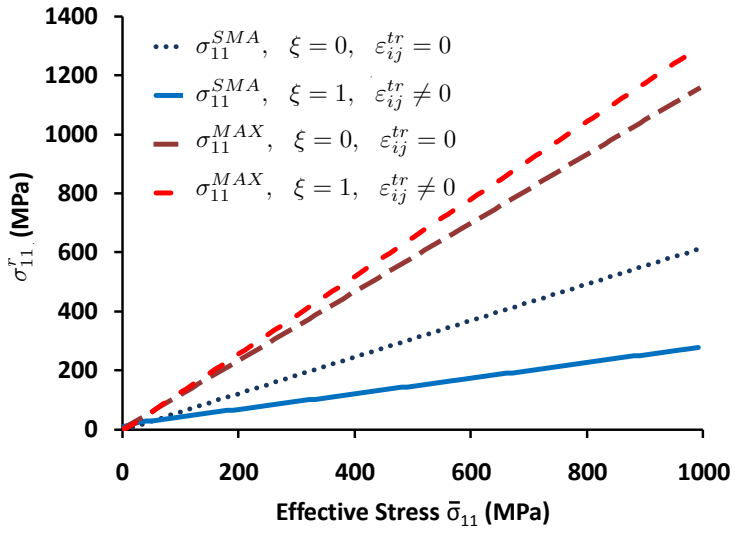

Figure 5: Stress in the direction of applied uniaxial loading in each phase before (at M_s) and after (M_f) forward transformation for a SMA composite with spherical inhomogeneities, as a function of the effective uniaxial stress $\bar{\sigma}_{11}$.

phase. Secondly, as previously noted, transformation modifies the composite stress state such that stresses are redistributed amongst the SMA and the MAX phase. As transformation strain magnitude is proportional to the stress on the SMA, both reductions in SMA stress lead to decreases in the transformation strains generated. It is further observed that the evolution of the transformation strains with respect to applied stress for the composite does not reach a saturation value in the range of applied stress considered, as it is observed for the bulk case.

Using the information provided by the analysis of the local stress state and transformation strains, it becomes clear that the redistribution of stress due to the transformation strain results in the nearly vertical slopes for the transformation limits M_f and A_s observed in Fig. 4. Indeed, even when the applied stress is high, the

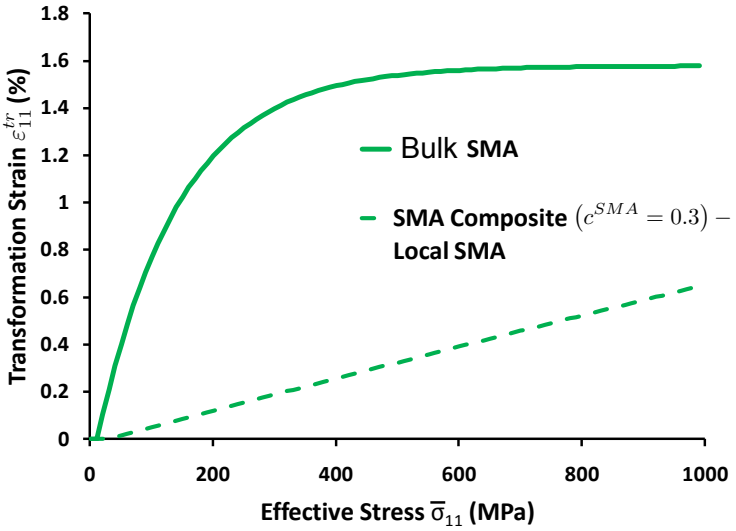

Figure 6: Transformation strain in the direction of applied loading, ε_{11}^{tr}, as a function of applied stress for a SMA composite with spherical inhomogeneities ($c^{\text{SMA}} = 0.3$) and bulk SMA.

redistribution of stress induced by the appearance of transformation strains results in a low stress state in the SMA inhomogeneities. Therefore, the transformation temperatures stay close to the zero stress temperatures M_f^0 and A_s^0, which explains the almost vertical transformation limit in the stress-temperature diagram when the SMA is in the martensitic state.

The previous results in this section are all determined by considering only the initial and completion states of the composite. An important question is to consider if solving for only these states is in agreement with what is observed considering the evolution of the composite state. To address this question, a one-dimensional isostrain model of the composite is implemented. The isostrain approximation is introduced due to the stiff character of the Ti_2AlC phase. Details of the model are given in Appendix A. The phase diagram numerically determined through such a

model is presented in Fig. 7a while the stresses in the various phases through forward transformation of a 300 MPa actuation cycle are given in Fig. 7. First, it may be observed that the results of Fig. 7a exhibit the same qualitative behaviors (and reasonable quantitative agreement) as in Fig. 4. Additionally, in Fig. 7, it is noted during initial cooling the SMA has a lower stress than the applied. As forward transformation progresses, however, the SMA stress is substantially reduced due to the development of transformation strains. Therefore, the same composite behaviors noted in the micromechanical model may be observed via the simpler 1D isostrain approach. This agreement demonstrates that the consideration of only the initial and final composite states is a reasonable approximation.

As the response of a composite with spherical inhomogeneities under uniaxial

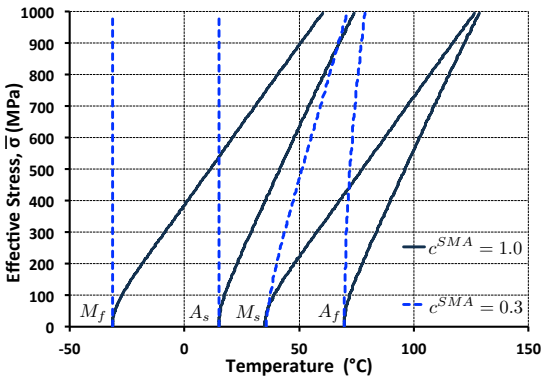

(a) Phase diagram of the bulk SMA ($c^{SMA} = 1.0$) and composite ($c^{SMA} = 0.3$)

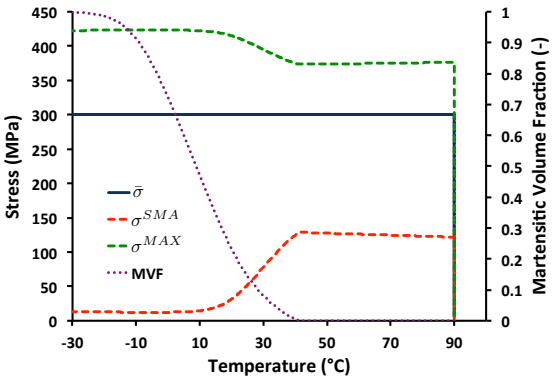

(b) Stress of both phases through forward transformation of an actuation loading path with an applied bias stress of 300 MPa

Figure 7: Results from a 1D, isostrain composite model of the NiTi-Ti_2AlC composite (with 30% SMA) through an actuation loading cycle.

loading has already been discussed, the response under shear and biaxial loadings shall be explored. Specifically, in the case of biaxial loadings, $\bar{\sigma}_{11}$ and $\bar{\sigma}_{22}$, the trans-

formation surfaces for the case of M_s and M_f are determined and presented in Figs. 8 and 9, respectively, for the composite and bulk SMA. In the σ_{11}-σ_{22} plane, the transformation surfaces are found to be Mises ellipsoids. As the transformation strain direction Λ_{ij}^{t-fwd}, it is dependent on the deviatoric stress tensor and the related J_2 invariant ($J_2 = \frac{1}{2}\sigma'_{ij}\sigma'_{ij}$), such a shape is to be expected. Additionally, the the concentration tensors are isotropic in the case of spherical inhomogeneities, therefore the same equivalent local stress in the SMA phase is obtained from any applied stress with an equivalent effective stress $\bar{\sigma}^{VMeff}$. This indicates that an effective phase diagram, expressed as a function of the effective Mises equivalent stress $\bar{\sigma}^{VMeff}$ is identical for any proportional loading path, that includes uniaxial, multiaxial and shear loading paths with spherical inhomogeneities.

It is also found that the size of these ellipsoids expands with increases in temper-

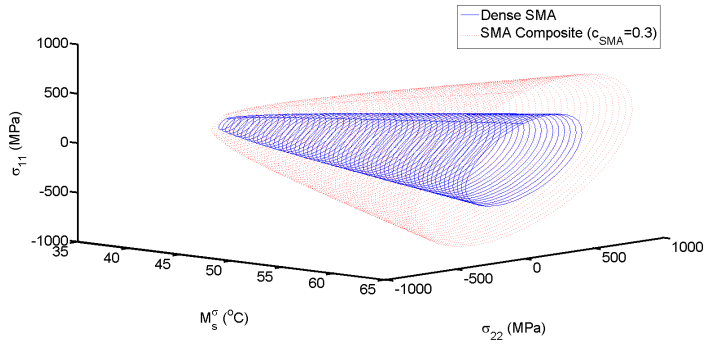

Figure 8: M_s transformation surfaces for SMA composite with spherical inhomogeneities c^{SMA} and a dense SMA under biaxial loading.

ature. In agreement with the results of Fig. 4, it is observed in Fig. 8 that to achieve

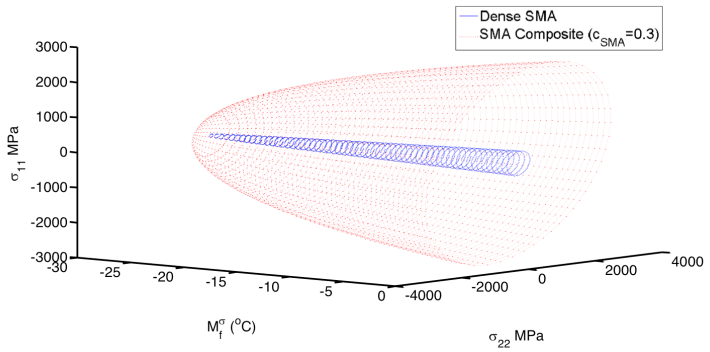

Figure 9: M_f transformation surfaces for SMA composite with spherical inhomogeneities (c^{SMA}) and a dense SMA under biaxial loading.

the necessary conditions on the SMA phase to initiate forward transformation, a larger applied stress for the composite case is required than for dense SMA. For the end of forward transformation, there is a "bowl-like" shape indicating that substantially more stress on the composite is necessary to produce the required stress in the SMA for transformation completion at a given temperature (see Fig. 9) in agreement with the transformation induced stress redistributions.

2.2.2 Transformation Characteristics with Cylindrical Inhomogeneities

To understand the influence of the geometry of the inhomogeneities and the effect of the loading direction, a composite with cylindrical SMA inhomogeneities aligned in the "1" direction is subjected to various loading conditions. As the concentration tensors are anisotropic in the case of non-spherical inhomogeneities, it is expected that the loading direction will influence the results. Specifically, four cases are considered:

1. L : Longitudinal uniaxial loading in the aligned direction - $\bar{\sigma}_{ij} = \bar{\sigma}\delta_{i1}\delta_{j1}$.

2. T : Transvere loading perpendicular to the axis of the inhomogeneities - $\bar{\sigma}_{ij} = \bar{\sigma}\delta_{i2}\delta_{j2}$.

3. LT : Pure in-plane shear - $\bar{\sigma}_{ij} = \bar{\tau}\left(\delta_{i1}\delta_{j2} + \delta_{i2}\delta_{j1}\right)$.

4. TT : pure out-of-plane shear - $\bar{\sigma}_{ij} = \bar{\tau}\left(\delta_{i2}\delta_{j3} + \delta_{i3}\delta_{j2}\right)$.

The results of these four cases are presented in Fig. 10. Figure 10a presents the

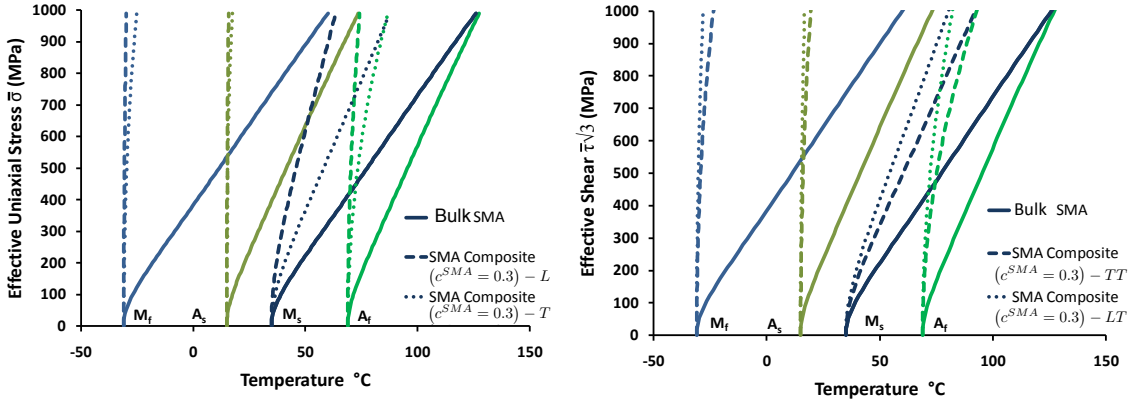

(a) Stress-temperature phase diagram for L and T loading cases

(b) Stress-temperature phase diagram for LT and TT loading cases

Figure 10: Phase diagram for a SMA composite with cylindrical SMA inhomogeneities (c^{SMA}) and for bulk SMA.

comparison between the two uniaxial loading cases (L and T) while in Fig. 10b the comparison between the two pure shear configurations (LT and TT) is given. Unlike in the case of spherical inhomogeneities in which the transformation surfaces were the same for a given $\bar{\sigma}^{VMeff}$, with cylindrical inhomogeneities the response is different depending on the loading. Indeed, in Fig. 10a, the transformation limits that correspond to loading in the longitudinal direction are steeper than the ones that

correspond to a transverse loading while in Fig. 10b the in-plane shear results (case LT) are steeper than those in the out-of-plane case (TT). It is also noted that the effect of loading direction has a larger impact on the martensitic start and austenitic finish limits than for the two other transformation limits. In these cases, when there is no transformation strain, the difference in the response is due to the anisotropy of the localization tensors resulting in different stress states in the SMA phase depending on the loading considered. When transformation strains are present (martensitic finish and austenitic start), all four cases show nearly vertical transformation limits demonstrating the influence of the transformation strain on the stress redistribution.

To observe clearly the effect of the loading direction, at a given temperature (T = 65°C), the composite transformation surface for cylindrical inhomogeneities aligned in the 1-direction were determined under the previously described biaxial loading conditions. The corresponding surface is presented in Fig. 11 along with the case of a composite with spherical inhomogeneities and the transformation surface of the bulk SMA at the same temperature. In Fig. 11, it is observed that the usage of cylindrical inhomogeneities lead to an anisotropic transformation surface, and it is clear that the stress necessary to initiate transformation in the longitudinal ("1") direction is higher than in the transverse ("2") direction.

2.2.3 Parametric Studies

As the stress distribution in the composite is dependent upon the concentration of each constituent phase and their respective stiffnesses, the influence of such parameters needs to be determined. Thus, parametric studies are performed on the matrix elastic modulus, E^{MAX}, and the SMA concentration to find the effective phase transformation temperatures. Since changes in the elastic properties of the

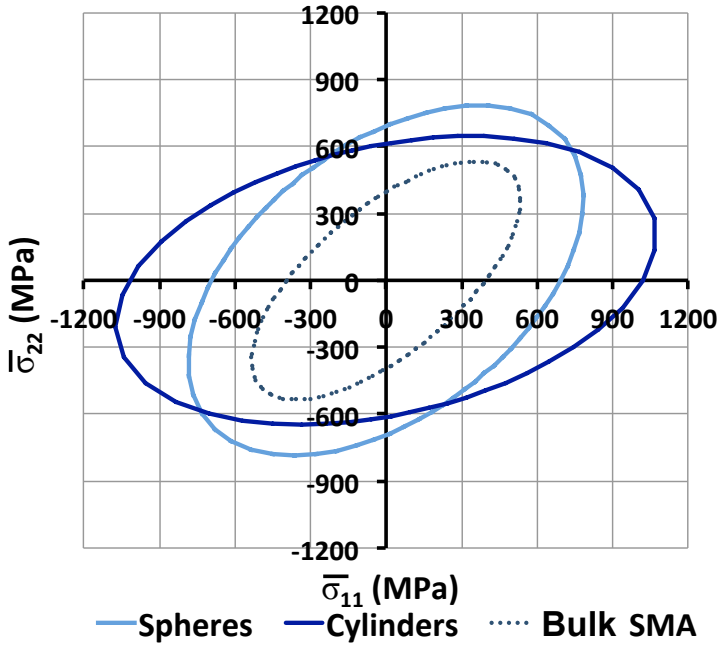

Figure 11: Bulk SMA and SMA Composite M_s transformation surfaces for spherical and cylindrical inhomogeneities under biaxial loading, at T=65°C.

SMA inhomogeneities also cause different transformation behavior, the SMA properties are not changed. All the analyses in this section are carried out on a SMA composite with spherical inhomogeneities. Note that, as discussed in the previous section, the resulting effective transformation temperatures are identical for any proportional loading path under the same Mises equivalent stress level.

To explore the effect of matrix elastic modulus, E^{MAX}, on the transformation response, the forward transformation temperatures, at different applied stress levels, are determined as a function of the ratio between the elastic modulus of the matrix and the SMA (E^A for M_s and E^M for M_f). In Fig. 12a, the martensitic start temperatures, M_s, normalized by M_s^0, are presented as a function of the normalized elastic

modulus of the matrix. Note that the bulk case is presented for comparison at the point $E^{MAX}/E^A = 1$. In this analysis, the composite is composed of 30% spherical SMA inhomogeneities and the Poisson ratio and coefficient of thermal expansion of the matrix is taken to be that of the SMA (for this composition $\nu^M = \nu^A = \nu^{MAX}$, $\alpha^M = \alpha^A = \alpha^{MAX}$) so that only the matrix modulus is varied. Figure 12b presents the results for the normalized martensitic finish, M_f, temperatures. The cases considered correspond to the elastic behavior of a wide range of matrix materials including polymers, metals and ceramics.

In Fig. 12a, a gradual decrease in the temperature needed to initiate transfor-

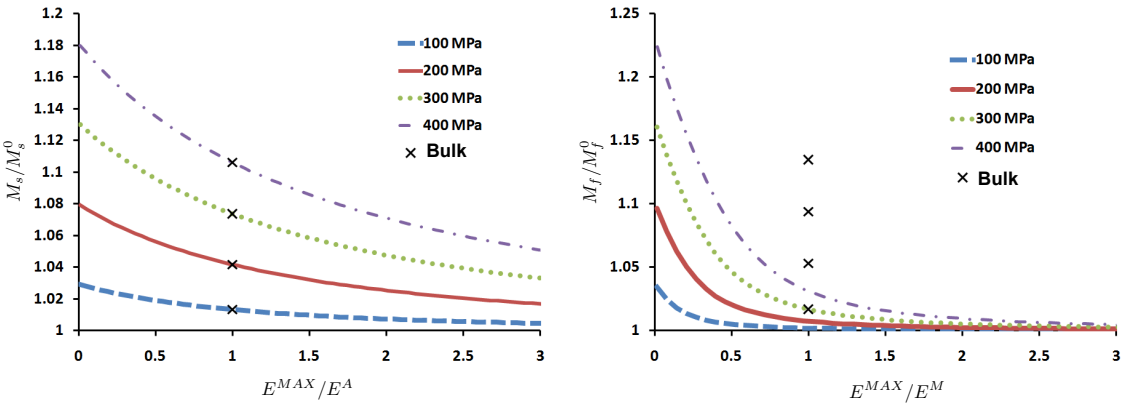

(a) Normalized martensitic start temperature M_s/M_s^0 as a function of normalized matrix elastic modulus

(b) Normalized martensitic finish temperature M_f/M_f^0 as a function of normalized matrix elastic modulus

Figure 12: Effect of matrix elastic modulus on forward transformation temperatures at a variety of $\bar{\sigma}_{11}$.

mation can be observed as the ratio of the elastic moduli increases. It is observed that as the stiffness of the matrix increases, M_s approaches M_s^0. Since there are no transformation strains in the system, this variation is due purely to the stress con-

centration effect that depends on the stiffness contrast of the two materials. For the end of transformation, Fig. 12b shows that the temperature M_f decreases rapidly toward the zero-stress limit M_f^0 as the ratio between the two elastic moduli increases. Although the stress concentration effect still influences the results in this case, the drastic decrease in M_f as the ratio of elastic moduli increases is attributed to the effect of transformation strains and the associated stress redistribution as discussed in Sec. 2.2.1. Importantly, the quick convergence of M_f to M_f^0 shows that the appearance of transformation strains is the dominant mechanism and therefore needs to be accounted for in a variety of composite designs - including those where the matrix has an equivalent or decreased stiffness as compared to the SMA. Note that when the stiffness of the matrix is lower than the elastic stiffness of the SMA (in the case of equal ν), the influence of the matrix has the opposite effect as observed with a stiff matrix, i.e. the transformation temperatures M_s are higher than the ones corresponding to the dense case for the same macroscopic stress level. This indicates that the the transformation limits of this class of composites are less steep than in the dense case. Indeed, the stress is distributed in such a manner that the local equivalent stress in the SMA is higher than the macroscopic stress. The change in the slopes of the transformation limits has been determined for the case of the onset of transformation in SMA/elastomer composites by [39]. It has been shown that the composite transformation slopes are in this case less steep than in the case of the dense SMA, which is in agreement with the results provided here. On the other hand, the transformation temperatures M_f corresponding to the composite matches the temperatures of the dense case when the stiffness of the matrix is significantly lower than the stiffness of the SMA (see Fig. 12b). The transformation strain that is developed in the SMA phase induces a supplementary stress redistribution which leads to a significantly lower stress level in the SMA, even if the stiffnesses are of the

same order of magnitude.

To understand the effect of SMA concentration on the transformation response of the composite a parametric study is also performed on SMA volume fraction. For this analysis, the Ti_2AlC ceramic is used as the matrix phase while the SMA concentration is varied. The resultant variations of M_s and M_f, normalized by the zero-stress temperatures M_s^0 and M_f^0, with SMA volume fraction are shown in Fig. 13. It is noted than in the case of high volume fraction of SMA (typically when $c^{\text{SMA}} > .5$), the SMA should be considered to be the matrix phase of the composite. In this case, non-homogeneous inelastic strains appear in the matrix and need to be treated slightly differently as discussed in Section. 2.1.2. Nonetheless, tn the following parametric study, the Ti_2AlC is considered to be the matrix even for high concentrations of SMA. Although this introduces an additional approximation, the results still yield important information regarding the trends of the composite response. Indeed, although not shown, the results when $c^{\text{SMA}} = 1$ match those of the bulk SMA.

For martensitic start temperatures, as c^{SMA} increases there is a corresponding increase in M_s. Again, this effect is attributed to the stress concentration effect that depends on the composition of the composite. With respect to the martensitic finish temperatures, M_f, it may be observed that the normalized temperatures grow with volume fraction. These changes, however, are much less substantial than in the M_s case as may be noted via the order of magnitude difference in the scales of Figs. 13a and 13b. Therefore, although they increase, the M_f temperature remain approximately equal to the zero stress values. To consider this further, the effective inelastic strains are plotted as a function of the SMA volume fraction in Fig. 14 at a variety of $\bar{\sigma}_{11}$ to investigate the previously described relationship between the two. As these strains are determined in the martensitic state, Fig. 14 presents the sum of the transformation and thermal strains. The thermal strains, however, do not vary with

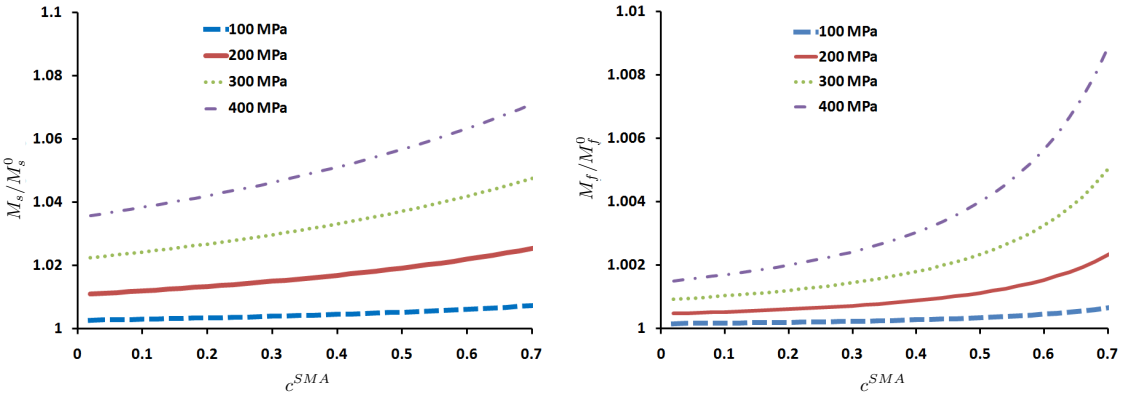

(a) M_s/M_s^0 as a function of c^{SMA} (b) M_f/M_f^0 as a function of c^{SMA}

Figure 13: Effect of SMA volume fraction on forward transformation temperatures at a variety of $\bar{\sigma}_{11}$.

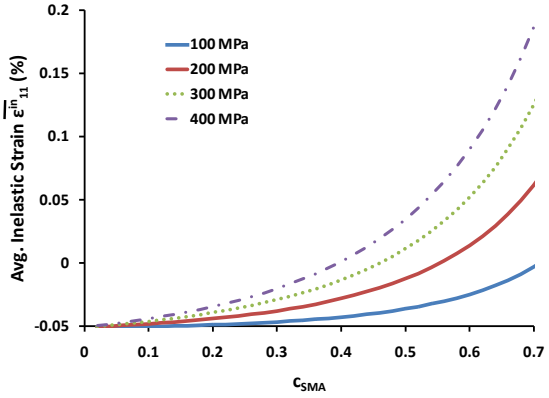

Figure 14: Effect of SMA volume fraction on inelastic strain component $\bar{\varepsilon}_{11}^{in}$ at a variety of $\bar{\sigma}_{11}$.

volume fraction or stress and are negligible due to the reference temperature chosen and the low thermal expansion mismatch. At low and moderate c^{SMA} in Fig. 14, very small effective inelastic (transformation) strains are present. As c^{SMA} reaches higher

values these strains start to increase. It is noted that this trend is similar to the evolution of the M_f temperatures with respect to the SMA volume fraction. It is concluded that, at low and moderate SMA concentrations, the stress redistribution keeps M_f approximately equal to M_f^0 and results in lower transformation strains.

To complete the parametric study, the effects of differing moduli and volume fraction are considered together. Therefore, Fig. 15 presents the evolution of M_s and M_f on a wide range of composites with various volume fraction of SMA and elastic modulus of the matrix, all subjected to an an isobaric loading path (400 MPa), normalized by the zero-stress temperatures M_s^0 and M_f^0. It is observed in

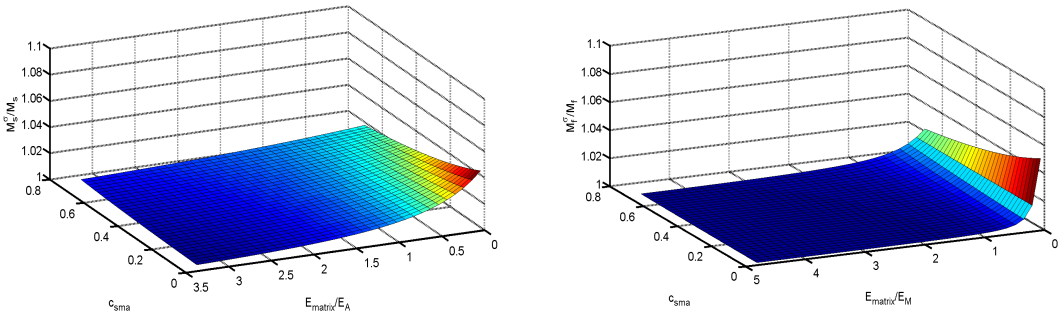

(a) M_s/M_s^0 as a function of c^{SMA} and E^{MAX}/E^A(b) M_f/M_f^0 as a function of c^{SMA} and E^{MAX}/E^M

Figure 15: Forward transformation temperatures as a function of SMA content and matrix modulus at an applied load of 400 MPa.

Fig. 15b that at a low matrix modulus (E^{MAX}/E^A <1), and a low volume fraction of the SMA phase, the transformation temperatures M_s and M_f differ significantly from the zero-stress temperatures since the stress in the SMA phase is significantly

increased due to the composite stress distribution. In the case of M_s (Fig. 15a), a gradual dependence can be observed across the c^{SMA}-E^{MAX} space due to the effect of the stress distribution. Indeed, according to the form of the stress concentration tensor B_{ijkl}^{SMA}, the stress in the SMA phase increases while the elastic stiffness of the matrix decreases and while the volume fraction of the SMA decreases. It is observed that the the transformation temperature corresponding to the end of transformation, M_f, rapidly approaches M_f^0 as the matrix modulus increases. This indicates that the transformation strain induced stress redistribution is a key mechanism that affects the transformation characteristics even for a matrix with a low elastic modulus.

2.3 Summary

In this section, a quick, efficient method to analyze and determine the effective transformation characteristics of SMA composites was developed. To facilitate this approach, the composite and material states corresponding to the initiation and completion of transformation were found by combining an Eshelby-based micromechanical approach with an SMA constitutive model. Through such a consideration, a coupling between the extent of martensitic transformation and composite stress state was observed. Although formulated such that transformation strains could be in either phase, the response of composites with SMA inhomogeneities in a stiff, elastic matrix were investigated. Specifically, effective transformation characteristics of the composite (in terms of phase diagram and effective transformation strains) were found. It was shown that when the material is austenitic (with no transformation strains), changes in the effective transformation surfaces are associated with micromechanical stress distributions. For martensitic cases (M_f and A_s), the generation of transformation strains leads to (i) a stress redistribution lowering the effective SMA stress and increasing the MAX phase stress (ii) near stress invariant

phase diagram surfaces (*iii*) decrease in the transformation strain magnitude of the SMA phase. Additional parametric studies were performed to investigate the impact of different matrix properties. Importantly, these observations demonstrate that, even with just the stiff thermoelastic nature of the MAX phase, martensitic transformation of these cases yields (*i*) altered transformation characteristics with a wider hysteresis and lower transformation strains and (*ii*) increased stresses in the MAX phase constituent that could induce nonlinear behaviors. These possibilities will be explored in subsequent sections in which nonlinear deformations are accounted for throughout the loading cycle.

3. ACTUATION RESPONSE OF SMA-MAX PHASE COMPOSITES*

The previous chapter presented important transformation characteristics of SMA-MAX phase composites highlighting the impact of transformation strains on the stress distribution in the composite. However, that analysis only considered the beginning and end of transformation and considered a thermoelastic response for the MAX phase constituent. Importantly, the response through a full actuation loading cycle needs to be considered to investigate the evolution of this stress redistribution. If a nonlinear constituent response is assumed for the MAX material, this evolution is especially important. These topics will be discussed in this chapter. First, in the remainder of this section, preliminaries regarding loading path and constitutive responses will be presented. Section 3.1 will then introduce results pertaining to a series of initial models of the composite material to explore this interaction. The analysis of an actual NiTi – Ti_2AlC will be given in Section 3.2. Finally,a summary of these various results are presented in Section 3.3.

Before proceeding, some common elements in each of the following analysis sections are presented. Specifically, as with any boundary value problem, the geometry (mesh), boundary conditions, and constitutive responses need to be defined. Although the geometry changes, in each section the analysis is performed considering an isobaric actuation loading path. Schematically, such a loading path is presented in Fig. 16. Four steps are considered. First, in an austenitic state, the composite is isothermally loaded to a predefined effective stress – 200 MPa in the case of Fig. 16a. This effective, composite load level is then held constant as the composite is cooled

*Portions of this section (Section 3.1.1) are reproduced from "Hybrid Shape Memory Alloy Composites for Extreme Environments", B. T. Lester, Y. Chemisky, A. B. Geltmacker, S. M. Qidwai, R. K. Everett, and D. C. Lagoudas, 2011, *Proceedings of 22nd International Conference on Adaptive Structures and Technologies* [139]. Copyright authors.

and cooled (steps 2 and 3) through both forward and reverse transformation as indicated in the phase diagram in Fig. 16b. Finally, the composite is unloaded (step 4) back to its initial loading state. The methodology used to apply these stresses and corresponding boundary conditions will vary somewhat in the various simulations (depending on the geometry) and will discussed in the appropriate section. Nonetheless, the considered analysis is all performed considering this four-step cycle.

In all of the analyses in this chapter, an SMA (NiTi) and MAX phase constituent

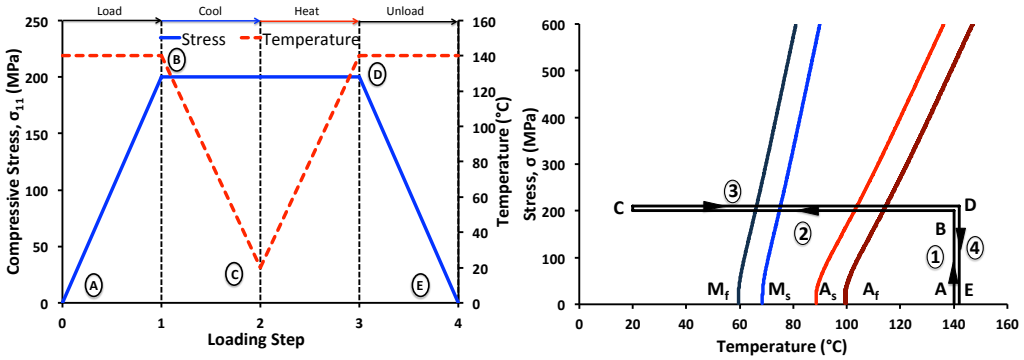

Figure 16: Considered isobaric (actuation) loading path: (a) applied load and temperature through the course of the simulation steps and (b) loading path overlaid on the phase diagram of the bulk NiTi.

(Ti_2AlC) are present. With respect to the SMA phase, the constitutive model discussed in Section 2.1.1 and previously implemented as an Abaqus User MATerial Subroutine (UMAT) [1] by Lagoudas *et al.* [124] is utilized. Model parameters are determined from experimental results of dense NiTi[4] produced through similar material processing routes to that used to manufacture the composites of interest. It is important to note that the presence of additional materials and subtle changes in

[4]Experimental results provided by Prof. Karaman (MSEN TAMU) and group.

the processing conditions during composite fabrication may lead to different chemistry or properties of the constituents versus that observed in the dense specimens. Such a consideration is especially important in NiTi in which slight changes in chemistry can lead to substantial changes in material properties (especially transformation temperatures) [170, 222]. Recently, some combined numerical-experimental methods have been developed using the FEM with digital image correlation (DIC) methods to determine the material parameters of bulk SMAs in an inverse fashion [156, 233] that could eventually address this issue with SMA composites. At this time, however, such methods are not available and it is assumed the the material properties in the composite do not vary substantially from the bulk specimens. Regarding the MAX phases, both recoverable and irrecoverable deformations are expected due to the combination of mechanisms and behaviors discussed in Section 1.1. Additionally, that same discussion highlighted a lack of existing 3D models capable of describing the inelastic thermomechanical response of these materials. Although this problem will be alleviated in forthcoming sections, it is important to first establish a baseline response in terms using an approximate representation of the MAX phase behavior. Specifically, it is important to capture both the thermoelastically stiff nature of MAX phases and the development of permanent deformations in the assumed constitutive response. These are important with respect to the stress redistribution expected through transformation and for the development of any residual stress states that may develop through such loading paths. Therefore, an elastic-plastic assumption of the MAX phase behavior is introduced and Abaqus' isotropic hardening elastic-plastic model is used. The experimental results of Poon *et al.* [186] are used to calibrate this model as they extensively characterize this response domain. Using these approaches, the constitutive responses of the two phases are presented in Fig. 17 and characteristic model parameters are given in Tables 3.1 and 3.2 for

the NiTi and Ti_2AlC phases, respectively.

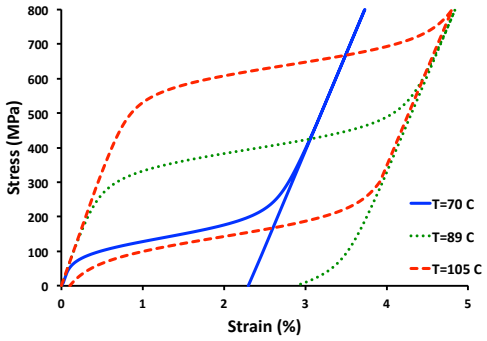

(a) Strain-temperature response of NiTi under different compressive biasing loads

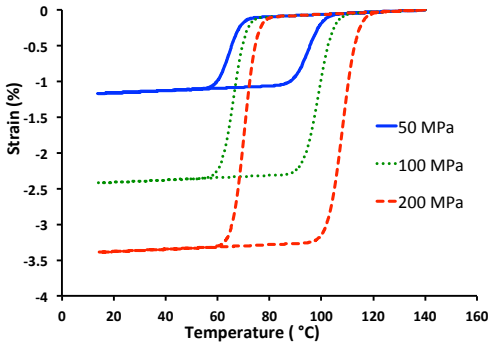

(b) Stress-strain response of NiTi at different isothermal temperatures

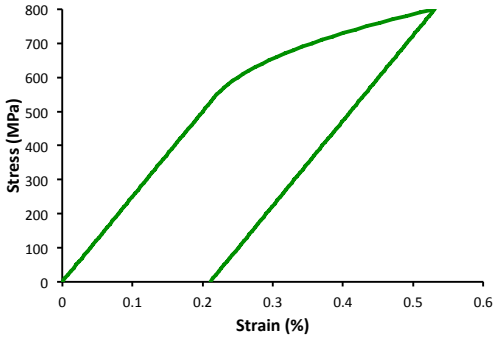

(c) Strain-temperature response of Ti_2AlC

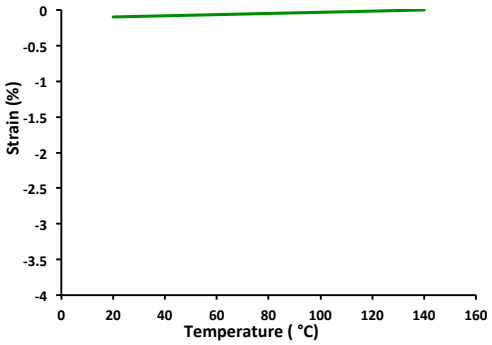

(d) Stress-strain response of Ti_2AlC

Figure 17: Simulated constitutive responses of the NiTi and Ti_2AlC phases.

3.1 Reference Composite Response

As will be pointed out in the following section, the actual NiTi-Ti_2AlC composite that will be studied has a number of additional complications that are accounted for. Therefore, before proceeding to the more complex examples, simpler two-phase reference composites are considered. First, simpler representative microstructures are considered. This study may not only illuminate the interaction of the various

Table 3.1: Model parameters for the transformable bulk NiTi

Parameter	Value
E^A	67 GPa
E^M	56 GPa
$\nu^M = \nu^A$	0.33
$\alpha^M = \alpha^A$	16 x 10^{-6} $^\circ C^{-1}$
M_s^0	68°C
M_f^0	60°C
A_s^0	86°C
A_f^0	99°C
C^A	11 MPa/°C
C^M	25 MPa/°C
H_{sat}	0.0345

Table 3.2: Thermoelastic properties for Ti_2AlC [186].

Parameter	Value
E^{MAX}	250 GPa
ν^{MAX}	0.17
α^{MAX} (from [18])	8.20 x 10^{-6} $^\circ C^{-1}$
σ^y	540 MPa

phases but also play an important role in analyzing the impact of the composite. Secondly, a realistic composite with a heterogeneous composite similar to that may be expected in the actual composite is investigated.

3.1.1 Realistic Microstructure

To investigate the effective response of SMA-MAX Phase composites, a heterogeneous microstructure of a representative two-phase composite is constructed. The construction of the FE-model and additional modeling details are presented in Section 3.1.1.1 and corresponding results are given in Section 3.1.1.2

3.1.1.1 Numerical Microstructure Generation and Modeling Approach

To account for the influences of an irregular microstructure, a numerical model based on actual microstructures is necessary. To this end, an image-based technique which develops numerical microstructures from x-ray tomography results is utilized. These techniques have been used to analyze of a wide variety of material responses (*e.g*, yield in polycrystalline β-Ti [193]) incorporating the 3D effects of the microstructure. The basis of this technique is first identifying and characterizing an appropriate microstructure. First, it is noted that one of the proposed methods for the SMA-MAX composites and used with other SMA systems (like the Mg-NiTi composite studied by Li *et al.* [145]) is a melt infiltration approach. In this case, a porous backbone is manufactured and the second phase is then infiltrated into this skeleton. Therefore, a porous NiTi specimen[5] was selected for use as a base, representative microstructure. The resultant microstructure was then characterized via x-ray microtomography using a SkyScan 1172 tomography machine[6]. A FE mesh was then created based on these results by treating each volume pixel (voxel) as a single element and segmenting the elements as either NiTi material or pore. The porosity was then considered to be the MAX phase material to approximate complete infiltration of the base specimen. A reduction was applied to the mesh to maintain geometric fidelity while achieving reasonable computational cost. Examples of this are shown in Fig. 18 in which a 2D tomograph and reconstructed 3D numerical microstructure are shown in Figs. 18a and b, respectively. The FE mesh used in this study is then presented in Fig. 18c. The resultant mesh is comprised of 48% (volume) Ti_2AlC.

The considered composite is virtually processed through an actuation loading

[5]Specimen provided by Prof. Karaman and group (MSEN TAMU)

[6]Microstructure characterization and mesh generation of this material was performed at the US Naval Research Laboratory with assistance from Drs. Andrew B. Geltmacher, Alexis Lewis, Siddiq Qidwai, and Rick Everett

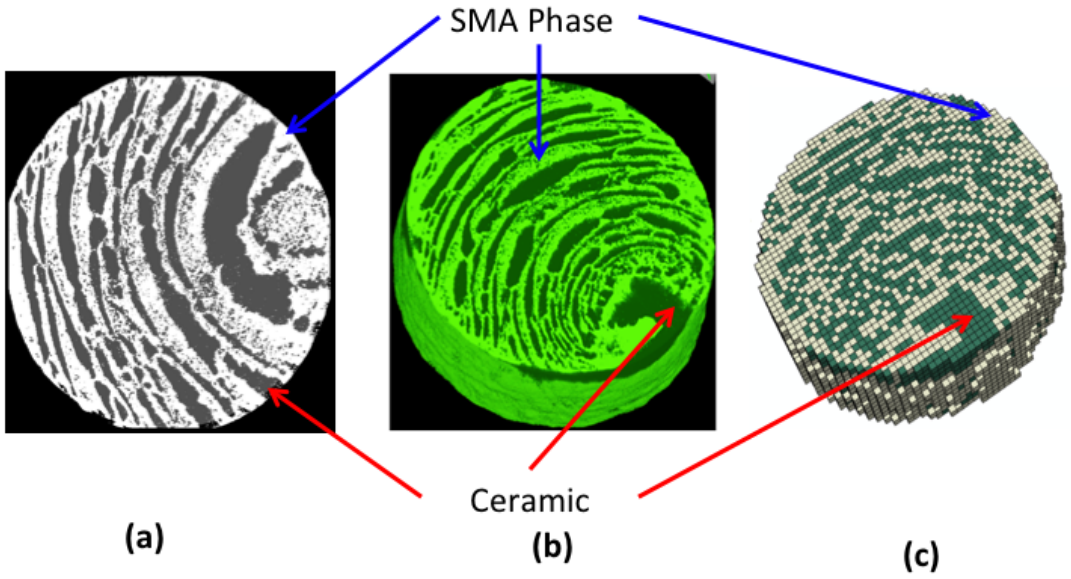

Figure 18: Numerical microstructure and mesh generation of a NiTi-Ti_2AlC phase composite: (a) segmented 2D x-ray tomograph of the characterized porous NiTi cross-section (b) reconstructed 3D microstructure of the considered composite and (c) the finite element mesh of the composite. Reproduced with permission from [139].

path like that presented in Fig. 16. Specifically, a mechanical load of 200 MPa is applied to the cylindrical specimen in the axial, through-thickness ("3") direction at an initial temperature of 500°C. The tensile load is applied through distributed concentrated forces along the top face shown in Fig. 18c while the bottom face is fixed in the 3-direction. One node (approximately at the center) along this bottom face is also fixed in the 1- and 2-directions to suppress rigid body motion. With respect the material properties, these simulations were performed prior to characterization efforts leading to the properties in Tables 3.1 and 3.2. Therefore, the SMA properties

presented in Table 2.1 were used to model the SMA phase. For the Ti_2AlC, an elastic modulus of 278 GPa was used [198] while a yield stress of 200 MPa was used based on the observations of Radovic *et al.* [197] regarding the tensile loading of a Ti_3SiC_2 specimen. The plastic hardening modulus of 1755 MPa with an exponent of 1.05 was selected based on a reference material. The effect of the hardening exponent in similar cases has been previously considered and does not strongly influence the stress state [140].

3.1.1.2 Results and Discussion

As the stress distribution and interaction of the inelastic mechanisms is of particular interest here, the stress states of the Ti_2AlC phase in the direction of applied (axial) loading, σ_{33}, at the points labeled A-E in Fig. 16 are shown in Fig. 19. Note, the temperature and load values are slightly different in Fig. 16 than used in this simulation (*e.g*, a maximum temperature of 500°C). Nonetheless, as they represent the same points in the actuation load path they are used here for the corresponding discussion. For clarity, the SMA content has been removed from the images through post processing. Initially, at point A in Fig. 16, the composite is unloaded and the Ti_2AlC material is stress free (Fig. 19a). After mechanical loading, point B in Fig. 16, the ceramic phase has a tensile stress state in the direction of applied loading with areas of high local Ti_2AlC content having lower stresses than areas of higher SMA content as observed in Fig. 19b. After the composite is cooled (Fig. 16 point C), the Ti_2AlC phase, as shown in Fig. 19c, has an increased stress in the direction of applied loading. After the composite is subsequently heated back to the maximum temperature (point D), a large reduction in the Ti_2AlC stress is noted in Fig. 19d. Finally, after mechanical unloading (point E), the composite returns to its initial

external loading state although the Ti_2AlC phase has a residual stress state which is mostly compressive as shown in Fig. 19e . Importantly, by comparing points with the same external loading conditions (points A and E and points B and D) different ceramic stress states are observed in the corresponding figures in Fig. 19. In both cases, the difference between the two points is the effect of the thermal cycle through forward and reverse transformation.

From the results of Fig. 19, it is demonstrated that a residual stress state does

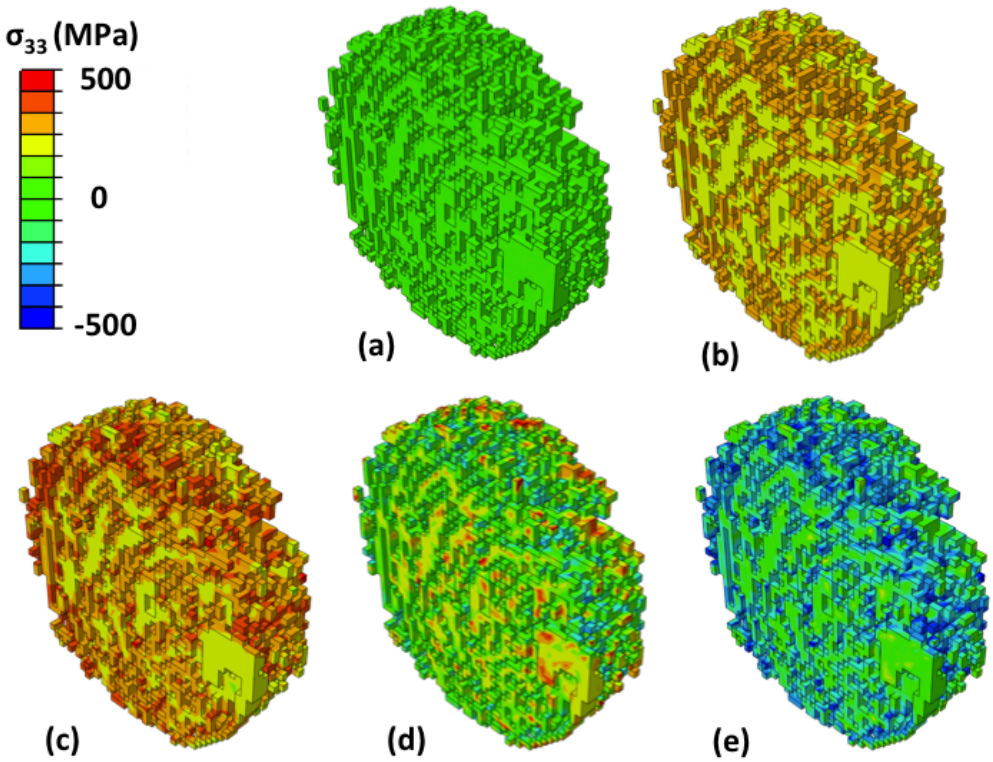

Figure 19: Stress state in the Ti_2AlC phase in the direction of applied loading ("3") through an actuation loading path under 200 MPa applied load (SMA phase has been removed for clarity): (a) at the beginning of the loading cycle (b) after mechanical loading (c) after cooling through forward transformation (d) following heating through reverse transformation and (e) subsequent to mechanical unloading. Reproduced with permission from [139].

develop in the composite through a thermomechanical loading cycle incorporating complete transformation. One essential question then is whether or not a simpler cycle can produce such a state. If so, this path must be identified to avoid operational conditions which would increasingly lead to further permanent deformations and eventually failure. Additionally, if such a path is identified that could simplify the training process needed to produce such states. Therefore, the possibility of using purely mechanical or purely thermal loading path is considered here. To consider this issue, the final stress states in the direction of applied loading are presented below in Fig. 20 for the previous thermomechanical and pure mechanical and thermal loading paths along. The loading path used in each analysis is also presented in Fig. 20 to highlight the different cases. For the cases of the pure thermal or mechanical loading, it is observed in Figs. 20a and c that both loading paths produce a negligible residual stress state. Thus, to produce a residual stress state a coupled thermomechanical loading path is necessary. As such, by careful consideration of the desired operational conditions of the material, a thermomechanical loading path may be designed resulting in a compressive residual stress state.

Although the ability to generate a residual stress state, which qualitatively appears compressive, through an actuation cycle has been demonstrated, it has not been quantitatively considered. To this end, Fig. 21 presents the Ti_2AlC phase average stress in the direction of applied loading, $\bar{\sigma}_{33}$, along with the average SMA martensitic volume fraction (MVF), ξ. It is observed in Fig. 21 that during step 1, the mechanical loading corresponding to A$\rightarrow$B in Fig. 16, the response is initially elastic although at higher stresses there is a small change in slope indicating the beginning of irrecoverable strain generation. During the initial cooling of step 2 (B$\rightarrow$C of Fig. 16), prior to the initiation of forward transformation, the average stress in the direction of loading decreases due to thermal expansion mismatch of the the two

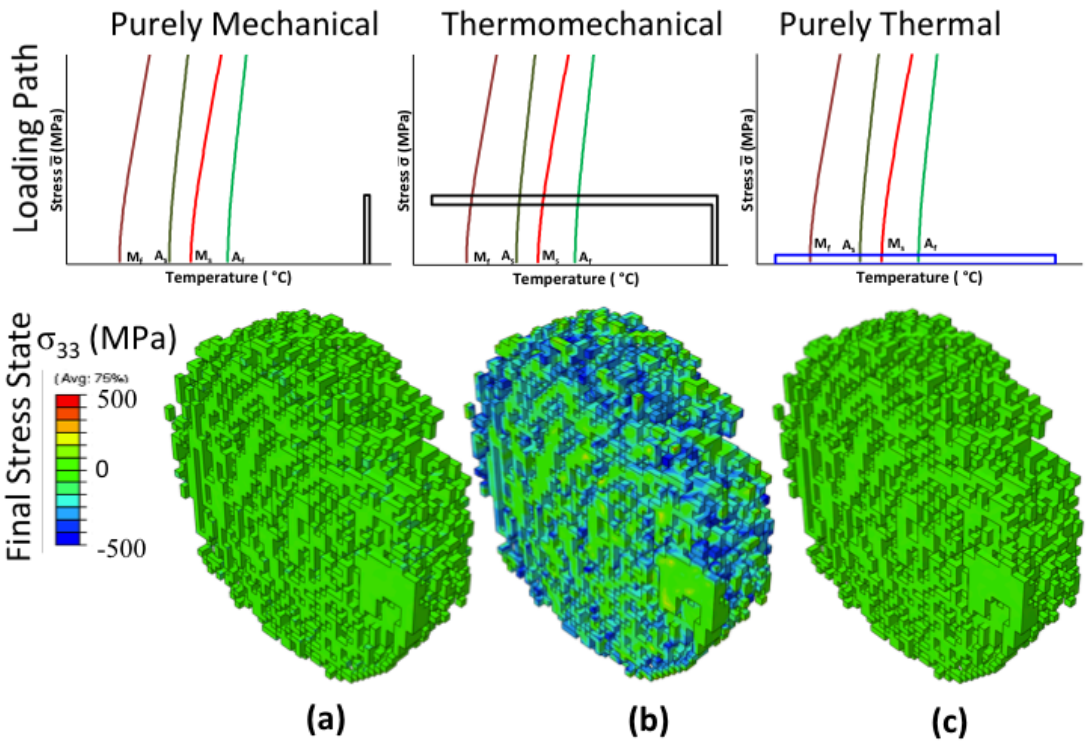

Figure 20: Effect of load path on the final residual stress state of the considered SMA-MAX phase composite. The top row shows the different considered loading paths while the bottom row shows the final stress in the direction of applied loading of the MAX phase following the completion of the (a) purely mechanical (b) thermomechanical and (c) purely thermal loading paths. Reproduced with permission from [139].

constituent phases. During forward transformation, as indicated by the increase in SMA phase average Martensitic Volume Fraction (MVF), ξ, a sharp rise of nearly 100 MPa is noted in the Ti_2AlC phase. Upon the completion of transformation, a further reduction in the phase average stress in the direction of applied loading is observed as the composite is further cooled. During the heating stage, step 3 in Fig. 21 corresponding to C→D in Fig. 16, the thermal expansion mismatch yields

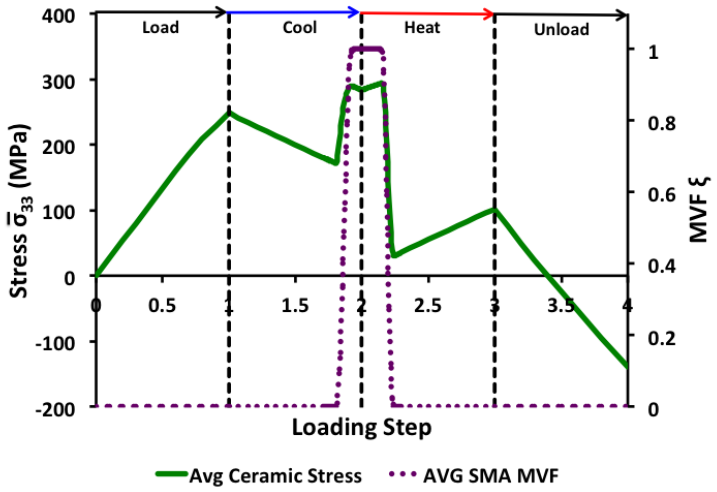

Figure 21: Phase average stress of the MAX phase in the direction of applied loading over the course of the loading cycle. Reproduced with permission from [139].

higher MAX phase average stress in the direction of applied loading. When the SMA phase undergoes reverse transformation, indicated by the SMA phase average MVF going to 0, a large drop of over 200 MPa is noted in the ceramic phase as the SMA contracts allowing for a stress relaxation in the MAX phase. As the composite is heated back to the original temperature, the phase average ceramic stress in the direction of applied loading continues to increase. At the end of the heating step, point D in Fig. 16, the ceramic has a lower phase average stress that at the same point (B) prior to transformation. Thus, when the composite is unloaded during Step 4 (D→E) the MAX phase average stress in the direction of applied loading decreases past zero and achieves a final average stress of -140 MPa.

As the previously discussion has indicated, the composite residual stress state in the composite develops from the generation of irrecoverable strains in the MAX phase. To consider the evolution of such strains over the course of the loading cycle,

the ceramic phase average irrecoverable strain in the direction of applied loading, $\bar{\varepsilon}^{p}_{33}$, is presented in Fig. 22 along with the SMA phase average MVF. During the

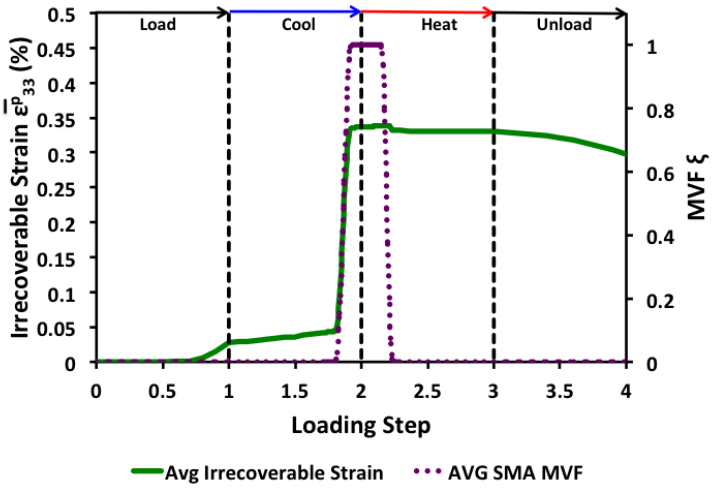

Figure 22: Phase average irrecoverable strain of the MAX phase in the direction of applied loading over the course of the loading cycle. Reproduced with permission from [139].

mechanical loading of step 1 in Fig. 22, it is noted that the response is initially elastic although towards the end of the loading step some irrecoverable strains are generated. During cooling, step 2, prior to forward transformation a small increase in the average irrecoverable strain in the direction of applied loading is observed. When forward transformation occurs, a much larger quantity of irrecoverable strains are generated in the direction of applied loading. Small amounts of irrecoverable strain are generated during further cooling of step 2 and the initial heating of step 3 prior to reverse transformation as observed in Fig. 22. Through reverse transformation, a small amount of irrecoverable strains in the direction opposite of loading are

generating leading to a decrease in the magnitude of irrecoverable strain in the direction of loading as noted in Fig. 22. These strains are the result of local effects and highlight the importance of microstructure in such composites as incorporation of specific features through microstructure design could be used to increase or decrease such effects. Over the course of further cooling, minor decreases in the magnitude of irrecoverable strain in the direction of loading are observed in Fig. 22. By mechanically unloading the composite, step 4 in Fig. 22, a more substantial decrease in the magnitude of the plastic strains in the direction of applied loading is noted although such reductions are much smaller than the amount of strain generated during forward transformation. The final irrecoverable strain magnitude in the direction of applied loading of $\approx$0.3%.

3.1.2 Impact of Microstructure

The previous section investigated the response of a complex heterogeneous microstructure. Although some qualitative assessments in terms of microstructure can be made through such an analysis, the actual specific impact of different features can be hard to extract from the effective response. Therefore, in this section, these influences are investigated (in terms of actuation and residual stress results) via the consideration of simplified UCs with different basic geometries. In these analysis, the first-order metric of volume fraction of the NiTi reinforcement is kept fixed ($\approx 40\%$) but the geometry is varied. The microstructures being investigated are presented in Fig. 23 and are comprised of three cases: (*i*) distributed spherical (*ii*) continual unidirectional fiber and (*iii*) continual interpenetrating phase reinforcements. These three cases will be denoted "Sphere", "Fiber", and "IPC" (for interpenetrating phase composite), respectively, in what follows. The first two configurations represent common particulate and unidirectional fiber reinforcement architectures. In the fiber case,

the reinforcement is aligned with the direction of loading. Interpenetrating configurations, on the other hand, represent continual reinforcement in all three directions and is a representation of what might be observed in a melt-infiltrated composite. In this case, it is assumed that the reinforcement is equal in all three direction. As shown in Fig. 24, the ratio a/b in introduced to describe the relevant reinforcement in each direction. The radius of the reinforcement (assumed to be a fiber-like geometry) in the direction of loading is denoted as a while b is used to represent the radius of the fibers in the two transverse directions. In this fashion, $a/b = 1$ is the case considered here with equal reinforcement, while $a/b = \infty$ would be the continual, fiber case depicted in Fig. 23b.

Given the simplified nature of the microstructures, repeating units are easily

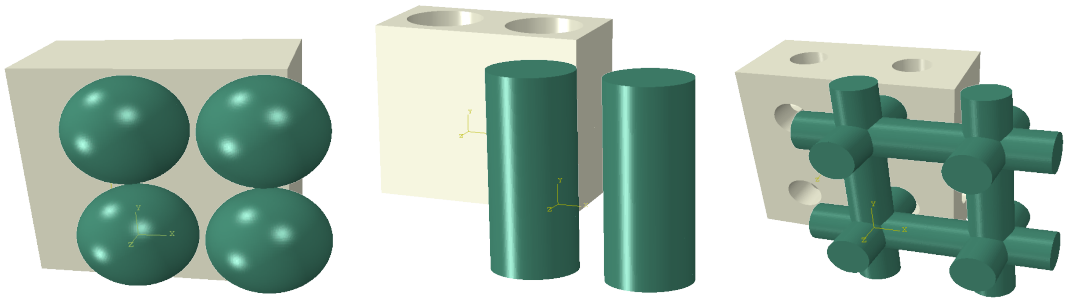

(a) Distributed, spherical reinforcement

(b) Continual, fiber reinforcement

(c) Continual, interpenetrating phase composite (IPC)

Figure 23: Example microstructure investigated to determine the impact of the architecture. The SMA reinforcement is colored green and is removed and presented in front of the tan colored Ti_2AlC matrix for clarity

identified and symmetry in three directions may be readily observed. Therefore, one-eighth symmetry unit cells like those presented in Fig. 24 for the IPC configuration are constructed and used in this analysis. As discussed in Section 1.2, Kanit *et al.* [115] extensively studied the impact of applied boundary conditions on the

analysis of various RVEs and other computational volumes. Specifically, that work investigated both the impact of the size of the RVE and applied boundary condition (either homogeneous strain, stress, or fully periodic boundary conditions) on the determination of effective properties. From their results, Kanit and coworkers [115] first noted that accurately determining the effective properties of the composite requires fewer realizations for larger sized RVEs while smaller computational domains require more realizations. Additionally, as the numerical microstructure increases in size the impact of the boundary conditions becomes less pronounced. Nonetheless, in smaller domains, it was observed that kinematic (strain) boundary conditions tend towards the upper Voigt bound while traction conditions are closer to a lower Reuss bound. [115] Bearing all of this in mind, the objective of this study is to consider the relative impact of the microstructure on the performance of a composite. The intent being to extract the impact of different base features on the composite response rather than specific properties. Therefore, a constant (tensile) traction is applied along one-edge while the symmetry planes have corresponding displacements fixed as shown in Fig. 24. The remaining edges are given traction-free conditions and the composite is assumed to have a homogeneous temperature field. A thermomechanical loading corresponding to the actuation cycle as presented in Fig. 16 is applied.

The effective strain–temperature response of the composites through an actuation loading path with a bias stress of 250 MPa is presented in Fig. 25. In considering these results, it is first noted that although the effective actuation strains are much smaller than that of the bulk SMA, a clear actuation behavior is present in all three microstructures. By comparing the results, it is observed that the largest strains are induced in the spherical reinforcement while the fiber case has the smallest actuation strain (roughly half that of the sphere case). Interestingly, the interpenetrating result is closer to the spherical case. Similarly, the nonlinear regime characteristic of

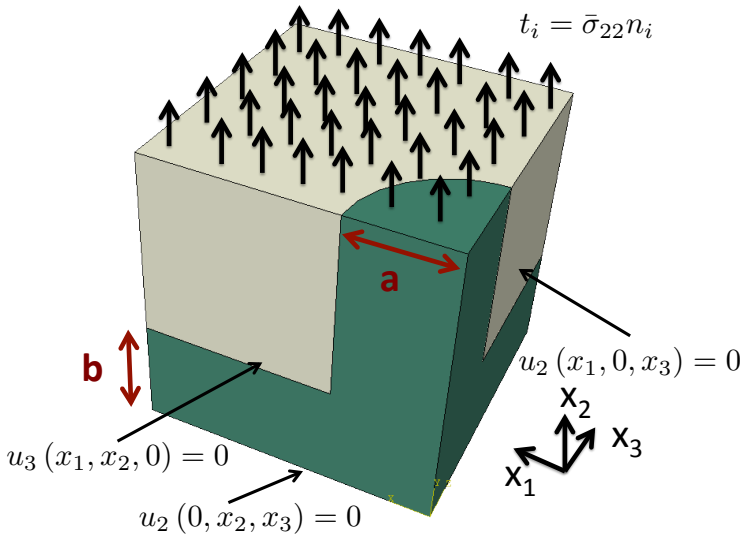

Figure 24: Boundary conditions and one-eighth symmetry computational domain of the IPC microstructure. Green reinforcement is the SMA phase while the tan matrix is the Ti_2AlC content.

transformation occurs in very similar temperature domains for the sphere and IPC cases. For the fiber case, on the other hand, transformation occurs at slightly higher temperature. Finally, in all three cases, the development of permanent deformations (indicated by the difference in the strains at $T = 140°C$ before and after transformation) is noted. Such irrecoverable strains are indicative of residual stress states like those observed in the preceding section.

To consider these results more carefully, the phase average stress in the direction of applied loading, $\bar{\sigma}^r_{22}$ (where r is SMA or MAX), over the course of the loading cycle is presented in Fig. 26. Similar to the previous results, it is noted that in all cases initial loading leads to elastic loadings and the start of cooling induces stresses associated with the thermal expansion mismatch. Upon transformation, the sphere and IPC results follow the previous trends in that a sharp increase is noted in the

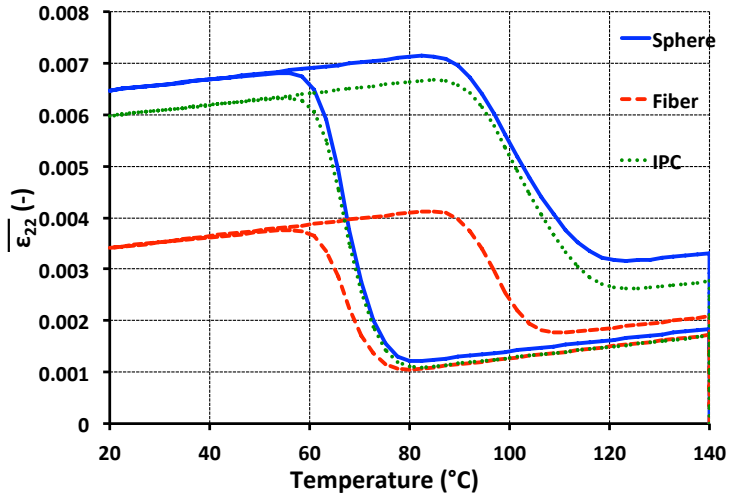

Figure 25: Effective strain–temperature response of composites with the different reinforcement types under a constant applied biasing load of 250 MPa.

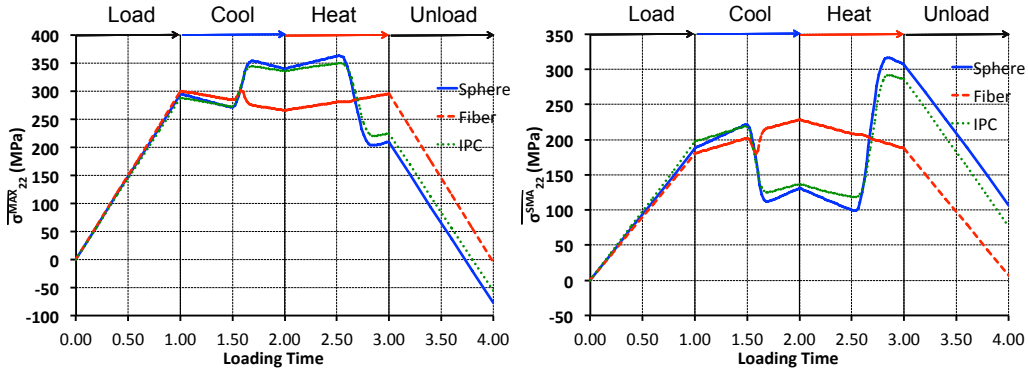

(a) Ti_2AlC (b) NiTi

Figure 26: Phase average stress of the different constituents in the direction of applied loading through an actuation loading cycle with an applied tensile stress of 250 MPa.

Ti_2AlC with a corresponding decrease in the NiTi phase. These trends are reversed upon heating leading to a residual stress state. The fiber case, however, shows a different trend. Interestingly, upon transformation, the stress results initially follow the other cases. Quickly these results diverge and the changes are eliminated and the

stress state in both phases is comparable to what would be expected if only thermal expansion were present. Upon reverse transformation, only minor changes to the stress states are noted. Therefore, upon unloading, small residual stresses (-5 MPa in the Ti_2AlC phase) are present. This evolution in the stress states stands in contrast to the other case and understanding the origin can be important in subsequent material design.

To consider this problem, the various components of the SMA phase average stress tensor, $\bar{\sigma}_{ij}^{SMA}$, of the sphere and fiber case are presented in Fig. 27a and b, respectively. Before proceeding, it is important to note that in both cases the 11 and

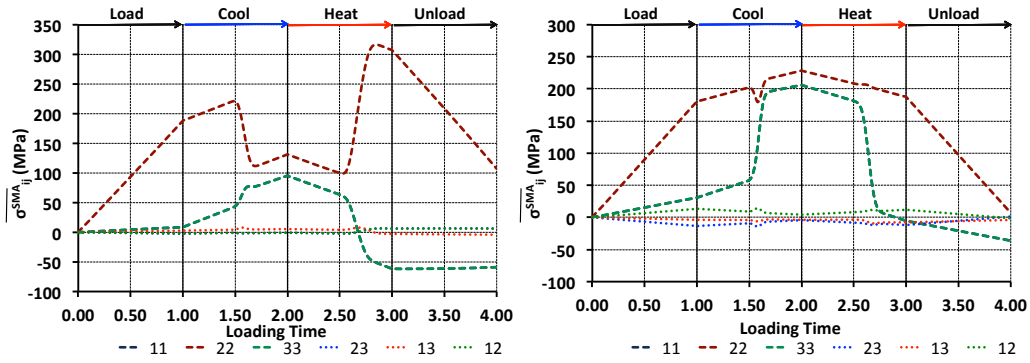

(a) Spherical Reinforcement

(b) Fiber Reinforcement

Figure 27: Components of the NiTi phase average stress ($\bar{\sigma}_{ij}^{SMA}$) for different reinforcement cases through an actuation loading cycle with an applied tensile stress of 250 MPa.

33 (transverse to loading) results lie on top of each other in Fig. 27. In comparing the two cases, both Fig. 27a and b show similar trends prior to transformation. Once transformation occurs, as Fig. 26b showed, the results quickly differ. Importantly, in Fig. 27b it is observed that transverse components ($\bar{\sigma}_{11}^{SMA}$ and $\bar{\sigma}_{33}^{SMA}$) increase

in magnitude substantially more than in the spherical case. This is associated with the deviatoric nature of the transformation strains in the SMA phase (Eqn. 2.4). Specifically, given the cylindrical nature, as the SMA expands in the direction of loading a corresponding contraction is produced in the lateral directions. Given the thermoelastically stiff nature of the Ti_2AlC phase, this deformation produces stresses opposing that contraction leading to an increase in the tension in the transverse directions. As presented in Fig. 28, this greatly increases the mean stress of the NiTi case versus the sphere and IPC case. As a consequence of this changing stress state, the magnitude of the strains generated in the direction of applied loading (Λ_{22}^{tr}) actually decreases in the fiber case. These leads to the reduced actuation strain and residual stresses observed in the fiber case in Figs. 25 and 26.

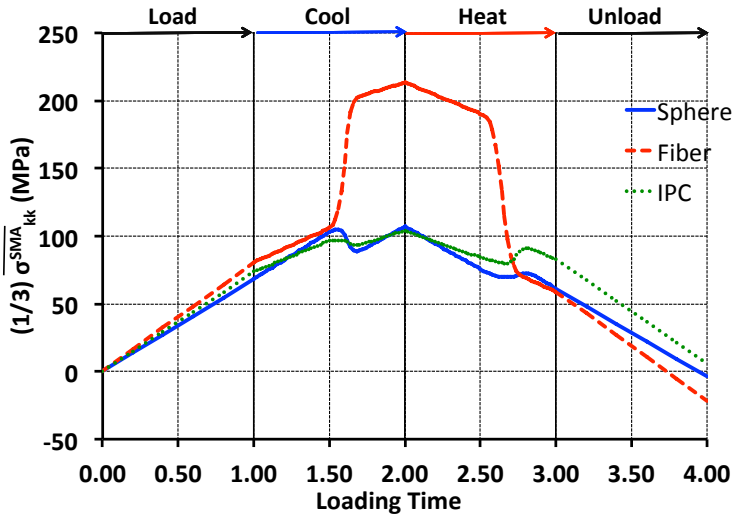

Figure 28: Phase average mean stress of the NiTi phase ($\frac{1}{3}\bar{\sigma}_{kk}^{SMA}$) through an actuation loading cycle with an applied tensile stress of 250 MPa

The spherical and fiber reinforcement cases represent two "extreme" cases with respect to reinforcement architecture. This difference is manifest in the results just discussed. Importantly, for microstructure design, a key question may be what happens between these cases. To address this, the IPC case is studied in more detail. In Figs. 25 and 26, it may be seen that the results of $a/b = 1$ are similar to that of the spherical reinforcement case. At larger a/b ratios, the interpenetrating case is close in configuration to the fiber case. Therefore, the impact of this parameter on the residual stress state to see investigate the response in the regions between the sphere and fiber cases. Therefore, a series of unit cells with different ratios are constructed and subjected to the same loading path and the final phase averaged stresses in the direction of applied loading as a function of the a/b ratio is presented in Fig. 29. From the results in Fig. 29, it is observed that the residual stress magnitude quickly decreases as the a/b ratio increases. At values of two and above, the values of the residual stress are nearly zero and approximate the values of the unidirectional fiber case.

At this point, the previous discussion of boundary conditions is briefly recalled. Specifically, all of the results presented to this point correspond to uniform applied traction cases. To consider the impact of this assessment, additional simulations of the sphere case are considered with revised boundary conditions along the $(x_1, x_2, x_3) = (x_1, L, x_3)$ (top) edge. Specifically, multipoint constraints are applied along that edge such that the displacements on that face are constrained to be the same while a point load corresponding to the desired traction is applied at the corresponding reference node. The stress in the direction of applied loading of the MAX phase is presented in Fig. 30. From these results, it may be observed that the same general behaviors as shown in Fig. 26a. In comparing the two results, in this revised boundary condition case, it may be noted that during cooling and heating

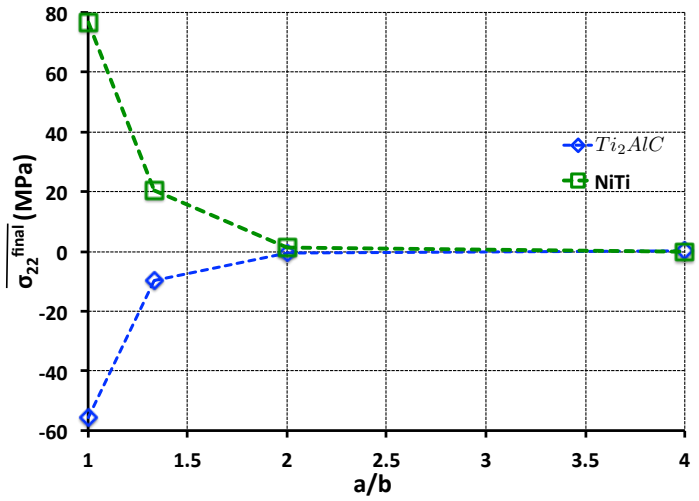

Figure 29: Phase average residual stress in the direction of applied loading of the different constituents after an actuation cycle with an applied tensile load of 250 MPa. Results are for IPC architecture with different fiber radius ratios, a/b.

more substantial changes in the MAX phase stress (steeper slopes) than in the previous case. A slightly larger magnitude final residual stress is noted while a smaller maximum stress during cooling is evident. A larger difference is noted between the cooling and heating phase. Although not shown, the same analysis with the IPC case demonstrates similar behaviors. In that case, however, a lower final residual stress is noted. Nonetheless, even with these differences, the same relative behaviors are observed – which is the objective of this work.

3.2 NiTi – Ti_2AlC Composite

The previous section highlighted the possibility of generating residual stresses in NiTi-MAX phase composites using simplified or approximate microstructures. In this section, a model of an actual NiTi-Ti_2AlC composite is explored. Beyond just the difference in microstructure, it is noted that in the actual composite there are

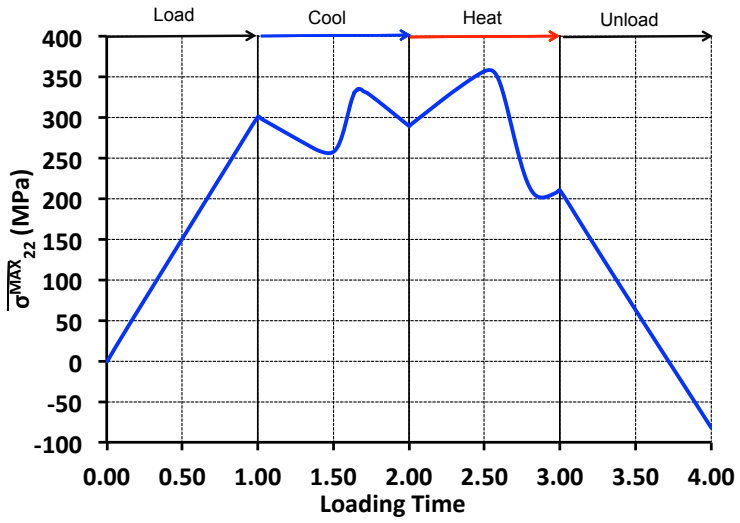

Figure 30: Phase average stress in the direction of applied loading of the MAX phase ($\bar{\sigma}_{22}^{MAX}$) of the sphere case through an actuation loading cycle with an applied tensile stress of 250 MPa

additional phases (namely porosity and a reaction layer/interphase) present further complicating the process. Therefore, in Section 3.2.1 the generation of the micromechanical FE model is discussed while corresponding results are presented in Section 3.2.2. Both the actuation response and generation of residual stress state are explored and a series of parametric studies are performed on a number of microstructural features to investigate their impact.

3.2.1 Composite FE Model Generation

To include the effects of the heterogeneous microstructure, a numerical mesh of composite is developed using image based techniques. These techniques utilize x-ray microtomography, serial sectioning and other techniques to generate digital images of the microstructure under investigation and turn them into finite element meshes [91, 92, 143, 144, 193]. Such methodologies have been used to investigate the

role of texture in the yield of polycrystalline β-Ti [193] and thermal stress induced damage on the effective properties of Cr-Al_2O_3 composites [230]. Here, a SkyScan 1172 high-resolution micro-CT was used to image the NiTi-Ti_2AlC composite specimen utilized in subsequent experiments. The specimen was a 50 vol% NiTi - 50 vol.% Ti_2AlC composite processed at a sintering temperature of 960°C for a holding time of 10 minutes under a 100 MPa applied stress using the spark plasma sintering technique. Further details of the processing methodology and approach may be found in the work of Hu *et al* [108]. A finite element mesh was then created from the tomography results by treating each volume pixel (voxel) discretely and applying different thresholds to differentiate the three phases present in the material system (NiTi, Ti_2AlC and porosity). In this case, a mesh corresponding to the entire characterized material domain is constructed. This is done as (*i*) essential microstructural characteristics have not been determined *a priori* and (*ii*) lack of statistical analysis demonstrating homogeneity in the microstructure. Therefore, the entire domain is used in lieu of a smaller sub RVE whose representative nature has not been established. The porosity was a result of the manufacturing and was calculated to be 10.6% of the specimen volume by using Archimedes' principle as specified in ASTM C20-00 [11]. As equal amounts of both Ti_2AlC and NiTi powders were used in the manufacturing, the remaining dense volume was assumed to be split evenly between Ti_2AlC and NiTi phases resulting in volume fractions of 44.7%. These volume fractions were used with the histogram of the composite pixel values to find threshold levels which best fit the expected concentrations. This approach was adopted here because the densities of NiTi and Ti_2AlC are close enough such that x-ray microtomography does not result in easily discernible, discrete thresholds. Given the large data set associated with the microtomography, a mesh reduction is applied which maintains geometric fidelity while decreasing the computational cost of the simula-

tions. Namely, a prescribed reduction factor is applied such that the given number of elements in each direction are reduced to a single element and assigned the most common material value. This process results in a mesh of roughly 44,000 linear 3D elements and is represented schematically in Fig. 31

Preliminary differential scanning calorimetry (DSC) experiments[7] (Fig. 32) were

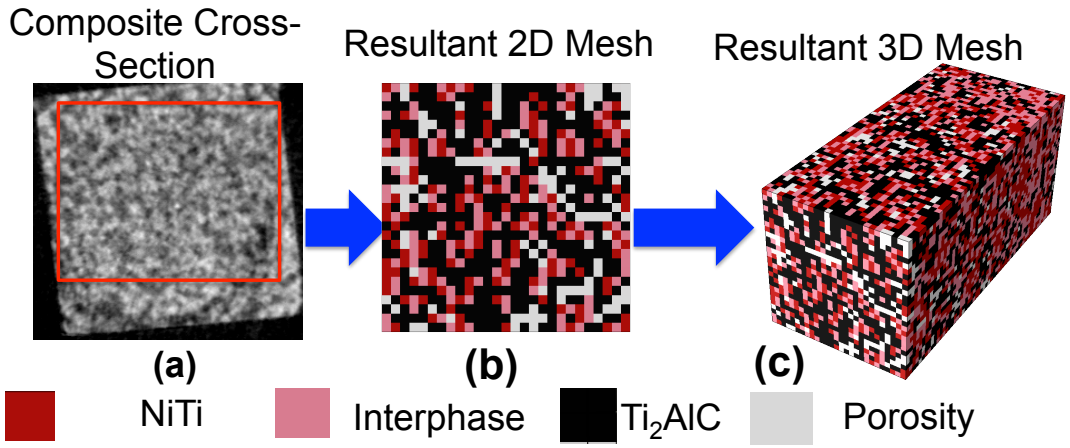

Figure 31: Development of finite element mesh used in this study: (a) Single 2D image resultant from micro-tomography (b) Mesh of the cross section after applying threshold values and mesh reduction and (c) the final 3D constructed mesh.

conducted using a TA Instruments, Q20^{TM} DSC and indicated the composite has a lower latent heat than is expected for the given concentration of NiTi. The reduced latent heat indicates that some of the NiTi content does not transform and is indicative of the the presence of a non-negligible reaction layer or interphase. This interphase material is likely due to a combination of effects including internal stress fields, compositional gradients, and interfaces between the NiTi-Ti_2AlC as well as other microstructure imperfections and has been extensively discussed by Hu *et*

[7]DSC results provided by A. Kothalkar and Profs. Radovic and Karaman (TAMU MSEN).

al. [108]. A similar effect has also been observed by Mari and Dunand in NiTi-TiC composites who noted a reduction in transformation enthalpy and postulated it was due to the presence of either retained, stabilized martensite or austenite [155]. Past investigations into bulk NiTi have also shown that internal stress fields lead to retained, or non-transforming, martensite [121]. As such, and although the actual constitutive response of this interphase is unknown and likely gradient, all of this reaction layer is assumed to be retained martensite. This assumption is investigated in more depth in Section 3.2.2 as a parametric study. Following the experimental results, the NiTi was split into transforming (45% of the total NiTi volume) and non-transforming, interphase groups. Although more detailed investigation is needed to determine spatial locations of the non-transforming NiTi, as diffusional and interface effects will be more pronounced near the Ti_2AlC-NiTi interface, NiTi elements closer to Ti_2AlC material were taken to be non-transforming.

The mesh generation methodology described above results in four distinct phases - Ti_2AlC, active NiTi, interphase, and porosity. Elements corresponding to the active NiTi and Ti_2AlC phases are described according to the constitutive models described previously at the start of this section. The two other phases (porosity and interphase) present in the system are assumed to behave elastically. First, as the porosity is treated discretely, it is defined to be an elastic material with negligible stiffness ($\approx$ 10 Pa) and zero Poisson ratio and coefficient of thermal expansion. This results in an elastic modulus of the porosity that is $\approx 10^{-9}$ of the SMA phase in line with past studies by Qidwai and DeGiorgi [188] and Panico and Brinson [174]. Although the constitutive properties of the interphase are unknown, it is assumed that this phase behaves as retained martensite and the elastic properties are assigned to be those of the martensitic phase used for the transforming NiTi.

As described at the start of this chapter, the composite is subjected to an ac-

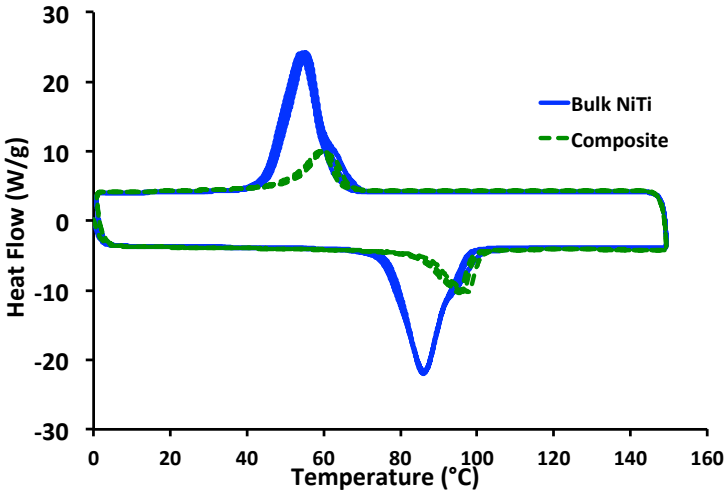

Figure 32: Heat flow of bulk NiTi and the NiTi-Ti_2AlC composite measured through 3 heating-cooling cycles via DSC.

tuation loading path as shown in Fig. 16. Both the loading and cooling rates are assumed to be sufficiently slow to ensure quasi-static loading conditions so that latent heat and temperature gradient effects may be neglected. To implement this loading path, the long, axial direction ("x_3") is used as the loading direction. As further statistical analysis is needed to determine an appropriate representative volume element (RVE) size for this material, periodic boundary conditions are not utilized. Such a consideration also represents experimental conditions used to investigate this material. Therefore, one edge ($x_3 = 0$) is taken to be the bottom and fixed in the loading direction. A single point at the center of the composite on the bottom edge is fixed in all directions to prevent rigid body motion. A rigid plate is then placed in contact with the top surface with a no penetration contact condition. A concentrated force is applied equivalent to the desired stress is then applied at the center of the rigid plate to evenly distribute the applied load. The remaining edges are assumed to be traction-free. Following the experimental procedure, the initial temperature, T_0,

is 140°C and the composite is cooled to room temperature (20°C). As temperature gradients are neglected and a homogeneous temperature field exists in the composite, the temperature field is prescribed throughout the material body.

3.2.2 Results and Discussion

To explore the response of the present NiTi-Ti_2AlC composite, the effective actuation behavior of the composite is investigated - both numerically and experimentally. First, the experimental results of actuation cycles are presented and some unique characteristics of the composite response are discussed. Numerical simulations are presented and the two results compared. The computational results are then used to explore elements of the composite response not easily accessible experimentally. Specifically, the simulations are probed to examine the interaction of the two phases and, importantly, the development of any residual stress states in the composite. Finally, parametric studies on different composite microstructural and themomechanical loading parameters are performed to identify and quantify their influences on the composite response.

3.2.2.1 Effective Actuation Response

The effective actuation response of the composite is first characterized experimentally[8]. Isobaric heating-cooling cycles were conducted under uniaxial compressive bias loads on an MTS Insight electromechanical test frame. Details of these tests may be found in the work of Kothalkar *et al.* [120] on the experimental characterization of NiTi-Ti_3SiC_2 composites. Unlike the loading path described at the start of the chapter, however, the composite is not unloaded at the end of each

[8]Experimental results of the NiTi-Ti_2AlC composites provided by A. Kothalkar and Profs. Radovic and Karaman (TAMU MSEN).

heating-cooling cycle. Instead, after heating back to the reference temperature the load on the composite is increased to the next test condition. The heating-cooling results of these experiments are presented in Fig. 33. For clarity, and as the response through thermal cycling is of specific interest here, only the heating-cooling cycles are presented. To facilitate comparisons of the results, all experimental results start from zero strain at the reference temperature.

A number of key characteristics may be observed from the experimental results

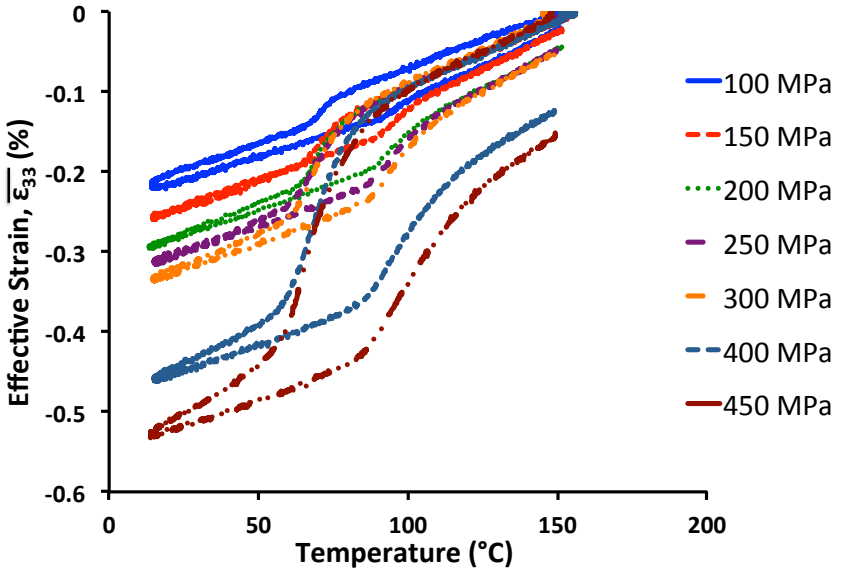

Figure 33: Effective strain vs. temperature results of the NiTi-Ti_2AlC composite thermally cycled at different constant applied compressive biasing loads

in Fig. 33. First, the composite shows a hysteretic behavior when subjected to an actuation path. The presented loops are similar to that observed in bulk NiTi albeit approximately an order of magnitude smaller in the measured strain. Importantly, the development of these hysteresis indicates this material system maintains some of

the important characteristics necessary for actuator applications. In further agreement with bulk NiTi behavior, the size of the hysteresis loop grows with the applied stress magnitude. Initially, at lower applied stress levels, the non-linear deformations are small and primarily recoverable as indicated by the mostly closed hysteresis loop. The slight opening of the hysteresis loop at the reference temperature indicates the development of some irrecoverable deformation although which is likely associated with cyclic effects (namely TRIP in the SMA phase). At these stages, as the inelastic responses are mostly recoverable, the mechanism driving these behaviors is the reversible martensitic transformation of the active NiTi phase. As the applied stress level increases, so does the size of the hysteresis loop. When sufficient stress levels are applied (above 200 MPa), the hysteresis loops open further and the amount of irrecoverable, permanent deformations associated with these cycles also increases. Interestingly, the irrecoverable strains generated through the 200, 250, and 300 MPa cycles are nearly the same while subsequent cycles at higher loads exhibit a stress dependency. Thus, the actuation loops have both a recoverable and irrecoverable component which points to the activation of both the recoverable (martensitic transformation) and irrecoverable (permanent deformations of the Ti_2AlC or NiTi phases) mechanisms. Another important result of the activation of these mechanisms is a change in the behavior of the effective martensitic finish (M_f) temperature. For bulk SMAs, this temperature must increase with the applied stress magnitude. From Fig. 33, however, a decrease in the temperature is observed as the applied stress increases.

The elastic modulus of the composite material was also determined. Due to the various inelasticities of the system, resonant ultrasound spectroscopy (RUS) [157,199] was performed to accurately determine the elastic modulus of the composite [108]. The composite elastic modulus was measured to be 124 GPa through these RUS

techniques.

To further explore the transformation characteristics of the composite under investigation, the effective (composite) response is numerically simulated under the loading path described at the start of the chapter with different applied compressive bias loads. Each simulation is initiated from an undeformed, stress-free configuration. The effective composite strain in the direction of loading-temperature results are presented in Fig. 34 although the loading and unloading portions of the cycle are not shown in the figure for clarity. The results presented in Fig. 34 show many

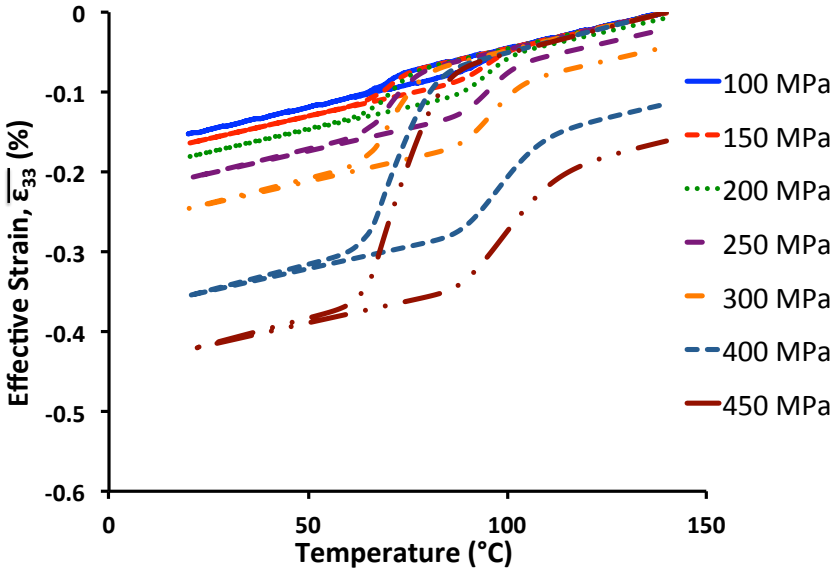

Figure 34: Numerical simulation of the effective strain-temperature response of the composite under different applied compressive bias loads.

important characteristics in qualitative agreement with the experimental results in Fig. 33. First, both open and closed hysteresis loops are observed. At the smaller applied load levels, those below 200 MPa, a closed hysteresis is observed with trans-

formation strain magnitudes similar to those of the experimental results and much lower than in bulk NiTi ($<\approx 0.5\%$). As these inelastic deformations are recoverable, this behavior is associated with the reversible martensitic transformation of the SMA phase. Above 200 MPa, however, open loops are observed indicating the development of irrecoverable strain through the heating-cooling cycle. In this case, and similar to what is observed experimentally, the presence of both recoverable and irrecoverable inelastic strains associated with the activation of SMA-related transformation and irrecoverable deformations of the MAX phase, respectively, is noted. Furthermore, by increasing the applied stress magnitude the transformation strains generated in a heating-cooling cycle increases and the martensitic finish temperature decreases. Examination of the numerical results also produces an effective elastic modulus of 117 GPa - a $\approx 5\%$ difference from the experimental measurement.

Although good qualitative agreement is observed , some quantitative differences between the results are evident. One such difference lies in the effective coefficient of thermal expansion. In this case, the model predicts a lower value than experimentally observed. Part of this difference may be associated with the experimental extensometer measurement of the strain incorporating a portion of the test frame grips. Although only a very small segment of the grips is included in this measurement, given the sensitivity of the thermal expansion coefficient this may produce some of the discrepancy. Interestingly, the thermal expansion coefficient is smaller in the experimental 100 MPa case than in subsequent cooling-heating paths indicating the cause may be related to cyclic effects and possibly retained martensite. Secondly, the modeling results also predict lower effective inelastic (both transformation and irrecoverable) strains than the experimental results. This disagreement, however, may be due to subtle, albeit influential, differences between the experimental and numerical investigations.

To properly compare the two results, important distinctions between the experimental methodology and numerical simulations must be pointed out. First, in performing the experiments, one virgin material specimen was used for all the experiments. Although using only one specimen enables the utilization of one microstructurally informed finite element mesh, this means that the affect of any damage, residual stresses, cyclic hardening, or other permanent deformations is propagated into subsequent thermomechanical cycles. All modeling simulations, on the other hand, assume an initial stress-free composite configuration. Thus, some differences between the numerical and experimental results are expected as the history effects of previous actuation cycles are present in one set of results (experimental) but not the other (numerical). As the composite investigated here was originally a virgin specimen, some cyclic instabilities, particularly TRIP associated with the untrained NiTi content, are to be expected which alter subsequent thermomechanical cycles. The TRIP effects may be further magnified by the external surfaces of porosity near NiTi grains relaxing stored energy leading to retained martensite. This distinction complicates comparisons between the experimental and numerical results and would require using new specimens for each cycle to eliminate these effects.

Another source of possible uncertainty lies in the thermomechanical properties of the different phases. Specifically, although their constitutive responses were determined through the bulk responses of material manufactured in a similar fashion, processing of the composite results in a different manufacturing path. Thus, some variation in the actual material properties is likely resulting in slightly different constitutive responses. Furthermore, localization effects may lead to activation of some mechanisms such as plasticity in either the active NiTi or interface constituents which are not currently accounted for in the model. Even considering these possible sources of uncertainty, the qualitative agreement in terms of important characteristics of the

thermal mechanical cycle and agreement in the predicted effective elastic modulus indicate the developed model provides an appropriate conservative estimate of the composite behavior and is useful for further investigation of the unique inelastic response.

In the previous discussions, the influences of the various mechanisms on the effective composite actuation response have been discussed and explored. Notable amongst these behaviors is the reversible martensitic transformation of the NiTi phase and the irreversible deformations of the Ti_2AlC phase. With these different materials and behaviors another unique possibility remains. Specifically, the possibility of using the inelastic responses of the different phases to develop an effective behavior not found in either constituents needs to be assessed. In a similar material system, Kothalkar et al. [120] have shown that a NiTi-Ti_3SiC_2 composite subjected to thermomechanical actuation cycles develops residual stresses in the composites. As a result of these residual stresses, further cooling-heating cooling cycles after removing bias loads produce a hysteresis loop characteristic of shape memory materials under compression. The capability of the current material system to produce such residual stresses is qualitatively explored here both experimentally and computationally. Experimentally, at the end of all of the thermomechanical cycles in Fig. 33, the composite is unloaded to a minimum load (10 MPa) and subjected to another cooling-heating cycle. Similarly, a numerical simulation of a composite subjected to a 450 MPa actuation path, unloaded to 10 MPa, and thermally cycled was also performed. The unloaded strain-temperature results are presented for both cases in Fig. 35. As was discussed previously, an important difference between the two cases is that the experimental case incorporates the effect of all the actuation cycles while the numerical simulation only includes the highest load cycle.

From the results in Fig. 35, it is observed that both the numerical and exper-

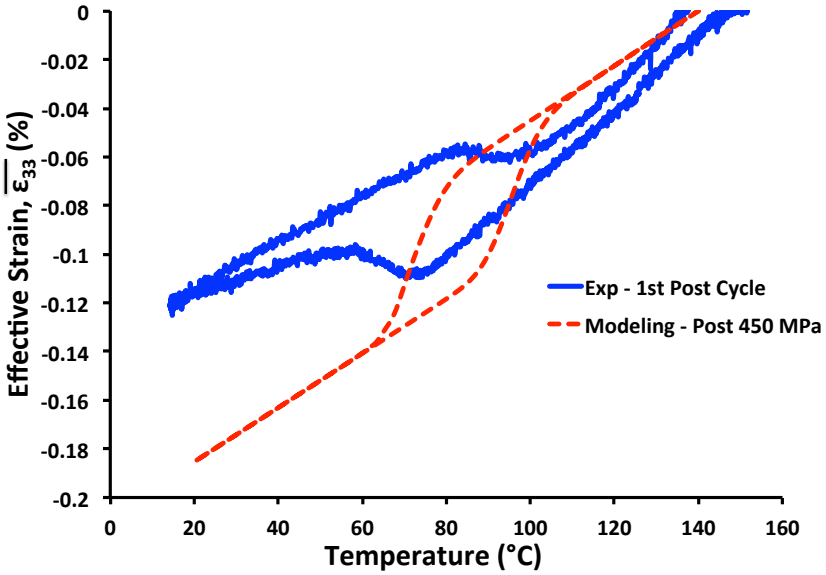

Figure 35: Effective strain-temperature response of the NiTi-Ti_2AlC composite thermally cycled under a 10 MPa compressive bias load experimentally measured after repeated actuation cycles and numerically predicted after a 450 MPa cycle.

imental results exhibit hysteretic behaviors and develop reversible transformation strains. Due to the presence of these transformation strains it may be reasoned that both composites have non-zero residual stress states. Importantly, such results also indicate a two-way shape memory (TWSME) behavior has been trained into the composite by using a combination of the one way shape memory effect (OWSME) of the NiTi phase and irrecoverable strain generation of the Ti_2AlC phase. In comparing the two results, however, it is noted that there is a derivation from the predicted composite response in the experimental response. Specifically, instead of contracting through transformation the experimental results indicate the composite is trying to expand. Even with this difference, as the strains observed are relatively small the difference between the two results remains small - $<\approx 0.08\%$.

Although small, this difference does indicate an important composite response.

Specifically, in the modeling simulations, the effective response of the composite attempts to contract through transformation indicating the SMA phase has a compressive residual stress. In the experimental results, however, the effective composite response tries to expand through transformation which is typical when an SMA is subjected to a tensile load. This experimental result is quite interesting as the specimen is only subjected to compressive thermomechanical loading cycles which result in a tensile no-load response. Furthermore, experiments on a similar material system (NiTi-Ti_3SiC_2) [120] subjected to a similar loading path and history has an effective, no-load response which contracts similar to the current modeling results. Thus, in order to get this small change from a residual compressive to tensile stress state, another mechanism must be active in the composite and have a large individual effect. As indicated in previous discussions in this section, irrecoverable strains from mechanisms such as localized damage, irrecoverable cyclic effects, and plasticity in the interface or NiTi phase may be generated and playing a large role in the effective response. Specifically, the irrecoverable strains associated with these sources are interacting with those of the Ti_2AlC producing the unexpected residual stress state. To fully explore those result, further study is required to identify the source and magnitude of the different irrecoverable strains.

3.2.2.2 Residual Stress States

Both the numerical and experimental results of the effective actuation response of the composite qualitatively indicate the development of permanent deformations and associated residual stress states. To quantitatively explore the impact of these permanent deformations on the residual composite stress state, further analysis of the numerical results is performed. Specifically, the Ti_2AlC and NiTi phase average

stress, $\bar{\sigma}_{33}$, and irrecoverable strain, $\bar{\varepsilon}_{33}^{irr}$, in the direction of applied loading through the course of an actuation cycle with an applied compressive load of 350 MPa are considered and presented in Figs. 36a and 36b, respectively. These simulations assume that the composite is initially stress-free to highlight the effect of the actuation cycle even though some residual stresses may exist due to previous cyclic or manufacturing causes. The NiTi phase average martensitic volume fraction, $\bar{\xi}$, is also presented to indicate the occurrence of forward and reverse transformation. In Fig. 36a, it is observed that initially the phase average stress in the direction of applied loading for both the Ti_2AlC and NiTi phases increases in magnitude over the course of mechanical loading (step $0 \rightarrow 1$). Due to the differences in the elastic moduli, the Ti_2AlC phase carries substantially more load at 1 than the NiTi. Through cooling ($1 \rightarrow 2$), differences in the thermal expansion coefficients lead to a stress magnitude gain in the Ti_2AlC phase and a corresponding drop in the NiTi stress level. When cooling induces forward transformation (indicated in Fig. 36a by the change in $\bar{\xi}$ from 0 to 1), however, a large change in the stress magnitudes in the direction of applied loading is noted. Specifically, higher and lower magnitude stresses are noted in the Ti_2AlC and NiTi phases, respectively, following the transformation. This difference is caused by the stress redistribution from the SMA phase to the stiffer ceramic phase associated with martensitic transformation [138]. Heating of the composite ($2 \rightarrow 3$) leads to relatively small reductions in stress magnitudes in the direction of applied loading of the Ti_2AlC phase and corresponding gains in the NiTi phase. Reverse transformation, as indicated by the return of the average martensitic volume fraction, $\bar{\xi}$ to zero, leads to much larger changes in stress magnitude - larger than even those observed during forward transformation. Specifically, the Ti_2AlC phase average stress magnitude decreases while a large increase is noted in the NiTi phase. Both of these changes are larger than during forward transformation indicating the impact of the

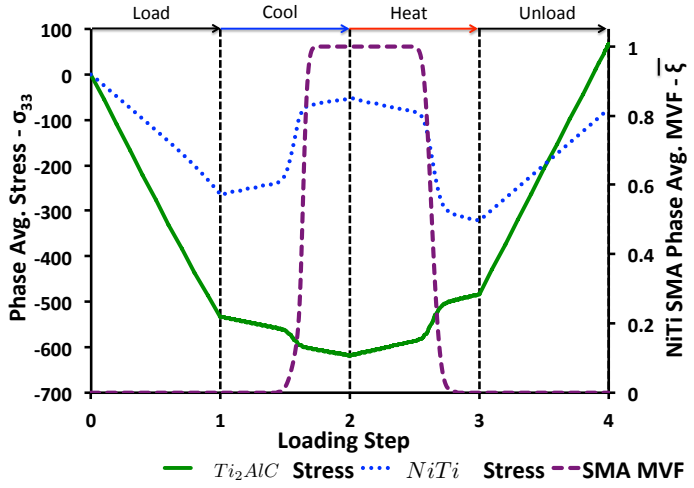

(a) Ti_2AlC phase average stress in the direction of applied loading, $\bar{\sigma}_{33}$

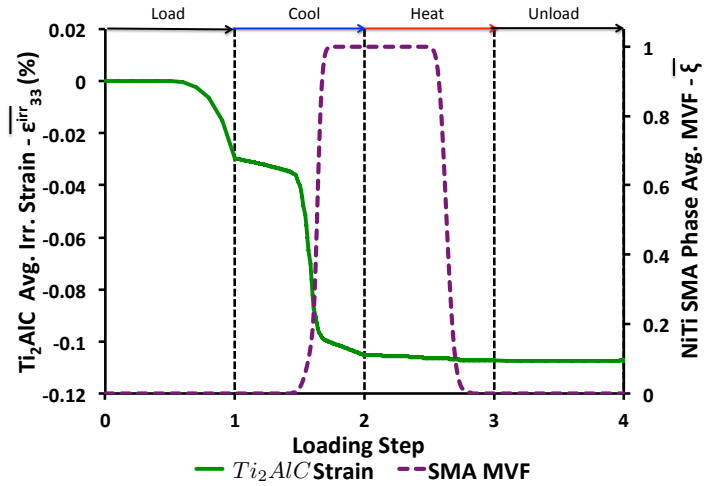

(b) Ti_2AlC phase average irrecoverable strain in the direction of applied loading, $\bar{\varepsilon}^{irr}_{33}$

Figure 36: Ti_2AlC phase average stress, $\bar{\sigma}_{33}$, and irrecoverable strain, $\bar{\varepsilon}^{irr}_{33}$, in the direction of applied loading and phase average NiTi martensitic volume fraction, $\bar{\xi}$, through the course of an actuation cycle with a compressive 350 MPa applied load

transformation cycle. At the end of the heating cycle (loading step 3), however, the two phase average stresses are different than at the start of the heating cycle (1). Thus, when the mechanical load is removed (step 3 $\rightarrow$ 4) a non-zero final stress-state

is produced. Specifically, a final tensile phase averaged stress in the Ti_2AlC of ≈50 MPa is developed through the course of this actuation cycle with a corresponding compressive NiTi stress.

To consider the cause of the final residual stresses noted in Fig. 36a, the irrecoverable strain in the direction of applied loading of the Ti_2AlC phase through the course of the loading cycle is presented in Fig. 36b. During the mechanical loading step, no strains are initially generated. As the load reaches higher values, some irrecoverable strain associated with local stress concentrations and microstructural effects is observed. Subsequent stress magnitude increases associated with cooling also lead to creation of small quantities of irrecoverable strain. During transformation, however, the corresponding inelastic strains of the active SMA phase have to accommodated. As was observed in Fig. 36a, one effect of this accommodation is the associated stress redistribution leading to increased stress on the Ti_2AlC phase. Substantial quantities, more than seen prior to transformation, of irrecoverable strains are then generated in the Ti_2AlC due to these stresses. Subsequent cooling similarly creates small amounts of irrecoverable strains. During heating, which reduces the Ti_2AlC stress magnitude, no change in irrecoverable strain magnitude is noted - even during reverse transformation. This fact leads to the difference in the stress magnitude recovery observed during reverse transformation. Specifically, the inelastic strains associated with martensitic transformation recover while the associated irrecoverable strains generated in the Ti_2AlC phase are not. Thus, elastic strains are generated to compensate leading the altered stress change during recovery and, ultimately, a residual stress state. In this case, an applied compressive loading results in a final tensile residual stress in the Ti_2AlC phase and a compressive residual in the NiTi.

For the NiTi-Ti_2AlC composite investigated here, it has been proposed that a compressive residual stress on the ceramic phase may take advantage of superior

mechanical properties (specifically toughness). With an applied compressive load on the composite, however, a tensile residual stress was produced on the Ti_2AlC phase. Thus, to explore the possibility of a compressive residual stress, the response of the composite under a tensile applied load is explored. As is common in ceramics, Ti_2AlC, like other MAX phases, exhibits a strong tension-compression asymmetry in terms of mechanical response. Even with this difference, there are limited reports in the literature of the tensile response of MAX phases (and Ti_2AlC in particular) [196, 197, 221]. The only report on the tensile behavior of Ti_2AlC characterized the materials creep response [221]. Past investigations by Radovic and colleagues have, however, explored the mechanical response of Ti_3SiC_2 under various tensile conditions [196,197]. Importantly, both closed and open hysteresis loops characteristic of incipient and permanent kink bands, respectively, were observed during cyclic monotonic tensile testing at room temperature [196]. A decrease in the strength when loaded under tension rather than compression was noted, however [196]. For this work, due to the lack of the data on the tensile Ti_2AlC response, the tension-compression asymmetry shall not be considered. Although this assumption impacts the quantitative assessment of these results, qualitative analysis is still possible as the relevant mechanisms are still observed under tensile loadings.

The phase average stress of the Ti_2AlC and NiTi constituents in the direction of applied loading are presented in Fig. 37a while the Ti_2AlC phase average irrecoverable strain in the direction of applied loading is given in Fig. 37b for a actuation loading path with a tensile applied load of 350 MPa. In both figures, the NiTi phase average martensitic volume fraction is also presented to indicate the onset of transformation. The results of Fig. 37 have many similarities to the compressive applied loading case (Fig. 36). First, mechanical loading ($0 \rightarrow 1$) results in the average stress of both phases increasing such that they are in tension prior to the thermal load-

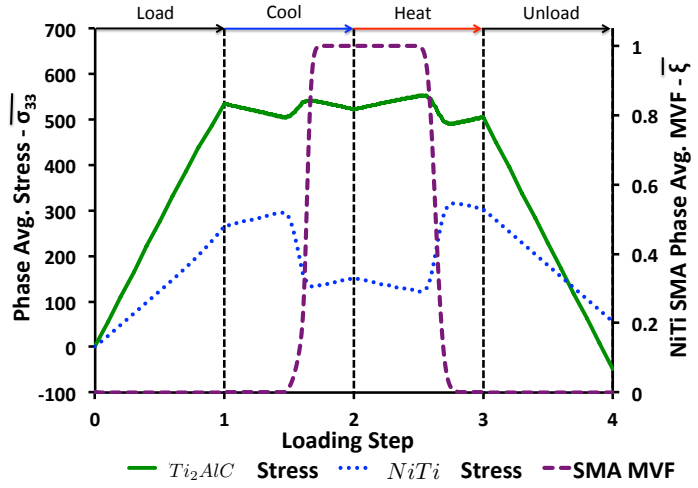

(a) Ti_2AlC phase average stress in the direction of applied loading, $\bar{\sigma}_{33}$

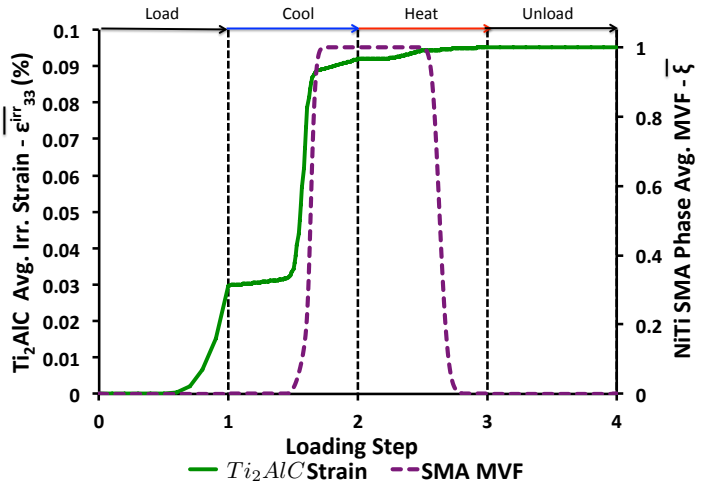

(b) Ti_2AlC phase average irrecoverable strain in the direction of applied loading, $\bar{\varepsilon}^{irr}_{33}$

Figure 37: Ti_2AlC phase average stress, $\bar{\sigma}_{33}$, and irrecoverable strain, $\bar{\varepsilon}^{irr}_{33}$, in the direction of applied loading and phase average NiTi martensitic volume fraction, $\bar{\xi}$, through the course of an actuation cycle with a tensile 350 MPa applied load

ing cycle as indicated in Fig. 37a. During cooling, the thermal expansion mismatch has the opposite effect seen during the compression cycle and small decreases in the Ti_2AlC phase average stress magnitude are observed. Upon transformation, how-

ever, the same gain and reduction in Ti_2AlC and NiTi, respectively, phase average stress magnitudes evident during compression are noted. Further cooling and subsequent heating produces small changes associated with thermal expansion mismatch until reverse transformation. Similar to the compression cycle, the Ti_2AlC and NiTi phases undergo a substantial phase average stress magnitude decrease and increase, respectively, upon reverse transformation. Again, the size of these changes are larger than noted during forward transformation leading to a non-zero final stress state after completing heating and mechanical unloading. Importantly, unlike the compression case, with the tensile applied bias load the Ti_2AlC has a negative final phase average stress with a corresponding positive state in the NiTi phase.

The phase average Ti_2AlC irrecoverable strain generation in the direction of applied loading (Fig. 37b) again points to martensitic transformation as the cause of this effect. Specifically, as noted during the compressive cycle, mechanical loading results in some irrecoverable strain generation. Cooling, however, decreases the Ti_2AlC stress magnitude with a tensile applied load leading to no real changes in the Ti_2AlC phase average irrecoverable strain. Forward transformation, and the associated stress magnitude increase, does induce the creation of additional irrecoverable strains in the direction of applied loading. Subsequent cooling and heating and the associated thermal expansion mismatch produces small gains in the irrecoverable strain magnitude. Again, upon reverse transformation, the irrecoverable strains associated with permanent deformation in the Ti_2AlC are not recovered leading to the observed residual stress state. Importantly, in both cases the final phase average irrecoverable strain is $\approx 0.1\%$ - meaning the desired residual stress states may be developed with relatively modest permanent deformations. Thus, by selecting an appropriate bias load, a desired residual stress state (either tensile or compressive) may be induced.

The results above describe the response of the composite under a specific applied

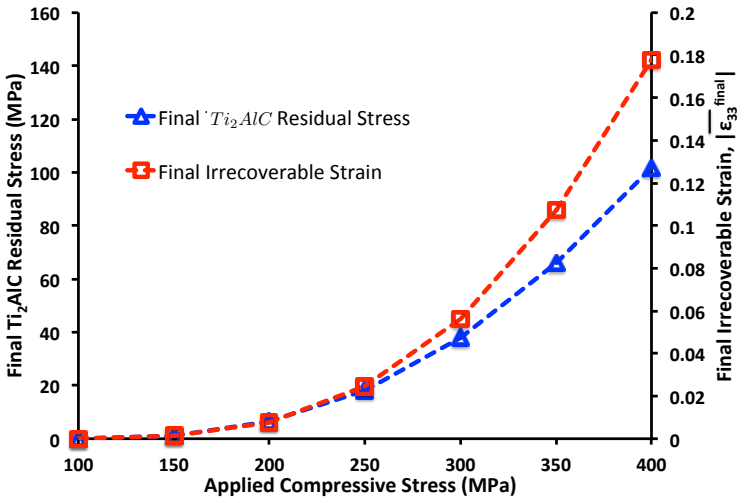

Figure 38: Final residual stress in the Ti_2AlC phase and absolute value of the composite irrecoverable strain, $|\bar{\varepsilon}_{33}^{final}|$ at different applied compressive stress levels

loading level. To consider the impact of different applied stresses, the final residual stress in the Ti_2AlC and the final irrecoverable strain in the direction of applied loading, $\bar{\varepsilon}_{33}^{final}$, are presented for different applied compressive loadings. It is observed from Fig. 38 that initially, at low applied loads, very little irrecoverable strain is generated. Correspondingly, little residual stress is developed in the composite. As increasing mechanical loads are applied, greater quantities of irrecoverable strains are generated which in turn lead to higher residual stress magnitudes. Interestingly, a nearly linear relationship between the final irrecoverable strain and residual stress magnitude is observed allowing for the possibility of selecting a final residual stress magnitude through appropriate biasing load determination.

The previous results consider only the average response of the different phases. However, local effects associated with the microstructure also need to be considered and analyzed to aid in material design and determine how well the average response

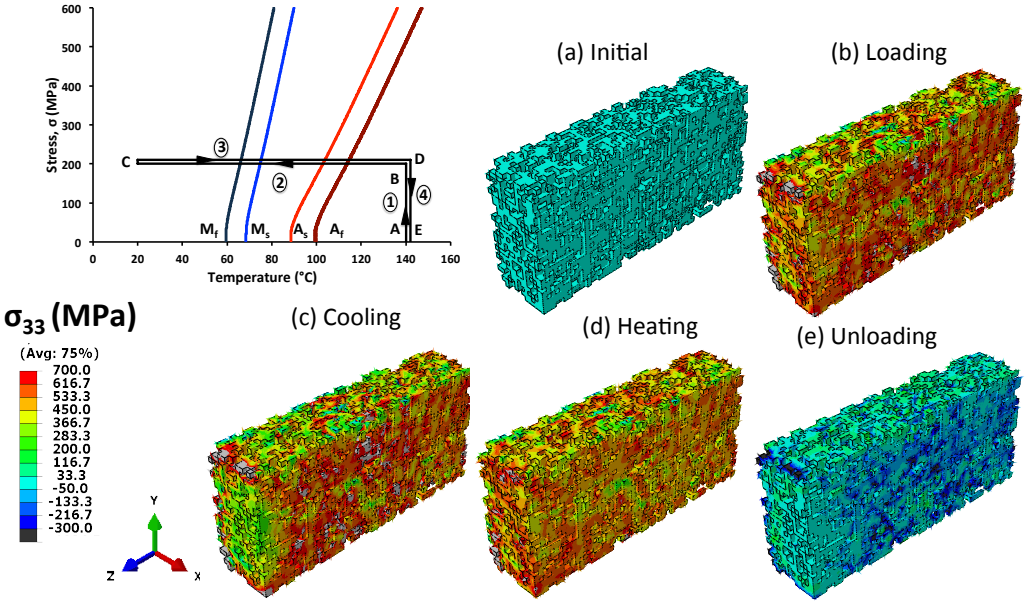

Figure 39: Ti_2AlC phase stress field in the direction of applied loading, σ_{33}, along the composite centerline with a tensile bias load of 350 MPa: (a) initial configuration (b) after mechanical loading (end of step 1) (c) following cooling (step 2) (d) at end of heating cycle (step 3) and (e) mechanical unloading (step 4)

represents the local constituent response. To this end, the stress fields in the direction of applied stress, σ_{33}, of the Ti_2AlC phase are presented in Fig. 39 for different loading points of the 350 MPa tension loading case. As the state of the ceramic phase is of primary interest here, visualization of other elements is suppressed. Furthermore, the specimen is cut along the center $x_2 - x_3$ plane to remove edge effects and emphasize what is happening in the bulk of the composite. Initially, at point A in Fig. 39, the composite is in a stress-free configuration. At the end of mechanical loading, point B, a heterogeneous, tensile stress state is observed throughout the Ti_2AlC

phase. After cooling and undergoing forward martensitic transformation, point C, interesting changes are observed in the Ti_2AlC stress state. Namely, the stress in the direction of applied loading has decreased along some of the edges while increases in the local stress may be noted on the interior of the composite. Upon heating back to the original temperature and the SMA phase transforming back to austenite, a heterogeneous tensile state is present in Fig. 39d. Importantly, in comparing the states at points B and D - which have the same temperature and applied stress conditions - the Ti_2AlC stress in the direction of loading is generally lower after undergoing the heating cooling cycle. Thus, the loading path history is observed to influence the composite response and through the transformation cycle the stress magnitude has been reduced in the composite. When the composite is unloaded, Fig. 39e, this reduction leads to the compressive residual stress in the Ti_2AlC. In general, after unloading the Ti_2AlC appears to be mostly in compression with pockets of tensile residual stress. To further consider the local stress state, the distribution of the final residual stress in the direction of applied loading of the different field points is presented in Fig. 40. Through this distribution, the results of Fig. 40 show that most of the ceramic phase is under compression (58.2%) with a mean value of -48.3 MPa and a standard deviation of 106.2 MPa. These measures may be further discussed by again looking at the spatial distribution of the stresses. Specifically, the results of Fig. 39e are rescaled and presented in Fig. 41 such that all areas of tension are shaded black. From Fig. 41 it is noted that the tensile areas are primarily located in the edge and thus associated with edge effects. In considering the results of both Figs. 40 and 41, in addition to the final average residual stress, locally the composite is primarily in a compressive stress state.

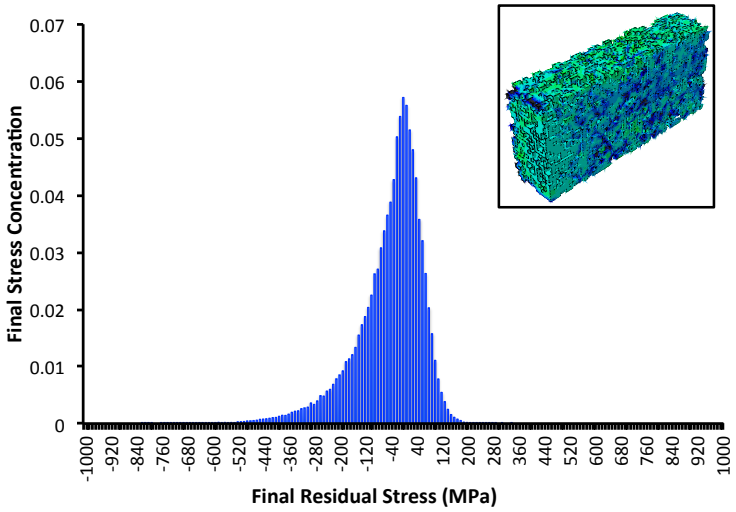

Figure 40: Distribution of final residual stress in the direction of applied loadings measured at all the field points of the Ti_2AlC phase. Final stress distribution of the Ti_2AlC phase (Fig. 39e) is inserted for reference.

3.2.2.3 Parametric Studies

Parametric studies are performed on different composite characteristics to determine their effect on the effective response. Specifically, four parameters are considered: porosity, fraction of transformable NiTi, elastic modulus of the non-transforming NiTi and the zero-stress reference temperature, T_0. This group of four characteristics is selected to assess the validity of the assumed values and study their influence on the composite response.

Porosity – Porosity in these composites are formed as a result of the incomplete sintering of the Ti_2AlC phase in SPS. The role of these imperfections in the composite response needs to be determined. Importantly, in their recent study, Hu *et al.* [108] characterized the mechanical response and compressive strength of Ti_2AlC and noted a strong dependence on porosity while Poon *et al.* [186] noted a reduction

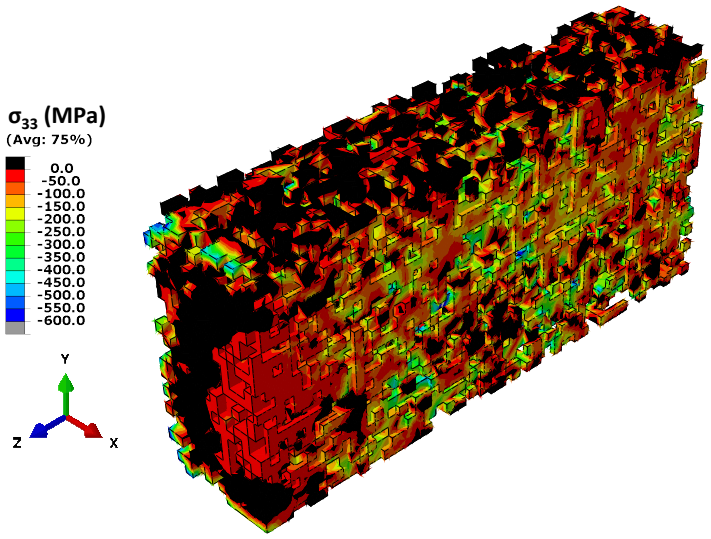

Figure 41: Residual stresses in the direction of applied loading, σ_{33}, in the ceramic phase with tensile areas colored black

of ≈20% in modulus and a 75% decrease in yield strength in a 10% porous specimen. Thus, the effects of the porosity on the composite response are considered here. This is necessary as the porosity content is determined assuming no reaction between the individual phases during sintering leading to uncertainty in the calculation. Therefore, a range of 5-12.5% porosity is considered to represent a likely range of porosity.

To consider the impact of the porosity, simulations were performed using different porosity levels as input while maintaining equal volume fractions of total NiTi and Ti_2AlC. The total quantity of active NiTi was also kept constant. The results of simulations with different porosities under a compressive applied load of 200 MPa are shown in Fig. 42 with the 10% case being the previously studied result. In Fig. 42, it is observed that porosity has a small impact on the effective actuation response. Specifically, minor increases in the hysteresis size and associated transformation strain are noted with increases in porosity. Similarly at higher porosities,

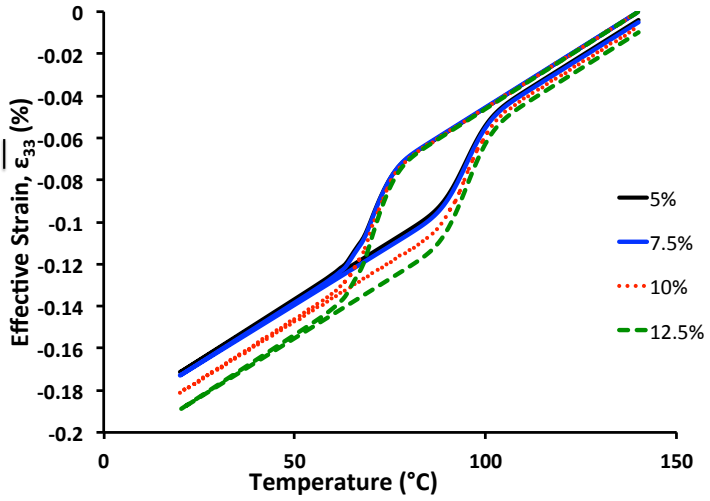

Figure 42: Effective actuation response of the composites with different porosity levels

the hysteresis loops have slight openings indicating the generation of irrecoverable strains. Both of the effects may be explained by considering the increased load each phase will carry due to the increased porosity content. Notably, although differences are present, their magnitude is not large. This is especially evident in the two lower porosity cases in which the responses are quite nearly the same. To consider the influence of the porosity further, the final residual stress in the direction of applied loading and the composite irrecoverable strain at the different porosity levels are presented in Fig. 43. For comparison purposes, the results are normalized by the results of the case studied in Section 3.2.2.1 (labeled the 10% case here). In this case, changing the porosity from 5% to 12.5% leads to changes of 67% and 87% of the normalized final residual stress and irrecoverable strain, respectively. Furthermore, the rate of increase in the normalized final irrecoverable strain is higher than the residual stress.

Active NiTi Volume Fraction – As has been discussed previously, the stress

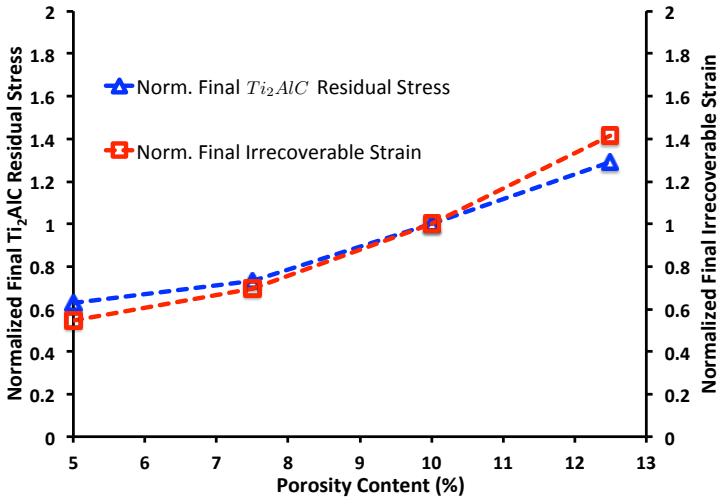

Figure 43: Final applied residual stress in the Ti_2AlC phase and composite irrecoverable strain with different porosities normalized by the results for the 200 MPa 10% case

distribution associated with martensitic transformation is responsible for many of the unique characteristics of the effective composite response. Interestingly, however, much of the NiTi considered in the composite does not transform due to other reaction phases or compositional changes near the interface [120]. Due to the different possible causes, some variation in the interphase content versus that measured is likely. Furthermore, improvements in the material manufacturing are likely to be able to substantially reduce this additional phase by controlling the interface thickness through adjustments in the processing parameters. Thus, understanding the effect of the interphase content on the effective response is important for future development. To identify the effect of this manufacturing consequence on the composite, the effective actuation response at 200 MPa was determined with different fractions of the active NiTi. For this study, the total NiTi (active and interphase) volume

fraction was held constant while the concentration of the active material was varied. In the following, the percentages used will refer to the fraction of total NiTi content that is active. The previous results correspond to 45% of the total NiTi being active with 55% being the interphase. The effective actuation response for these different cases is presented in Fig. 44.

It is evident from the results presented in Fig. 44 that the fraction of the ac-

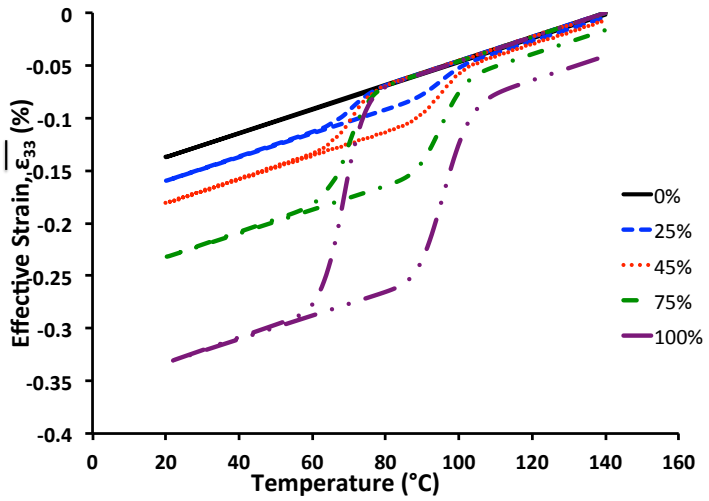

Figure 44: Effective actuation response of the composites with different fractions of the active NiTi. The percentages listed for the different cases correspond to the fraction of total NiTi content which is active.

tive NiTi has a substantial impact on the effective response of the composite. First, as would be expected, no hysteresis loop is observed in the case of no active NiTi. As the concentration of active NiTi increases, so does the size of the corresponding hysteresis loops. In fact, a nearly order of magnitude increase in the transformation strain is observed in going from the 25% to 100% case. Furthermore, such an increase in the transformation strain also leads to increases in the stress redistri-

bution between the phases. This may be noted in Fig. 44 through the increase in final irrecoverable strain with active NiTi concentration. This relationship is further studied in Fig. 45 which presents the final residual stress of the Ti_2AlC and effective irrecoverable strain in the direction of applied loading. These results are normalized by the baseline (45% active NiTi) case for comparison reasons.

In determining the influence of active NiTi content on the final composite con-

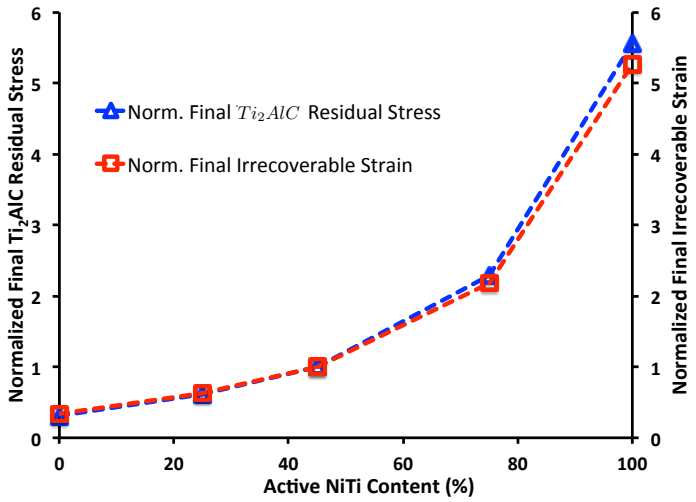

Figure 45: Final Ti_2AlC phase average residual stress in the direction of applied loading and final effective irrecoverable strain normalized by the baseline case with different fractions of active NiTi.

figuration, it is first noted that in going from 0 to 100% active NiTi results in a more than five-fold increase in the normalized final stresses and irrecoverable strains. Initially, at 0% active NiTi, very low permanent deformations are present due to microstructural effects. As the active NiTi concentration grow, increased amounts of composite material are undergoing martensitic transformation and the corresponding

stress redistribution leads to larger stress magnitudes on the Ti_2AlC phase. These increased loadings generate more permanent deformations and thus more irrecoverable strains and greater residual stresses. The rate at which both the final residual stress and irrecoverable strain grows also increases with concentration. Thus, it may be observed, that the interphase is quite detrimental to using martensitic transformation to create residual stress states. Specifically, by eliminating this phase, lower applied stresses may be used to generate a specific magnitude residual stress.

Elastic Modulus of the Interphase – The interphase represents approximately 20% of the composite which is likely due to diffusional and manufacturing effects associated with the reactivity of the constituent phases. The properties of this phase, however, are unknown and are likely actually spatially gradient due to the compositional variations in the phase. Furthermore, given the disparate elastic properties of the base constituents, a wide range of possible values are possible. Therefore, the effect of this phase and its effective elastic properties on the composite response needs to be assessed. To this end, the actuation response of the composite loaded at 200 MPa with different elastic moduli of the interphase material, ranging from a stiffer material more representative of the ceramic phase to compliant responses possible for a martensitic material, is shown in Fig. 46. In this analysis, only the elastic modulus of the interphase is changed in each simulations - the response of the active NiTi is unchanged. As was discussed in Section 3.2.1, the interphase is distributed throughout the composite in elements near the Ti_2AlC content to approximate the interface. Similar to the effects seen with the active NiTi content, decreases in the interphase modulus leads to higher transformation and irrecoverable strains are observed. This difference is associated with the greater loads on the active NiTi and Ti_2AlC due to the reduced load carrying capabilities of the interphase. The change in transformation strain is not as pronounced as in the case of the active NiTi fraction.

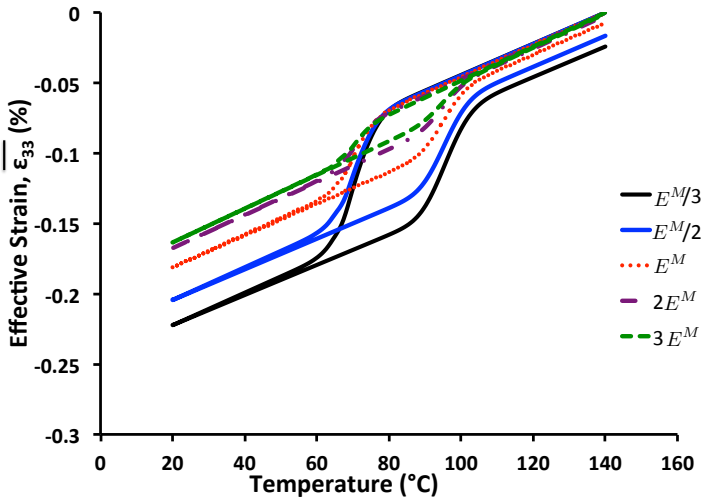

Figure 46: Effective actuation response of the composites with different elastic moduli (E) of the interphase.

Specifically, a decrease in the modulus by a factor of 9 produces only a 36% increase in the transformation strain and 0.02% larger irrecoverable strain.

Loading Path Reference Temperature, T_0 – As with all metal-ceramic composites, the mismatch between the coefficients of thermal expansion lead to residual stresses. The temperature at which these stresses are zero, however, is not certain and the influences of these stresses need to be accounted for. At the higher sintering temperatures, relaxation through creep is also likely leading to a different stress-free reference temperature. Thus, to further investigate this effect, finite element simulations were performed with different strain-free reference temperatures, T_0. For these analysis, an initial small biasing load (5 MPa) is applied at the reference temperature and the composite is cooled to T =140°C. At this temperature, the composites are loaded to the full biasing load, in these cases 200 MPa, and a heating cooling cycle is performed. The results of the actuation cycle are presented in Fig. 47 where the strains of each

case are zeroed at T =140°C to facilitate comparisons. For each of the different

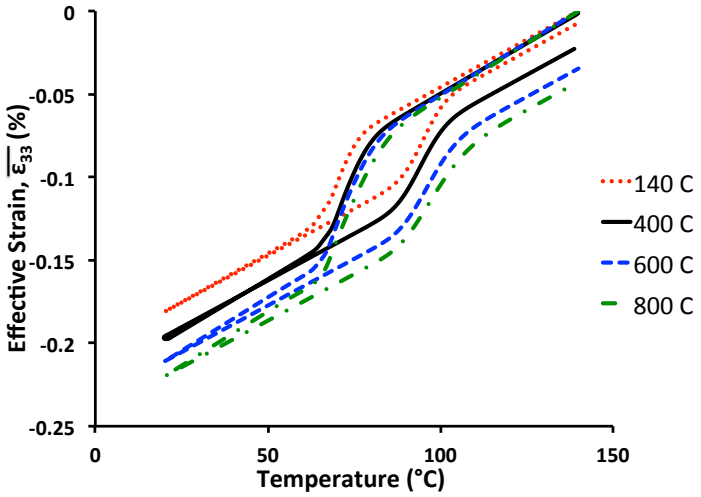

Figure 47: Effective actuation response with composites considering different stress-free reference temperatures, T_0.

reference temperatures, a compressive hysteresis is observed in all cases. Both the transformation and irrecoverable strains generated increase with reference temperature due to the presence of the additional compressive stresses associated with the coefficient of thermal expansion mismatch. For instance, the transformation strain increases by 21% in raising the reference temperature from 140°C to 800°C. In going from the 600°C to the 800°C, a smaller growth in strains is noted than in going from 400°C to 600°C. Thus, proper determination of the reference temperature is necessary to precisely determine the irrecoverable strain.

3.3 Summary

For this effort, the effective actuation response of NiTi-Ti_2AlC composites were explored via finite element methods. These simulations (primarily) differed from those of the previous section by (*i*) use of a nonlinear elastic-plastic constitutive model for the MAX phase and (*ii*) consideration of the whole thermomechanical loading path. In this way, the interaction of the separate inelastic mechanisms and their impact on the effective response could be considered. Three different cases were explored: (*i*) a representative microstructure (*ii*) simplified microstructural units and (*iii*) an actual NiTi-NiTi $-$ Ti_2AlC composite. The first and the third utilized image-based techniques to directly incorporate microstructure features while the second considered three simplified microstructural units to explore their impact on the response. From these different cases, it was observed that like the previous study a reduction in transformation strain and similar shift in transformation temperatures was observed. Importantly, it was also shown that the stress redistribution identified in the previous case was sufficient to induce permanent, irrecoverable deformations in the MAX phase material. As such, when the SMA recovers elastic deformations are induced in the MAX phase. Upon unloading this combination leads to a residual stress state in the composite which can be controlled via the thermomechanical loading condition. An actual composite was then investigated and the numerical results were compared to experimental results. Importantly, additional phases associated with porosity and inactive NiTi (resulting from species diffusion during processing) were accounted for. The resulting analysis showed good qualitative agreement with the experimental in predicting decreasing transformation strain, an initially closed hysteresis loop that transitions to open as the stress increases, and the development of an effective two-way shape memory behavior (associated with

the aforementioned residual stress state). Some quantitative differences between the experimental and numerical results were noted. These variations likely arise from differences between material properties used (calibrated from bulk not composite specimens), microstructural uncertainty (*e.g.* differences in porosity, active NiTi content), or assumed constitutive behavior. A series of parametric studies were performed considering the first two categories. Through such a study, it was shown that the active NiTi content had the strongest impact and substantially influenced the effective response. The effect of the assumed constitutive response of the MAX phase model will be explored in subsequent sections.

To further investigate these materials additional experiments would also prove quite informative. First, as mentioned in the previous paragraph, additional full field characterization efforts should be performed such that the response of the individual constituents can be extracted. Such efforts can extract the actual constitutive response of the base materials and account for processing effects and influences. This is especially true for the non-transforming phase as the constitutive response of these phases is unknown. Furthermore, investigations like this are essential to determining any cyclic effects (like TRIP in the SMA phase) that may develop and needs to be accounted for. Macroscopically, measurements (whether through spectroscopy or mechanical unloading) of the effective modulus should be made. In this way the evolution of any damage (and permanent kink bands) in the MAX phases could be determined and investigated.

4. MAX PHASE CONSTITUTIVE MODELING

In the previous chapter, the inelastic response of the MAX phase constituent was captured via an elastic-plastic approximation. Experimentally, however, both recoverable and irrecoverable deformations have been observed in MAX phase materials due to multiple active deformation mechanisms [22]. As discussed in Section 1.1, no current model exists capable of describing the unique responses of the MAX phase - yet alone in a manner well suited and efficient for the analysis of MAX phase structures. Therefore, in this section, efforts to develop a model which consider both the recoverable, repeatable, and hysteretic response of MAX phases associated with IKB formation and irrecoverable deformations arising from the development of kink bands (KB) and plasticity are discussed and presented. Importantly, the development of kink bands also leads to formation of cracks, delaminations, and damage that must be accounted for in any constitutive formulation adding an additional degree of complexity. Before proceeding further, it is important to consider if models of other materials with comparable responses may be found in the literature for use as a basis. With respect to the recoverable mechanisms, modeling of the reversible hysteretic response associated with martensitic transformation in SMAs has long been studied [55, 124, 127, 178] and a number of models coupling the martensitic transformation with rate-independent plasticity [100] and rate-dependent viscoplasticity [54, 97] have been developed. A recent preliminary effort has also been taken to consider fatigue damage [98], although in this case the irrecoverable deformations evolve with martensitic transformation (not as a separate mechanism) and are formulated for fatigue degradation of the material rather than through critical loading levels. In coming from the other perspective, substantial effort has been devoted

in the past half-century to predictive modeling of damage through the continuum damage mechanics framework [135]. In this regard a number of investigations have focused on the modeling of damage evolution and plasticity (e.g. [3, 103, 135, 228] to name a few) and some recent works have looked at "recovery" in the sense of an external self-healing agent [15, 227] but there is, to the author's best knowledge, no model currently considering the coupling and combination of a reversible/recoverable mechanism and that inducing permanent deformations and damage. Thus, a new model is developed here.

To facilitate and aid in the model development, the responses of interest for the MAX phases are shown below in Fig. 48[1] for a Ti_2AlC specimen. Specifically, in Fig. 48a, the recoverable, hysteretic response of MAX phases that has motivated much of the interest is shown. Clearly, the response of this material exhibits a hysteretic response and although the strains may be small with respect to SMAs, the applied stress levels are quite high leading to large energy dissipation. With respect to this behavior, it is noted that upon unloading the initial slope (and corresponding modulus) does not exhibit a substantial drop versus that observed during loading. This is indicative of an initially elastic unloading. Additionally, with a damage based mechanism a difference between the loading and unloading modulus would be expected. Therefore, it can be assumed that this recoverable mechanism is not associated with damage formation. Furthermore, the elastic unloading regime is much smaller than that predicted by Jones and coworkers [113] in their Bauschinger-like EPSC model indicating a difference from kinematic-hardening plasticity. Considering these facts, this response is attributed to the development and subsequent annihilation of IKB type-dislocation structures as discussed in Section 1.1. The strain to

[1]In what follows, experimental results and material specimens are provided courtesy of Prof. M. Radovic, R. Benitez, and group

failure response of a Ti_2AlC specimen is provided in Fig. 48b. In such a response, it can be clearly seen that a both a surprising amount of nonlinear strain and material softening (both atypical for ceramics) are evident in the response. It must be noted that although Figs. 48a and b are both of Ti_2AlC they are produced from different base powders. This is primarily important for the latter response which has shown a strong dependence on grain size and impurity content and the result shown in Fig. 48b seems to lie on the ductile side of that spectrum. Regardless, Fig. 48b does clearly show that permanent irrecoverable damage-based mechanisms are active in the material and need to be accounted for in the subsequent model.

With this in mind, a three-dimensional phenomenological model of MAX phase

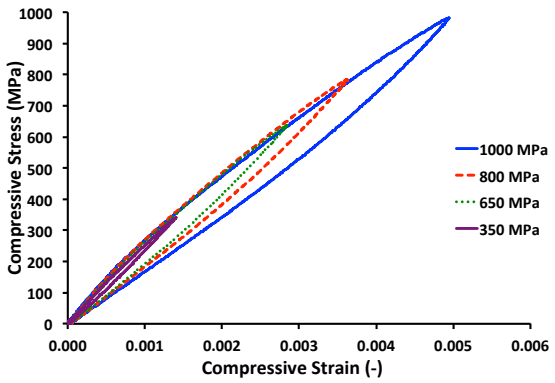

(a) Reversible, hysteretic compressive response of Ti_2AlC attributed to IKB formation. Results shown are for second cycles and cycles are performed sequentially with increasing monotonic load.

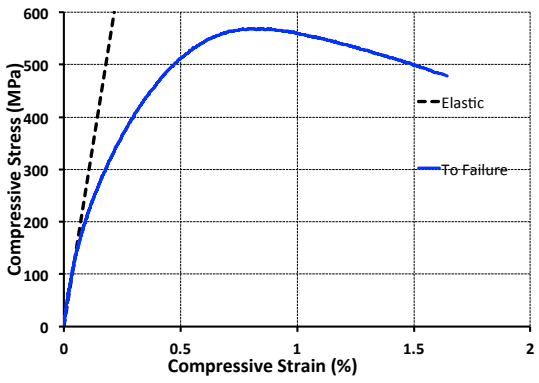

(b) Strain to failure experiment highlighting the development and damage and permanent deformations

Figure 48: Bulk response of Ti_2AlC materials. Note: results shown correspond to Ti_2AlC specimens made from two different powders.

materials will be developed in this section. The underlying theory and constitutive formulation is presented in Section 4.1 while details of the numerical implementation

are discussed in Section 4.2. Results of example problems are then given in Section 4.3 while a summary of these efforts is presented in Section 4.4.

4.1 Theoretical Development

Before delving into the details of the formulation, the framework, objectives, and some assumptions are first introduced. First, the model being developed is intended for use in capturing the meso- or macroscale response of polycrystalline MAX phases. Therefore, a phenomenological approach is adopted and used to describe this response. Such a selection is also motivated by the continuing debate in the literature as to the underlying physical mechanisms giving rise to the behaviors of interest. Additionally, as the applications of interest are low–temperature (for a ceramic), the developed framework is intended for use in temperature ranges below 900°C. In fact, the experiments studied (both for the bulk and composite cases) are below 200°C. Previous experimental studies have shown that the MAX phase response is athermal and rate-independent under quasi-static loadings in this regime [23, 237]. This temperature also lies below those observed for the brittle to ductile transition [196] and such effects are not considered here. Instead, the response and behaviors associated with three inelastic mechanisms are considered. Detailed discussions will be found in the forthcoming sections, but the three mechanisms of interest are:

1. *Incipient Kink Band (IKB) Formation* – The reversible, repeatable hysteretic response presented in Fig. 48a and extensively characterized in the literature [22, 23, 237] has been attributed to the formation of kink-band like dislocation structures that have not yet disassociated.

2. *Kink Band (KB) Formation* – Dissassociation of aforementioned IKB's into permanent structures creating kink bands. Such deformations lead to perma-

nent deformations and delaminations and crack producing macroscopic damage. Macroscopically, this mechanism manifests both as permanent deformations and damage in the sense of loss of load bearing capabilities.

3. *Plastic Slip* – Permanent, plastic deformations may occur in grains not oriented favorably for the formation of IKBs. Experimental results have indicated the possibility of permanent deformations in impurity content in the Ti_2AlC ensemble or potentially glide in non-kinking grains. Collectively, these contributions will be referred to as the plasticity mechanism.

To capture the individual and coupled response of these distinct behaviors, a multi-mechanism model will be developed via a phenomenological, internal state variable (ISV) based continuum thermodynamics [59, 60, 149] approach. In this case, it is assumed that each material point is comprised of a statistically significant and representative set of grains representative of the bulk specimen such that the model captures the effective behavior of such an ensemble. A model for the material response may then be constructed by developing an free energy function including terms associated with the internal variables. Such variables are used to describe microstructural changes and evolutions associated with inelastic deformation and thermodynamic considerations and physical observations will be used to determine appropriate yield and evolution behaviors. For the above described responses, it is assumed that each of the three listed mechanisms may occur individually or simultaneously. For convenience, in the following discussion the superscripts "r", "d", and "p" will be used for variables related to the recoverable (IKB), damaging (KB), and plastic mechanisms.

To begin this process, the total (Gibbs) free energy of the material is decomposed

such that,

$$G\left(\sigma_{ij}, T, \boldsymbol{\Upsilon}\right) = G^{te}\left(\sigma_{ij}, T, \boldsymbol{\Upsilon}\right) + G^{r}\left(\sigma_{ij}, T, \boldsymbol{\Upsilon}\right) + G^{d}\left(\sigma_{ij}, T, \boldsymbol{\Upsilon}\right) + G^{p}\left(\sigma_{ij}, T, \boldsymbol{\Upsilon}\right) \quad (4.1)$$

where G^{te} is the thermoelastic energy and $G^{r},\ G^{d}$, and G^{p} are the inelastic energies associated with the respective mechanisms. The set of internal state variables (scalar and tensorial) that will be introduced in the sequel is denoted as $\boldsymbol{\Upsilon}$. Splitting the free energy in this fashion assumes that the corresponding inelastic contributions of the different processes are additive and enables the treatment of each term individually. With this decomposition, the thermoelastic energy, G^{te}, is,

$$\begin{aligned} G^{te}\left(\sigma_{ij},\ T,\ \boldsymbol{\Upsilon}\right) = \ & -\frac{1}{2\rho}\sigma_{ij}M_{ijkl}\sigma_{kl} - \frac{1}{\rho}\sigma_{ij}\alpha_{ij}\left(T - T_0\right) + \\ & c\left[\left(T - T_0\right) - T\ln\left(\tfrac{T}{T_0}\right)\right] - s_0 T + u_0, \end{aligned} \quad (4.2)$$

where $\rho,\ \sigma_{ij},\ M_{ijkl},\ \alpha_{ij},\ c,\ T,\ T_0,\ s_0$, and u_0 are the mass density, symmetric Cauchy stress tensor, current fourth-order compliance tensor, thermal expansion tensor, specific heat, current absolute temperature, reference temperature, reference entropy, and reference internal energy. The specific energetic contributions of the different mechanisms and the corresponding energies will be discussed individually in detail in Sections 4.1.1–4.1.3. The coupling of the different mechanisms and corresponding combined model is then presented in Section 4.1.4.

4.1.1 Incipient Kink Band Formation

One of the key physical responses of MAX phases that has made these materials so appealing is the repeatable hysteresis loops observed even under relatively high-loads (up to 1 GPa) [23]. Although the inelastic strains remain rather small in

comparison to some active materials (notably shape memory alloys), the recoverable deformations remain large for a bulk ceramic with stiffnesses in the neighborhood of 300 GPa. Importantly, however, these repeatable hysteresis loops dissipate roughly a quarter of the applied energy giving the material excellent damping characteristics and subsequent permanent kinking (see the following section) yield a "damage" tolerant ceramic (with many other interersting possibilities) [20].

As discussed in Section 1.1, the exact mechanism responsible for this behavior is still being debated in the literature [24, 43, 93, 113, 186]. A variety of explanations ranging from crack sliding [186] to an extreme Baushinger-like effect [113] have been proposed and supported with a variety of experimental observations. Nonetheless, in this work, the *incipient kink band* (IKB) concept is invoked and used to motivate the phenomenoligical model. This theory is used as (*i*) the relevant features have been extensively characterized (*e.g.*, [22, 23, 237]), (*ii*) substantial circumstantial observations (like greater absolute dissipation of porous versus bulk specimens [220, 238]) and (*iii*) recent, unpublished electron backscatter (EBSD) results[2] indicating the presence of kink band-like dislocation structures. In the IKB theory put forth by Barsoum and coworkers [23,24], these structures form as a result of a limited number of plastic slip systems in grains poorly aligned with respect to (parallel) the loading axis after a critical applied load. Although recent EBSD results differ from this explanation in that the observed dislocations were in grains with moderate Schmid factor, the observation of such structures gives credence to such an explanation. Specifically, the formation of these bands is necessitated as deformation may only occur via basal slip and twinning is unlikely due to the high c/a ratios of the crystal structure [23]. The resultant IKBs take the form of parallel dislocation walls with opposite signs and the end dislocations remain attached. Upon load reversal, the attractive forces

[2]Private communication with R. Benitez and Prof. Radovic

between the dislocations enable these structures to run-back upon each other and annihilate the dislocations nucleated during loading [24]. As no damage occurs, this process may be repeated multiple times.

To capture the response of the reversible hysteretic , an internal state variable approach is adopted. Such variables are meant to capture and describe the evolution of the microstructure through inelastic deformations. Specifically, four state variables are utilized - two tensorial and two scalar. First, a scalar *kinked volume fraction*, ζ, is introduced. Physically, such a volume fraction is interpreted as the total volume of the material comprised of kink-band dislocation structures. With this definition, it is important to note that ζ incorporates both incipient and permanent kink bands with the restriction that permanent kink bands may only form from incipient structures. Therefore, changes in the total kinked volume fraction are only achieved through the development of annihilation of IKBs. Additionally, as will be discussed in subsequent sections, a volume fraction variable is selected to better enable efforts to couple the different mechanisms. Secondly, an inelastic strain tensor, ε^r_{ij} is introduced as an ISV to capture the inelastic deformations associated with IKB formation. Finally, two variables capturing the hardening effects are introduced - β^r_{ij} and g^r representing the kinematic and isotropic hardening, respectively. Importantly, the backstress associated with the kinematic hardening variable may be interpreted as the internal stresses associated with the attractive/repulsive forces of the dislocation walls of opposite sign. Isotropic hardening effects are then captured by the independent g^r state variable representing effects including various kink bands interacting with each other and texture effects.

Before proceeding further and giving specific functional forms, some specific assumptions regarding the assumed physical process will be introduced and discussed to better illuminate the derived model. To this end, recent compressive stress-strain

experimental results of dense Ti_2AlC will be used[3]. First, numerous experimental results indicate a strong dependence of the functional form on the grain size (and presumably texture although such experimental results are not as strongly established) of the bulk specimens. It is assumed that these effects are captured through calibration of model parameters. Subsequent efforts may more strongly establish a relationship on these parameters although they are neglected for the time being. To highlight these response, Fig. 49 shows the room-temperature response of Ti_2AlC subjected to different maximum stress values. In these results, it is important to note that the presented cycles correspond to the second cycle at the given maximum load. The first cycles showed a small permanent deformation like those reported in the literature. However, as the repeatable behavior is of interest here, the second cycles are considered. From Fig. 49, a number of interesting behaviors of the MAX phases may be observed. First, the dotted black lines are used to denote a perfect elastic response during loading and upon unloading in the 800 MPa case. With this as a comparison, it is readily apparent that the material response exhibits significant nonlinearity (roughly 30% of the strain is inelastic at 800 MPa). Additionally, from this result, it may readily be seen that the nonlinear behavior begins at a modest stress level (200 MPa) and that the loading trajectories are the same. Some differences are noted at the higher stress response of the 800 MPa case although previous studies have reported slight hardening in the material response with permanent deformation [237]. Thus, this hardening is assumed to be a result of some of the permanent deformations during previous cycles. With respect to unloading, by comparing the 800 MPa case in Fig. 49 to the corresponding elastic path, the initial response seems to have an initially elastic unloading. Such a response is important as

[3]All experimental results provided by Prof. Radovic and R. Benitez. To the author's knowledge the corresponding results are currently unpublished.

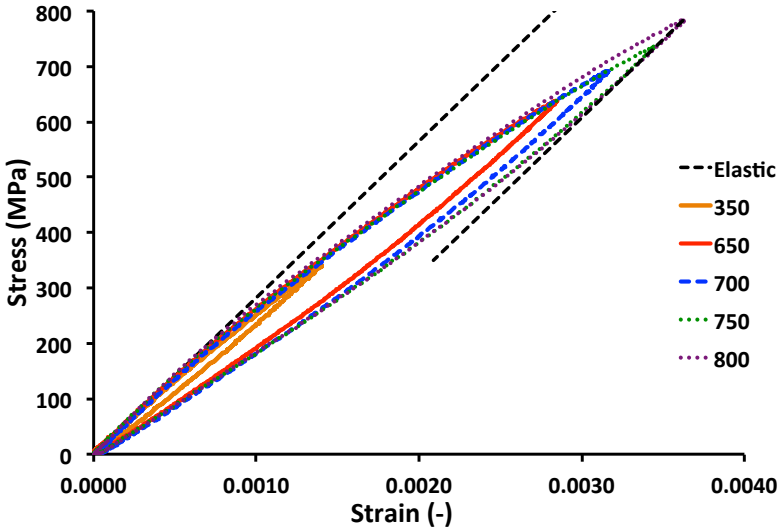

Figure 49: Repeatable, hysteretic room temperature compressive stress-strain response of Ti_2AlC at different maximum compressive stress values. Results shown correspond to the second cycle at the given stress level and the results correspond to the same material specimen loaded incrementally.

it would indicate that the material is undamaged through the IKB loading process. Additionally, the sequential loading trajectories and response repeatability during increasingly higher loadings indicate no permanent effects of the IKB formation. Thus, it is assumed that the IKB process does not damage the material or change the thermoelastic properties ($G^{te} \neq \hat{G}^{te}(\zeta)$).

Further consideration of the unloading of Fig. 49 yields additional information in regards to the hysteretic behavior of the MAX phases. Specifically, it is noted that at lower stress levels the unloading trajectories fall on the same path. Such a path appears to be near linear and, interestingly, ends at the zero stress level. Therefore, it would seem that the nonlinear unloading doesn't complete until complete external load removal. Additionally, in comparing the unloading behavior to that of the loading, it can be seen that in some ways the unloading response mirrors that of the

loading. Specifically, at the onset of the inelastic phenomena, a nonlinear hardening is observed. As the behavior progresses, the hardening appears in Fig. 49 to settle into more of a linear response. Finally, by visual inspection, it would seem that the elastic regimes during both IKB growth and annihilation (loading and unloading, respectively) occur over a similar stress magnitude. These issues will be expanded upon in subsequent analysis.

To further expand upon this point, the experimental hardening is considered. Specifically, in this case, the change in stress with inelastic strain is defined to be hardening and is plotted for three experimental cases in Fig. 50. The results come from the same set used to produce Fig. 49 and correspond to compressive stress-strain cycles (in Fig. 50 compressive stresses and strains are taken to be positive). For these results, the inelastic strain is simply defined as the difference between the measured total strain and elastic strain which is taken to be the recorded stress divided by an elastic modulus value found from analysis of the experimental results. Lower stress regions in which the inelastic strain is approximately zero are taken to be elastic regimes. Both unloading and loading curves portions of the loading cycle and for comparison reasons the unloading stress is taken as $|\sigma^{rev} - \sigma|$ such that the initial point corresponds to the start of unloading and the maximum value is at completion. In considering these results, it is also important to note that here no distinction is made between any inelastic mechanisms. Specifically, the hardening here is the total inelastic hardening observed in the system. Although these results correspond to the repeatable, second cycles of the experiments whose behavior is attributed to the formation and subsequent removal of IKB loops, the incorporation of other mechanisms cannot be ruled out.

From the results of Fig. 50 a number of important results may be observed. First, as discussed with regard to Fig. 49 the loading and unloading curves show

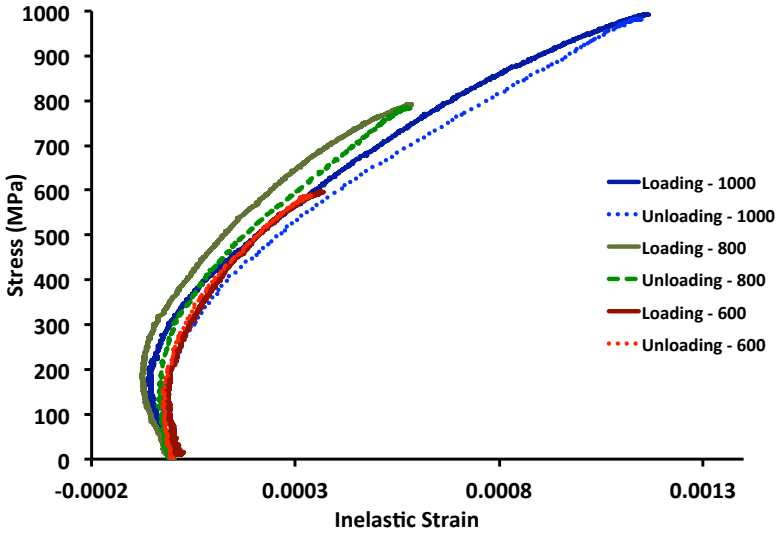

Figure 50: Inelastic hardening during loading and unloading of MAX phases at different maximum stress values

surprising similarities - this is especially true in the 600 MPa case. Specifically, after the onset of inelastic deformation an initially nonlinear character transitions to an increasingly linear evolution as the material is subject to further inelastic response. The 800 and 1000 MPa cases show the same general trend although some difference is noted at higher stress values where a seemingly slight variation in the curve is noted. Such a difference, although slight, could be associated with additional active mechanisms (*e.g*, plasticity) during loading. The small variation in elastic modulus between loading and unloading of the different load cases (manifest by the different slopes in the linear range) is potentially associated with damage formation in prior cycles or similar effects and as such isn't assumed to be a part of the IKB response. Interestingly, however, the unloading cycles demonstrate similar nonlinear to linear hardening evolutions. As the material is unloading, the only operative mechanism is expected to be IKB contraction and this evolution is associated with that behavior.

Additionally, although some scatter exists, the various results (*e.g*, 600 and 1000 MPa cases) seem to lie on similar trajectories. One surprising observation in these behaviors is in regards to the onset of nonlinear deformation. By assuming the nonlinear behavior begins at the inflection point (when the inelastic strain starts increasing), it is noted that the stress difference needed to initiate (both forward and reverse) IKB motion is roughly the same between loading and unloading (at least to the resolution of these results). This observation will be important in the subsequent discussion and motivation of the appropriate yield surfaces. To elaborate, consider for a moment an elastic-plastic material with a yield stress, σ^y. Assuming for a second that the material exhibits pure isotropic hardening and undergoes a proportional deformation sufficient to initiate plastic flow, then if the load is reversed and increased in the opposite direction (say a tension-compression loading) plastic flow will begin again after a change in stress of $2\left(\sigma^y + \sigma^{hard}\right)$, where σ^{hard} is some non-zero stress associated with the isotropic hardening. In the corresponding pure kinematic hardening case, the change in stress would be $2\sigma^y$. With these experimental results, however, the needed change in stress would seem to be σ^y. This observation would seem to preclude the possibility that this material response is simply an extreme Bauschinger effect. Instead, one potential phenomenological explanation in this case is that σ^y is the stress necessary to initially form the IKBs most favorably oriented for such deformations. As the applied stress increases, additional IKBs are nucleated in grains in less preferential grains that require higher loads to form. Previously generated IKBs grow and expand in such a way that the microstructural forces keeping the IKBs attached offset the additional external loads. Therefore, once the loading is reversed, IKB annihilation begins as soon as the initial nucleation loading is removed and the internal attractive forces dominate.

Given the above described internal variable set list and the previously stated

assumption that IKB growth does not affect the thermoelastic energy, the inelastic free energy contribution associated with the presence of IKBs may be given as,

$$G^r = (\sigma_{ij}, \boldsymbol{\Upsilon}^r) = \frac{1}{\rho} g^r + \frac{1}{3\rho} \kappa^r \beta^r_{ij} \beta^r_{ij} - \frac{1}{\rho} \sigma_{ij} \varepsilon^r_{ij}, \tag{4.3}$$

with κ^r being the backstress modulus. As stated previously, at this time, temperature and rate-dependencies are not included as the model is intended for low and mid temperature regimes. At higher temperatures, a temperature dependence is expected due to the increase dislocation mobility. Rate effects are neglected for similar reasons. The two hardening terms, g^r and $\frac{1}{3}\kappa^r \beta^r_{ij} \beta^r_{ij}$, describe the energy stored in the IKB structures – for instance that associated with the intra-dislocation forces. The elastic energy associated with the perturbation arising from the corresponding strains is captured by the final $\sigma_{ij}\varepsilon^r_{ij}$ term.

The corresponding rate of mechanical energy dissipation due to the growth or contraction of IKBs, ξ^r, may then be written as,

$$\xi^r = -\rho \frac{\partial G^r}{\partial \boldsymbol{\Upsilon}^r} \dot{\boldsymbol{\Upsilon}}^r = -\rho \frac{\partial G}{\partial \varepsilon^r_{ij}} \dot{\varepsilon}^r_{ij} - \rho \frac{\partial G}{\partial \beta^r_{ij}} \dot{\beta}^r_{ij} - \rho \frac{\partial G}{\partial g^r} \dot{g}^r. \tag{4.4}$$

Using the defined energy in Eqn. 4.3 with the dissipation given by Eqn. 4.4 leads to the modified dissipation expression of the form,

$$\xi^r = \sigma_{ij} \dot{\varepsilon}^r_{ij} - X^r_{ij} \dot{\beta}^r_{ij} - \dot{g}^r, \tag{4.5}$$

where X^r_{ij} is the backstress associated with kinematic hardening ($X^r_{ij} = \frac{2}{3}\kappa^r \beta^r_{ij}$). At this stage, a further assumption is introduced. Specifically, the evolution of these internal variables (and the corresponding dissipation) occurs only with changes in the kinked volume fraction, $\dot{\zeta}$. In this way, $\dot{\zeta}$ plays the role of consistency multiplier in

classical plasticity and a similar assumption in utilized in the modeling of martensitic transformation and other inelastic mechanisms in SMA [97,100,124]. Additionally, it is assumed that the isotropic hardening energy is a function of this volume fraction and only the kinked volume fraction. With these assumptions in mind, evolution equations of the form,

$$\dot{\varepsilon}^r_{ij} = \Lambda^r_{ij}\dot{\zeta}, \tag{4.6}$$

$$\dot{\beta}^r_{ij} = \Lambda^r_{ij}\dot{\zeta}, \tag{4.7}$$

$$\dot{g}^r = \frac{\partial g}{\partial \zeta}\dot{\zeta} = f^r\dot{\zeta}, \tag{4.8}$$

are assumed. The specific form of these functions will be discussed in the following sections for the growth/annihilation (loading/unloading) stages. For clarity, the subscripts "g" and "a" will be used for the growth (loading) and annihilation (unloading) states, respectively. Finally, with these relations, the dissipation may be rewritten,

$$\xi^r = \sigma_{ij}\Lambda^r_{ij}\dot{\zeta} - X^r_{ij}\Lambda^r_{ij}\dot{\zeta} - f^r\dot{\zeta} = \left(\mu^r_{ij}\Lambda^r_{ij} - f^r\right)\dot{\zeta}, \tag{4.9}$$

where the effective stress, μ^r_{ij} is introduced and defined as,

$$\mu^r_{ij} = \sigma_{ij} - X^r_{ij}. \tag{4.10}$$

By inspecting Eqn. 4.9, a total thermodynamic driving force conjugate to IKB generation, π^r, may be defined. Specifically,

$$\xi^r = \pi^r\dot{\zeta}, \tag{4.11}$$

where $\pi^r = \mu^r_{ij}\Lambda^r_{ij} - f^r$.

4.1.1.1 IKB Growth (Loading)

To describe the response of the material through IKB growth, expressions for Λ_{ij}^r and f^r need to be determined. First, in defining Λ_{ij}^r, a von Mises flow rule is utilized to describe the direction of strain generation. This selection is motivated by the fact that although the formation of IKB nucleation and growth relies on forming a parallel set of dislocation walls, it is still a shear-based dislocation mechanism. At this stage, an additional model parameter describing the magnitude of strain per unit kinked volume, γ^r, is introduced to scale the strain generation with kinked volume fraction. Unlike SMAs, this parameter is not easily observable from macroscopic experiments. Therefore, values for this parameter will be assumed and fit to experimental data. Such a value is expected to be quite small and depends on grain size. For instance, Kalidindi *et al.* [114] note the theoretical maximum nonlinear strain for a fully reversibly kinked Ti_3SiC_2 would be 0.035 and a value of similar magnitude would be expected. Therefore, the IKB strain evolution tensor is assumed to be (during IKB growth) as,

$$\Lambda_{ij}^r = \gamma^r \frac{3}{2} \frac{\mu_{ij}^{r'}}{\mu^{r-VMeff}}, \tag{4.12}$$

where the "$'$" denotes a deviatoric tensor ($\mu_{ij}^{r'} = \mu_{ij}^r - \frac{1}{3}\mu_{kk}^r \delta_{ij}$) and the Mises effective stress is defined as $\mu^{r-VMeff} = \sqrt{\frac{3}{2}\mu_{ij}^{r'}\mu_{ij}^{r'}}$. In considering the hardening of the IKB, it is assumed that, initially, at low kinked volume fractions the IKBs are distributed throughout the relevant grains and the forces acting on them from other IKBs are small. Thus, the hardening in this regime is tied primarily to hardening effects associated with constraints from grain boundaries and texture. As more IKBs are nucleated and growth of existing loops become more important, the effects of the internal forces become more dominant. With this interpretation in mind, a decaying

exponential form of the rate of isotropic hardening change, f_g^r is utilized and given as,

$$f_g^r(\zeta) = \frac{B}{k}\left(1 - e^{-k\zeta}\right)., \tag{4.13}$$

where B and k are experimental fit parameters.

With these terms defined, a yield function for IKB growth, Φ^r, may be proposed. Specifically, a function of the form,

$$\Phi_g^r = \pi_g^r - Y^r, \tag{4.14}$$

is proposed where Y^r is the critical energy needed to grow an IKB.

4.1.1.2 IKB Annihilation (Unloading)

During unloading, the IKBs contract and eventually the dislocations walls of opposite sign annihilate each other returning the material to its initial state. It is important to note that if some of the IKB's disassociate into permanent kink bands, full recovery is not possible and the associated deformations are not recovered (this interaction will be discussed in more detail in later sections). Given the coupling between the loading and unloading stages, however, it is desirable to describe the response in a fashion analogous to a reversible inelastic mechanism.

To capture the inelastic response upon unloading, two things needed to be defined - the evolution of the internal variables and the yield function. First, the new forms of the former functions shall be described and used to motivate a form of the latter. During loading, it was assumed that kinking strains develop in the direction of the effective stress, μ_{ij}^r. Upon unloading, a similar argument could be made for proportional (radial) loading cases. If the material is subjected to a complex non-proportional loading, however, using the same definition of loading could lead

to non-zero strains with a zero IKB volume fraction. This is a non-physical situation. Therefore, an analogy is made to reverse transformation of in phenomenological shape memory alloy models [40, 124, 192], and a direction tensor of the form,

$$\Lambda_{ij}^{r} = \frac{\varepsilon_{ij}^{r-rev}}{\zeta^{rev}}, \tag{4.15}$$

with the superscript "*rev*" denoting the values at loading reversal. In such a fashion, the strain is normalized per unit volume fraction and upon any unloading path it is ensured that the recoverable strain is zero.

For the change in isotropic hardening, the discussion and observations of Figs. 49 and 50 are revisited. Specifically, as was noted in the associated discussion, a distinct similarity is evident in the evolution of the hardening during loading and unloading. That is the initial hardening shows a more nonlinear nature while at further progression of the inelastic mechanisms a more linear character is observed. In the previous section, this was attributed to the relative contributions of effects like grain boundary interactions and texture (isotropic) and backstresses from developed IKBs (kinematic). Here a similar argument is made. Specifically, effects such as grain boundary pinnings are the first to be relieved while the backstresses are relaxed more slowly along with the decrease in applied stress necessary to keep the IKBs open. In keeping with this analogy, an unloading hardening of the form,

$$f_a^r = \frac{B}{k}\left(1 - e^{-(\zeta^{rev}-\zeta)}\right), \tag{4.16}$$

is assumed such that it essentially mirrors the effect upon unloading with the subscript a indicating annihilation of the IKBs through unloading.

With these relationships defined, the remaining consideration is the determina-

tion of the yield function for annihilation (unloading). As previously discussed, it is assumed that during loading an equilibrium is established between the external load and internal configuration forces that keep the IKBs open but associated. Upon reversal, the internal forces remain unchanged while the external load is gradually removed. In this frame, it is assumed that the annihilation process is controlled by the attractive, internal forces formed during the growth process. Initially, as the external stress is decreased, the applied load is still sufficient to prevent any dislocation motion due to the attractive, configurational forces. This accounts for the initial elastic regime observed in Fig. 49 and other MAX phase experiments. Eventually, however, the externally applied load is insufficient to maintain an equilibrium with the internal configurational forces and inhibit dislocation motion. Thus, the IKBs begin to contract. This continues until no load remains to keep the IKBs open. With such an interpretation, it is noted that the IKB structures already exist at the start of the unloading process. Therefore, IKB annihilation does not require the nucleation of additional dislocations, but is instead based merely on their motion. In such a fashion, the critical thermodynamic force necessary for the onset of IKB contraction is not that needed for dislocation formation (like during growth) but instead is the energy needed to *contract* and *move* the dislocation structures. This critical value is tied to the established hardening in the material which serves to inhibit IKB motion. In this way, the unloading yield function may be defined as,

$$\Phi^r_{con} = -\left(\sigma_{ij} - \frac{2}{3}\kappa^r \beta^r_{ij}\right)\Lambda^r_{ij} - f^r_a + f^{r-rev}_g, \tag{4.17}$$

where the signs are reversed due to the fact that this mechanism occurs during unloading. Additionally, such a form is selected such that independent of the maximum applied load, the annihilation process begins after the maximum stress is reduced by

the yield values to match the observations in Fig. 50.

4.1.2 Permanent Kink Band Formation

Unlike the incipient kink bands, experimental evidence observations have observed permanent deformations in the form of delaminations, kink bands, shear bands, grain buckling, and and microcracking [20, 73, 74, 220]. Specifically, Barsoum and El-Raghy [20] observed deformation via a combination of permanent kinking and delaminations in large-grain oriented Ti_3SiC_2 in areas lacking constraint. Similarly, Sun and coworkers [220] observed kink bands in 43% porous Ti_3SiC_2 and noted the presence of the pores aid in the formation of the permanent kink bands. The combination of these mechanisms is largely associated with the damage-tolerant nature of the MAX phases [20, 73]. Given these observations, the phenomenological effects of these deformation modes are incorporated into the proposed model. To capture these effects, a continuum damage mechanics (CDM) framework is adopted and the the incorporation of such a model is incorporated here. Continuum damage approaches have been well established over the last 50 years to describe the influences of microcrack formation and permanent deformations through mechanical, fatigue, and viscoplastic loadings. Such approaches focus on the effective stress concept of Kachanov and incorporate damage effects through stiffness degradation associated with a damage variable (either scalar or tensorial). Detailed discussion of this topic may be found in various texts (*e.g*, Lemaitre and Chaboche [135]) although recent efforts have extended these principles to ductile [3, 103], brittle [50], quasi-brittle [202, 228], and composite [38] materials.

To model the effects associated with kink band formation and the associated deformations, a set of internal variables associated with damage, $\boldsymbol{\Upsilon}^d$, are introduced. Five internal variables are introduced in this fashion – ζ^d, D_{ij}, ε^d_{ij}, β^d_{ij}, and g^d. The

scalar variable ζ^d is the isotropic variable used to physically represent the total propagation of damage through the material. The second order tensor D_{ij} then describes the loss of load bearing capability due to damaged areas. Note, at this time no assumption is made on the relationship between ζ^d and D_{ij}. Instead, they are assumed to act independently although some interdependency is expected and the relationship between them will be expanded upon in subsequent sections. As alluded to in the previous section, much of the coupling between the different mechanisms in this formulation is captured through relationships on the volumes undergoing different inelastic mechanisms. Therefore, ζ^d is interpreted as the permanently kinked volume fraction. An additional restriction is imposed such that $\zeta^d \leq \zeta$ as it is assumed that any volume must be first incipiently kinked before separating into the permanent state.

With ζ^d defined in this fashion, an additional note is need in the description of D_{ij}. In most previous cases, the damage tensor is related to the damage area and microcrack densities [3,161]. Specifically, $D_{ij} = \sqrt{\rho_i \rho_j}$ where $\rho_i = A_i^d / A_i$ (no sum) with A_i^d being the damaged area in the i-th direction and A_i the total area in the same direction [3]. If both the scalar ζ^d and tensorial D_{ij} variables have geometric interpretations, however, issues of independence or contradiction could exist. To address this point, the tensorial variable D_{ij} is instead interpreted as the variable capturing anisotropic stiffness degredation associated with kink band formation without invoking the microcrack density concept. Specifically, this argument is used as the loss of stiffness may not just be associated with microcracks but instead kinked or buckled volumes and associated effects. Additionally, the damage, kinking process occurs via multiple mechanisms (*e.g*, kinking and delimitation) and a purely microcrack density argument may be insufficient to capture the complex effects of such modes. In this way, any issues with contradictory definitions and independence are avoided.

It is noted, however, that in the isotropic damage limit, ζ^d does play the role of the damage variable and the tensorial representation is unnecessary. Initially, however, the two variables are treated independently to allow for anisotropic damage.

Additionally, an inelastic strain of the form ε_{ij}^d is added to the internal variable set list. Specifically, this term is used to describe *permanent* strains developed as a result of the damage process. Changes in elastic strain due to changes in the material stiffness are not included in this term and thus there is no reversible nature in this strain. In previous efforts [3], such strains were attributed random geometries, orientations, and distributions of cracks which remain open and cannot be recovered upon unloading. With respect to the MAX Phases, similar deformations may be attributed to the formation of kink bands and resulting kinematic incompatabilities, cracks, and delaminations formed when IKBs separate into permanent kink bands. Finally, kinematic and isotropic hardening effects are captured through the introduction of β_{ij}^d and g^d, respectively. With all of these in mind, and assuming a rate and temperature independent mechanism, the inelastic energy associated with permanent kink band formation is,

$$G^d\left(\sigma_{ij}, \boldsymbol{\Upsilon}^d\right) = \frac{1}{\rho} g^d + \frac{1}{3\rho}\kappa^d \beta_{ij}^d \beta_{ij}^d - \frac{1}{\rho}\sigma_{ij}\varepsilon_{ij}^d, \tag{4.18}$$

where κ^d is the modulus of kinematic hardening variable. Additionally, the inclusion of the damage tensor, D_{ij} also modifies the thermoelastic free energy of the system such that,

$$\begin{aligned} G^{te}\left(\sigma_{ij}, T, D_{ij}\right) = \; & -\frac{1}{2\rho}\sigma_{ij} Q_{ijmn}^T M_{mnrs}^0 Q_{rskl}\sigma_{kl} - \frac{1}{\rho}\sigma_{ij}\alpha_{ij}\left(T - T_0\right) \\ & + c\left[\left(T - T_0\right) - T\ln\left(\tfrac{T}{T_0}\right)\right], \end{aligned} \tag{4.19}$$

with M^0_{ijkl} being the undamaged compliance tensor, superscript "T" denoting the tensor transpose and Q_{ijkl} being the map between the undamaged and damaged materials defined as [228],

$$Q_{ijkl} = \frac{1}{2}\left[\delta_{ij}\left(\delta_{kj} - D_{kj}\right)^{-1} + \left(\delta_{il} - D_{il}\right)^{-1}\delta_{kj}\right], \tag{4.20}$$

and δ_{ij} being the kroneker delta. The current damaged compliance tensor is then defined as,

$$M_{ijkl} = Q^T_{ijmn} M^0_{mnrs} Q_{rskl} \tag{4.21}$$

With the relevant variables and free energy defined, the corresponding rate of mechanical dissipation of the kinking, damage process, ξ^d is given as,

$$\xi^d = -\rho\frac{\partial G^d}{\partial \boldsymbol{\Upsilon}^d}\dot{\boldsymbol{\Upsilon}}^d = -\rho\frac{\partial G}{\partial D_{ij}}\dot{D}_{ij} - \rho\frac{\partial G}{\partial \varepsilon^d_{ij}}\dot{\varepsilon}^d_{ij} - \rho\frac{\partial G}{\partial \beta^d_{ij}}\dot{\beta}^d_{ij} - \rho\frac{\partial G}{\partial g^d}\dot{g}^d. \tag{4.22}$$

The corresponding derivatives (and conjugate thermodyanmic driving forces) are determined to be,

$$-\rho\frac{\partial G}{\partial D_{ij}} = \quad Y_{ij} = -\rho\frac{\partial G^{te}}{\partial D_{ij}} = \frac{1}{2}\sigma_{mn}\frac{\partial M_{mnkl}}{\partial D_{ij}}\sigma_{kl}, \tag{4.23}$$

$$-\rho\frac{\partial G}{\partial \varepsilon^d_{ij}} = \quad \sigma_{ij}, \tag{4.24}$$

$$-\rho\frac{\partial G}{\partial \beta^d_{ij}} = \quad -\frac{2}{3}\kappa^d\beta^d_{ij}, \tag{4.25}$$

producing a dissipation of,

$$\xi^d = Y_{ij}\dot{D}_{ij} + \sigma_{ij}\dot{\varepsilon}^d_{ij} - \frac{2}{3}\kappa^d\beta^d_{ij}\dot{\beta}^d_{ij} - \dot{g}^d. \tag{4.26}$$

To complete the discussion, evolution equations for the various internal state variables must be prescribed. Similar to the IKB dissipation, it is assumed that the the damage process occurs with the evolution of the damage volume fraction, ζ^d. Additionally, the isotropic energy is taken to be a function of ζ^d and ζ^d alone. With this mind, the following evolution equations are postulated:

$$\dot{D}_{ij} = \Lambda^d_{ij}\dot{\zeta}^d, \tag{4.27}$$

$$\dot{\varepsilon}^d_{ij} = \Lambda^d_{mn}\frac{\partial M_{ijkl}}{\partial D_{mn}}\sigma_{kl}\dot{\zeta}^d, \tag{4.28}$$

$$\dot{\beta}^d_{ij} = \Lambda^d_{ij}\dot{\zeta}^d, \tag{4.29}$$

$$\dot{g}^d = \frac{\partial g^d}{\partial \zeta^d}\dot{\zeta}^d = f^d\dot{\zeta}^d. \tag{4.30}$$

The damage variable direction tensor is taken to be,

$$\Lambda^d_{ij} = \gamma^d\left(\frac{W_{ij}}{\sqrt{W_{mn}W_{mn}}} + \tilde{\nu}\delta_{ik}\delta_{jk}\right) \tag{4.31}$$

with $W_{ij} = Y_{ij} - \frac{2}{3}\kappa^d\beta^d_{ij}$, $\tilde{\nu}$ being a pressure dependence coefficient, and γ^d a scaling coefficient relating the magnitude of the evolution of D_{ij} with ζ^d. In this fashion, the damage evolves in the direction of the changing elastic strain energy. Additionally, the damage strain evolution, Eqn. 4.28, is proportional to the loss of elastic strain due to the damage process. Similar to previous damage models [3, 103], a decaying exponential form of the change in isotropic hardening energy function is also adopted of the form,

$$f^d = q\left(1 - e^{-c\zeta^d}\right), \tag{4.32}$$

where q and c are fit parameters. Introducing these relations into Eqn. 4.26, yields a damage dissipation expression of,

$$\xi^d = \left[\left(Y_{ij} - \frac{2}{3}\kappa^d\beta^d_{ij}\right)\Lambda^d_{ij} + \sigma_{ij}\Lambda^d_{mn}\frac{\partial M_{ijkl}}{\partial D_{mn}}\sigma_{kl} - f^d\right]\dot{\zeta}^d. \tag{4.33}$$

It is noted that by using Eqn. 4.23,

$$\sigma_{ij}\frac{\partial M_{ijkl}}{\partial D_{mn}}\sigma_{kl}\Lambda^d_{mn} = 2Y_{mn}\Lambda^d_{mn}, \tag{4.34}$$

yielding,

$$\xi^d = \left[3\left(Y_{ij} - \frac{2}{3}\kappa^d\beta^d_{ij}\right)\Lambda^d_{ij} - f^d\right]\dot{\zeta}^d. \tag{4.35}$$

Thus, the dissipation associated with deformation may be described through the use of a single scalar thermodynamic driving force, π^d, such that

$$\xi^d = \pi^d\dot{\zeta}^d. \tag{4.36}$$

Additionally, with such a form, a yield function for the damage mechanisms of the form,

$$\Phi^d = \pi^d - Y^d, \tag{4.37}$$

is postulated where Y^d is the (constant) critical energy for damage propagation.

4.1.2.1 Isotropic Damage Reduction

The tensorial damage form used in the previous section, D_{ij}, is used to describe the anisotropic evolution and development of damage (e.g. cracks aligned in different directions). One common reduction used for such analysis is the consideration of an isotropic damage variable. In this case, the permanently kinked volume current

fraction, ζ^d, assumes the role of the isotropic damage variable. In this way, the current compliance tensor becomes,

$$M_{ijkl} = \psi M^0_{ijkl} \tag{4.38}$$

where $\psi = \dfrac{1}{1-\zeta^d}$ or $\psi = \dfrac{1}{(1-\zeta^d)^2}$ using the equivalent strain or equivalent strain energy, respectively. Voyiadjis and Katten [226] present an in depth discussion of the different damage variables, although for know the general form Eqn. 4.38 is used. With the reduction in order of the damage tensor, the corresponding thermodynamic driving force also becomes a scalar relation and simplifies to,

$$Y = -\rho \frac{\partial G^{te}}{\partial \zeta^d} = \frac{1}{2}\sigma_{ij}\frac{\partial \psi}{\partial \zeta^d} M^0_{ijkl}\sigma_{kl}. \tag{4.39}$$

Similarly, the kinematic variable reduces to a scalar variable, leading to an equation of the form,

$$\Lambda^d_{ij} \rightarrow \lambda^d = \gamma^d \left(1 + \tilde{\nu}\right). \tag{4.40}$$

The evolution of the permanent kinking strain and damage kinematic variable (which also becomes a scalar variable) similarly reduce such that,

$$\dot{\beta}^d = \quad \lambda^d \dot{\zeta}^d, \tag{4.41}$$

$$\dot{\varepsilon}^d = \quad \lambda^d \frac{\partial \psi}{\partial \zeta^d} M^0_{ijkl}\sigma_{kl}\dot{\zeta}^d. \tag{4.42}$$

These simplifications lead to an equivalent thermodynamic driving force of,

$$\pi^d = \left[3\left(Y - \frac{2}{3}\kappa^d \beta^d\right)\lambda^d - f^d\right]. \tag{4.43}$$

4.1.3 Irrecoverable Permanent Deformations

In addition to the above mentioned effects of kink band formation (incipient and permanent), the possibilities of other inelastic plastic deformation – specifically glide in non-kinking grains. Such deformations are accounted for via a plasticity type formulation. To capture these effects of this mechanism, four internal variables are assumed to comprise $\boldsymbol{\Upsilon}^p$ - p, ε_{ij}^p, β_{ij}^p, and g^p. In this context, p is a scalar internal variable representing *the volume fraction of plastically deformed material* and not an effective strain measure like those used in most classical continuum plasticity theories. An analogy could be made to p being a dislocation density via the reintrepetation of the variable and corresponding evolution equation, but in this case a volume fraction is selected for connection with the previous described kinking mechanisms. Specifically, this selection is made as the volume $1 - p$ could be interpreted as a plastically deformed volume incapable of kinking thereby placing an upper bound on ζ. A parameter, γ^p, is introduced representing the plastic slip magnitude per unit volume of plastically deformed material. It should be noted, however, that in practice the determination of such a parameter experimentally is not trivial and difficult to implement. By setting $\gamma^p = 1$, the variable p may be viewed as the effective plastic strain in the classical sense. The macroscopic, inelastic strain is selected as another internal variable and denoted as ε_{ij}^p. Two variables (one tensorial and one scalar) are also introduced to describe hardening effects - β_{ij}^p and g^p. Specifically, isotropic effects are described via the total isotropic hardening energy g^p and may include energies corresponding to dislocation pinning (for example). Kinematic hardening effects are captured through the tensorial variable β_{ij}^p and used to captureany associated backstresses. Importantly, at this time it is assumed that this mechanism represented rate-independent plastic effects and any temperature-softening is neglected. With

these definitions, the total inelastic energy of this mechanism is written as,

$$G^p\left(\sigma_{ij}, \boldsymbol{\Upsilon}^p\right) = \frac{1}{\rho} g^p + \frac{1}{3\rho} \kappa^p \beta_{ij}^p \beta_{ij}^p - \frac{1}{\rho} \sigma_{ij} \varepsilon_{ij}^p, \tag{4.44}$$

where κ^p is the corresponding hardening modulus.

In further defining the problem, the rate of mechanical dissipation associated with plasticity, ξ^p is now explored and written as,

$$\xi^p = -\rho \frac{\partial G^p}{\partial \boldsymbol{\Upsilon}^p} \dot{\boldsymbol{\Upsilon}}^p = -\rho \frac{\partial G}{\partial \varepsilon_{ij}^p} \dot{\varepsilon}_{ij}^p - \rho \frac{\partial G}{\partial \beta_{ij}^p} \dot{\beta}_{ij}^p - \rho \frac{\partial G}{\partial g^p} \dot{g}^p, \tag{4.45}$$

where the derivates are also the corresponding thermodynamic driving forces and are given as,

$$-\rho \frac{\partial G}{\partial \varepsilon_{ij}^p} = \quad \sigma_{ij}, \tag{4.46}$$

$$-\rho \frac{\partial G}{\partial \beta_{ij}^p} = \quad -\frac{2}{3} \kappa^p \beta_{ij}^p. \tag{4.47}$$

Using these definitions, the mechanical dissipation is rewritten as,

$$\xi^p = \sigma_{ij} \dot{\varepsilon}_{ij}^p - \frac{2}{3} \kappa^p \beta_{ij}^p \dot{\beta}_{ij}^p - \dot{g}^p. \tag{4.48}$$

In a similar fashion to the previous cases, it is assumed that the plastic mechanism and its dissipation evolves with, and only with, the plastic volume fraction, p. Furthermore, the isotropic energy is taken to be purely a function of this same volume fraction. With this assumption, the evolution equations need to be determined and

are postulated as:

$$\dot{\varepsilon}^p_{ij} = \Lambda^p_{ij}\dot{p}, \tag{4.49}$$

$$\dot{\beta}^p_{ij} = \Lambda^p_{ij}\dot{p}, \tag{4.50}$$

$$\dot{g}^p \;=\; f^p\dot{p}, \tag{4.51}$$

where Λ^p_{ij} is tensor the direction of the flow and f^p is the change in isotropic energy. Additionally, an effective plastic stress, μ^p_{ij}, is introduced of the form $\mu^p_{ij} = \sigma_{ij} - X^p_{ij}$ where $X^p_{ij} = \frac{2}{3}\kappa^p\beta^p_{ij}$ is the plastic back stress. The plasticity is assumed to be shear-based and the classic, J_2-type von Mises form,

$$\Lambda^p_{ij} = \gamma^p\frac{3}{2}\frac{\mu^{p'}_{ij}}{\mu^{p-VMeff}}, \tag{4.52}$$

is assumed for the flow direction. A power-law form is used for the change in plastic isotropic energy. Therefore, $f^p = Lp^n$ where L and n are material fit parameters. Combining these relations, leads to a total dissipation form of,

$$\xi^p = \left[\left(\sigma_{ij} - \frac{2}{3}\kappa^p\beta^p_{ij}\right)\Lambda^p_{ij} - f^p\right]\dot{p}. \tag{4.53}$$

By defining π^p to be the total thermodynamic driving force conjugate to the evolution of plastic volume fraction the total mechanical dissipation becomes,

$$\xi^p = \pi^p\dot{p}. \tag{4.54}$$

A plastic yield function of the form,

$$\Phi^p = \pi^p - Y^p, \tag{4.55}$$

where Y^p is the (constant) critical thermodynamic driving force for plastic volume formation, is then assumed.

4.1.4 Multiple Couple Mechanisms (MCM) Model

With the models of the various mechanisms described, the coupled and combined response of the considered material may now be discussed. First, the total free energy of the system is written as,

$$\begin{aligned} G\left(\sigma_{ij}, T, \boldsymbol{\Upsilon}\right) = & -\frac{1}{2\rho}\sigma_{ij}M_{ijkl}\sigma_{kl} - \frac{1}{\rho}\sigma_{ij}\alpha_{ij}\left(T - T_0\right) \\ & + c\left[\left(T - T_0\right) - T\ln\left(\frac{T}{T_0}\right)\right] - s_0 T - \frac{1}{\rho}\sigma_{ij}\left(\varepsilon^r_{ij} + \varepsilon^d_{ij} + \varepsilon^p_{ij}\right) \\ & + \frac{1}{\rho}\left(g^r + g^d + g^p\right) + \frac{1}{3\rho}\left(\kappa^r\beta^r_{ij}\beta^r_{ij} + \kappa^d\beta^d_{ij}\beta^d_{ij} + \kappa^p\beta^p_{ij}\beta^p_{ij}\right), \end{aligned} \tag{4.56}$$

where M_{ijkl} is the current compliance tensor defined via Eqn. 4.21. In considering the above free energy, it is observed that there is no coupling between the various states variables of the different mechanisms. That is to say, the different configurational driving forces are not coupled and do not directly interact. With respect to the plasticity and kinking mechanisms, such an assumption is motivation by the fact that these deformations occur in different grains and the long range effects are taken to be negligible. In terms of the kinking, permanent kink bands and the corresponding damage are taken to interact with the other inelastic deformations through the redistribution of the stresses and not via the internal variables. Additional couplings may be observed in this system, however, and they are presented first.

In the given material model, the coupling is addressed in a variety of fashions. First, additional interactions between the evolution of incipient and permanent kink bands terms are noted. Although it has been stated that these mechanisms are not mixed in the free energy, physically their values (and volumes) must be related. For

instance, as already mentioned a constraint is imposed such that the material must be incipiently kinked prior it begin permanently disassociated. Additionally, any volumes undergoing plastic deformation are poorly aligned for kinking and will not undergo such deformations. Mathematically, this restriction results in the following inequality,

$$0 \leq \zeta^d \leq \zeta \leq 1 - p \leq 1. \tag{4.57}$$

Furthermore, if a IKB disassociates into a permanent form it logically follows that the recoverable deformations associated with those structures are now permanent. These observations lead to modifications of the evolution laws of the form,

$$\dot{\varepsilon}^r_{ij} = \Lambda^r_{ij}\dot{\zeta} - \Lambda^{rg}_{ij}\dot{\zeta}^d, \tag{4.58}$$

$$\dot{\varepsilon}^d_{ij} = \Lambda^d_{mn}\frac{\partial M_{ijkl}}{\partial D_{mn}}\sigma_{kl}\dot{\zeta}^d + \Lambda^{rg}_{ij}\dot{\zeta}^d, \tag{4.59}$$

where Λ^{rg}_{ij} is the IKB strain direction tensor, Λ^r_{ij}, evaluated during the growth (loading) regime. In considering Eqns. 4.58 and 4.59, it is noted that by summing these expressions the $\Lambda^{rg}_{ij}\dot{\zeta}^d$ terms cancel. Thus, the total inelastic strain tensor is preserved and this additional interaction is not in and of itself dissipative. Therefore, this modification to the evolution equations serves primarily to track what strains are recoverable and irrecoverable.

With these interactions established, constitutive equations for the fully coupled MAX phase material are sought. To accomplish this task, the 2^{nd} law of Thermodynamics, in the form of the Clausius-Planck inequality,

$$-\rho\dot{G} - \dot{\sigma}_{ij}\varepsilon_{ij} - \rho s\dot{T} \geq 0, \tag{4.60}$$

is recalled. By considering the postulated free energy (Eqn. 4.56), the selected internal variables, this inequality may be rewritten:

$$-\left(\varepsilon_{ij}+\rho\frac{\partial G}{\partial\sigma_{ij}}\right)\dot{\sigma}_{ij}-\rho\left(s+\frac{\partial G}{\partial T}\right)\dot{T}+\left(-\rho\frac{\partial G}{\partial\zeta}\dot{\zeta}-\rho\frac{\partial G}{\partial\beta^r_{ij}}\dot{\beta}^r_{ij}-\rho\frac{\partial G}{\partial\varepsilon^r_{ij}}\dot{\varepsilon}^r_{ij}\right.$$
$$\left.-\rho\frac{\partial G}{\partial g^r}\dot{g}^r\right)+\left(-\rho\frac{\partial G}{\partial\zeta^d}\dot{\zeta}^d-\rho\frac{\partial G}{\partial\beta^d_{ij}}\dot{\beta}^d_{ij}-\rho\frac{\partial G}{\partial D_{ij}}\dot{D}_{ij}-\rho\frac{\partial G}{\partial\varepsilon^d_{ij}}\dot{\varepsilon}^d_{ij}-\rho\frac{\partial G}{\partial g^d}\dot{g}^d\right)$$
$$+\left(-\rho\frac{\partial G}{\partial p}\dot{p}-\rho\frac{\partial G}{\partial\beta^p_{ij}}\dot{\beta}^p_{ij}-\rho\frac{\partial G}{\partial\varepsilon^p_{ij}}\dot{\varepsilon}^p_{ij}-\rho\frac{\partial G}{\partial g^p}\dot{g}^p\right)\geq 0. \tag{4.61}$$

Most of the thermodynamic driving forces and evolution equations have been expressed and discussed in the previous sections. The additional derivatives,

$$-\rho\frac{\partial G}{\partial\sigma_{ij}}= M_{ijkl}\sigma_{kl}+\alpha_{kl}\left(T-T_0\right)+\varepsilon^r_{ij}+\varepsilon^d_{ij}+\varepsilon^p_{ij}, \tag{4.62}$$

$$-\rho\frac{\partial G}{\partial T}= \sigma_{ij}\alpha_{ij}+\rho c\ln\left(\frac{T}{T_0}\right)+\rho s_0, \tag{4.63}$$

are specified here to complete those definitions. By invoking the arguments of Coleman and Noll [60], constitutive equations for the material may be derived from Eqn. 4.61. Specifically, it is noted that Eqn. 4.61 must be satisfied for any admissible thermodynamic path. In the case of arbitrary, independent, and elastic stress or temperature excursions, this statement means the bracketed terms associated with $\dot{\sigma}_{ij}$ and $\dot{T}$ must be zero. Therefore,

$$\varepsilon_{ij}= M_{ijkl}\sigma_{kl}+\alpha\left(T-T_0\right)+\varepsilon^r_{ij}+\varepsilon^d_{ij}+\varepsilon^p_{ij}, \tag{4.64}$$

$$s= \frac{1}{\rho}\sigma_{ij}\alpha_{ij}+c\ln\left(\frac{T}{T_0}\right)+s_0. \tag{4.65}$$

$$\tag{4.66}$$

The remaining expressions in Eqn. 4.61 correspond to inelastic dissipation. By recalling the previous equations in this chapter, the dissipation may be rewritten,

$$\begin{aligned} &\left(\mu_{ij}^{r}\Lambda_{ij}^{r} - f^{r}\right)\dot{\zeta} - \sigma_{ij}\Lambda_{ij}^{rg}\dot{\zeta}^{d} \\ &+ \left[\left(3Y_{ij} - X_{ij}^{d}\right) - f^{d}\right]\dot{\zeta}^{d} + \sigma_{ij}\Lambda_{ij}^{rg}\dot{\zeta}^{d} \\ &+ \left(\mu_{ij}^{p}\Lambda_{ij}^{p} - f^{p}\right) \geq 0, \end{aligned} \tag{4.67}$$

or

$$\pi^{r}\dot{\zeta} + \pi^{d}\dot{\zeta}^{d} + \pi^{p}\dot{p} \geq 0. \tag{4.68}$$

The final coupling results from the stress and load redistribution arising from the loss of load bearing capacity due to the damage process. To address this point, the well established *effective stress concept* is introduced. This theory is well established and a cornerstone of continuum damage mechanics and the text of Lemaitre and Chaboche [135] is referenced for details and a review. Specifically, through this approach, it is assumed that a material point or element under consideration is comprised of undamaged and damaged volumes. The state variables (both external and internal) of such a material point then represent the average response of the constituent with its damaged and undamaged material volumes. Through the effective stress concept, however, it is taken that any deformation, be it elastic or inelastic, occurs only in the undamaged configuration and corresponding constitutive response should be written in this configuration. Therefore, a mapping is needed between the effective response and the undamaged material. To perform such an operation an *effective configuration* comprised only of the undamaged material is introduced. By then noting that the damaged portion of the material carries no load and the total force applied to both the damaged and effective, undamaged configurations are equal

yielding the classical isotropic relationship that,

$$\bar{\sigma} = \frac{\sigma}{1 - D} \tag{4.69}$$

where $\bar{\sigma}$ is the stress in the effective configuration, σ is the stress of the damaged material point, and D is the isotropic damage variable defined as A_d/A where A_d and A are the damaged and total areas of the effective and damaged configurations. In the model developed here, ζ^d is this damage variable.

With this in mind, the effective stress concept is expanded here for use with the various mechanisms observed in the MAX phases. Specifically, it is noted that in the preceding sections three mechanisms were introduced - IKB formation, permanent kink band formation, and permanent (here considered as plastic) inelastic deformations. Although such mechanisms operate independently, they are not unrelated. Specifically, as was noted previously, IKB formation is a precursor to permanent kink band formation and thus such a mechanism should be restricted to occurring in the incipiently kinked domain. Additionally, given that both incipient and permanent kink formation is associated with the formation of dislocation loops on basal planes aligned with applied loading, a strong dependence on the texture of the material on the macroscopic behavior is expected. Such effects are accounted for through the calibration constants and material properties given the scale (and nature) of the proposed model, but it can also be reasoned that in a material volume element represented by a material point kinking will only occur in some of the grain and material assemblage. This is an important distinction as remaining volume will not kink and may instead be subject to other forms of inelastic deformation. In the described previously, one such possibility is plastic slip in any impurities or poorly aligned grains leading to the plasticity mechanisms considered here.

Bearing these restrictions in mind, the concept of an effective configuration is

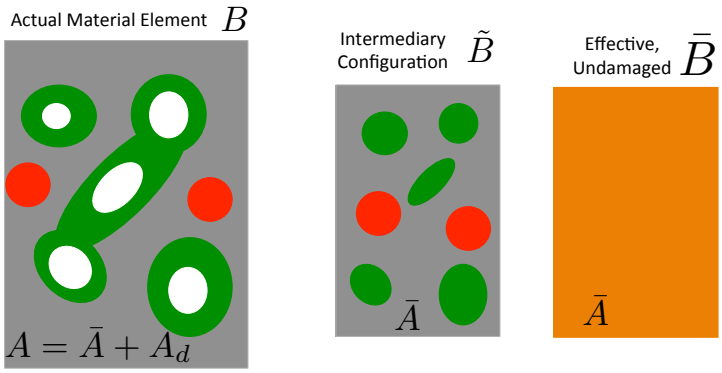

Figure 51: Schematic depicting various material configurations. Schematically, gray areas are elastically deforming materials, green represents volumes incipiently kinked, red those plastically deforming and white the damaged, permanently kinked volumes

utilized to investigate the couplings between various mechanisms. First, as shown in Fig. 51, a two-dimensional[4] material volume element with total area A with various volumes deformed by different mechanisms is considered. The actual material volume is referred to as the B configuration and corresponding state variables of the total material volume element shall be denoted without any additional accent is considered. This configuration has total area A and is comprised of permanently kinked (damaged), incipiently kinked, plastically deforming, and elastic areas denoted by A^d, A^ζ, A^p, and A^0, respectively such that $A = A^d + A^\zeta + A^p + A^0$. By normalizing

[4]a 2D argument is utilized for construction and as a though experiment. The concept is readily extended to a 3D model as proposed here

with respect to the total area, the previously defined internal variables ζ, ζ^d, and p may be defined as $\left(A^\zeta + A^d\right)/A$, A^d/A and A^p/A. Following the previous CDM concept, an intermediary configuration denoted by $\tilde{B}$ is created by removing all of the damaged area. This configuration, however, still has heterogeneous and distinct areas corresponding to the different volumes. Therefore, to get an effective, homogenized representation another configuration, $\bar{B}$, is introduced such that constant incipiently kinked and plastic volume fractions ($\bar{\zeta}$ and $\bar{p}$) are found in the domain. The total area of both the intermediary and effective configurations ($\tilde{B}$ and $\bar{B}$) are the same and denoted as $\bar{A}$ defined as $\bar{A} = A - A^d$. At this point it is essential to note a key difference between ζ and $\bar{\zeta}$. Specifically, in the damaged configuration B, ζ represents the total kinked (incipient and damaged) volume fraction. In constructing the intermediary and effective configurations, however, the damaged area is removed as it does not contribute to the response of the material. Thus, $\bar{\zeta}$ does not represent the total kinked volume in that configuration. Instead, it represents only the *incipiently* kinked volume fraction. To determine the relationship between these variables, $\bar{\zeta}$ is defined to be $A^\zeta/\bar{A}$ and $\bar{p}$ is given as $\bar{p} = A^p/\bar{A}$. Substituting the various definitions above yields the following relationships,

$$\bar{\zeta} = \frac{\xi - \zeta^d}{1 - \zeta^d}, \tag{4.70}$$

$$\bar{p} = \frac{p}{1 - \zeta^d}. \tag{4.71}$$

Interestingly, for a fixed value of ζ, $\bar{\zeta}$ may actually decrease with increases in the permanently kinked material volume.

The impact of these configurational assumptions is observed in the dissipation of

the material. Recalling Eqn. 4.68, the total dissipation may be written as,

$$\xi = \pi^r \dot{\zeta} + \pi^d \dot{\zeta^d} + \pi^p \dot{p} \geq 0. \tag{4.72}$$

where the configurational forces and controlling state variables are written in the damaged configuration (B). The constitutive assumptions discussed in the previous section for the incipient kinking and plastic formation, however, were written and developed without consideration of the formation of damage. Thus, it is beneficial to consider there responses in terms of the *effective* configuration. Additionally, considering that the mechanisms act only in undamaged materials and the net dissipation between the different configurations is the same, the dissipation potential may be rewritten as,

$$\xi = \bar{\pi}^r \dot{\bar{\zeta}} + \pi^d \dot{\zeta^d} + \bar{\pi}^p \dot{\bar{p}}. \tag{4.73}$$

In returning to Eqns. 4.70, however, it is readily observed that both $\bar{\zeta}$ and $\bar{p}$ may change with variation in ζ^d only. Such a consideration leads to the possibility that effective dissipations in such a fashion could be non-zero even if the respective mechanism is not active. Therefore, a different form of the effective dissipation is necessary. Specifically, the rate of change of the volume fractions in the effective volume fraction used in defining the dissipation are taken to be the total time derivative of $\bar{\zeta}$ and $\bar{p}$ with ζ^d fixed ($\dot{\zeta^d} = 0$). Physically, such an assumption also corresponds to all dissipation tied to the formation of permanent kinks is captured by ξ^d. Additionally, the permanent kinking is taken to act in the damage configuration and its dissipation remains unchanged. Therefore, the total dissipation becomes,

$$\xi = \bar{\pi}^r \frac{\dot{\zeta}}{1 - \zeta^d} + \pi^d \dot{\zeta^d} + \bar{\pi}^p \frac{\dot{p}}{1 - \zeta^d}. \tag{4.74}$$

In formulating the constitutive model, it is desirable to cast all of the terms in the current, damaged configuration. Therefore, terms for $\bar{\pi}^r$ and $\bar{\pi}^p$ in terms of the current configuration need to be considered. To this end, an analogy may be made between these thermodynamic driving forces (fluxes of the respective internal state variables) and the total corresponding force and the mechanical case of stress and force. Given that these terms are also scalar relations simple relations of the form,

$$\bar{\pi}^r = \frac{\pi^r}{1-\zeta^d}, \tag{4.75}$$

$$\bar{\pi}^p = \frac{\pi^p}{1-\zeta^d}, \tag{4.76}$$

may be derived leading to a final mechanical dissipation of the form,

$$\xi = \frac{\pi^r}{1-\zeta^d}\frac{\dot{\zeta}}{1-\zeta^d} + \pi^d\dot{\zeta}^d + \frac{\pi^p}{1-\zeta^d}\frac{\dot{p}}{1-\zeta^d}. \tag{4.77}$$

With the total dissipation of the material constituent under investigation given in Eqn. 4.77, yield functions for the different mechanisms in the damaged configuration may be given as,

$$\Phi^r = \pm\frac{\pi^r}{1-\zeta^d} - Y^r \leq 0, \tag{4.78}$$

$$\Phi^d = \pi^d - Y^d \leq 0, \tag{4.79}$$

$$\Phi^p = \frac{\pi^p}{1-\zeta^d} - Y^p \leq 0. \tag{4.80}$$

Complementary Kuhn-Tucker conditions are then given as

$$\frac{\dot{\zeta}}{1-\zeta^d}\Phi^r = 0, \qquad \Phi^r \leq 0, \qquad \frac{\dot{\zeta}}{1-\zeta^d} \geq 0, \tag{4.81}$$

$$\dot{\zeta}^d\Phi^d = 0, \qquad \Phi^d \leq 0, \qquad \dot{\zeta}^d \geq 0, \tag{4.82}$$

$$\frac{\dot{p}}{1-\zeta^d}\Phi^p = 0, \qquad \Phi^p \leq 0, \qquad \frac{\dot{p}}{1-\zeta^d} \geq 0 \tag{4.83}$$

to find the solution addressing multiple dissipation. In the Kuhn-Tucker conditions for the incipient kinking and plasticity mechanism, it may also be noted that by assuming ζ^d bounded such that $0 \leq \zeta^d \leq 1$ the term may be taken as positive and removed from the relation.

A final note with regard to this coupling. Specifically, the derivation of this model proceeded by considering each mechanism independently and reducing the dissipation to a single scalar thermodynamic force and internal state variable conjugate pair. The consideration of an effective configuration was then used with respect to the scalar thermodynamic driving force to relate the force/ISV pair in the effective and damaged configurations. Existing models, however, typically map each thermodynamic driving force (e.g. stress, backstresses, and rate of change of hardening) from the damaged to the effective configuration separately (*e.g*, [3, 228]). Such a formulation can better account for anisotropic damage and evolution that is not capture via the scalar relations used here. Nonetheless, the current formulation comes with a tremendous computational advantage by using such a formulation (one scalar configurational mapping rather than multiple scalar and tensorial mappings). As the current focus is on the mechanistic coupling rather than anisotropic effects, the use of such an assumption would seem justified. Furthermore, as the anisotropic effects are not being used in these yield functions, the isotropic reduction of the kinking model (Section 4.1.2.1) is used in the remainder of this work.

4.1.5 Consistency Relations

In the previous section, the constitutive equation, yield functions, and evolution equations of a MAX phase consisting of multiple coupled mechanisms was presented. To determine the response of the material through a loading path, however, methods to determine the increments of inelastic deformation are needed. Such a task may be accomplished by determining the increment of the controlling (consistency) parameter of the relevant mechanism ($d\zeta, d\zeta^d$, and dp) which are found via the consistency relations of the relevant yield surface. As a rate independent formulation is used, the time derivative is dropped in favor of the total derivate (*e.g*, $\dot{\zeta} = d\zeta$). Therefore, these relations are presented in this section. Specifically, in returning to the yield functions defined by Eqns. 4.78–4.80, it is noted that these relations define the admissible domain of the material state. The thermoelastic domain of the i-th mechanism ($i = r,\ d,\ p$) is defined by $\Phi^i < 0$ while inelastic states occur on the surface $\Phi^i = 0$. Therefore, even after the activation of any inelastic mechanism, the material must like on the surface thereby leading the consistency constraint $d\Phi^i = 0$ where the d is used to define the total derivative (for a complete discussion of the thermodynamics, please see Qidwai and Lagoudas [192] or the text of Lubliner [149]). Enforcement of this criteria may then be used to solve for the relevant consistency parameters.

Recalling Eqns. 4.78–4.80, the various yield functions may be considered as,

$$\Phi^r = \hat{\Phi}^r \left(\sigma_{ij}, \zeta, \beta^r_{ij}, \zeta^d\right), \tag{4.84}$$

$$\Phi^d = \hat{\Phi}^d \left(\sigma_{ij}, \zeta^d, \beta^d_{ij}\right), \tag{4.85}$$

$$\Phi^p = \hat{\Phi}^p \left(\sigma_{ij}, \zeta^d, \beta^p_{ij}, p\right), \tag{4.86}$$

which, when expanding via the chain rule leads to,

$$d\Phi^r = \frac{\partial \Phi^r}{\partial \sigma_{ij}} d\sigma_{ij} + \frac{\partial \Phi^r}{\partial \zeta} d\zeta + \frac{\partial \Phi^r}{\partial \zeta^d} d\zeta^d + \frac{\partial \Phi^r}{\partial \beta^r_{ij}} d\beta^r_{ij} = 0, \tag{4.87}$$

$$d\Phi^d = \frac{\partial \Phi^d}{\partial \sigma_{ij}} d\sigma_{ij} + \frac{\partial \Phi^d}{\partial \zeta^d} d\zeta^d + \frac{\partial \Phi^d}{\partial \beta^d} d\beta^d = 0, \tag{4.88}$$

$$d\Phi^p = \frac{\partial \Phi^p}{\partial \sigma_{ij}} d\sigma_{ij} + \frac{\partial \Phi^p}{\partial p} dp + \frac{\partial \Phi^p}{\partial \zeta^d} d\zeta^d + \frac{\partial \Phi^p}{\partial \beta^p_{ij}} d\beta^p_{ij} = 0. \tag{4.89}$$

The set of three scalar equations, Eqn. 4.87–4.89, need to be solved simultaneously for the scalar multipliers, $d\zeta$, $d\zeta^d$, and dp. Therefore, the remainder of the derivatives and increments need to be identified. First, by differentiating Eqn. 4.62 and using the postulated evolution equations, the increment of stress is written,

$$d\sigma_{ij} = L_{ijkl}\left(d\varepsilon_{kl} - \alpha_{kl} dT - \Lambda^r_{kl} d\zeta - \Lambda^p_{kl} dp - \left(\lambda^d + 1\right) \frac{\partial \psi}{\partial \zeta^d} M^0_{klmn} \sigma_{mn} d\zeta^d \right), \tag{4.90}$$

where $d\varepsilon_{kl}$ and dT are taken to be prescribed via the boundary value problem being solved. The increments $d\beta^r_{ij}$, $d\beta^d$, and $d\beta^p_{ij}$ are given by Eqns. 4.7, 4.41 and 4.50, respectively. Therefore, only the yield function derivatives are needed to determine the above relations. For the reversible, IKB mechanism these may be defined as,

$$\frac{\partial \Phi^r}{\partial \sigma_{ij}} = \pm \frac{1}{1-\zeta^d} \Lambda^r_{ij}, \tag{4.91}$$

$$\frac{\partial \Phi^r}{\partial \beta^r_{ij}} = \mp \frac{1}{1-\zeta^d} \frac{2}{3} \kappa^r \Lambda^r_{ij}, \tag{4.92}$$

$$\frac{\partial \Phi^r}{\partial \zeta^d} = \pm \frac{1}{\left(1-\zeta^d\right)^2} \pi^r, \tag{4.93}$$

$$\frac{\partial \Phi^r}{\partial \zeta} = \pm \frac{1}{1-\zeta^d} \begin{cases} B e^{-k\zeta} & d\zeta > 0 \\ B e^{-k(\zeta^{rev} - \zeta)} & d\zeta < 0 \end{cases}, \tag{4.94}$$

where "±" is used to distinguish between the grown (loading) and annihilation (unloading) portions of IKB formation. With respect to Eqns. 4.91 and 4.92, these

relations are arrived at by noting in scalar form the stress component of the yield function ($\mu^r_{ij}\Lambda^r_{ij}$) is $\gamma^r\mu^{r-VMeff}$. Therefore, by noting the well established relationship $\frac{\partial\sigma^{VM-eff}_{ij}}{\partial\sigma_{ij}} = \frac{3}{2}\frac{\sigma'_{ij}}{\sigma^{VMeff}}$ the expressions in Eqns. 4.91 and 4.92 are established. Regarding the kinking mechanism, the derivatives,

$$\frac{\partial\Phi^d}{\partial\sigma_{ij}} = 3\lambda^d\frac{\partial\psi}{\partial\zeta^d}M^0_{ijkl}\sigma_{kl}, \tag{4.95}$$

$$\frac{\partial\Phi^d}{\partial\zeta^d} = \frac{3}{2}\lambda^d\frac{\partial^2\psi}{\left(\partial\zeta^d\right)^2}\sigma_{ij}M^0_{ijkl}\sigma_{kl} - cqe^{-c\zeta^d}, \tag{4.96}$$

$$\frac{\partial\Phi^d}{\partial\beta^d} = -\frac{2}{3}\kappa^d\lambda^d, \tag{4.97}$$

are found. Finally, the derivatives of the plastic yield function are specified as,

$$\frac{\partial\Phi^p}{\partial\sigma_{ij}} = \frac{1}{1-\zeta^d}\Lambda^p_{ij}, \tag{4.98}$$

$$\frac{\partial\Phi^p}{\partial p} = -\frac{1}{1-\zeta^p}Lnp^{n-1}, \tag{4.99}$$

$$\frac{\partial\Phi^p}{\partial\zeta^d} = \frac{1}{\left(1-\zeta^d\right)^2}\pi^p, \tag{4.100}$$

$$\frac{\partial\Phi^p}{\partial\beta^p_{ij}} = -\frac{1}{1-\zeta^p}\frac{2}{3}\kappa^p\Lambda^p_{ij}. \tag{4.101}$$

where the arguments used in determining Eqns. 4.91 and 4.92 are again used for Eqns. 4.101 and 4.101

4.2 Numerical Implementation

In the previous section, a three-dimensional constitutive model for the MAX phase response was developed. The intent of such a model is to be used in solving for the response of various geometries (in this case, composite RVEs) in different boundary value problems. For such cases, the problem may be separated into two considerations. The first is the global boundary value problem incorporating the

different boundary conditions and geometric configurations. This scale is typically handled via the utilization of finite element based approaches. In such cases, the updated response of the material to applied loading increments must be solved at each material point (the local scale). With respect to the global problem, numerous software packages and implementations exist and have been extensively tested. The package Abaqus has been and will be used in this work. A numerical implementation of the MAX phase model capable of addressing the local problem, however, is not yet developed. Thus, in this section, approaches for the developed material model are presented. Specifically, the solution method for the updated material state is presented in Section 4.2.1 while tangent moduli needed for the implicit formulations of interest are given in Section 4.2.2.

4.2.1 Return Mapping Algorithm

In a displacement-driven finite element formulation (as is used by Abaqus), an approach for determining the material state subject to arbitrary strain and temperature increments is needed. Methods to this regard have been extensively developed for nonlinear materials (especially plasticity [47, 214, 216]) and are extensively leveraged in this case. The text of Simo and Hughes [216] provides numerous insightful discussions to this regard and the interested reader is referred there. Specifically, if the material state is known at loading increment n the objective of this model is to determine the corresponding $n+1$ state subject to loadings $d\varepsilon_{ij}^{n+1}$ and dT^{n+1}. The total strain increment, $d\varepsilon_{ij}^{n+1}$, and temperature increment dT^{n+1} are passed in from the global FE solver. In this case, although a temperature increment is being passed in it is a prescribed loading condition and not a solution variable. Therefore, only the mechanical field is being solved for.

To determine the updated material state, an *elastic-predictor inelastic-corrector* scheme is utilized [216]. In such a case, it is initially assumed that the loading increments correspond to an elastic loading such that,

$$^{trial}d\sigma_{ij}^{n+1} = L_{ijkl}\left(d\varepsilon_{kl}^{n+1} - \alpha_{kl}dT^{n+1}\right) \tag{4.102}$$

and the inelastic variables are unchanged from the previous increment (*e.g*, $^{trial}\zeta^{n+1} = \zeta^{n}$, $^{trial}\varepsilon_{ij}^{r-n+1} = d\varepsilon_{ij}^{r-n}$ etc.). The $n+1$ stress tensor is written as,

$$\sigma_{ij}^{n+1} = \sigma_{ij}^{n} + d\sigma_{ij}^{n+1}, \tag{4.103}$$

and the current trial stress corresponds to the one in which the trial increment (Eqn. 4.102) is used. With these trial values established, the various yield-like functions may be checked for inelastic deformations,

$$^{trial}\Phi^{r-n+1} = \hat{\Phi}^{r}\left(^{trial}\sigma_{ij}^{n+1}, ^{trial}\zeta^{n+1}, ^{trial}\zeta^{d-n+1}, ^{trial}\beta_{ij}^{r-n+1}\right), \tag{4.104}$$

$$^{trial}\Phi^{d-n+1} = \hat{\Phi}^{d}\left(^{trial}\sigma_{ij}^{n+1}, ^{trial}\zeta^{d-n+1}, ^{trial}\beta^{d-n+1}\right), \tag{4.105}$$

$$^{trial}\Phi^{p-n+1} = \hat{\Phi}^{p}\left(^{trial}\sigma_{ij}^{n+1}, ^{trial}\zeta^{d-n+1}, ^{trial}\beta_{ij}^{p-n+1}, ^{trial}p^{n+1}\right). \tag{4.106}$$

If all the trial yield functions satisfy the thermoelastic constraints that $^{trial}\Phi^{i-n+1} \leq 0$ where $i = r,\ d,\ p$ then the trial solutions are accepted as the correct ones ($d\sigma_{ij}^{n+1} = ^{trial} d\sigma_{ij}^{n+1}$ etc.) and the new material state is returned to the global solver. On the other hand, if any of the three yield functions are greater than zero an inelastic response is predicted and the material state must be corrected. Before proceeding, it is important to note that there are seven possible inelastic cases: (*i*) just IKB (*ii*) just KB (*iii*) just plasticity (*iv*) IKB-KB (*v*) IKB-plasticity (*vi*) KB-plasticity (*vii*) IKB-KB-

plasticity. Although some of these cases are not expected to physically occur (just damage or damage-plasticity), routines to handle all seven cases must be introduced. Many of these cases may be determined as reductions of the others.

The multisurface cases also necessitate an additional consideration. Specifically, multiple positive yield surfaces indicating inelastic deformation does not mean that multiple inelastic mechanisms are active [216]. To explain this, Fig. 52 is used as an illustrative example. Specifically, two yield surfaces (generically, Φ^1 and Φ^2) are represented in Fig. 52. At state n, it is evident that σ_{ij}^n lies on the surface Φ^{1-n} and inside the domain $\Phi^{2-n} \leq 0$. After an elastic solution, the trial solution ${}^{trial}\sigma_{ij}^{n+1}$ lies outside both of these surfaces, ${}^{trial}\Phi^{1-n+1} > 0$, ${}^{trial}\Phi^{2-n+1}$. Upon correction, however, it is noted that σ_{ij}^{n+1} lies on the surface $\Phi^{1-n+1} = 0$ and remains inside the domain $\Phi^{2-n+1} \leq 0$. Thus, although the trial yield functions indicate two active mechanisms, it can be observed that this does not necessarily mean both inelastic mechanisms are operative. Therefore, additional checks are needed in the correction routines to ensure physically meaningful increments are determined. Specifically, in the case presented in Fig. 52, Φ^2 would have to contract to achieve the converged solution therefore needing negative increments in the internal state variables – a physically inadmissable solution. Such cases are used as checks in the developed algorithm and if violated they are used to correct the operative mechanisms evaluated in the correction routine. Additionally, this illustration may be used to conceptually introduce one other concept – solutions methodologies for multiple surface cases should be solved simultaneously. Concurrent or sequential simulations can overcorrect with one mechanism making it difficult to satisfy both conditions simultaneously.

To perform the inelastic correction, *Return Mapping Algorithms* (RMAs) are used in which the single surface case is presented in Fig. 53. These algorithms perform a series of inelastic correction iterations to return from the initial trial solution

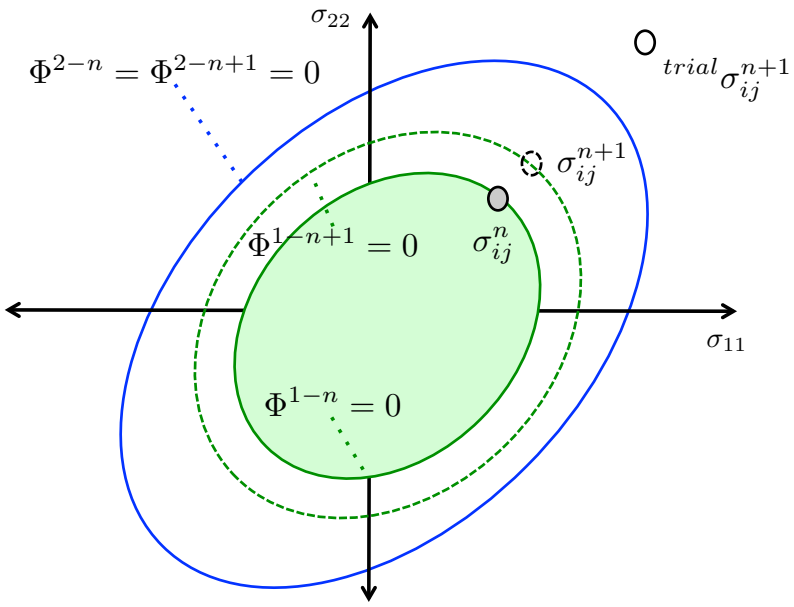

Figure 52: Schematic of a case in which the elastic trial solution results in the indication of multiple inelastic activations even though only one really is.

to the correct $n+1$ yield surface. The theory and implementation of these algorithms is extensively treated in the text of Simo and Hughes [216] with an emphasis on plastic constitutive laws while Qidwai and Lagoudas [191] discussed their application to shape memory alloys. These efforts are used to motivate and inform the construction of the routines used in this effort. First, with respect to terminology, "increment" will be used to denote sequential loading steps related to the global boundary value problem. "Iteration" refers to inelastic steps performed as a part of the correction routine. With respect to variable nomenclature, a general form of ${}^{k}x^{n+1}$ will be used for the k^{th} correction iteration of the $n+1^{th}$ loading increment of variable x. In this fashion, the trial solution corresponds to $k = 0$ and will be referred to as such in the following.

A number of different RMAs are found through the literature and the reader

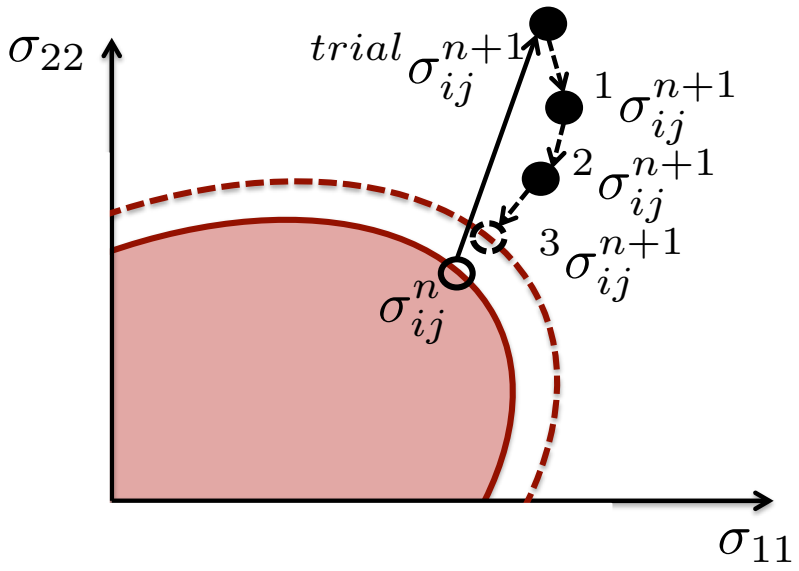

Figure 53: Schematic illustration of the general return matting algorithm inelastic iteration correction scheme.

is referred to the work of Simo and Hughes [216] for many of these. Two of the more common approaches utilized are the *closest point projection* and *convex cutting plane*. In distinguishing the two approaches, the former method is implicit and enforces normality on the final $(k+1)$ iteration. The latter is an explicit method in which normality is enforced on the initial (k) iteration [216]. In comparing the two cases, a key difference is the need to calculate the gradient of the inelastic direction tensor in the closest point approach that is not needed in the convex cutting plane method. This results in the closest point approach being computationally more intensive than the convex cutting plane. Furthermore, the closest point is capable of determining an algorithmic tangent modulus while the convex cutting point utilizes a continuum tangent modulus. This difference will be discussed in more detail in Section 4.2.2, but it is important to point out that the algorithmic modulus is more expensive than the continuum approach. Both methods have been investigated for

the case of SMAs by Qidwai and Lagoudas [191] who noted a preference for the convex cutting plane approach due to much improved computational speed. As part of this conclusion, however, the authors noted that the convex cutting plane may present an instability under reverse transformation. Additionally, the simulations are dominated by local constitutive stress evaluations rather than global boundary value problems so the impact of the difference in tangent modulus may not be of great consequence in the studied cases. Subsequent efforts regarding SMAs [95,96,100,124] have extensively utilized the convex cutting plane approach to analyze a variety of SMA structures. In this study, although both methods have been implemented, the closest point projection is utilized. This selection is motivated by the more complex global boundary value problems the composite RVEs of interest represent versus those studied by Qidwai and Lagoudas [191]. In this case, the more complex tangent moduli and the corresponding robustness can aid in the global convergence properties and initial simulations demonstrated improvement in this regard. Therefore, although more expensive, the improved robustness is of more interest in this study and the closest point projection is utilized.

In the following sections, although there are seven distinct cases, a subset of the algorithms are presented to demonstrate the development and various considerations. Section 4.2.1.1 first introduces the use of the closest point projection for the single mechanism IKB case. The extension to all three mechanisms is presented in Section 4.2.1.2 which case will also be referred to as "Multiple Coupled Mechanisms" and denoted by MCM for short. The remaining cases all represent simplifications from the fully coupled case.

4.2.1.1 IKB Formation

First, to introduce the usage of the RMA scheme closest point projection method, the single-mechanisms reversible, IKB is presented and discussed. As mentioned before, it is assumed that all state variables at state "n" are known and the loading increment is applied in the form of $d\varepsilon_{ij}^{n+1}$ and dT^{n+1}. Furthermore, given the multiple mechanisms, it is taken that ${}^0\Phi^r > 0$ while ${}^0\Phi^d \leq 0$, ${}^0\Phi^p \leq 0$ such that only the IKB-related mechanisms is active. As such, all state variables related to those mechanisms (denoted by a superscript p or d) are taken to be unchanged from the n state (*e.g*, $d\varepsilon_{ij}^{p-n+1} = d\varepsilon_{ij}^{p-n}$ etc.). Therefore, the numerical approach needs to determine: σ_{ij}^{n+1}, ε_{ij}^{n+1}, ε_{ij}^{r-n+1}, ζ^{n+1}, β_{ij}^{r-n+1}, and T^{n+1}. Trivially, given the known loading increments, $\varepsilon_{ij}^{n+1} = \varepsilon_{ij}^{n} + d\varepsilon_{ij}^{n+1}$ and $T^{n+1} = T^n + dT^{n+1}$. The remaining 19 solution variables may be defined as,

$$\sigma_{ij}^{n+1} = \sigma_{ij}^{n} + d\sigma_{ij}^{n+1}, \tag{4.107}$$

$$\varepsilon_{ij}^{r-n+1} = \varepsilon_{ij}^{r-n} + d\varepsilon_{ij}^{r-n+1} = \varepsilon_{ij}^{r-n} + \Lambda_{ij}^{r-n+1} d\zeta^{n+1}, \tag{4.108}$$

$$\beta_{ij}^{r-n+1} = \beta_{ij}^{r-n} + d\beta_{ij}^{r-n+1} = \beta_{ij}^{r-n} + \Lambda_{ij}^{r-n+1} d\zeta^{n+1}, \tag{4.109}$$

$$\zeta^{n+1} = \zeta^{n} + d\zeta^{n+1}, \tag{4.110}$$

in which the evolution equations have been applied. To solve these equations, it is first noted that at any correction iteration k the incremental constitutive law may be written as,

$${}^k d\sigma_{ij}^{n+1} = L_{ijmn} \left(d\varepsilon_{mn}^{n+1} - \alpha_{mn} dT^{n+1} - {}^k d\varepsilon_{mn}^{r-n+1} \right), \tag{4.111}$$

and note the the converged yield function at the $n+1$ converged must still be satisfied, ${}^{k}\Phi^{r-n+1} = \hat{\Phi}^{r}\left({}^{k}\sigma_{ij}^{n+1}, {}^{k}\beta_{ij}^{r-n+1}, {}^{k}\zeta^{n+1}, \zeta^{d-n+1}\right) = 0$. Furthermore, given the implicit nature of the closest point projection routine, residuals of the form,

$$ {}^{k}R_{ij}^{\varepsilon^{r}-n+1} = -{}^{k}\varepsilon_{ij}^{r-n+1} + \varepsilon_{ij}^{r-n} + {}^{k}\Lambda_{ij}^{r-n+1} d\zeta^{n+1}, \tag{4.112} $$

$$ {}^{k}R_{ij}^{\beta^{r}-n+1} = -{}^{k}\beta_{ij}^{r-n+1} + \beta_{ij}^{r-n} + {}^{k}\Lambda_{ij}^{r-n+1} d\zeta^{n+1}, \tag{4.113} $$

are defined where ${}^{k}\Lambda^{r-n+1}$ is used to denote the dependence of the tensor on the incremented state variables (${}^{k}\Lambda_{ij}^{r-n+1} = \hat{\Lambda}_{ij}^{r}\left({}^{k}\sigma_{ij}^{n+1}, {}^{k}\beta_{ij}^{r-n+1}\right)$). The 12 residual, 6 constitutive, and 1 yield equations form a set of 19 equations that can be solved for the updated material state. To accomplish this fact, each equation is linearized via the Newton-Rhapson iteration method as described by Simo and Hughes [216] and by noting that the residuals and yield function at the $n+1$ state should be zero. Additionally, over an inelastic correction increment, it is noted the variables at the n^{th} state and the applied loading increments do not change. Such a process results in the following system of equations,

$$ {}^{k}\Delta\sigma_{ij}^{n+1} = -L_{ijmn}\ {}^{k}\Delta\varepsilon_{mn}^{r-n+1}, \tag{4.114} $$

$$ 0 = {}^{k}\ \Phi^{r-n+1} + \frac{\partial\Phi^{r}}{\partial\sigma_{ij}}\ {}^{k}\Delta\sigma_{ij}^{n+1} + \frac{\partial\Phi^{r}}{\partial\zeta}\ {}^{k}\Delta\zeta^{n+1} + \frac{\partial\Phi^{r}}{\partial\beta_{ij}^{r}}\ {}^{k}\Delta\beta_{ij}^{r-n+1}, \tag{4.115} $$

$$ 0 = {}^{k}\ R_{ij}^{\varepsilon^{r}-n+1} - {}^{k}\ \Delta\varepsilon_{ij}^{r-n+1} + {}^{k}\ \Delta\Lambda_{ij}^{r-n+1} d\zeta^{n+1} + {}^{k}\ \Lambda_{ij}^{r-n+1}\ {}^{k}\Delta\zeta^{n+1}, \tag{4.116} $$

$$ 0 = {}^{k}\ R_{ij}^{\beta^{r}-n+1} - {}^{k}\ \Delta\beta_{ij}^{r-n+1} + {}^{k}\ \Delta\Lambda_{ij}^{r-n+1} d\zeta^{n+1} + {}^{k}\ \Lambda_{ij}^{r-n+1}\ {}^{k}\Delta\zeta^{n+1}, \tag{4.117} $$

where Δ denotes the change over an inelastic increment – ${}^{k}\Delta x = {}^{k+1}\ x - {}^{k}\ x$.

First, as all of the variables in Eqns. 4.115–4.117 correspond to the k^{th} iteration of the $n+1^{th}$ increment, those superscripts will be neglected in the remainder of this section. Secondly, in Eqns. 4.116 and 4.117 it is noted that the change in the direction

tensor, $\Delta\Lambda^r_{ij}$ is introduced. In the case of IKB growth ($d\zeta > 0$), the direction tensor is defined by the effective stress and this increment may be written as,

$$\Delta\Lambda^r_{ij} = \frac{\partial\Lambda^r_{ij}}{\partial\sigma_{mn}}\Delta\sigma_{mn} + \frac{\partial\Lambda^r_{ij}}{\partial\beta^r_{mn}}\Delta\beta^r_{mn} = A^\sigma_{ijmn}\Delta\sigma_{mn} + A^\beta_{ijmn}\Delta\beta^r_{mn}, \tag{4.118}$$

in which A^σ_{ijmn} and A^β_{ijmn} are introduced for convenience. These two tensors are the direction gradients which distinguish the closest point projection method from the convex cutting plane and represent an additional cost to evaluate. Following the approach of Simo and Hughes [216] and Qidwai and Lagoudas [191], these tensors may be written as,

$$A^\sigma_{ijmn} = \frac{3}{2}\gamma^r \frac{1}{\mu^{r-VMeff}}\left(I_{ijmn} - \frac{1}{3}\delta_{ij}\delta_{mn} - \frac{1}{\left(\mu^{r-VMeff}\right)^2}\mu^{r'}_{ij}\mu^{r'}_{mn}\right), \tag{4.119}$$

$$A^\beta_{ijmn} = -\gamma^r\kappa^r \frac{1}{\mu^{r-VMeff}}\left(I_{ijmn} - \frac{1}{\left(\mu^{r-VMeff}\right)^2}\mu^{r'}_{ij}\mu^{r'}_{mn}\right). \tag{4.120}$$

The differences in the two terms arise from (i) the kinematic hardening modulus $\frac{2}{3}\kappa^r$ and (ii) β^r_{ij} is a deviatoric tensor (by construction) while σ_{ij} is not. Furthermore, during IKB contraction both of these tensors are null.

The directionality of IKB growth versus contraction is captured via the form of the direction tensor Λ^r_{ij} and the partial derivatives of the yield function. These derivatives may be found in Eqns. 4.91–4.94. With these terms defined, Eqns. 4.116–4.117 can be rewritten as a set of 13 equations for the correction increments as,

$$\begin{bmatrix} \frac{\partial\Phi^r}{\partial\zeta} & \frac{\partial\Phi^r}{\partial\sigma_{mn}} & \frac{\partial\Phi^r}{\beta^r_{mn}} \\ \Lambda^r_{ij} & M_{ijmn} + d\zeta A^\sigma_{ijmn} & d\zeta A^\beta_{ijmn} \\ \Lambda^r_{ij} & d\zeta A^\sigma_{ijmn} & -I_{ijmn} + d\zeta A^\beta_{ijmn} \end{bmatrix} \begin{Bmatrix} \Delta\zeta \\ \Delta\sigma_{mn} \\ \Delta\beta^r_{mn} \end{Bmatrix} = \begin{Bmatrix} -\Phi^r \\ -R^{\varepsilon^r}_{ij} \\ -R^{\beta^r}_{ij} \end{Bmatrix}, \tag{4.121}$$

in which $\Delta\varepsilon_{ij}^{r} = -M_{ijmn}\Delta\sigma_{mn}$ is used to eliminate six equations. This procedure is used to iteratively correct the solution until convergence (in terms of residual magnitude and yield function) is achieved.

4.2.1.2 Multiple Coupled Mechanisms

The previous section only considered the solution of a single mechanism. In this section, the case of the solution with all three mechanisms is treated. As with before, it is assumed that all of the state variables at state "n" are known and increments $d\varepsilon_{ij}^{n+1}$ and dT^{n+1} are applied and the corresponding material state at "$n+1$" needs to be determined. Additionally, the trial solution of the three yield functions are all assumed to lie outside the thermoelastic domain – ${}^{0}\Phi^{r} > 0$, ${}^{0}\Phi^{d} > 0$ and ${}^{0}\Phi^{p} > 0$. Furthermore, for this case, it is taken that the loading criteria for all three mechanisms are satisfied and they are active. Therefore, beyond the trivial case of ε_{ij}^{n+1} and T^{n+1}, the solution scheme to be presented needs to find the following 40 unknowns: σ_{ij}^{n+1}, ε_{ij}^{r-n+1}, ζ^{n+1}, β_{ij}^{r-n+1}, ε_{ij}^{d-n+1}, ζ^{d-n+1}, β^{d-n+1}, $\varepsilon_{ij}^{p-n+1}, p^{n+1}$, and

β_{ij}^{p-n+1}. The incrementation of these terms are written as,

$$\sigma_{ij}^{n+1} = \sigma_{ij}^{n} + d\sigma_{ij}^{n+1}, \tag{4.122}$$

$$\varepsilon_{ij}^{r-n+1} = \varepsilon_{ij}^{r-n} + d\varepsilon_{ij}^{r-n+1} = \varepsilon_{ij}^{r-n} + \Lambda_{ij}^{r-n+1} d\zeta^{n+1} - \Lambda_{ij}^{rg-n+1} d\zeta^{d-n+1}, \tag{4.123}$$

$$\beta_{ij}^{r-n+1} = \beta_{ij}^{r-n} + d\beta_{ij}^{r-n+1} = \beta_{ij}^{r-n} + \Lambda_{ij}^{r-n+1} d\zeta^{n+1}, \tag{4.124}$$

$$\zeta^{n+1} = \zeta^{n} + d\zeta^{n+1}, \tag{4.125}$$

$$\begin{aligned} \varepsilon_{ij}^{d-n+1} &= \varepsilon_{ij}^{d-n} + d\varepsilon_{ij}^{d-n+1} \\ &= \varepsilon_{ij}^{d-n} + \left(\Lambda_{ij}^{rg-n+1} + \lambda^{d} \frac{\partial \psi}{\partial \zeta^{d}} M_{ijmn} \sigma_{mn} \right) d\zeta^{d-n+1}, \end{aligned} \tag{4.126}$$

$$\zeta^{d-n+1} = \zeta^{d-n} + d\zeta^{d-n+1}, \tag{4.127}$$

$$\beta^{d-n+1} = \beta^{d-n} + d\beta^{d-n+1} = \beta^{d-n} + \lambda^{d} d\zeta^{d-n+1}, \tag{4.128}$$

$$\varepsilon_{ij}^{p-n+1} = \varepsilon_{ij}^{p-n} + d\varepsilon_{ij}^{p-n+1} = \varepsilon_{ij}^{p-n} + \Lambda_{ij}^{p-n+1} dp^{n+1}, \tag{4.129}$$

$$p^{n+1} = p^{n} + dp^{n}, \tag{4.130}$$

$$\beta_{ij}^{p-n+1} = \beta_{ij}^{p-n} + d\beta_{ij}^{p-n+1} = \beta_{ij}^{p-n} + \Lambda_{ij}^{p-n+1} dp^{n+1}. \tag{4.131}$$

Additionally, with all three mechanisms active, the incremental constitutive equation may be written as:

$$\begin{aligned} d\varepsilon_{ij}^{n+1} = {}^{k}\left(\frac{\partial \psi}{\partial \zeta^{d}} \right) M_{ijmn}^{0} \, {}^{k}\sigma_{mn}^{n+1} d\zeta^{d-n+1} + M_{ijmn} \, {}^{k}d\sigma_{mn} + \alpha_{ij} dT^{n+1} + {}^{k} d\varepsilon_{ij}^{r-n+1} \\ + {}^{k}d\varepsilon_{ij}^{d-n+1} + {}^{k} d\varepsilon_{ij}^{p-n+1}. \end{aligned} \tag{4.132}$$

It is recalled that $\psi = \hat{\psi}\left(\zeta^d\right)$ and $M_{ijkl} = \hat{M}_{ijkl}\left(\zeta^d\right)$ and the three coupled constitutive equations may be denoted,

$$ {}^k\Phi^{r-n+1} = \hat{\Phi}^r\left({}^k\sigma_{ij}^{n+1}, {}^k\,\beta_{ij}^{r-n+1}, {}^k\,\zeta^{n+1}, {}^k\,\zeta^{d-n+1}\right), \tag{4.133} $$

$$ {}^k\Phi^{d-n+1} = \hat{\Phi}^d\left({}^k\sigma_{ij}^{n+1}, {}^k\,\beta^{d-n+1}, {}^k\,\zeta^{d-n+1}\right), \tag{4.134} $$

$$ {}^k\Phi^{p-n+1} = \hat{\Phi}^p\left({}^k\sigma_{ij}^{n+1}, {}^k\,\zeta^{d-n+1}, {}^k\,\beta_{ij}^{p-n+1}, {}^k\,p^{n+1}\right). \tag{4.135} $$

Residuals for the inelastic strain and kinematic hardening variables may then be formed and defined such that,

$$ {}^kR_{ij}^{\varepsilon^r-n+1} = -{}^k\varepsilon_{ij}^{r-n+1} + \varepsilon_{ij}^{r-n} + {}^k\,\Lambda_{ij}^{r-n+1}d\zeta^{n+1} - {}^k\,\Lambda_{ij}^{rg-n+1}d\zeta^{d-n+1}, \tag{4.136} $$

$$ {}^kR_{ij}^{\beta^r-n+1} = -{}^k\beta_{ij}^{r-n+1} + \beta_{ij}^{r-n} + {}^k\,\Lambda_{ij}^{r-n+1}d\zeta^{n+1}, \tag{4.137} $$

$$ {}^kR_{ij}^{\varepsilon^p-n+1} = -{}^k\varepsilon_{ij}^{p-n+1} + \varepsilon_{ij}^{p-n} + {}^k\,\Lambda_{ij}^{p-n+1}dp^{n+1}, \tag{4.138} $$

$$ {}^kR_{ij}^{\beta^p-n+1} = -{}^k\beta_{ij}^{p-n+1} + \beta_{ij}^{p-n} + {}^k\,\Lambda_{ij}^{p-n+1}dp^{n+1}, \tag{4.139} $$

$$ {}^kR_{ij}^{\varepsilon^d-n+1} = -{}^k\varepsilon_{ij}^{d-n+1} + \varepsilon_{ij}^{d-n} + \left({}^k\Lambda_{ij}^{rg-n+1} + \lambda^d\ {}^k\frac{\partial\psi}{\partial\zeta^d}M_{ijmn}^0\ {}^k\sigma_{mn}^{n+1}\right)d\zeta^{d-n+1}, \tag{4.140} $$

$$ {}^kR^{\beta^d-n+1} = -{}^k\beta^{d-n+1} + \beta^{d-n} + \lambda^d d\zeta^{d-n+1}. \tag{4.141} $$

Following the same linearization procedure used in the IKB case (and past works [191, 216]) results in the following set of equations:

$$
\begin{aligned}
0 = & \left[{}^k\psi + {}^k\left(\frac{\partial \psi}{\partial \zeta^d}\right) d\zeta^{d-n+1} \right] M^0_{ijmn}\ {}^k\Delta\sigma^{n+1}_{mn} + \\
& \left\{ \left[{}^k\left(\frac{\partial^2 \psi}{\left(\partial \zeta^d\right)^2}\right) d\zeta^{d-n+1} + {}^k\left(\frac{\partial \psi}{\partial \zeta^d}\right) \right] M^0_{ijmn}\ {}^k\sigma^{n+1}_{mn} \right. \\
& \left. + {}^k\left(\frac{\partial \psi}{\partial \zeta^d}\right) M^0_{ijmn} d\sigma^{n+1}_{mn} \right\}\ {}^k\Delta\zeta^{d-n+1} \\
& + {}^k\Delta\varepsilon^{r-n+1}_{ij} + {}^k\Delta\varepsilon^{d-n+1}_{ij} + {}^k\Delta\varepsilon^{p-n+1}_{ij}, \qquad (4.142)
\end{aligned}
$$

$$
\begin{aligned}
0 = & {}^k\Phi^{r-n+1} + \frac{\partial \Phi^r}{\partial \sigma_{ij}}\ {}^k\Delta\sigma^{n+1}_{ij} + \frac{\partial \Phi^r}{\partial \zeta^d}\ {}^k\Delta\zeta^{d-n+1} + \\
& \frac{\partial \Phi^r}{\partial \zeta}\ {}^k\Delta\zeta^{n+1} + \frac{\partial \Phi^r}{\partial \beta^r_{ij}}\ {}^k\Delta\beta^{r-n+1}_{ij}, \qquad (4.143)
\end{aligned}
$$

$$
\begin{aligned}
0 = & {}^k\Phi^{d-n+1} + \frac{\partial \Phi^d}{\partial \sigma_{ij}}\ {}^k\Delta\sigma^{n+1}_{ij} + \frac{\partial \Phi^d}{\partial \zeta^d}\ {}^k\Delta\zeta^{d-n+1} + \\
& \frac{\partial \Phi^d}{\partial \beta^d}\ {}^k\Delta\beta^{d-n+1}, \qquad (4.144)
\end{aligned}
$$

$$
\begin{aligned}
0 = & {}^k\Phi^{p-n+1} + \frac{\partial \Phi^p}{\partial \sigma_{ij}}\ {}^k\Delta\sigma^{n+1}_{ij} + \frac{\partial \Phi^p}{\partial \zeta^d}\ {}^k\Delta\zeta^{d-n+1} + \\
& \frac{\partial \Phi^p}{\partial p}\ {}^k\Delta p^{n+1} + \frac{\partial \Phi^p}{\partial \beta^p_{ij}}\ {}^k\Delta\beta^{p-n+1}_{ij}, \qquad (4.145)
\end{aligned}
$$

$$
\begin{aligned}
0 = & {}^kR^{\varepsilon^r-n+1}_{ij} - {}^k\Delta\varepsilon^{r-n+1}_{ij} + {}^k\Delta\Lambda^{r-n+1}_{ij} d\zeta^{n+1} + {}^k\Lambda^{r-n+1}_{ij}\ {}^k\Delta\zeta^{n+1} \\
& - {}^k\Delta\Lambda^{rg-n+1}_{ij} d\zeta^{d-n+1} - {}^k\Lambda^{rg-n+1}_{ij}\ {}^k\Delta\zeta^{d-n+1}, \qquad (4.146)
\end{aligned}
$$

$$
0 = {}^kR^{\beta^r-n+1}_{ij} - {}^k\Delta\beta^{r-n+1}_{ij} + {}^k\Delta\Lambda^{r-n+1}_{ij} d\zeta^{n+1} + {}^k\Lambda^{r-n+1}_{ij}\ {}^k\Delta\zeta^{n+1}, \qquad (4.147)
$$

$$
0 = {}^kR^{\varepsilon^p-n+1}_{ij} - {}^k\Delta\varepsilon^{p-n+1}_{ij} + {}^k\Delta\Lambda^{p-n+1}_{ij} dp^{n+1} + {}^k\Lambda^{p-n+1}_{ij}\ {}^k\Delta p^{n+1}, \qquad (4.148)
$$

$$
0 = {}^kR^{\beta^p-n+1}_{ij} - {}^k\Delta\beta^{p-n+1}_{ij} + {}^k\Delta\Lambda^{p-n+1}_{ij} dp^{n+1} + {}^k\Lambda^{p-n+1}_{ij}\ {}^k\Delta p^{n+1}, \qquad (4.149)
$$

$$
\begin{aligned}
0 = & {}^kR^{\varepsilon^d-n+1}_{ij} - {}^k\Delta\varepsilon^{d-n+1}_{ij} + d\zeta^{d-n+1}\ {}^k\Delta\Lambda^{rg-n+1}_{ij} + \\
& d\zeta^{d-n+1}\lambda^d\ {}^k\left(\frac{\partial \psi}{\partial \zeta^d}\right) M^0_{ijmn}\ {}^k\Delta\sigma^{n+1}_{mn} + \\
& \left\{ \left[\lambda^d d\zeta^{d-n+1}\ {}^k\left(\frac{\partial^2 \psi}{\left(\partial \zeta^d\right)^2}\right) + \lambda^d\ {}^k\left(\frac{\partial \psi}{\partial \zeta^d}\right) \right] M^0_{ijmn}\ {}^k\sigma^{n+1}_{mn} \right. \\
& \left. + {}^k\Lambda^{rg-n+1}_{ij} \right\}\ {}^k\Delta\zeta^{d-n+1}, \qquad (4.150)
\end{aligned}
$$

$$
0 = {}^kR^{\beta^d} - {}^k\Delta\beta^{d-n+1} + \lambda^d\ {}^k\Delta\zeta^{d-k}. \qquad (4.151)
$$

In the same fashion as with the single mechanism case, as all of the terms are defined on the k^{th} iteration and the $(n+1)^{th}$ incrementation, those superscripts will be assumed and not presented for clarity in the remaining part of the section. The change in the normal direction of the IKB mechanism, $\Delta\Lambda^r_{ij}$ is defined in Eqn. 4.118. For the other cases,

$$\Delta\Lambda^p_{ij} = \frac{\partial\Lambda^p_{ij}}{\partial\sigma_{mn}}\Delta\sigma_{mn} + \frac{\partial\Lambda^p_{ij}}{\partial\beta^p_{mn}}\Delta\beta^p_{mn} = B^{\sigma}_{ijmn}\Delta\sigma_{mn} + B^{\beta}_{ijmn}\Delta\beta^r_{mn}, \tag{4.152}$$

$$\Delta\Lambda^{rg}_{ij} = \frac{\partial\Lambda^{rg}_{ij}}{\partial\sigma_{mn}}\Delta\sigma_{mn} + \frac{\partial\Lambda^{rg}_{ij}}{\partial\beta^r_{mn}}\Delta\beta^r_{mn} = C^{\sigma}_{ijmn}\Delta\sigma_{mn} + C^{\beta}_{ijmn}\Delta\beta^r_{mn}. \tag{4.153}$$

where,

$$B^{\sigma}_{ijmn} = \frac{3}{2}\gamma^p\frac{1}{\mu^{p-VMeff}}\left(I_{ijmn} - \frac{1}{3}\delta_{ij}\delta_{mn} - \frac{1}{\left(\mu^{p-VMeff}\right)^2}\mu^{p'}_{ij}\mu^{p'}_{mn}\right), \tag{4.154}$$

$$B^{\beta}_{ijmn} = -\gamma^p\kappa^p\frac{1}{\mu^{p-VMeff}}\left(I_{ijmn} - \frac{1}{\left(\mu^{p-VMeff}\right)^2}\mu^{p'}_{ij}\mu^{p'}_{mn}\right). \tag{4.155}$$

and $C^{\sigma}_{ijkl} = A^{\sigma}_{ijkl}$ and $C^{\beta}_{ijkl} = A^{\beta}_{ijkl}$ evaluated during the IKB growth (loading) regime. During most loadings, these tensors should be the same. Nonetheless, they are treated separately for such cases. The various derivatives are as defined in Section 4.1.5. These equations may then be rearranged in terms of the 40 incrementation variables as,

$$\begin{bmatrix}
1 & 0 & \lambda^d & 0 & 0 & 0 & 0 & 0 & 0 & 0 \\
0 & \frac{\partial\Phi^r}{\partial\zeta} & \frac{\partial\Phi^r}{\partial\zeta^d} & \frac{\partial\Phi^r}{\partial\beta^r_{ij}} & 0 & 0 & \frac{\partial\Phi^r}{\partial\sigma_{ij}} & 0 & 0 & 0 \\
\frac{\partial\Phi^d}{\partial\beta^d} & 0 & \frac{\partial\Phi^d}{\partial\zeta^d} & 0 & 0 & 0 & \frac{\partial\zeta^d}{\partial\sigma_{ij}} & 0 & 0 & 0 \\
0 & \Lambda^r_{ij} & 0 & C^3_{ijmn} & 0 & 0 & C^9_{ijmn} & 0 & 0 & 0 \\
0 & \Lambda^r_{ij} & -\Lambda^{rg}_{ij} & C^4_{ijmn} & -I_{ijmn} & 0 & C^5_{ijmn} & 0 & 0 & 0 \\
0 & 0 & C^7_{ij} & d\zeta^d C^\beta_{ijmn} & 0 & -I_{ijmn} & C^6_{ijmn} & 0 & 0 & 0 \\
0 & 0 & C^1_{ij} & 0 & I_{ijmn} & I_{ijmn} & C^2_{ijmn} & I_{ijmn} & 0 & 0 \\
0 & 0 & 0 & 0 & 0 & 0 & dpB^\sigma_{ijmn} & -I_{ijmn} & \Lambda^p_{ij} & dpB^\beta_{ijmn} \\
0 & 0 & \frac{\partial\Phi^p}{\partial\zeta^d} & 0 & 0 & 0 & \Lambda^p_{ij} & 0 & \frac{\partial\Phi^p}{\partial p} & \frac{\partial\Phi^p}{\partial\beta^p_{ij}} \\
0 & 0 & 0 & 0 & 0 & 0 & dpB^\beta_{ijmn} & 0 & \Lambda^p_{ij} & C^8_{ijkl}
\end{bmatrix}
\begin{Bmatrix}
\Delta\beta^d \\ \Delta\zeta \\ \Delta\zeta^d \\ \Delta\beta^r_{mn} \\ \Delta\varepsilon^r_{mn} \\ \Delta\varepsilon^d_{mn} \\ \Delta\sigma_{mn} \\ \Delta\varepsilon^p_{ij} \\ \Delta p \\ \Delta\beta^p_{ij}
\end{Bmatrix} =
\begin{Bmatrix}
-R^{\beta d} \\ -\Phi^r \\ -\Phi^d \\ -R^{\beta r}_{mn} \\ -R^{\varepsilon r}_{ij} \\ -R^{\varepsilon d}_{ij} \\ 0 \\ -R^{\varepsilon r}_{ij} \\ -\Phi^p \\ -R^{\beta p}_{ij}
\end{Bmatrix}, \tag{4.156}$$

where

$$\begin{aligned}
C^1_{ij} &= \left(\frac{\partial^2\psi}{\left(\partial\zeta^d\right)^2}d\zeta^d + \frac{\partial\psi}{\partial\zeta^d}\right)M^0_{ijmn}\sigma_{mn} + \frac{\partial\psi}{\partial\zeta^d}M^0_{ijmn}d\sigma_{mn}, \qquad C^2_{ijmn} = \left(\psi + \frac{\partial\psi}{\partial\zeta^d}\right)M^0_{ijmn}, \\
C^3_{ijmn} &= -I_{ijmn} + d\zeta A^\beta_{ijmn}, \qquad C^4_{ijmn} = d\zeta A^\beta_{ijmn} - d\zeta^d C^\sigma_{ijmn}, \qquad C^5_{ijmn} = d\zeta A^\sigma_{ijmn} - d\zeta^d C^\sigma_{ijmn}, \\
C^6_{ijmn} &= d\zeta^d\left(C^\sigma_{ijmn} + \lambda^d\frac{\partial\psi}{\partial\zeta^d}M^0_{ijmn}\right), \qquad C^7_{ij} = \lambda^d\left(d\zeta^d\frac{\partial^2\psi}{\left(\partial\zeta^d\right)^2} + \frac{\partial\psi}{\partial\zeta^d}\right)M^0_{ijmn}\sigma_{mn} + \Lambda^{rg}_{ij} \\
C^8_{ijmn} &= -I_{ijmn} + dpB^\beta_{ijmn}, \qquad C^9_{ijmn} = d\zeta A^\sigma_{ijmn}.
\end{aligned} \tag{4.157}$$

4.2.2 Tangent Moduli

The previous section described the method to integrate the constitutive equations and determine the $n+1^{th}$ material state after being subjected to applied increments of $d\varepsilon_{ij}^{n+1}$ and dT^{n+1}. Such methods address the *local* constitutive problem at each material point but not the *global* finite element boundary value problem. Although this global case is typically handled by external finite element software (here, Abaqus), the solution of problems of interest require the tangent matrix, $\mathcal{L}_{ijkl}$, of each material point be known [201]. This matrix is defined as:

$$d\sigma_{ij} = \mathcal{L}_{ijkl} d\varepsilon_{kl} - \Theta_{ij} dT, \tag{4.158}$$

with Θ_{ij} being the thermal tangent matrix. The determination of these matrices has been heavily investigated for various plastic materials [47,215,216]. Importantly, these derivations can be split into two categories – *continuum* and *consistent* (algorithmic). As defined by Simo and Taylor [215], the former case is determined from the constitutive formulation independent of the numerical implementation. The latter tensor, however, is derived in a fashion incorporating algorithmic considerations thereby resulting in a consistent linearization maintaining the quadratic convergence rate of the Newton-Rhapson method. With respect to SMAs, this distinction has been heavily discussed and explored by Qidwai and Lagoudas [191] while continuum tangent moduli for multimechanism cases such as plastic-damage [3], transformation-plasticity [100], and transformation-viscoplasticity [97] have all been determined. In the following, consistent tangent moduli used for this model are derived. First, in Section 4.2.2.1, the single mechanisms IKB mechanism case is presented while Section 4.2.2.2 gives the case for the multiple mechanisms case. Before proceeding, it is noted that these terms are derived for the converged $n+1$ state. Therefore, unless

specifically noted, all of the terms refer to those evaluated at the converged iteration of the $n+1^{th}$ increment.

4.2.2.1 IKB Formation

To determine the tangent modulus, the incremental constitutive equation,

$$d\sigma_{ij} = L_{ijkl}\left(d\varepsilon_{kl} - \alpha_{kl}dT - d\varepsilon^{r}_{kl}\right), \tag{4.159}$$

is recalled. From Section 4.2.1.1, it is noted that the recoverable strain at the $n+1^{th}$ iteration may be written as,

$$\varepsilon^{r-n+1}_{ij} = \varepsilon^{r-n}_{ij} + \left(\zeta^{n+1} - \zeta^{n}\right)\Lambda^{r-n+1}_{ij}, \tag{4.160}$$

which upon differentiating produces an algorithmic increment of,

$$d\varepsilon^{r-n+1}_{ij} = \left(\zeta^{n+1} - \zeta^{n}\right)d\Lambda^{r-n+1}_{ij} + \Lambda^{r-n+1}_{ij}d\zeta. \tag{4.161}$$

The difference between the continuum and the consistent formulations may be clearly seen in Eqn. 4.161. Specifically, in a continuum formation the $\left(\zeta^{n+1} - \zeta^{n}\right)d\Lambda^{r-n+1}$ term is not present although it accounts for changes in the direction of the inelastic response over a loading cycle. Under non-proportional loadings, this term can be important in global convergence to capture evolution in the stress state. Returning to Eqn. 4.159 and introducing $\tilde{\zeta} = \zeta^{n+1} - \zeta^{n}$, the constitute equation is rewritten,

$$d\sigma_{ij} = L_{ijkl}\left(d\varepsilon_{kl} - \alpha_{kl}dT - \tilde{\zeta}d\Lambda^{r-n+1}_{kl} - \Lambda^{r-n+1}_{kl}d\zeta\right). \tag{4.162}$$

Therefore, to determine the tangent modulus, the change in direction, $d\Lambda_{ij}^{r-n+1}$, and incipiently kinked volume fraction, $d\zeta$, need to be determined. First, referring to Eqn. 4.118, $d\Lambda_{ij}^{r}$ (dropping the $n+1$ superscript) is written as,

$$d\Lambda_{ij}^{r} = A_{ijkl}^{\sigma} d\sigma_{kl} + A_{ijkl}^{\beta} d\beta_{kl}^{r}, \tag{4.163}$$

where $d\beta_{ij}^{r}$, determined in the same algorithmic fashion as Eqn. 4.161, is

$$d\beta_{ij}^{r} = d\Lambda_{ij}^{r}\tilde{\zeta} + \Lambda_{ij}^{r} d\zeta. \tag{4.164}$$

Combining Eqns. 4.163 and 4.164 produces an expression for $d\Lambda_{ij}^{r}$ of the form,

$$d\Lambda_{ij}^{r} = D_{ijkl}^{r}\left(A_{klmn}^{\sigma} d\sigma_{mn} + A_{klmn}^{\beta}\Lambda_{mn}^{r} d\zeta\right), \tag{4.165}$$

with,

$$D_{ijkl}^{r} = \left(I_{ijkl} - A_{ijkl}^{\beta}\tilde{\zeta}\right)^{-1}. \tag{4.166}$$

By using Eqns. 4.165 and 4.166 in Eqn. 4.162, yielding a revised constitutive equation in which only $d\zeta$ is unknown,

$$d\sigma_{ij} = E_{ijmn} L_{mnkl}\left[d\varepsilon_{kl} - \alpha_{kl} dT - \left(I_{klrs} + \tilde{\zeta} D_{klop} A_{oprs}^{\beta}\right)\Lambda_{rs}^{r} d\zeta\right], \tag{4.167}$$

where

$$E_{ijkl} = \left(I_{ijkl} + \tilde{\zeta} L_{ijrs} D_{rsmn}^{r} A_{mnkl}^{\sigma}\right)^{-1}. \tag{4.168}$$

To determine $d\zeta$, the consistency equation,

$$0 = \frac{\partial \Phi^{r}}{\partial \sigma_{ij}} d\sigma_{ij} + \frac{\partial \Phi^{r}}{\partial \zeta} d\zeta + \frac{\partial \Phi^{r}}{\partial \beta_{ij}^{r}} d\beta_{ij}^{r}, \tag{4.169}$$

is used. Specifically, by introducing Eqns. 4.164, 4.165, and 4.167 into the consistency relation (4.169) $d\zeta$ is determined to be,

$$d\zeta = -\frac{1}{H}\left(\frac{\partial \Phi^r}{\partial \sigma_{ij}} + \tilde{\zeta}\frac{\partial \Phi^r}{\partial \beta^r_{op}} D^r_{opmn} A^{\sigma}_{mnij}\right) E_{ijrs} L_{rskl} \left(d\varepsilon_{kl} - \alpha_{kl} dT\right), \tag{4.170}$$

in which,

$$\begin{aligned} H = \; & -\left(\frac{\partial \Phi^r}{\partial \sigma_{ij}} + \tilde{\zeta}\frac{\partial \Phi^r}{\partial \beta^r_{op}} D^r_{opmn} A^{\sigma}_{mnij}\right) E_{ijrs} L_{rskl} \left(\tilde{\zeta} D^r_{klab} A^{\beta}_{abcd} + I_{klcd}\right) \Lambda^r_{cd} \\ & + \frac{\partial \Phi^r}{\partial \zeta} + \frac{\partial \Phi^r}{\partial \beta^r_{ij}} \Lambda^r_{ij} + \tilde{\zeta}\frac{\partial \Phi^r}{\partial \beta^r_{ij}} D^r_{ijmn} A^{\beta}_{mnkl} \Lambda^r_{kl}. \end{aligned} \tag{4.171}$$

In the previous relations, the loading/unloading dependence related to the recoverable mechanism is embedded in the various derivatives of the kinking function, Φ^r, which are given in Section 4.2.1.1. Equation 4.170 may then be substituted into the constitutive law (4.167) yielding a final expression of the form,

$$\begin{aligned} \mathcal{L}_{ijkl} = \; & E_{ijmn} L_{mnrs} \Bigg[I_{rskl} \\ & + \frac{1}{H}\left(I_{rsop} + \tilde{\zeta} D_{rsxy} A^{\beta}_{xyop}\right) \Lambda^r_{op} \left(\frac{\partial \Phi^r}{\partial \sigma_{ab}} + \tilde{\zeta}\frac{\partial \Phi^r}{\partial \beta^r_{ef}} D_{efcd} A^{\beta}_{cdab}\right) E_{abtu} L_{tukl} \Bigg], \end{aligned} \tag{4.172}$$

$$\Theta_{ij} = \mathcal{L}_{ijkl}\alpha_{kl}. \tag{4.173}$$

Before proceeding, and given the complexity of Eqn. 4.172, some reductions are considered to make comparisons to existing cases. First, the case of pure isotropic hardening is investigated by setting the relevant kinematic hardening terms to zero ($A^{\beta}_{ijkl} = \dfrac{\partial \Phi^r}{\partial \beta^r_{ij}} = 0$). With this simplification, $D^r_{ijmn} = I_{ijmn}$, and (by premultiplying E^{-1}_{ijkl} with M_{ijkl} and rearranging),

$$E_{ijkl} = \left(M_{ijmn} + \tilde{\zeta} A^{\sigma}_{ijmn}\right)^{-1} M_{mnkl} = \mathcal{E}_{ijmn} M_{mnkl}, \tag{4.174}$$

in which $\mathcal{E}_{ijmn}$ is defined in Eqn. 83 of Qidwai and Lagoudas [191]. By noting that $\frac{\partial \Phi^r}{\partial \sigma_{ij}} = \Lambda^r_{ij}$ (see Eqn. 4.91 – with $\zeta^d = 0$ for the purely IKB case), the tangent modulus becomes,

$$\mathcal{L}_{ijkl} = \mathcal{E}_{ijkl} - \frac{\mathcal{E}_{ijmn}\dfrac{\partial \Phi^r}{\partial \sigma_{mn}}\dfrac{\partial \Phi^r}{\partial \sigma_{ab}}\mathcal{E}_{abkl}}{\dfrac{\partial \Phi^r}{\sigma_{ij}}\mathcal{E}_{ijkl}\dfrac{\partial \Phi^r}{\partial \sigma_{kl}} - \dfrac{\partial \Phi^r}{\partial \zeta}}, \tag{4.175}$$

which is in same form as Eqn. 86 of Qidwai and Lagoudas [191] under similar assumptions. By further setting $\tilde{\zeta} = 0$, $\mathcal{E}_{ijkl} = L_{ijkl}$ and the continuum tangent modulus is returned.

4.2.2.2 Multiple Coupled Mechanisms

The single mechanism model of the preceding section is extended to the multimechanism case. In the same fashion as Eqn. 4.161 and using expressions from Section 4.2.1.2 (Eqns. 4.123-4.131), the strain and kinematic hardening variable increments may be written as,

$$d\varepsilon^r_{ij} = \tilde{\zeta} d\Lambda^r_{ij} + \Lambda^r_{ij} d\zeta - \tilde{\zeta}^d d\Lambda^{rg}_{ij} - \Lambda^{rg}_{ij} d\zeta^d, \tag{4.176}$$

$$d\varepsilon^p_{ij} = \tilde{p} d\Lambda^p_{ij} + \Lambda^p_{ij} dp, \tag{4.177}$$

$$d\varepsilon^d_{ij} = \tilde{\zeta}^d \left(d\Lambda^{rg}_{ij} + \lambda^d \frac{\partial^2 \psi}{\left(\partial \zeta^d\right)^2} M^0_{ijkl}\sigma_{kl} d\zeta^d + \lambda^d \frac{\partial \psi}{\partial \zeta^d} M^0_{ijkl} d\sigma_{kl} \right) \tag{4.178}$$

$$+ \left(\Lambda^{rg}_{ij} + \lambda^d \frac{\partial \psi}{\partial \zeta^d} M^0_{ijkl}\sigma_{kl} \right) d\zeta^d, \tag{4.179}$$

$$d\beta^r_{ij} = \tilde{\zeta} d\Lambda^r_{ij} + \Lambda^r_{ij} d\zeta, \tag{4.180}$$

$$d\beta^p_{ij} = \tilde{p} d\Lambda^p_{ij} + \Lambda^p_{ij} dp, \tag{4.181}$$

$$d\beta^d = \lambda^d d\zeta^d, \tag{4.182}$$

where $\tilde{\zeta} = \zeta^{n+1} - \zeta^n$, $\tilde{p} = p^{n+1} - p^n$, and $\tilde{\zeta}^d = \zeta^{d-n+1} - \zeta^{d-n}$. By using the definition of the derivative of the different direction tensors, Eqns. 4.119, 4.120, 4.154 and 4.155 with the increments of the IKB and plastic kinematic hardening variables (Eqn. 4.180 and 4.181, respectively), equations for $d\Lambda^r_{ij}$ and $d\Lambda^p_{ij}$ may be determined. Specifically, for the plastic term an expression of the form

$$d\Lambda^p_{ij} = D^p_{ijkl}\left(B^{\sigma}_{klmn} d\sigma_{mn} + B^{\beta}_{klmn}\Lambda^p_{mn} dp\right), \tag{4.183}$$

with

$$D^p_{ijkl} = \left(I_{ijkl} - \tilde{p}B^{\beta}_{ijkl}\right)^{-1}, \tag{4.184}$$

may be found while the expression for $d\Lambda^r_{ij}$ is given in Eqn. 4.163.

The incremental constitutive law is initially written as,

$$d\varepsilon_{ij} = dM_{ijkl}\sigma_{kl} + M_{ijkl}d\sigma_{kl} + \alpha_{ij}dT + d\varepsilon^r_{ij} + d\varepsilon^d_{ij} + d\varepsilon^p_{ij}. \tag{4.185}$$

By using relations Eqns. 4.177-4.182, 4.183, and 4.163, a revised constitutive law in terms of $d\zeta$, $d\zeta^d$, and dp is found,

$$d\sigma_{ij} = E^{MCM}_{ijkl}\left(d\varepsilon_{kl} - \alpha_{kl}dT - H^2_{kl}d\zeta - H^1_{kl}d\zeta^d - H^3_{kl}dp\right), \tag{4.186}$$

where,

$$E^{MCM}_{ijkl} = \left[\left(\psi + \tilde{\zeta}^d\lambda^d\tfrac{\partial\psi}{\partial\zeta^d}\right)M^0_{ijkl} + \tilde{p}D^p_{ijmn}B^{\sigma}_{mnkl} + \tilde{\zeta}D^r_{ijmn}A^{\sigma}_{mnkl}\right]^{-1}, \tag{4.187}$$

$$H^1_{ij} = \left(\frac{\partial\psi}{\partial\zeta^d} + \tilde{\zeta}^d\lambda^d\frac{\partial^2\psi}{(\partial\zeta^d)^2} + \lambda^d\frac{\partial\psi}{\partial\zeta^d}\right)M^0_{ijkl}\sigma_{kl}, \tag{4.188}$$

$$H^2_{ij} = \left[I_{ijkl} + \tilde{\zeta}D^r_{ijkl}A^{\beta}_{mnkl}\right]\Lambda^r_{ij}, \tag{4.189}$$

$$H^3_{ij} = \left[I_{ijmn} + \tilde{p}D^p_{ijkl}B^{\beta}_{klmn}\right]\Lambda^p_{mn}. \tag{4.190}$$

The variables $d\zeta,\ d\zeta^d$, and dp may then be found from three consistency equations,

$$0 = \frac{\partial \Phi^r}{\partial \sigma_{ij}} d\sigma_{ij} + \frac{\partial \Phi^r}{\partial \zeta} d\zeta + \frac{\partial \Phi^r}{\partial \zeta^d} d\zeta^d + \frac{\partial \Phi^r}{\partial \beta^r_{ij}} d\beta^r_{ij}, \tag{4.191}$$

$$0 = \frac{\partial \Phi^d}{\partial \sigma_{ij}} d\sigma_{ij} + \frac{\partial \Phi^d}{\partial \zeta^d} d\zeta^d + \frac{\partial \Phi^d}{\partial \beta^d} d\beta^d, \tag{4.192}$$

$$0 = \frac{\partial \Phi^p}{\partial \sigma_{ij}} d\sigma_{ij} + \frac{\partial \Phi^p}{\partial \zeta^d} d\zeta^d + \frac{\partial \Phi^p}{\partial p} dp + \frac{\partial \Phi^p}{\partial \beta^p_{ij}} d\beta^p_{ij}. \tag{4.193}$$

These three equations can be rearranged to produce a system of three equations in terms of the total strain and temperature increments by using the constitutive relation (4.186) and the same relations used to derive it. Specifically, the resultant system of equations is written as,

$$\begin{aligned} -K^r_{ij} E^{MCM}_{ijkl} \left(d\varepsilon_{kl} - \alpha_{kl} dT\right) = & \left[\frac{\partial \Phi^r}{\partial \zeta} + \frac{\partial \Phi^r}{\partial \beta^r_{ij}} \left(I_{ijmn} + \tilde{\zeta} D^r_{ijmn} A^\beta_{mnkl}\right) \Lambda^r_{kl} \right. \\ & \left. - K^r_{ij} E^{MCM}_{ijkl} H^2_{kl}\right] d\zeta + \left[\frac{\partial \Phi^r}{\partial \zeta^d} - \right. \\ & \left. K^r_{ij} E^{MCM}_{ijkl} H^1_{kl}\right] d\zeta^d - K^r_{ij} E^{MCM}_{ijkl} H^3_{kl} dp, \end{aligned} \tag{4.194}$$

$$\begin{aligned} -K^d_{ij} E^{MCM}_{ijkl} \left(d\varepsilon_{kl} - \alpha_{kl} dT\right) = & -K^d_{ij} E^{MCM}_{ijkl} H^2_{kl} d\zeta \\ & + \left(\frac{\partial \Phi^d}{\partial \zeta^d} + \lambda^d \frac{\partial \Phi^d}{\partial \beta^d} - K^d_{ij} E^{MCM}_{ijkl} H^1_{kl}\right) d\zeta^d \\ & - K^d_{ij} E^{MCM}_{ijkl} H^3_{kl} dp, \end{aligned} \tag{4.195}$$

$$\begin{aligned} -K^p_{ij} E^{MCM}_{ijkl} \left(d\varepsilon_{kl} - \alpha_{kl} dT\right) = & -K^p_{ij} E_{ijkl} H^2_{kl} d\zeta \\ & + \left(\frac{\partial \Phi^p}{\partial \zeta^d} - K^p_{ij} E^{MCM}_{ijkl} H^1_{kl}\right) d\zeta^d \\ & + \left[\frac{\partial \Phi^p}{\partial \beta^p_{ij}} \left(I_{ijmn} + \tilde{p} D^p_{ijkl} B^\beta_{klmn}\right) \Lambda^p_{mn} + \frac{\partial \Phi^p}{\partial p} \right. \\ & \left. - K^p_{ij} E^{MCM}_{ijkl} H^3_{kl}\right] dp, \end{aligned} \tag{4.196}$$

with,

$$K^r_{ij} = \frac{\partial \Phi^r}{\partial \sigma_{ij}} + \tilde{\zeta}\frac{\partial \Phi^r}{\partial \beta^r_{rs}} D^r_{rsmn} A^\sigma_{mnij} \tag{4.197}$$

$$K^d_{ij} = \frac{\partial \Phi^d}{\partial \sigma_{ij}} \tag{4.198}$$

$$K^p_{ij} = \frac{\partial \Phi^p}{\partial \sigma_{ij}} + \tilde{p}\frac{\partial \Phi^p}{\partial \beta^p_{mn}} D^p_{mnkl} B^\sigma_{klij}. \tag{4.199}$$

By rewriting the constitutive equations as,

$$-K^r_{ij} E^{MCM}_{ijkl} \left(d\varepsilon_{kl} - \alpha_{kl} dT\right) = a_{11} d\zeta + a_{12} d\zeta^d + a_{13} dp, \tag{4.200}$$

$$-K^d_{ij} E^{MCM}_{ijkl} \left(d\varepsilon_{kl} - \alpha_{kl} dT\right) = a_{21} d\zeta + a_{22} d\zeta^d + a_{23} dp, \tag{4.201}$$

$$-K^p_{ij} E^{MCM}_{ijkl} \left(d\varepsilon_{kl} - \alpha_{kl} dT\right) = a_{31} d\zeta + a_{32} d\zeta^d + a_{33} dp, \tag{4.202}$$

the increments may be determined to be,

$$\begin{Bmatrix} d\zeta \\ d\zeta^d \\ dp \end{Bmatrix} = - \begin{bmatrix} b_{11} & b_{12} & b_{13} \\ b_{21} & b_{22} & b_{23} \\ b_{31} & b_{32} & b_{33} \end{bmatrix} \begin{Bmatrix} K^r_{ij} \\ K^d_{ij} \\ K^p_{ij} \end{Bmatrix} E^{MCM}_{ijkl} \left(d\varepsilon_{kl} - \alpha_{kl} dT\right), \tag{4.203}$$

where $b_{ij} = a^{-1}_{ij}$. With these increments determined, the final tangent modulus may be given by,

$$\begin{aligned} \mathcal{L}_{ijkl} = \; & E^{MCM}_{ijmn} \left[I_{mnkl} + H^2_{mn} \left(b_{11} K^r_{rs} + b_{12} K^d_{rs} + b_{13} K^p_{rs} \right) E^{MCM}_{rskl} \right. \\ & H^1_{mn} \left(b_{21} K^r_{rs} + b_{22} K^d_{rs} + b_{23} K^p_{rs} \right) E^{MCM}_{rskl} \\ & \left. H^3_{mn} \left(b_{31} K^r_{rs} + b_{32} K^d_{rs} + b_{33} K^p_{rs} \right) E^{MCM}_{rskl} \right], \end{aligned} \tag{4.204}$$

$$\Theta_{ij} = \mathcal{L}_{ijkl} \alpha_{kl}. \tag{4.205}$$

4.3 Results

The previous two sections detail the theoretical development and numerical implementation of a multi-mechanism model for predicting and describing the constitutive response of MAX phase materials. Here, the capabilities of using this model to capture the response of the MAX phase. First, experimental results of compressive stress-strain cycles are investigated and used to calibrate the model. Some additional

To consider the accuracy of the developed MAX phase model, a series of compressive stress-strain experiments performed on a fine grain Ti_2AlC specimen at room-temperature and under quasi-static conditions are investigated[5]. Specifically, a series of monotonically increasing loading-unloading cycles under compression are performed and select cycles are shown in Fig. 54. From this experimental investiga-

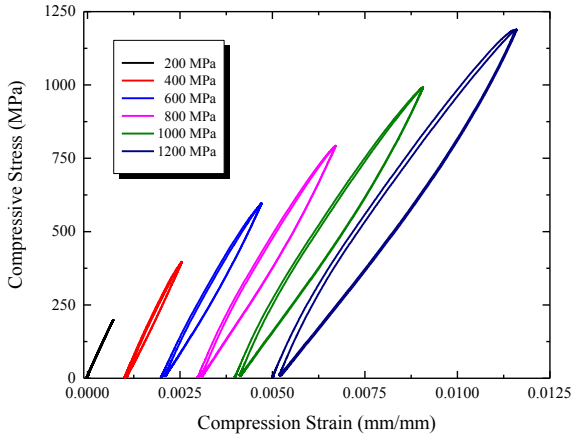

Figure 54: Experimental results of polycrystalline, fine-grained Ti_2AlC under monotonic, cyclic compressive loadings. Two cycles are shown at each load level (Figure and results provided by R. Benitez and Prof. M. Radovic, unpublished)

[5]Experimental results in this section are provided by R. Benitez and Prof. M. Radovic, TAMU MSEN. These results are currently unpublished and provided to the author via private communication.

tion a number of important characteristics may be observed. First, the repeatable hysteretic behavior of MAX phases is evident at many load levels and the size of these loops increases with applied stress. Additionally, and especially at 1200 MPa, it can be observed that the first cycle is open with corresponding permanent deformations resulting from the kinking and plastic mechanisms. As a part of this investigation, the relative Young's modulus (a measure of the damage) and irrecoverable strain developed over these cycles were also measured. Since all of these mechanisms are observed and characterized in this set of results, these experiments will be used to investigate the performance of the developed model.

Before analyzing the capabilities of the model, the relevant calibration parameters must first be identified. As uniaxial results are being studied the material is assumed to be elastically isotropic and isotropic damage is considered. Therefore, 19 parameters must be specified and are listed in Table 4.1 for summary. With respect to

Table 4.1: Necessary model parameters for the developed MAX phase model.

Response	Parameters
Thermoelastic	$E^0,\ \nu,\ \alpha$
IKB formation	$B,\ k, \kappa^r,\ \gamma^r,\ Y_r$
Kinking	$q,\ c,\ \tilde{\nu},\ \kappa^d,\ \gamma^d,\ Y_d$
Plastic	$L,\ n,\ \kappa^p,\ \gamma^p,\ Y_p$

thermoelastic properties, values of $E^0 = 278$ GPa, $\nu = 0.17$, and $\alpha = 8.2x10^{-6\circ}\mathrm{C}^{-1}$ as listed in Table 2.1 are utilized. The remaining properties, and corresponding, responses are now investigated individually.

First, the reversible IKB response is calibrated and studied by considering the second, stable cycles of Fig. 54. Five parameters must be identified for this purpose:

the strain per unit kinked volume, γ^r, critical thermodynamic driving force, Y_r, and three hardening parameters – B, k, and κ^r. The strain per unit kinked volume, is an assumed value used to relate the developed strain and the corresponding internal state variable. Experimentally, this parameter cannot be determined from direct observation and it is assumed that $\gamma^r = 0.035$. Kalidindi *et al.* [114] used the same value, in a comparable role albeit for Ti_3SiC_2, in their analysis and it is derived from the micromechanical model of Barsoum and colleagues [24]. The remaining parameters are all determined by analyzing the results of the 1200 MPa case. Specifically, the unloading portion of this curve is used to calibrate the remaining parameters. This selection is made as the reversible IKB mechanisms is the only one that should be active during unloading and the effects can be decoupled from any plasticity or damage based characteristics. In a similar fashion to Fig. 50, the nonlinear strain as a function of unloading stress is extracted and used for calibration. From such an analysis, an onset stress of 145 MPa may be determined. Noting that Y_r is the onset stress multiplied by γ^r, a value of $Y_r = 6.125$ MPa is determined. The remaining hardening parameters (B, k, and κ^r) are then determined as a best fit to the nonlinear strain versus stress (hardening) behavior. These are listed below in Table 4.2.

With these results determined, the second cycle of the 1200 MPa load cycles is simulated while the corresponding 800 and 1000 MPa results are predicted and presented in Fig. 55. Numerical simulations are performed via Abaqus using the UMAT developed in the previous section. A single 3D linear element is considered in which one node along the bottom is fixed in all directions to prevent rigid body motion. The bottom face is fixed in the "3" direction and a surface traction load is applied along the opposite face producing a uniaxial, homogeneous stress field across the element. From the these results it may be seen that overall good agreement is observed between the numerical and experimental data. With respect to the simulated 1200

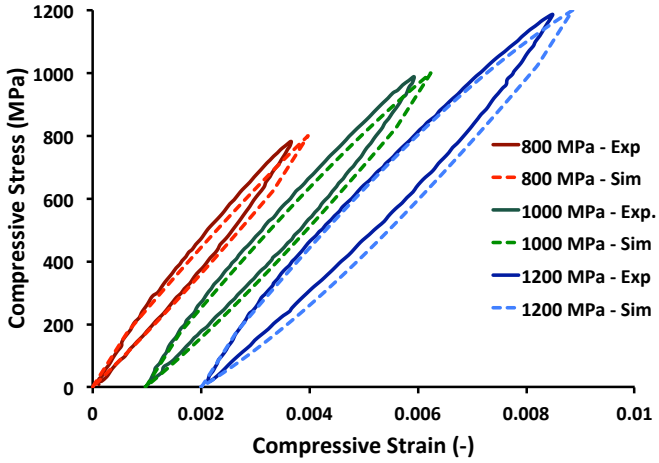

Figure 55: Experimental results of the IKB response of polycrystalline, fine-grained Ti_2AlC at maximum applied compressive loads of 800, 1000, and 1200 MPa. Corresponding simulation of the 1200 MPa and prediction of the 800 and 1000 MPa cycles are also given. The cycles are offset from each other for clarity.

MPa, the initial linear and nonlinear portions of the loading path show very good agreement. At higher load levels (above 1000 MPa), some deviation in the results may be observed associated with decreased hardening in the numerical simulation. As a result, the maximum strain is slightly over-predicted. Similar behaviors are also noted during unloading although importantly complete recovery is observed in both experimental and model results. The predicted results also show agreement. In general, however, the model results show a more compliant response during nonlinear behavior than the reference experimental cases. The loading domains are below the 1000 MPa deviation point noted during the simulation case so this distinction may be a result of differences in material response. Specifically, the same specimen is used in all experiments and repeatedly cycled so permanent nonlinear cyclic effects could contribute to the observed differences. With all of this noted, overall good agreement and capabilities with the developed model.

The experimental results indicate the development of permanent deformations and damage over the course of cycling. Contributions from plasticity and damage through various mechanisms are expected and have been reported. As the postulated model allows permanent deformations via both the permanent kinking and plasticity mechanisms, distinguishing these two effects from macroscopic experiments may be difficult. Therefore, the two behaviors are handled individually and their contributions established sequently. First, the permanent kinking (damage) mechanism is investigated. In the experimental study, the damage was determined via multiple resonant ultrasound spectroscopy (RUS) measurements and the results are presented in Fig. 56 in terms of relative Young's Modulus, E/E^0, over the course of the loading cycle. From these results, it is noted that even at high stress levels relatively low quantities of damage are measured (less than 1%). For use in modeling, these results are replotted in Fig. 56 in terms of the permanently kinked (damaged) volume fraction, ζ^d. In determining this value, it is noted that the equivalent strain energy assumption is utilized for the damaged material state such that $\psi = 1/\left(1-\zeta^d\right)^2$. This selection is made (over the effective strain) due to the presence of nonlinear strains in the system.

Six material parameters related to the kinking model must be determined prior to its use. First, as on compression experiments are investigated, the pressure-dependent coefficient ($\tilde{\nu}$) is set to zero. Similarly, for simplicity and given the experiments are only presented as maximum stress, the kinematic hardening modulus, κ^d is neglected ($\kappa^d = 0$). The scaling coefficient, γ^d is assumed to be one such that the damage and ζ^d scale one-to-one. That leaves three parameters to be determined – the two isotropic hardening variables q and c and the critical driving force, Y_d. With respect to the latter parameter, it is noted that with these simplifications and by

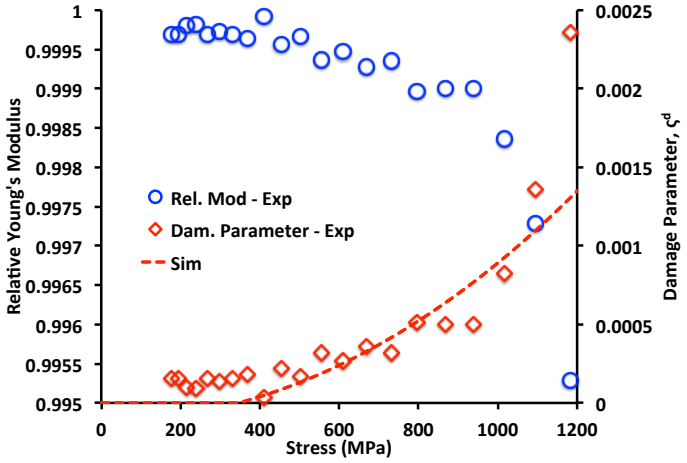

Figure 56: Damage measures of the Ti_2AlC as a measure of applied stress. Experimentally, the damage was measured as the relative Young's Modulus (E/E^0) via resonant ultrasound spectroscopy. The experimental results are replotted in terms of the model damage, ζ^d. Results of a 1200 MPa loading cycle considering both damage and IKB is also presented.

setting $\zeta^d = 0$,

$$Y_d = 3\frac{\sigma^d}{E^0}, \tag{4.206}$$

where σ^d is the stress value corresponding to damage initiation. Based on the when the damage begins to deviate, this parameter is taken to be $\sigma^d = 350$ MPa and the remining two parameters are found such that they best fit the hardening response and are given in Table. 4.2. It is noted that given the relatively small damage accumulates in the experimental domain, multiple parameter sets could probably capture the relevant features to an accurate degree. Using these parameters, and those developed previously for the IKB, the two mechanism (IKB-KB) model is utilized. Specifically, two load-unload cycles up to a maximum of 1200 MPa are simulated and the stress-strain results are given in Fig. 57. In these results, it is noted that the results of the two cycles are nearly identical. Some, small permanent deformations

are observed at the end of the first loading cycle although by comparison to Fig. 54. Additionally, the damage parameter over the course of the first loading cycle is presented in Fig. 56 and reasonable agreement between the experimental and numerical results is noted. As such, it is reasonable to attribute the difference in permanent strains to the plastic mechanism not yet incorporated.

To incorporate the plastic deformations developed in the Ti_2AlC through the

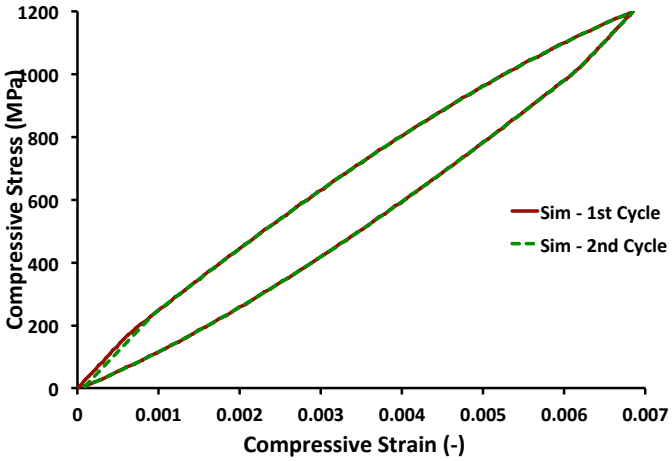

Figure 57: Numerical results of a simulation considering IKB and KB formation in the MAX phase through two repeated compressive 1200 MPa load-unload cycles of the Ti_2AlC under investigation.

loading cycles, the experimentally determined, irrecoverable strain as a function of applied stress is presented in Fig. 58 along with the permeant strain developed in the prior simulation. In distinguishing the two, the prior simulation only considered deformations arising from the the kinking process whereas the experimental result does not distinguish a source. As was noted in the corresponding discussion, the irrecoverable strain from the previous simulation is substantially lower than the ex-

perimental values. The difference between the two is assumed to arise from plasticity in non-kinking grains and is associated with the plastic mechanism and is determined (by using a natural logarithmic fit of the experimental data) and given in Fig. 58. This result is used to calibrate the plastic model. It is also noted that this corresponds to a two-part calibration procedure where the KB related damage response must first be determined and used to isolate the plastic strain.

There are five parameters that must be specified for the plastic portion of

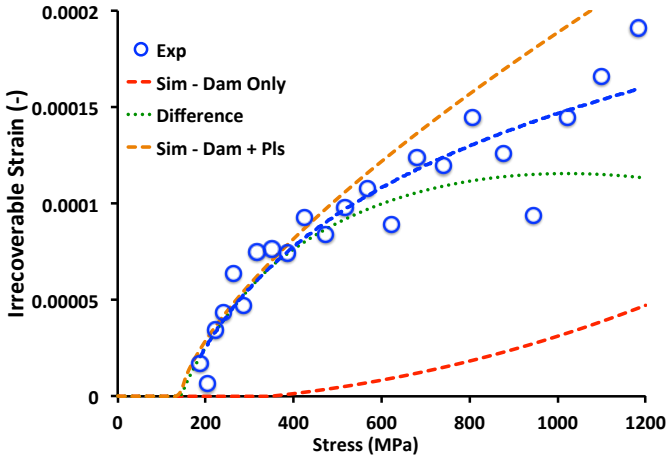

Figure 58: Irrecoverable strain as a function of the applied stress for the Ti_2AlC being considered. The experimentally determined value is presented along with simulation results of the permanent strain for the IKB-KB case (Fig. 57) and of the fully coupled, multimechanism model. Simulation results determined from a a 1200 MPa loading cycle. The difference between the experimental and IKB-KB simulation results is also presented.

the model. First, it is assumed that a purely isotropic hardening is responsible for this mechanism and the kinematic hardening modulus is set to zero. As only the macroscopic response is reported and no detailed, microscopic results are available to determine the plastic strain per unit volume, it is assumed that $\gamma^p = 1$ and p may be

interpreted as the effective plastic strain. The critical thermodynamic driving force takes the form of the plastic yield stress and by using the experimental fit of Fig. 58 it may be determined to be 142 MPa. The two hardening parameters are then found from by fitting to the inelastic strain-applied stress hardening. As the results from Fig. 58 indicate a difference between the onset of plastic deformation and damage, the hardening in this regime is used to determine the fit to avoid any interactions.

Using the calibrated model developed over the preceding section (and with the pa-

Table 4.2: Calibrated model parameters for the developed MAX phase model.

Response	Parameters
E^0	278 GPa
ν	0.17
α	$8.2x10^{-6\circ}C^{-1}$
B	1008 MPa
k	11
κ^r	6 MPa
γ^r	.035
Y_r	6 MPa
q	300 MPa
c	37
Y_d	1.32 MPa
L	$1.92x10^8$ MPa
n	1.44
Y_p	142 MPa

rameters of Table 4.2), the numerical response of two compressive loading-unloading cycles up to 1200 MPa is simulated and presented in Fig. 59 along with the corresponding experimental response. Before comparing the results, it is noted that the calibration process uses the second-stabilized cycle at 1200 MPa and damage and irrecoverable strain to determine the model parameters. The first-cycle response of the material is not used at any part and the interactions between the mechanisms

arise as a prediction. First, in comparing the experimental and numerical results of

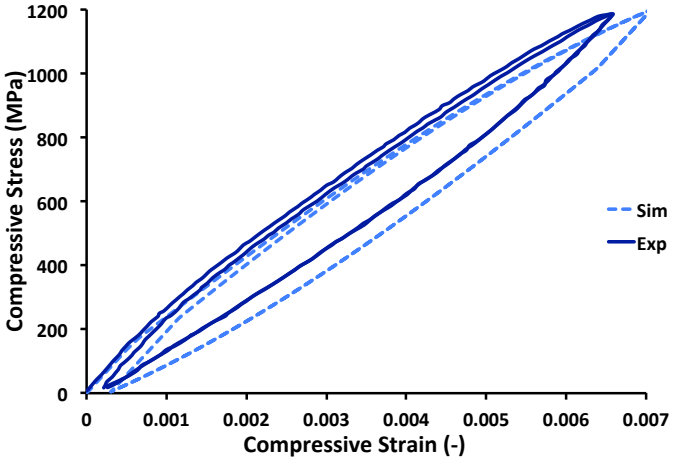

Figure 59: Stress-strain response of a Ti_2AlC specimen through two compressive loading-unloading cycles up to 1200 MPa. Experimental and numerical results (using the coupled, multimechanism model) are presented.

Fig. 59 good agreement may be observed. Qualitatively, the simulated results exhibit important behaviors of the experiments. Specifically, the first cycle results in permanent deformation. Upon reloading, the material follows a similar trajectory and returns to the initial unloading point. Secondly, in both experiments and modeling, the unloading paths of the first and second cycle lie on top each other. Therefore, permanent deformations occur during the first cycle and a stabilized hysteresis loop is observed afterward. Quantitatively, some small differences are noted although overall good agreement is observed. Specifically, in comparing the results it is noted that slightly more irrecoverable strain is noted in the simulation case than the experiments. This may also be seen in Fig. 58. In that result, it is important to note that calibration is only performed prior to the damage initiation. Excellent agreement

is observed during that regime although the irrecoverable strain is overpredicted at higher stress levels. Secondly, the nonlinear hardening of the computation response is lower than in the experiments. This is especially true in the first cycle and is likely a result of using the unloading portion of the second, stabilized cycle for calibration as discussed with the previous results. As such, the final total strain is slightly higher in the numerical rather than the experimental results.

To expand on these results, the evolution of five internal variables through the first loading cycle are presented in Fig. 60. Specifically, two volume fractions (the total kinked, ζ, and damage (permanently kinked), ζ^d) are given along with the inelastic strain components in the direction of applied loading of the different mechanisms. First, it is noted that even at 1200 MPa the IKB volume fraction is still only 7%. Although no experimental measurement of this value has been determined, based on the proposed theory and dependence on grain orientation it is not expected to be a large value. In this case, the permanent kinked volume fraction remains quite low. In considering the inelastic strains, the largest contribution in Fig. 60 comes from recoverable mechanisms while the permanent strains of the damage remains quite low. In terms of the model, these results yield one other important result. Specifically, it may be observed that different sets of internal variables are active at different times. Therefore, the implemented form of the model is sufficiently flexible as to study different combinations of the mechanisms.

Before proceeding, two other cases are presented. First, the possibility of using the model to simulate paths to multiple load levels is explored in Fig. 61a. Specifically, a two cycle (loading-unloading) similar to that previously studied. In this case, however, the first cycle only goes to 600 MPa while the second cycle then increases the applied load. From these results, it is observed that after the initial loading cycle some small permanent deformations are established upon unloading. When

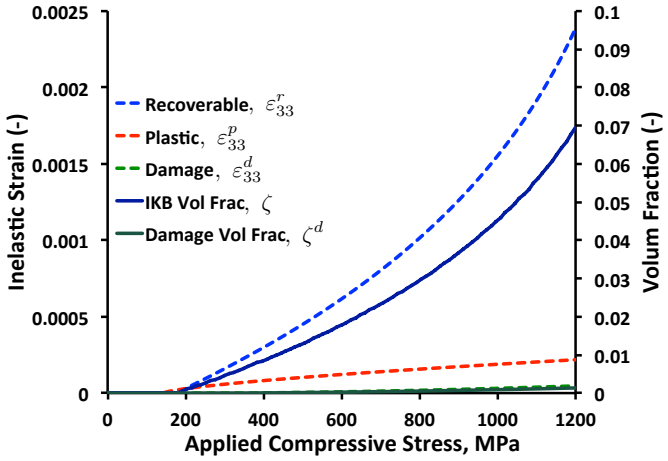

Figure 60: Internal state variables predicted by the MAX phase model through a 1200 MPa compressive loading cycle. Strain values correspond to those in the direction of applied load.

reloaded, the specimen follows a similar trajectory. At the end of this cycle, additional irrecoverable deformations are observed and the behaviors in Fig. 61 follow what is qualitatively expected. Therefore, the ability of the model to handle such loading paths is established. Finally, a parametric study is performed on the assumed parameter kinking strain per unit volume fraction, γ^r. Values of $\gamma^r = 0.025,\ 0.035,$ and 0.045 are considered and the results are presented in Fig. 61b. In this case, only the recoverable mechanism is considered to isolate the effect of this parameter on the appropriate mechanism. From these results, it may be observed that as γ^r increases the hysteresis size (and therefore energy dissipated) and inelastic strain. Similarly, the hardening decreases with γ^r. Although not presented, it is noted that the the IKB volume fraction, ζ, also scales with γ^r. Specifically, values of 8.5 and 2.4% at 1000 MPa are returned for the $\gamma^r = 0.045$ and 0.025 cases, respectively. Qualitatively, these trends follow those observed with increasing the grain size of MAX phase materials [23, 237] and a connection between these parameters could be

made and useful in subsequent investigations.

Briefly, in this section a theoretical model for MAX phase materials was estab-

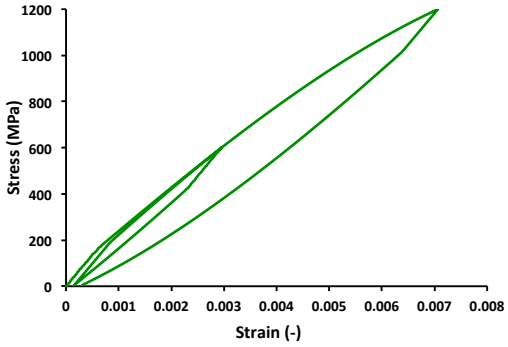

(a) Simulated response of a Ti_2AlC specimen through two sequential loading cycles. The first load is to 600 MPa and the the second is to 1200 MPa.

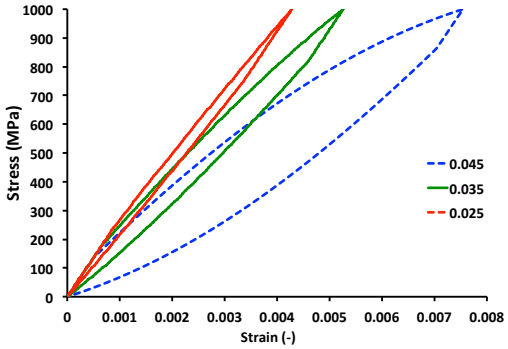

(b) Effect of γ^r on the simulated, recoverable response of Ti_2AlC through a 1000 MPa loading cycle.

Figure 61: Additional simulations of the MAX phase model.

lished considering three distinct mechanisms (recoverable IKB, damaging KB, and irrecoverable plasticity). The different responses were then coupled and a numerical 3D implementation was developed and implemented. This model was then used to simulate and analyze the response of experimental results of a Ti_2AlC specimen and good agreement was observed. Therefore, this model is considered as reasonable for use in more complex analysis of MAX phase materials.

4.4 Summary

During this chapter, a constitutive model for MAX phase ceramics was established. This effort sought to address the lack of a 3D phenomenological models for such materials and enable study of the interactions of these responses in the composites. Three mechanisms were considered in the model: (i) a reversible mechanism

assumed to be associated with incipient kink band formation (*ii*) permanent irrecoverable and damage deformations tied to the transition of incipient kink bands to their permanent counter parts and (*iii*) permanent plastic deformations corresponding to plastic slip in non-kinking grains. In developing the model, each mechanisms is developed independently with corresponding internal state variables and evolution equations and then coupled. In coupling the model it is assumed that each mechanism is largely independent and coupling occurs through two primary fashions. First, it is taken that any permanent kink bands may only form after being incipiently kinked and any such volumes are no longer recoverable. Secondly, and following the effective stress concept, a mapping is introduced to take the thermodynamic driving forces associated with incipient kinking and plastic deformation from the effective, current configuration to the undamaged one. An elastic predictor-inelastic corrector numerical implementation of the model via the closest-point projection return mapping algorithm is developed for all of the various independent and coupled models. Algorithmic (consistent) tangent moduli of the different cases are also derived and both the inelastic correction and tangent moduli are implemented as an Abaqus UMAT. To consider both the theoretical model and numerical implementation, recent experimental results of a Ti_2AlC specimen are investigated. The calibration procedure for the various material parameters and mechanisms is discussed and the relevant properties determined. Simulated results show good agreement with experimental and predictions of other loadings are also performed. Importantly, the developed model is shown to be able to capture the relevant behaviors of the MAX phase model. In considering the various mechanisms, it is also demonstrated that both the damage associated with kink band formation and plastic slip-based deformation is necessary to produce the opening during the initial loop. Additional simulations are used to investigate the capabilities of the model such that it may be considered for use in

subsequent composite efforts.

The developed model represents the first evolution towards a multimechanism model of these MAX phases. These efforts can be expanded and built upon through additional information gleaned through experimental investigations. First, as previously mentioned, many of the hardening parameters and responses are dependent on the grain size. Detailed experimental investigations characterizing the composite at different grain sizes could allow for a functional form of all of the different parameters (*e.g.* strain per unit kinked volume, critical value for kinking, and modulus). Such a parameterization could greatly expand the set of results the model can capture. Furthermore, in this effort it is assumed that the hardening of the different mechanisms is independent. Systematic investigations allowing for progressively evolving permanent mechanisms (*e.g.* plastic strain and damage) followed by characterization of the reversible IKB mechanism would shed light on these relationships and allow for more complex forms of the hardening and additional couplings.

5. INTERACTION OF INELASTIC MECHANISMS IN SMA-MAX PHASE COMPOSITES

In the previous chapter (Chapter 4) a multimechanism model to describe the phenomenological behavior of MAX phase materials was developed and implemented. Previous investigations (Chapter 2 and 3) developed models of this composite but the investigations were limited to considering (at most) only a single inelastic mechanism in the MAX phase constitutive behavior. Here, those investigations are expanded upon by using the model developed as a part of this work to study the behaviors. Specifically, the interaction of the martensitic transformation behavior of the SMA constituent and kinking response of the MAX phase is considered such that a range of deformation mechanisms are studied.

First, for this investigation the FE continual fiber reinforcement model developed in Section 3.1.2 is revisited. As the focus of this investigation is on the interaction of the mechanisms, this two-phase microstructure is utilized in lieu of the image-based microstructure in Section 3.2 to remove any influences of the interphase or porosity and focus on the constitutive interactions. The effects of many such microstructural features were studied in Section 3.2.2.3. Therefore, the continual fiber geometry of Fig. 23b is utilized and FE boundary value problem described by Fig. 24 is considered. With respect to the MAX phase material, Ti_2AlC is again utilized and the 3D UMAT developed as a part of Chapter 4 is used to capture the response. For the purposes of this study, a modified constitutive response is considered. Specifically, as the only small amounts of damage were reported experimentally (Fig. 56) and the corresponding effect was minor (Fig. 57) this mechanism is neglected in this section. This serves to not only help focus on just two mechanisms in the MAX

phase and separate their influences but also aid in computations as the cost of every numerical constitutive iteration is reduced. Secondly, in the previous section only minor irrecoverable plastic deformations were observed. The hardening response in this section is modified to (i) enable higher quantities of irrecoverable deformations and (ii) the onset stresses are modified such that distinct reversible and reversible and plastic regimes are noted. This latter change is made such that the impact of each mechanism can be separated. The SMA is taken to be NiTi and the assumed strain-temperature and stress-strain responses of the two phases are presented in Fig. 62a and b, respectively. In Fig. 62a, the elastic unloading is also indicated (by the dotted black line). From this, it may be observed that the irrecoverable strain is substantially larger than the recoverable strain associated with IKB formation. Both of these deformations, however, pale in magnitude with respect to those of the SMA constituent.

The aim of this investigation is to look at the interaction of the various mech-

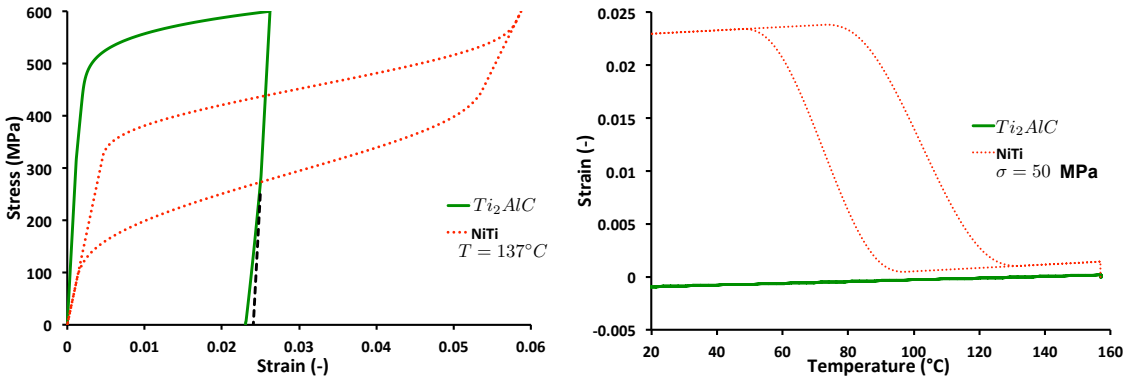

(a) Stress-strain response of the NiTi and Ti_2AlC phases. The former refers to a loading $T = 137°C$ and the dotted line on the unloading of the latter is elastic unloading limit.

(b) Strain-Temperature (under a constant bias load of 50 MPa) of the NiTi and Ti_2AlC phases

Figure 62: Assumed constitutive responses of the NiTi and Ti_2AlC phases used in this study.

anisms. Therefore, forward transformation of the SMA phase is studied and considered. To that end, the response of a NiTi-Ti_2AlC composite under an applied compressive loading of 250 MPa is studied via the constructed model. The effective stress in the direction of loading of each phase determined in this fashion is presented in Fig. 63a while the evolution of the phase average internal state variables (ISVs) is given in Fig. 63b. First, as expected at the start of the cooling path the MAX phase constituent is at a higher stress level due to it more substantial mechanical stiffness. Additionally, it is noted from Fig. 63b that some IKBs have been generated during pure mechanical loading. As cooling progresses, and like previous results, some small changes in the stress associated with thermal expansion mismatch occur. Eventually, transformation is initiated through the cooling process. Initially this results in a stress increase in the Ti_2AlC phase pursuant to previous discussions. At this point, additional IKBs are formed and it may be observed that additional kink bands continue to expand throughout transformation. Part of the way through transformation, however, the directional stresses of Fig. 63 begin to show a different trend. Specifically, the Ti_2AlC stress magnitude starts to decrease while the SMA constituent exhibits an increase. It is pointed out that the complementary von Mises stress does increase and this qualitative trend was evident in the responses of Fig. 27 and was associated with this specific geometric configuration. Nonetheless, this interaction does point out an interesting trend with respect to these processes. Specifically, as this directional change occurs in close combination to the onset of plastic deformation the difference in the impact of the mechanisms may be observed. From Fig. 63b, it can be observed that at the end of cooling the effective plastic strain is more than .2% – roughly an order of magnitude more than the corresponding recoverable strain from the IKB process. Therefore, the change in direction is likely associated with (i) the larger magnitude deformations of the plastic mechanism and (ii) the more

compliant tangent modulus resulting from these extra processes.

To build upon these results, additional simulations are performed with different

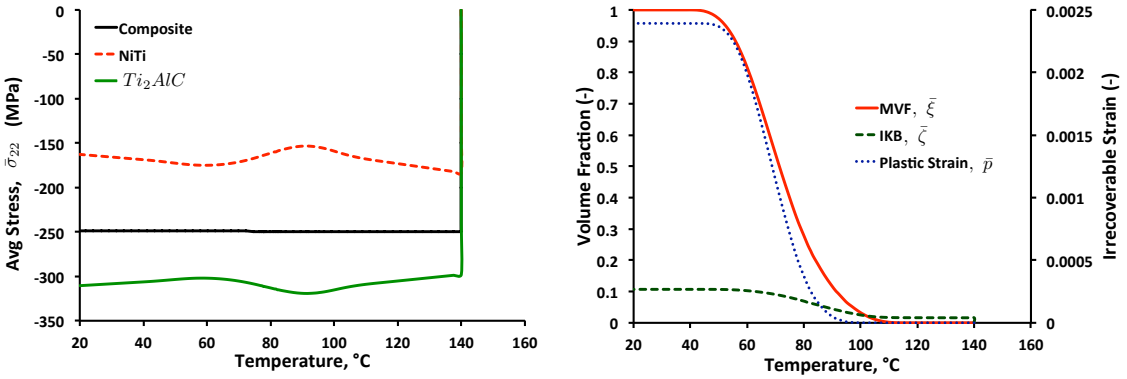

(a) Effective stress of the composite, $\bar{\sigma}_{22}$, and constituents, $\bar{\sigma}^r_{22}$.

(b) Phase averaged martensitic volume fraction, $\bar{\xi}$, IKB volume, ζ, and Ti_2AlC effective plastic strain, $\bar{p}$.

Figure 63: Evolution and constituent response through a cooling path and forward transformation.

applied compressive bias stresses. Specifically, compressive bias loadings of magnitude 100, 175, 250, and 325 MPa are considered and will be referred to by their magnitude (neglecting the sign) in the following discussions for conveince. The 250 MPa case corresponds to the results in Fig. 63. The evolution of the phase averaged IKB volume fraction, $\bar{\zeta}$, effective plastic strain, $\bar{p}$, and martensitic volume fraction, $\bar{\xi}$, through the cooling portion of these different loading paths is presented in Fig. 64a, b, and c, respectively. First, from Figs. 64, it is noted that in the 100 MPa case negligible amounts of plastic strain and IKBs develop. Therefore, this case may be considered the elastic simulation. With respect to the 175 MPa simulation, IKB formation is seen to occur while mere traces of plasticity are observed. As such, this case will be taken to be a purely IKB case. The two higher load levels, 250 and 325 MPa, both show the activity of both mechanisms and are taken to be the multimechanism

results. Distinguishing the two, as was noted with respect to Fig. 63, a temperature portion of IKB only deformation during transformation was observed. In comparing Figs. 64b and c, however, both MAX phase mechanisms seem to activate with the onset of forward transformation. In all cases, as the applied bias load increases the amount of inelastic deformations increase as well. It is also observed that in the multimechanism cases IKB formation occurs during the mechanical loading process prior to transformation. From Fig. 64c, even though the change in applied bias

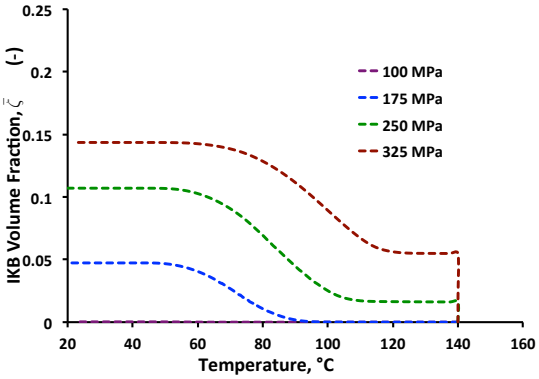

(a) Ti_2AlC phase averaged IKB volume fraction, $\bar{\zeta}$.

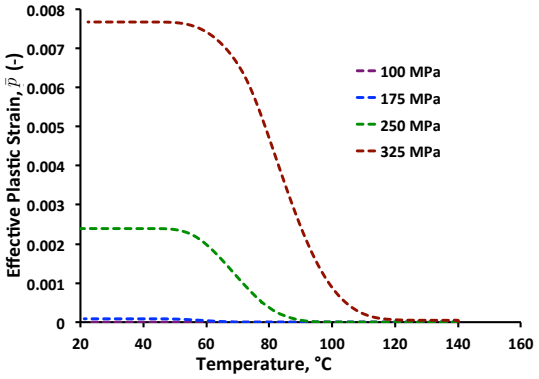

(b) Ti_2AlC phase averaged effective plastic strain, $\bar{p}$

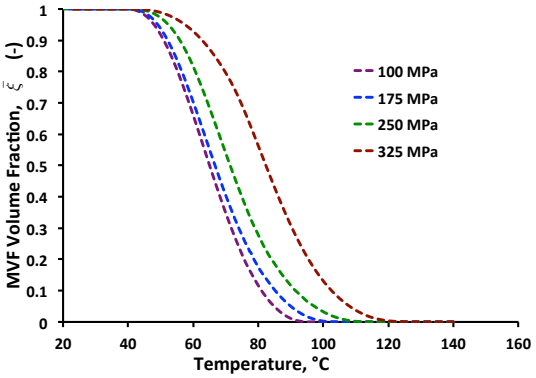

(c) NiTi phase averaged martensitic volume fraction, $\bar{\xi}$.

Figure 64: Evolution of different internal state variables through cooling paths with different applied effective compressive bias loads.

load remains constant the temperature difference between initiation of transformation does not and the 325 MPa case is shifter versus the other results. Whether this arises from SMA behavior or the earlier activation of nonlinear behaviors in the MAX phase cannot be determined but does point to an additional interaction.

The impact of these different responses is explored in Fig. 65 in which the phase averaged stress in the direction of loading of the different constituents is presented. Specifically, the Ti_2AlC and NiTi stresses are presented in Fig 65a and b, respectively. First, with respect to the Ti_2AlC phase, the results observed for the four cases show all show similar trends to those discussed with respect to Figfig:Ch5:250Case. Specifically, in all cases, an initial increase in magnitude with respect due to thermal expansion mismatch is noted followed by a small increase during initial transformation. A decrease in the stress magnitude is then observed during the latter stages of transformation. Although the cases vary in magnitude and intensity this general trend is followed and limited information may be gleaned from this result. It may be observed, however, that the transformation induced stress decrease is more pronounced in the elastic and IKB cases and the additional plastic mechanisms seem to diminish this effect. The NiTi results (Fig. 65, on the other hand, demonstrates this effect more clearly. Lower bias load cases show a pronounced stress magnitude increase through transformation. At larger load levels, and as additional plasticity is generated, this change in loading state is nearly damped out and only small nonlinearities in the stress evolution are noted.

Finally, the effective and constituent strains through the cooling cycle are presented in Fig. 66. The Ti_2AlC phase average stress is presented in Fig. 66a while the NiTi results are presented in Fig. 66b. In all cases, it can be observed that the SMA strain is larger than the corresponding deformations in the Ti_2AlC. With respect to the Ti_2AlC, the strains are primarily elastic although some small nonlinear defor-

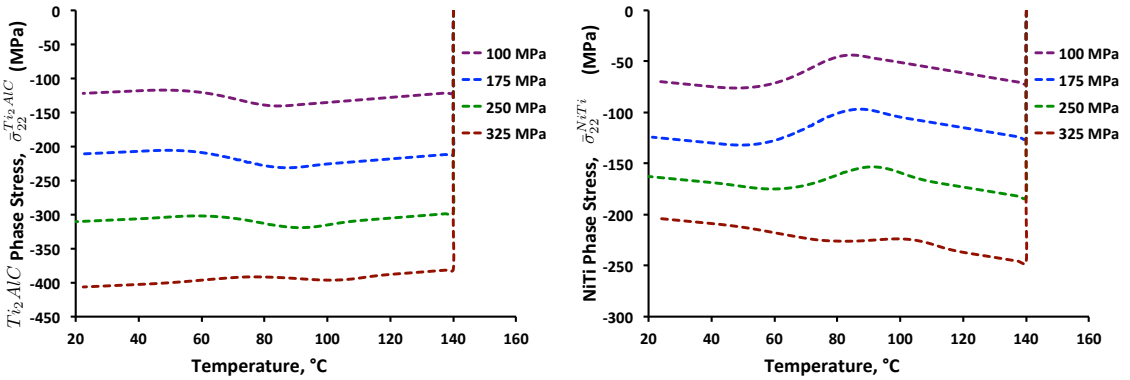

(a) Ti_2AlC phase averaged stress in the direction of applied loading, $\bar{\sigma}_{22}^{Ti_2AlC}$.

(b) NiTi phase averaged stress in the direction of applied loading, $\bar{\sigma}_{22}^{NiTi}$.

Figure 65: Evolution of constituent phase averaged stress in the direction of applied loading through cooling paths with different applied effective compressive bias loads.

mations are evident in the 175 MPa case. Through the plastic cases, larger strains are observed and generated through the transformation process. With respect to the NiTi content, larger strains are noted due to the transformation process. As was previously reported, these strains are lower than what would be expected for the bulk SMA due to the stress evolution through cooling. Therefore, in the effective results of Fig. 66c, nonlinear actuation strains are evident. Importantly, in these results, the presence of the IKB strains are not seen to substantially change the results versus that expected of the pure plasticity cases.

In taking the previous results together, it may be seen that the recoverable IKB mechanism incorporated into the MAX phase response does not substantially alter the behavior or interaction of the different phases. By comparing the observed behaviors in the 175 MPa case with only the IKB mechanism active and the 100 MPa elastic case, it can be seen that the two behaviors exhibit the same qualitative characteristics and most of the quantitative differences is likely associated with the load level. For instance, in the effective MVF response (Fig. 64c), transformation

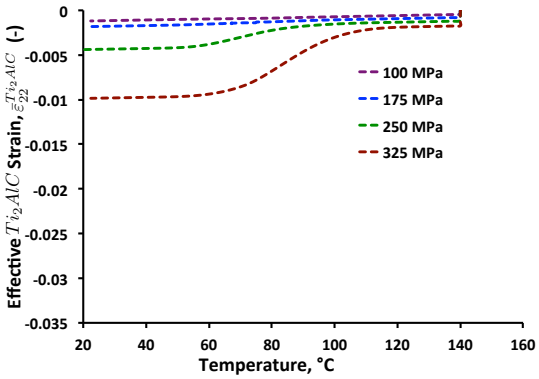

(a) Ti_2AlC phase averaged strain in the direction of applied loading, $\bar{\varepsilon}_{22}^{Ti_2AlC}$.

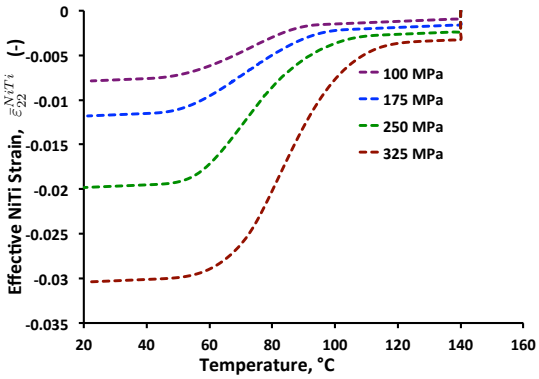

(b) NiTi phase averaged stain in the direction of applied loading, $\bar{\sigma}_{22}^{NiTi}$.

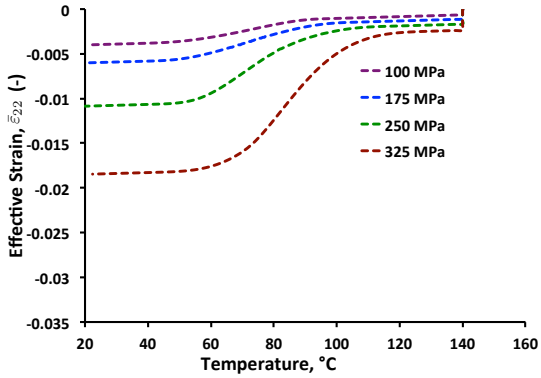

(c) Effective composite phase averaged strain in the direction of applied loading, $\bar{\varepsilon}_{22}$.

Figure 66: Evolution of phase averaged strain in the direction of applied loading through cooling paths with different applied effective compressive bias loads.

completes at nearly the same temperature at effective loads of 100 and 175 MPa. This stress invariance is characteristic of the elastic results presented and discussed in Chapter 2. In these cases, the stress redistribution effects are likely associated with the specific configurations here. When the plastic mechanism is activated at higher load levels, its response and features are observed to dominate the effective characteristics. Although this behavior is somewhat exaggerated in the assumed constitutive response, its influences are seen to quickly dominate and mask those of

the recoverable mechanism. This is likely associated with two effects. First, during nonlinear deformations the mechanical tangent modulus of the MAX phase materials is still substantially stiffer than the SMA – especially during transformation. Therefore, elastic like interactions result. Secondly, the kinking strains are substantially smaller than the plastic and especially transformation strains. The contributions of the kinking strain are essentially hidden due to these larger deformations. If the plastic strain magnitude is decreased the reversible strains may play a larger role, but they are still dominated by the transformation deformations.

6. CONCLUSIONS

In this work, the nonlinear, thermomechanical response of SMA-MAX phase composites was investigated. Experimental results have shown these materials to have a complex microstructure with dissimilar thermoelastic properties leading an already complex micromechanical problem. The nonlinear constitutive responses of the two base SMA and MAX phases only served to complicate this response and motivate the need for complementary modeling investigations. To accomplish this task, a series of models were constructed to investigate different features with an emphasis on the effective actuation behavior and associated interactions through temperature induced martensitic transformation. In this section, closure is brought to these investigations. First, in Section 6.1, a summary of the various methods and results are presented. Potential future endeavors are then presented in Section 6.2 to highlight the next steps.

6.1 Summary

Given the complex micromechanical and constitutive responses, a series of models were constructed to explore different features. First, an Eshelby-based micromechanical model was constructed in Chapter 2 and used to establish the effective transformation characteristics and the interaction of the stiff thermoelastic phase. Inelasticity associated with martensitic transformation was captured via the utilization of eigenstrains and a model coupling the micromechanical stress state with the SMA constitutive response was developed. Importantly, a transformation induced stress redistributed was observed that lead to near stress invariant martensitic finish and austenitic start transformation surfaces. Additionally, the reduction in transfor-

mation strain due to the presence of a stiff, blocking material was demonstrated. The developed model was then used to explore the impact of various material parameters on the effective behaviors.

To explore the response these composites through actuation loading paths, finite element techniques were utilized. Specifically, a series of reference microstructures were generated and used to investigate the nonlinear thermomechancial response. Image based methods using microtomography were adopted and used to generate both a reference and actual composite microstructure based on different material specimens. By considering the interaction of an SMA constitutive response incorporating martensitic transformation and an elastic-plastic approximation to the MAX phase behaviors, the evolution through an isobaric cooling–heating cycle was capture. In these cases, it was shown that thermally induced transformation leads to additional stress generation in the MAX phase and corresponding permanent deformations. Upon recovery, these irrecoverable strains produce a residual stress state and the development of this state was extensively explored via both geometries. The realistic microstructure included additional observations regarding the presence of porosity and a reaction layer resulting from processing. As such, a series of parametric studies were performed investigating the impact of these different parameters on the effective behaviors. The reaction layer content was demonstrated to have an especially pronounced impact on the residual stress state. Additionally, the numerical microstructures generated through image based techniques included a number of features and exhibited complicated architectures. To distill the impact of different characteristic features on the effective response, a series of simplified unit cells were constructed. By parameterizing these different features, the impact was identified and it was shown that continual, fiber reinforcement has a lower effective transformation strain and residual stress than either interpenetrating or spherical cases.

The results previously described focused on using a single-mechanism elastic-plastic model for the MAX phase response. Previous experiments have demonstrated MAX phases exhibit a more complicated, multimechanism response with recoverable, irrecoverable, a damage characteristics. To date, no model exists for this response. Therefore, a phenomenological, multimechanism model incorporating these different features was developed in this work and implemented as an Abaqus UMAT. A return mapping algorithm (RMA) implementation for the fully coupled case was developed along with a corresponding algorithmic tangent modulus. The model was then used to analyze experimental results of a Ti_2AlC specimen. Good agreement was seen between experimental and numerical results and permanent deformation as a result of damage and plasticity was demonstrated. The developed model was then used with a previous FE model to investigate the impact of the recoverable mechanisms on the effective response and the coupled response. Through these investigations, the prominence of the permanent mechanisms and stiff thermoelastic contrast over recoverable IKB formation was demonstrated in the composite response.

6.2 Future Work

This investigation focused on two key elements: MAX phase constitutive modeling and micromechanical modeling of the nonlinear composites. With respect to the former, the efforts here produced the first 3D model capable of capturing the relevant behaviors. Many of the interactions between the relevant mechanisms are treated in a first order way and as such a number of observed features and characteristics have yet to be incorporated. For instance, increased hardening with cycling has been experimentally observed but not incorporated into this model. High temperature, rate-dependent responses have been shown to produce interesting behaviors

but are not treated here as they are outside the domain of interest. Nonetheless, these effects pose an interesting challenge to be tackled. Of particular relevance to this work, an IKB explanation was adopted to explain the relevant results and used to motivate the model in this work. Experimentally and theoretically, the detailed understanding of this mechanism is still being investigated and additional results to this regard should be used to refine the interactions and responses used in this work. Furthermore, a multistep calibration process was adopted in this work to determine the relevant model parameters. Such an approach was necessary as distinguishing the contributions of the different behaviors (especially with respect to the permanent mechanisms) is not a trivial exercise from macroscopic experimental results. Improved methods to decouple the different responses from such results is an important task for not just model calibration but also model motivation and remains an exciting challenge – for many nonlinear materials, not just MAX phases. Numerically, the coupled multi surface problem posed by the constitutive model provides for a complex implementation. In general, methods to improve (*i*) speed and efficiency and (*ii*) global convergence properties should be investigated. These improvements are especially important for the composite case, as in some the results here the interactions between the responses lead to a non-proportional loading necessitating a robust implementation.

The SMA-MAX phase composites studied here provide a rich challenge in many aspects due to the complex material responses. Interestingly, and especially in the NiTi case, subtle changes in composition and processing can strongly influence the effective behavior. As discussed in Chapter 3, the sintering process used to produce these novel materials may lead to heterogeneous composition gradients. Accurate determination of the constituent material parameters in this case remains difficult because of this variation. Specifically, in the studies of this work, calibration of material

properties was performed off of bulk specimens produced via similar methods. The variations in composition and pressure states between the actual and idealized methods can substantially affect this process and substantial uncertainty exists around these properties. Therefore, and similar to the MAX phase responses, methodologies to distinguish and determine the actual properties need to be introduced and used to better identify the relevant responses. Along a similar vein, cyclic effects in the SMA phase were not directly treated. Shape memory alloys, and particularly NiTi, are well known to need a "training" cycle to thermomechanically stabilize the constitutive response. How this training evolves in this composite and its impact is not clear and both experimental and numerical investigations are needed to clarify the impact of this response – especially on load transfer characteristics. Finally, and potentially most interestingly, these composites exhibit multiple uncertainties and their impact needs to be quantified. Specifically, variability is expected both in terms of microstructural features like grain size, reaction layer thickness, pore size and shape amongst others and constitutive properties as was just discussed. Many of these features are unknown *a priori* and are subject to change due to subtle changes in manufacturing or processing conditions. Statistical investigations of the impact of both constitutive and microstructural uncertainties are needed to determine the relevant impact of each and help establish bounds on the relationships. With respect to shape memory alloys, these methods remain in their infancy but efforts towards this end could be essential in establishing not only effective property ranges but also correlations to different parameters.

REFERENCES

[1] Abaqus: Analysis User's Manual. Dassault Systèmes of America Corp., Woodlands Hills, CA (2007)

[2] Aboudi, J.: The generalized method of cells and high-fidelity generalized method of cells micromechanical models - a review. Mechanics of Advanced Materials and Structures **11**, 329–366 (2004)

[3] Abu Al-Rub, R.K., Voyiadjis, G.Z.: On the coupling of anisotropic damage and plasticity models for ductile materials. International Journal of Solids and Structures **40**, 2611–2643 (2003)

[4] Alecci, V., Bati, S.B., Ranocchiai, G.: Numerical homogenization techniques for the evaluation of mechanical behavior of a composite with SMA inclusions. Journal of the Mechanics of Materials and Structures **4**(10), 1675–1688 (2009)

[5] Anderson, A., Pedersen, D., Sivertsen, A., Sangesland, S.: Detailed study of shape memory alloys in oil well applications. Sintef petroleum research, Trondheim,Norway (1999)

[6] Angioni, S.L., Meo, M., Foreman, A.: Impact damage resistance and damage suppression properties of shape memory alloys in hybrid composites - a review. Smart Materials and Structures **20**, 013,001 (2011)

[7] Armstrong, W.D., Kino, H.: Martensitic transformations in a NiTi fiber reinforced 6061 aluminum matrix composite. Journal of Intelligent Material Systems and Structures **6**, 809–816 (1995)

[8] Arnaboldi, S., Bassani, P., Biffi, C.A., Tuissi, A., Carnevale, M., Lecis, N., LoConte, A., Previtali, B.: Simulated and experimental damping properties of a SMA/Fiber glass laminated composite. Journal of Materials Engineering and Performance **20**(4–5), 551–558 (2011)

[9] Ashby, M.F., Bréchet, Y.J.M.: Designing hybrid materials. Acta Materialia **53**, 5801–5821 (2003)

[10] Ashrafi, M.J., Arghavani, J., Naghdabadi, R., Sohrabpour, S.: A 3-D constitutive model for pressure-dependent phase transformation of porous shape memory alloys. Journal of the Mechanical Behavior of Biomedical Materials **42**, 292–310 (2015)

[11] ASTM: C20-00 Standard test methods for apparent porosity, water absorption, apparent specific gravity, and bulk density of burned refractory brick and shapes by boiling water. ASTM International (2004)

[12] Auricchio, F., Petrini, L.: A three-dimensional model describing stress-temperature induced solid phase transformations: thermomechanical coupling and hybrid composite applications. International Journal for Numerical Methods in Engineering **61**, 716–737 (2004)

[13] Aydogmus, T.: Processing of interpenetrating Mg-TiNi composites by spark plasma sintering. Material Science & Engineering A **624**, 261–270 (2015)

[14] Bansiddhi, A., Dunand, D.C.: Niobium wires as space holder and sintering aid for porous NiTi. Advanced Engineering Materials **13**(4), 301–305 (2011). DOI 10.1002/adem.201000241

[15] Barbero, E.J., Greco, F., Lonettie, P.: Continuum damage-healing mechanics with application to self-healing composites. International Journal of Damage Mechanics **14**, 51–81 (2009)

[16] Barrett, R., Gross, R.S.: Super-active shape-memory alloy composites. Smart Materials and Structures **5**, 255–260 (1996)

[17] Barsoum, M.W.: The $M_{N+1}AX_N$ phases: A new class of solids; thermodynamically stable nanolaminates. Progress in Solid State Chemistry **28**, 201–281 (2000)

[18] Barsoum, M.W., Ali, M., El-Raghy, T.: Processing and characterization of Ti_2AlC, Ti_2AlN, and $Ti_2AlC_{0.5}N_{0.5}$. Metallurgical and Material Transactions A **31A**, 1857–1865 (2000)

[19] Barsoum, M.W., El-Raghy, T.: Synthesis and characterization of a remarkable ceramic: Ti_3SiC_2. Journal of the American Ceramic Society **79**(7), 1953–1956 (1996)

[20] Barsoum, M.W., El-Raghy, T.: Room-temperature ductile carbides. Metallurgical and Material Transactions A **30A**, 363–369 (1999)

[21] Barsoum, M.W., Farber, L., El-Raghy, T.: Dislocations, kink bands, and room-temperature plasticity of Ti_3SiC_2. Metallurgical and Material Transactions A **30A**, 1727–1738 (1999)

[22] Barsoum, M.W., Radovic, M.: Elastic and mechanical properties of MAX phases. Annual Review of Materials Research **41**, 195–227 (2011)

[23] Barsoum, M.W., Zhen, T., Kalidindi, S.R., Radovic, M., Murugaiah, A.: Fully reversible, dislocation-based compressive deformation of Ti_3SiC_2 to 1 GPa. Nature Materials **2**, 107–111 (2003)

[24] Barsoum, M.W., Zhen, T., Zhou, A., Basu, S., Kalidindi, S.R.: Microscale modleing of kinking nonlinear elastc solids. Physical Review B **71**, 134,101 (2005)

[25] Baxevanis, T., Cox, A., Lagoudas, D.C.: Micromechanics of precipitated near-equiatomic Ni-rich NiTi shape memory alloys. Acta Mechanica **225**(4–5), 1167–1185 (2014)

[26] Baz, A., Ro, J.: Thermo-dynamic characteristics of nitinol reinforced composite beams. Composites Engineering **2**(5-7), 527–542 (1992)

[27] Baz, A., Ro, J.: Torsional stiffness of NiTiNOL-reinforced composite drive shafts. Composites Engineering **3**(12), 1119–1130 (1993)

[28] Bellouard, Y.: Shape memory alloys for microsystems: A review from a material perspective. Material Science & Engineering A **481-482**, 582–589 (2008)

[29] Benafan, O., Brown, J., Calkins, F.T., Kumar, P., Stebner, A.P., Turner, T.L., Vaidyanathan, R., Webster, J., Young, M.L.: Shape memory alloy actuator design: CASMART collaborative best practices and case studies. International Journal of Mechanics and Materials in Design **10**, 1–42 (2014). DOI 10.1007/s10999-013-9227-9

[30] Benveniste, Y.: A new approach to the application of mori-tanaka's theory in composite materials. Mechanics of Materials **6**, 147–157 (1987)

[31] Bewerse, C., Brinson, L.C., Dunand, D.C.: NiTi with 3D-interconnected micro channels produced by liquid phase sintering and electrochemical dissolution of steel tubes. Journal of Materials Processing Technology **214**, 1895–1899 (2014)

[32] Bhattacharya, R., Benitez, R., Radovic, M., Goulbourne, N.C.: High strain-rate response and deformation mechanisms in polycrystalline ti_2alc. Material Science & Engineering A **598**, 319–326 (2014)

[33] Bhattacharyya, A., Lagoudas, D.C.: The probabilistic influence of material uncertainties on the inelastic response of SMA composites. In: Proceedings of American Society of Mechanical Engineers - Materials Division: Recent Advances in Composite Materials, vol. 56, pp. 237–251 (1995)

[34] Birman, V.: Effect of elastic or shape memory alloy particles on the properties of fiber-reinforced composites. Journal of Mechanics of Materials and Structures **4**(7-8), 1209–1225 (2009)

[35] Birman, V.: Properties and response of composite material with spheroidal super elastic shape memory alloy inclusions subject to three dimensional stress state. Journal of Physics D: Applied Physics **43**, 225,402 (2010)

[36] de Blonk, B., Lagoudas, D.: Actuation of elastomeric rods with embedded two-way shape memory alloy actuators. Smart Materials and Structures **7**, 771–783 (1998)

[37] Bo, Z., Kurdila, A.J., Lagoudas, D.C., Webb, G.: Identification for a class of nonlinear models for SMA embedded elastomeric rods. In: Proceedings of SPIE, 1995 Smart Structures and Materials Conference, Smart Structures and Intelligent systems, vol. 2427, pp. 93–106 (1993)

[38] Boyd, J.G., Costanzo, F., Allen, D.H.: A micromechanics approach for constructing locally averaged damage dependent constitutive equations in inelastic composites. International Journal of Damage Mechanics **2**, 209–228 (1993)

[39] Boyd, J.G., Lagoudas, D.C.: Thermomechanical response of shape memory composites. Journal of Intelligent Material Systems and Structures **5**, 333–346 (1994)

[40] Boyd, J.G., Lagoudas, D.C.: A thermodynamical constitutive model for shape memory materials. Part I. The monolithic shape memory alloy. International Journal of Plasticity **12**(6), 805–842 (1996)

[41] Boyd, J.G., Lagoudas, D.C.: A thermodynamical constitutive model for shape memory materials. Part II. The SMA composite material. International Journal of Plasticity **12**(7), 843–873 (1996)

[42] Briggs, J.P., Ponte Castaneda, P.: Variational estimates for the effective response of shape memory alloy actuated fiber composites. Journal of Applied Mechanics **69**, 470–480 (2002). DOI 10.1115/1.1464873

[43] Brüsewitz, B., Vetter, U., Hofsäss, H., Barsoum, M.W.: Perturbed angular correlation studies of uniaxial compressive stressed zinc, titanium, rutile, Ti_2AlN, and Nb_2AlC. Journal of Physics: Condensed Matter **26**, 295,501 (2014)

[44] Buehler, W.J., Gilfrich, J.V., Wiley, R.C.: Effects of low-temperature phase changes on the mechanical properties of alloys near composition TiNi. Journal of Applied Physics **34**, 1475 (1963)

[45] Burton, D., Gao, X., Brinson, L.: Finite element simulation of a self-healing shape memory alloy composite. Mechanics of Materials **38**(5–6), 525–537 (2006)

[46] Calkins, F.T., Mabe, J.H.: Shape memory alloy based morphing aerostructures. Journal of Mechanical Design **132**, 111,012 (2010)

[47] Chaboche, J., Cailletaud, G.: Integration methods for complex plastic constitutive equations. Computer methods in Applied Mechanics and Engineering **133**, 125–155 (1996)

[48] Chaboche, J., Kanouté, P., Roos, A.: On the capabilities of mean-field approaches for the description of plasticity in metal matrix composites. International Journal of Plasticity **21**, 1409–1434 (2005)

[49] Chaboche, J., Kruch, S., Maire, J.F., Pottier, T.: Towards a micromechanics based inelastic and damage modeling of composites. International Journal of Plasticity **17**, 411–439 (2001)

[50] Chaboche, J.L., Lesne, P.M., Maire, J.F.: Continuum damage mechanics, anisotropy and damage deactivation for brittle materials like concrete and ceramic composites. International Journal of Damage Mechanics **4**, 5–22 (1995)

[51] Chatzigeorgiou, G., Chemisky, Y., Meraghni, F.: Computational micro to macro transitions for shape memory alloy composites using periodic homogenization. Smart Materials and Structures **24**, 035,009 (2015)

[52] Chaudhry, Z., Rogers, C.A.: Response of composite beams to an internal actuator force. Journal of Mechanical Design **114**, 343–348 (1992)

[53] Chaudhury, Z., Hailat, M., Liu, Y., Newaz, G.: Aluminum-based composites reinforced with SiC particles and NiTi fibers: influence of fiber dimensions and aging time on mechanical properties. Journal of Materials Science **46**, 1945–1955 (2011)

[54] Chemisky, Y., Chatzigeorgiou, G., Kumar, P., Lagoudas, D.C.: A constitutive model for cyclic actuation of high-temperature shape memory alloys. Mechanics of Materials **68**, 120–136 (2014)

[55] Chemisky, Y., Cuval, A., Patoor, E., Ben Zineb, T.: Constitutive model for shape memory alloys including phase transformation, martensitic reorientation and twins accommodation. Mechanics of Materials **43**(7), 361 – 376 (2011)

[56] Chemisky, Y., Duval, A., Piotrowski, B., Ben Zineb, T., Tahiri, V., Patoor, E.: Numerical tool for SMA material simulation: Application to composite structure design. Smart Materials and Structures **18**(104012) (2009). DOI 10.1088/0964-1726/18/10/104012

[57] Cheng, F., Hu, L., Reddy, J.N., Karaman, I., Hoffman, E., Radovic, M.: Temperature-dependent thermal properties of a shape memory alloy/MAX phase composite: Experiments and modeling. Acta Materialia **68**, 267–278 (2014)

[58] Cherkaoui, M., Sun, Q.P., Song, G.Q.: Micromechanics modeling of composite with ductile matrix and shape memory alloy reinforcement. International Journal of Solids and Structures **37**(11), 1577 – 1594 (2000)

[59] Coleman, B.D., Gurtin, M.E.: Thermodynamics with internal state variables. The Journal of Chemical Physics **47**(2), 597–613 (1967)

[60] Coleman, B.D., Noll, W.: The thermodynamics of elastic materials with heat conduction and viscosity. Archive for Rational Mechanics and Analysis **13**, 167–178 (1963)

[61] Collard, C., Ben Zineb, T.: Simulation of the effect of elastic precipitates in SMA materials based on a micromechanical model. Composites: Part B **43**, 2560–2576 (2012)

[62] Collard, C., Ben Zineb, T., Patoor, E., Salah, M.O.B.: Micromechanical analysis of precipitate effects on shape memory alloys behavior. Material Science & Engineering A **481–482**, 366–370 (2008)

[63] Cox, A., Franco, B., Baxevanis, T., Karaman, I., Lagoudas, D.: Predictive constitutive modeling of precipitated Ni-rich NiTi SMAs. in preparation

[64] Damanpack, A.R., Aghdam, M.M., Shakeri, M.: Micromechanics of shape memory alloy fiber-reinforced composites subjected to multi-axial non-proportional loadings. Journal of Intelligent Material Systems and Structures p. In Press (2014). DOI 10.1177/1045389X14556165

[65] Damanpack, A.R., Aghdam, M.M., Shakeri, M.: Micro-mechanics of composite with SMA fibers embedded in metallic/polymeric matrix under off-axial loadings. European Journal of Mechanics A/Solids **49**, 467–480 (2015)

[66] Dixit, M., Newkirk, J.W., Mishra, R.S.: Properties of friction stir-processed AL 1100-NiTi composite. Scripta Materialia **56**, 34–52 (2007)

[67] Doghri, I., Adam, L., Bilger, N.: Mean-field homogenization of elasto-viscoplastic composites based on a general incrementally affine linearization method. International Journal of Plasticity **26**, 219–238 (2010)

[68] Doghri, I., Brassart, L., Adam, L., Gérard, J.S.: A second-moment incremental formulation for the mean-field homogenization of elasto-plastic composites. International Journal of Plasticity **27**, 352–371 (2011)

[69] Dong, J., Cai, C.S., Okeil, A.M.: Overview of potential and existing applications of shape memory alloys in bridges. Journal of Bridge Engineering **16**, 305–315 (2011)

[70] Drugan, W.J., Willis, J.R.: A micromechanics–based nonlocal constitutive equation and estimates of representative volume element size for elastic composites. J. Mech. Phys. Solids **44**(4), 497–524 (1996)

[71] Duerig, T., Pelton, A., Stöckel, D.: An overview of NiTiNOL medical applications. Material Science & Engineering A **273–275**, 149–160 (1999)

[72] Dunand, D.C., Mari, D., Bourke, M.A.M., Roberts, J.A.: NiTi and NiTi-TiC composites: Part IV. neutron diffraction study of twinning and shape-memory recovery. Metallurgical and Material Transactions A **27A**, 2820–2836 (1996)

[73] El-Raghy, T., Barsoum, M.W., Zavaliangos, A., Kalidindi, S.R.: Processing and mechanical properties of ti$_3$sic$_2$: II, effect of grain size and deformation temperature. Journal of the American Ceramic Society **82**(10), 2855–2860 (1999)

[74] El-Raghy, T., Zavaliangos, A., Barsoum, M.W., Kalidindi, S.R.: Damage mechanisms around hardness indentations in Ti_3SiC_2. Journal of the American Ceramic Society **80**(2), 513–516 (1997)

[75] Entchev, P.B., Lagoudas, D.C.: Modeling porous shape memory alloys using micromechanical averaging techniques. Mechanics of Materials **34**(1), 1–24 (2002)

[76] Entchev, P.B., Lagoudas, D.C.: Modeling of transformation-induced plasticity and its effect on the behavior of porous shape memory alloys: Part II: Porous SMA response. Mechanics of Materials **36**(9), 893–913 (2004)

[77] Eshelby, J.D.: The determination of the elastic field of an ellipsoidal inclusion, and related problems. Proceedings of the Royal Society of London. Series A, Mathematical and Physical Sciences **241**(1226), 376–396 (1957)

[78] Farvizi, M., Ebadzadeh, T., Vaezi, M.R., Yoon, E.Y., Kim, Y.J., Kim, H.S., Simchi, A.: Microstructural characterization of HIP consolidated NiTi-nano Al_2O_3 composites. Journal of Alloys and Compounds **606**, 21–26 (2014)

[79] Feng, X., Sui, J., Cai, W.: Processing of multi-walled carbon nanotube-reinforced TiNi composites by hot pressed sintering. Journal of Composite Materials **45**(15), 1553–1557 (2011). DOI 10.1177/0021998310383734

[80] Firstov, G.S., Van Humbeeck, J., Koval, Y.N.: High temperature shape memory alloys problems and prospects. Journal of Intelligent Material Systems and Structures **17**, 1041 (2006)

[81] Frank, F.C., Stroh, A.N.: On the theory of kinking. Proceedings of the Physical Society. Section B **65**(1), 811–821 (1952)

[82] Freed, Y., Aboudi, J.: Micromechanical investigation of plasticity-damage coupling of concrete reinforced by shape memory alloy fibers. Smart Materials and Structures **17** (2008). DOI 015046

[83] Freed, Y., Aboudi, J.: Micromechanical prediction of the two-way shape memory effect in shape memory alloy composites. International Journal of Solids and Structures **46**, 1634–1647 (2009)

[84] Freed, Y., Aboudi, J.: Thermomechanically coupled micromechanical analysis of shape memory alloy composites undergoing transformation induced plasticity. Journal of Intelligent Material Systems and Structures **20**, 23–38 (2009)

[85] Freed, Y., Aboudi, J., Gilat, R.: Thermomechanically micromechanical modeling of prestressed concrete reinforced with shape memory alloy fibers. Smart Materials and Structures **16**, 717–727 (2007)

[86] Freed, Y., Aboudi, J., Gilat, R.: Investigation of shape memory alloy honeycombs by means of a micromechanical analysis. Modeling and Simulation in Materials Science and Engineering **56**, 3003–3020 (2008)

[87] Fukami-Ushiro, K.L., Dunand, D.C.: NiTi-NiTi-TiC composites: Part III. shape-memory recovery. Metallurgical and Material Transactions A **27A**, 193–203 (1996)

[88] Fukami-Ushiro, K.L., Mari, D., Dunand, D.C.: NiTi-NiTi-TiC composites: Part II. compressive mechanical properties. Metallurgical and Material Transactions A **27A**, 183–191 (1996)

[89] Gavazzi, A.C., Lagoudas, D.C.: On the numerical evaluation of eshelby's tensor and its application to elastoplastic fibrous composites. Computational Mechanics **7**, 13–19 (1990)

[90] González, C., Segurado, J., LLorca, J.: Numerical simulation of elasto-plastic deformation of composites: evolution of stress microfilms and implications for

homogenization models. Journal of the Mechanics and Physics of Solids **52**, 1573—1593 (2004)

[91] Groeber, M., Ghosh, S., Uchic, M.D., Dimiduk, D.M.: A framework for automated analysis and simulation of 3D polycrystalline microstructures. Part 1: Statistical characterization. Acta Materialia **56**, 1257–1273 (2008)

[92] Groeber, M., Ghosh, S., Uchic, M.D., Dimiduk, D.M.: A framework for automated analysis and simulation of 3D polycrystalline microstructures. Part 2: Synthetic structure generation. Acta Materialia **56**, 1274–1287 (2008)

[93] Guitton, A., Van PPetegem, S., Tromas, C., Joulain, A., Van Swygenhoven, H., Thilly, L.: Effect of microstructure anisotropy on the deformation of MAX polycrystals studied by *in-situ* compression combined with neutron diffraction. Applied Physics Letters **104**, 241,910 (2014)

[94] Hahnlen, R., Dapino, M.J.: NiTi-Al interface strength in ultrasonic additive manufacturing composites. Composites: Part B **59**, 101–108 (2014)

[95] Hartl, D., Lagoudas, D., Mabe, J., Calkins, F.: Use of Ni60Ti shape memory alloy for active jet engine chevron application, Part I: Thermomechanical characterization. Smart Materials and Structures **19**(1), 015,020 (2009)

[96] Hartl, D., Lagoudas, D., Mabe, J., Calkins, F., Mooney, J.: Use of Ni60Ti shape memory alloy for active jet engine chevron application, Part II: Experimentally validated numerical analysis. Smart Materials and Structures **19**(1), 015,021 (2009)

[97] Hartl, D.J., Chatzigeorgiou, G., Lagoudas, D.C.: Three-dimensional modeling and numerical analysis of rate-dependent irrecoverable deformation in shape memory alloys. International Journal of Plasticity **26**, 1485–1507 (2010)

[98] Hartl, D.J., Chemisky, Y., Meraghni, F.: Three-dimensional constitutive model considering transformation-induced damage and resulting fatigue failure in shape memory alloys. In: Proceedings of SPIE, Smart Structures and Materials, vol. 9058-905805, pp. 1–8. San Diego, CA (2014). DOI 10.1117/12.2046668

[99] Hartl, D.J., Lagoudas, D.: Aerospace applications of shape memory alloys. Proceedings of the Institution of Mechanical Engineers, Part G: Journal of Aerospace Engineering **221 (Special Issue)**, 535–552 (2007)

[100] Hartl, D.J., Lagoudas, D.: Constitutive modeling and structural analysis considering simultaneous phase transformation and plastic yield in shape memory alloys. Smart Materials and Structures **18**(10) (2009)

[101] Heller, L., Vokoun, D., Sittner, P., Finckh, H.: 3D flexible NiTi-braided elastomer composites for smart structure applications. Smart Materials and Structures **21** (2012). DOI 10.1088/0964-1726/21/4/045016

[102] Herzog, H., Jacquet, E.: From a shape memory alloys model implementation to a composite behavior. Computational Material Science **39**, 365–375 (2007)

[103] Hesebeck, O.: On an isotropic damage mechanics model for ductile materials. International Journal of Damage Mechanics **10**, 325–346 (2001)

[104] Hill, R.: Elastic properties of reinforced solids: some theoretical principles. Journal of the Mechanics and Physics of Solids **13**, 357–371 (1963)

[105] Hill, R.: A self-consistent mechanics of composite materials. Journal of the Mechanics and Physics of Solids **13**, 213–222 (1965)

[106] Hu, J., Wu, G., Zhang, Q., Gou, H.: Mechanical properties and damping capacity of $SiC_p/TiNi_f$/Al composite with different volume fraction of SiC particle. Composites: Part B **66**, 400–406 (2014)

[107] Hu, L., Benitez, R., Basu, S., Karaman, I., Radovic, M.: Processing and characterization of porous Ti_2AlC with controlled porosity and pore size. Acta Materialia **60**(18), 6266–6277 (2012)

[108] Hu, L., Kothalkar, A., Proust, G., Karaman, I., Radovic, M.: Fabrication and characterization of NiTi/ti_3sic_2 and NiTi/ti_2alc composites. Journal of Alloys and Compounds **610**, 635–644 (2014)

[109] Huang, M., Brinson, L.C.: A multi variant model for single crystal shape memory alloy behavior. Journal of the Mechanics and Physics of Solids **46**(8), 1379–1409 (1998)

[110] Huet, C.: Coupled size and boundary–condition effects in viscoelastic heterogeneous and composite bodies. Mech. Mater. **31**(12), 787–829 (1999)

[111] Jani, J.M., Leary, M., Subic, A., Gibson, M.A.: A review of shape memory alloy research applications and opportunities. Materials and Design **56**, 1078–1113 (2014)

[112] Jia, J., Rogers, C.A.: Formulation of a mechanical model for composites with embedded SMA actuators. Journal of Mechanical Design - Transactions of the ASME **114**, 670–676 (1992)

[113] Jones, N.G., Humphrey, C., Connor, L.D., Wilhelmsson, O., Hultman, L., Stone, H.J., Giuliani, F., Clegg, W.J.: On the relevance of kinking to reversible hysteresis in MAX phases. Acta Materialia **69**, 149–161 (2014)

[114] Kalidindi, S.R., Zhen, T., Barsoum, M.W.: Macroscale constitutive modeling of kinking nonlinear elastic solids. Material Science & Engineering A **418**, 95–98 (2006)

[115] Kanit, T., Forest, S., Galliet, I., Mounoury, V., Jeulin, D.: Determination of the size of the representative volume element for random composites: Statistical and numerical approach. Int. J. Solids Struct. **40**(13–14), 3647–3679 (2003)

[116] Karaca, H., Karaman, I., Basaran, B., Ren, Y., Chumlyakov, Y., Maier, H.: Magnetic field-induced phase transformation in NiMnCoIn magnetic shape-memory alloys - a new actuation mechanism with large work output. Advanced Functional Materials **19**, 983–998 (2009)

[117] Kim, H.J., Song, S.H., Ahn, S.H.: A turtle-like swimming robot using a smart soft composite (SSC) structure. Smart Materials and Structures **22**, 014,007 (2013)

[118] Kirkby, E.L., Rule, J.D., Michaud, V.J., Sottos, N.R., White, S.R., Månson, J.A.E.: Embedded shape-memory alloy wires for improved performance of self-healing polymers. Advanced Functional Materials **18**, 2253–2260 (2008)

[119] Kohlhaas, B., Klinkel, S.: An fe^2 model for the analysis of shape memory alloy fiber-composites. Computational Mechanics **55**, 421–437 (2015)

[120] Kothalkar, A.D., Benitez, R., Hu, L., Radovic, M., Karaman, I.: Thermomechanical response and damping behavior of shape memory alloy - max phase composites. Metallurgical and Material Transactions A **45A**, 2646–2658 (2014)

[121] Kumar, P.K., Caer, C., Atkinson, G., Patoor, E., Lagoudas, D.C.: The influence of stress and temperature on the residual strain generated during pseudoelastic cycling of niti sma wires. In: Proceedings of SPIE, vol. 7978, pp. 306–312 (2006)

[122] Lagoudas, D. (ed.): Shape Memory Alloys: Modeling and Engineering Applications. Springer-Verlag, New York (2008)

[123] Lagoudas, D., Entchev, P.: Modeling of transformation-induced plasticity and its effect on the behavior of porous shape memory alloys: Part I: Constitutive model for fully dense SMAs. Mechanics of Materials **36**(9), 865–892 (2004)

[124] Lagoudas, D., Hartl, D., Chemisky, Y., Machado, L., Popov, P.: Constitutive model for the numerical analysis of phase transformation in polycrystalline shape memory alloys. International Journal of Plasticity **32–33**, 155–183 (2012)

[125] Lagoudas, D.C., Bo, Z., Qidwai, M.A.: A unified thermodynamic constitutive model for SMA and finite element analysis of active metal matrix composites. Mechanics of Composite Materials and Structures **3**, 153–179 (1996)

[126] Lagoudas, D.C., Boyd, J.G., Bo, Z.: Micromechanics of active composites with SMA fibers. Journal of Engineering Materials and Technology **116**, 337–347 (1994)

[127] Lagoudas, D.C., Entchev, P.B., Popov, P., Patoor, E., Brinson, L.C., Gao, X.: Shape memory alloys, Part II: Modeling of polycrystals. Mechanics of Materials **38**(5–6), 430–462 (2006)

[128] Lagoudas, D.C., Gavazzi, A.C., Nigam, H.: Elastoplastic behavior of metal matrix composites based on incremental plasticity and the Mori-Tanaka averaging scheme. Computational Mechanics **8**, 193–203 (1991)

[129] Lagoudas, D.C., Moorthy, D., Qidwai, M.A., Reddy, J.N.: Modeling of the thermomechanical response of active laminates with SMA strips using the layerwise finite element method. Journal of Intelligent Material Systems and Structures **8**, 476–488 (1997)

[130] Lagoudas, D.C., Tadjbakhsh, I.G.: Active flexible rods with embedded SMA fibers. Smart Materials and Structures **1**, 162–167 (1992)

[131] Lagoudas, D.C., Tadjbakhsh, I.G.: Deformations of active flexible rods with embedded line actuators. Smart Materials and Structures **2**, 71–81 (1993)

[132] Lebensohn, R.A., Ponte Casta neda, P., Brenner, R., Castelnau, O.: Full-field vs. homogenization methods to predict microstructure-property relations for polycrystalline materials. In: S. Ghosh, D. Dimiduk (eds.) Computational Methods for Microstructure-Property Relationships, pp. 393–441. Springer-Verlag, New York (2011)

[133] Lee, J., Hwang, J., Lee, D., Ryu, H.J., Hong, S.H.: Enhanced mechanical properties of spark plasma sintered NiTi composites reinforced with carbon nanotubes. Journal of Alloys and Compounds **617**, 505–510 (2014)

[134] Lee, J.K., Taya, M.: Strengthening mechanism of shape memory alloy reinforced metal matrix composite. Scripta Materialia **51**, 443–447 (2004)

[135] Lemaitre, J., Chaboche, J.L.: Mechanics of Solid Materials. Cambridge University Press, Cambridge, UK (1990)

[136] Leng, J., Lan, X., Liu, Y., Du, S.: Shape-memory polymers and their composites: Stimulus methods and applications. Progress in Materials Science **56**, 1077–1135 (2011)

[137] Lester, B.T., Baxevanis, T., Chemisky, Y., Lagoudas, D.C.: Shape memory alloy composite systems: A review and current perspectives. Acta Mechanica **Submitted** (2015)

[138] Lester, B.T., Chemisky, Y., Lagoudas, D.C.: Transformation characteristics of SMA composites. Smart Materials and Structures **20**, 094,002 (2011)

[139] Lester, B.T., Chemisky, Y., Qidwai, S.M., Geltmacher, A.B., Everett, R.K., Lagoudas, D.: Hybrid shape memory alloy composites for extreme environments. In: Proceedings of 22nd International Conference on Adaptive Structures and Technologies, vol. 083, pp. 1–8 (2011)

[140] Lester, B.T., Chemisky, Y., Qidwai, S.M., Geltmacher, A.B., Everett, R.K., Lagoudas, D.: Virtual processing of hybrid shape memory alloy composites. In: Proceedings of ASME 2011 Conference on Smart Materials, Adaptive Structures, and Intelligent Systems, vol. 5083, pp. 1–10 (2011)

[141] Lester, B.T., Kothalkar, A., Karaman, I., Radovic, M., Lagoudas, D.C.:

[142] Levitas, V.I., Ozsoy, I.B.: Thermomechanical modeling of stress-induced transformations. Part 1. thermodynamics and kinetics of coupled interface propagation and reorientation. International Journal of Plasticity **25**, 239–280 (2009)

[143] Lewis, A.C., Geltmacher, A.B.: Image-based modeling of the response of experimental 3D microstructures to mechanical loading. Scripta Materialia **55**, 81–85 (2006)

[144] Lewis, A.C., Qidwai, S.M., Jackson, M., Geltmacher, A.B.: Strategies for of 3-D experimental data with modeling and simulation. Journal of the Minerals, Metals, and Materials Society **63**(3), 35–39 (2011)

[145] Li, D.S., Zhang, X.P., Mai, Y.W.: Lightweight NiTi shape memory alloy based composites with high damping capacity and high strength. Journal of Alloys and Compounds **490**, L15–L19 (2010)

[146] Liang, C., Jia, J., Rogers, C.A.: Behavior of shape memory alloy reinforced composite plates Part II: Results. In: Proceedings of the 30^{th} AIAA/ASME/ASCE/AHS/ACS Structures, Structural Dynamics and Materials Conference, vol. 1331, pp. 1504–1513 (1989)

[147] Liang, C., Rogers, C.A., Fuller, C.R.: Acoustic transmission and radiation analysis of adaptive shape-memory alloy reinforced laminated plates. Journal of Sound and Vibration **145**(1), 23–41 (1991)

[148] Lu, Z., Weng, G.: A two-level micromechanical theory for a shape-memory alloy reinforced composite. International Journal of Plasticity **16**(10-11), 1289–1307 (2000)

[149] Lubliner, J.: Plasticity Theory. Macmillan Publishing Company, New York (1990)

[150] Ma, J., Karaman, I., Noebe, R.D.: Medical applications of shape memory alloys. International Materials Reviews **55**(5), 257–315 (2010)

[151] Machado, L., Savi, M.: Medical applications of shape memory alloys. Brazilian Journal of Medical and Biological Research **36**, 683–691 (2003)

[152] Marfia, S.: Micro-macro analysis of shape memory alloy composites. International Journal of Solids and Structures **42**, 3677–3699 (2005)

[153] Marfia, S., Sacco, E.: Analysis of SMA composite laminates using a multi scale modelling technique. International Journal for Numerical Methods in Engineering **70**, 1182–1208 (2007)

[154] Marfia, S., Sacco, E.: Micromechanics and homogenization of SMA-wire reinforced materials. Journal of Applied Mechanics **72**, 259–268 (2007). DOI 10.1115/1.1839186

[155] Mari, D., Dunand, D.C.: NiTi and NiTi-TiC composites: Part I. transformation and thermal cycling behavior. Metallurgical and Material Transactions A **26A**, 2833–2847 (1995)

[156] Meraghni, F., Chemisky, Y., Piotrowski, B., Echchorfi, R., Bourgeois, N., Patoor, E.: Parameter identification of a thermodynamic model for superelastic shape memory alloys using analytical calculation of the sensitivity matrix. European Journal of Mechanics - A/Solids **45**, 226–237 (2014)

[157] Migliori, A., Sarrao, J.L., Visscher, W.M., Bell, T.M., Lei, M., Fisk, Z., Leisure, R.G.: Resonant ultrasound spectroscopic techniques for measurement of the elastic moduli of solids. Physica B **183**, 1–24 (1993)

[158] Morgan, N.B.: Medical shape memory alloy applications - the market and its products. Material Science & Engineering A **378**, 16–23 (2004)

[159] Mori, T., Tanaka, K.: Average stress in matrix and average elastic energy of materials with misfitting inclusions. Acta Metallurgica **21**, 571–574 (1973)

[160] Mura, T.: Micromechanics of Defects in Solids, 2nd revised edn. Mechanics of Elastic and Inelastic Solids. Kluwer Academic Publisher, Dordrecht (1987)

[161] Murakami, S.: Mechanical modeling of material damage. Journal of Applied Mechanics **55**, 288–286 (1988)

[162] Ponte Casta neda, P.: Second-order homogenization estimates for nonlinear composites incorporating field fluctuations: I – theory. Journal of the Mechanics and Physics of Solids **50**, 737–757 (2002)

[163] Ponte Casta neda, P.: Second-order homogenization estimates for nonlinear composites incorporating field fluctuations: II – applications. Journal of the Mechanics and Physics of Solids **50**, 759–782 (2002)

[164] Nemat-Nasser, S., Sui, Y., Guo, W., Isaacs, J.: Experimental characterization and micromechanical modeling of superelastic response of a porous NiTi shape-memory alloy. Journal of the Mechanics and Physics of Solids **53**, 2320–2346 (2005)

[165] Neuking, K., Abu-Zarifa, A., Eggeler, G.: Polymer/NiTi-composites: Fundamental aspects, processing and properties. Advanced Engineering Materials **481–482**, 1014–1023 (2008)

[166] Neurohr, A.J., Dunand, D.C.: Mechanical anisotropy of shape-memory NiTi with two-dimensional networks of micro-channels. Acta Materialia **59**, 4616–4630 (2011)

[167] Neurohr, A.J., Dunand, D.C.: Shape-memory NiTi with two-dimensional networks of micro-channels. Acta Biomaterialia **7**, 1862–1872 (2011)

[168] Ni, Q.Q., Zhang, R.X., Natsuki, T., Iwamoto, M.: Stiffness and vibration characteristics of SMA/ER3 composites with shape memory alloy short fibers. Composite Structures **79**, 501–507 (2007)

[169] Oehler, S.D., Hartl, D.J., Lopez, R., Malak, R.J., Lagoudas, D.C.: Design optimization and uncertainty analysis of SMA morphing structures. Smart Materials and Structures **21**, 094,016 (2012)

[170] Otsuka, K., Ren, X.: Physical metallurgy of Ti–Ni-based shape memory alloys. Progress in Materials Science **50**, 511–678 (2005)

[171] Otsuka, K., Wayman, C.M. (eds.): Shape Memory Materials. Cambridge University Press, Cambridge (1999)

[172] Ozbulut, O.E., Hurlebaus, S., Desroches, R.: Seismic response control using shape memory alloys: A review. Journal of Intelligent Material Systems and Structures **22**, 1531 (2011)

[173] Panico, M., Brinson, L.: A three-dimensional phenomenological model for martensite reorientation in shape memory alloys. Journal of the Mechanics and Physics of Solids **55**, 2491–2511 (2007)

[174] Panico, M., Brinson, L.C.: Computational modeling of porous shape memory alloys. International Journal of Solids and Structures **45**, 5613–5626 (2008)

[175] Park, J.S., Kim, S.H., Jung, S.N.: Optimal design of a variable-twist prop rotor incorporating shape memory alloy hybrid composites. Composite Structures **93**, 2288–2298 (2011)

[176] Park, J.S., Kim, S.H., Jung, S.N., Lee, M.K.: Design and analysis of variable-twist tilt rotor blades using shape memory alloy hybrid composites. Smart Materials and Structures **20**, 015,001 (2011)

[177] Patoor, E., Eberhardt, A., Berveiller, M.: Micromechanical modelling of superelasticity in shape memory alloys. Journal de Physique IV France **6**, C1—277–292 (1996)

[178] Patoor, E., Lagoudas, D.C., Entchev, P.B., Brinson, L.C., Gao, X.: Shape memory alloys, Part I: General properties and modeling of single crystals. Mechanics of Materials **38**(5–6), 391–429 (2006)

[179] Pierard, O., González, C., Seguarado, J., LLorca, J., Doghri, I.: Micromechanics of elasto-plastic materials reinforced with ellipsoidal inclusions. International Journal of Solids and Structures **44**, 6945–6962 (2007)

[180] Pierard, O., LLorca, J., Seguarado, J., Doghri, I.: Micromechanics of particle-reinforced elasto-vicscoplastic composites: Finite element simulations versus affine homogenization. International Journal of Plasticity **23**, 1041–1060 (2007)

[181] Pindera, M.J., Khatam, H., Drago, A., Bansal, Y.: Micromechanics of spatially uniform heterogeneous media: A critical review and emerging approaches. Composites Part B: Engineering **40**(5), 349–378 (2009)

[182] Pinto, F., Ciampa, F., Meo, M., Polimeno, U.: Multifunctional SMArt composite material for *in situ* NDT/SHM and de-icing. Smart Materials and Structures **21**, 105,010 (2012)

[183] Piotrowski, B., Ben Zineb, T., Patoor, E., Eberhardt, A.: A finite element-based numerical tool for $Ni_{47}Ti_{44}Nb_9$ SMA structures design: application to tightening rings. Journal of Intelligent Material Systems and Structures **23**, 141–153 (2012)

[184] Piotrowski, B., Ben Zineb, T., Patoor, E., Eberhardt, A.: Modeling of niobium precipitates effect on the $Ni_{47}Ti_{44}Nb_9$ shape memory alloy behavior. International Journal of Plasticity **36**, 130–147 (2012)

[185] Pons, J., Cesari, E., Seguí, C., Masdeu, F., Santamarta, R.: Ferromagnetic shape memory alloys: Alternatives to Ni-Mn-Ga. Material Science & Engineering A **481–482**, 57–65 (2008)

[186] Poon, B., Ponsoon, L., Zhao, J., Ravichandran, G.: Damage accumulation and hysteretic behavior of MAX phase materials. Journal of the Mechanics and Physics of Solids **59**(10), 2238–2257 (2011)

[187] Porter, G.A., Liaw, P.K., Tiegs, T.N., Wu, K.H.: Ni-Ti SMA-reinforced Al composites. Journal of the Minerals, Metals, and Materials Society **52**(10), 52–56 (2000)

[188] Qidwai, M.A., DeGiorgi, V.G.: A computational mesoscale evaluation of material characteristics of porous shape memory alloys. Smart Materials and Structures **11**, 435–443 (2002)

[189] Qidwai, M.A., DeGiorgi, V.G.: Numerical assessment of the dynamic behavior of hybrid shape memory alloy composite. Smart Materials and Structures **13**, 134–145 (2004)

[190] Qidwai, M.A., Entchev, P.B., Lagoudas, D.C., DeGiorgi, V.G.: Modeling of the thermomechanical behavior of porous shape memory alloys. International Journal of Solids and Structures **38**, 8653–8671 (2001)

[191] Qidwai, M.A., Lagoudas, D.C.: Numerical implementation of a shape memory alloy thermomechanical constitutive model using return mapping algorithms. International Journal for Numerical Methods in Engineering **47**, 1123–1168 (2000)

[192] Qidwai, M.A., Lagoudas, D.C.: On the thermodynamics and transformation surfaces of polycrystalline NiTi shape memory alloy material. International Journal of Plasticity **16**, 1309–1343 (2000)

[193] Qidwai, M.A.S., Lewis, A.C., Geltmacher, A.B.: Using image-based computational modeling to study microstructure-yield correlations in metals. Acta Materialia **57**, 4233–4247 (2009)

[194] Qiu, Z.X., Yao, X.T., Yuan, J., Soutis, C.: Experimental research on strain monitoring in composite plates using embedded SMA wires. Smart Materials and Structures **48**, 1047–1053 (2006)

[195] Qu, J., Cherkaoui, M.: Fundamentals of Micromechanics of Solids. John Wiley & Sons, Inc., Hoboken, NJ (2006)

[196] Radovic, M., Barsoum, M.W., El-Raghy, T., Seidensticker, J., Weiderhorn, S.: Tensile properties of Ti_3SiC_2 in the 25-1300°C temperature range. Acta Materialia **48**, 453–459 (2000)

[197] Radovic, M., Barsoum, M.W., El-Raghy, T., Weiderhorn, S.M., Luecke, W.E.: Effect of temperature, strain rate and grain size on the mechanical response of Ti_3SiC_2 in tension. Acta Materialia **50**, 453–459 (2002)

[198] Radovic, M., Barsoum, M.W., Ganguly, A., Zhen, T., Finkel, P., Kalindindi, S.R., Lara-Curzio, E.: On the elastic and mechanical damping of Ti_3SiC_2, Ti_3GeC_2, $Ti_3Si_{0.5}Al_{0.5}C_2$, and Ti_2AlC in the 300-1573 K temperature range. Acta Materialia **54**, 2757–2767 (2006)

[199] Radovic, M., Lara-Curzio, E., Riester, L.: Comparison of different experimental techniques for determination of elastic properties of solids. Material Science & Engineering A **368**, 56–70 (2004)

[200] Ratna, D., Karger-Kocsis, J.: Recent advances in shape memory polymers and composites: a review. Journal of Materials Science **43**, 254–269 (2008)

[201] Reddy, J.N.: An Introduction to Nonlinear Finite Element Analysis. Oxford University Press, New York (2004)

[202] Richard, B., Ragueneau, F.: Continuum damage mechanics based model for quasi brittle materials subjected to cyclic loadings: Formulation, numerical implementation and applications. Engineering Fracture Mechanics **98**, 383–406 (2013)

[203] Rogers, C.A., Barker, D.K.: Experimental studies of active strain energy tuning of adaptive composites. In: Proceedings of the 31^{st} AIAA/ASME/ASCE/AHS/ASC Structures, Structural Dynamics and Materials Conference, pp. 2234–2241 (1990)

[204] Rogers, C.A., Fuller, C.R., Liang, C.: Active control of sound radiation from panels using embedded shape memory alloy fibers. Journal of Sound and Vibration **136**(1), 164–170 (1990)

[205] Rogers, C.A., Liang, C., Fuller, C.R.: Modeling of shape memory alloy hybrid composites for structural acoustic control. Journal of the Acoustical Society of America **89**(1), 210–220 (1990)

[206] Rogers, C.A., Liang, C., Jia, J.: Behavior of shape memory alloy reinforced composite plates Part I: Model formulations and control concepts. In: Proceedings of the 30^{th} AIAA/ASME/ASCE/AHS/ASC Structures, Structural Dynamics and Materials Conference, pp. 2011–2017 (1989)

[207] Rogers, C.A., Robertshaw, H.H.: Development of a novel smart material. In: Proceedings of the 1988 Winter Annual Meeting of the American Society of Mechanical Engineers, pp. 1–5 (1988)

[208] San Juan, J., Nó, M.L.: Internal friction in a new kind of metal matrix composites. Material Science & Engineering A **442**, 429–432 (2006)

[209] Saunders, W.R., Robertshaw, H.H., Rogers, C.A.: Structural acoustic control of a shape memory alloy composite beam. Journal of Intelligent Material Systems and Structures **2**, 508–527 (1991)

[210] Segurado, J., LLorca, J.: Computational micromechanics of composites: The effect of particle spatial distribution. Mechanics of Materials **38**, 873–883 (2006)

[211] Segurado, J., Llorca, J., Gonzalez, C.: On the accuracy of mean-field approaches to simulate the plastic deformation of composites. Scripta Materialia **46**(7), 525–529 (2002)

[212] Seiani, H.A., Ghazavi, A.: A thermo-micro-mechanical modeling for smart shape memory alloy woven composite under in-plane biaxial deformation. International Journal of Mechanics and Materials in Design **5**, 111–122 (2009)

[213] Simo, J., Hughes, T.: Computational Inelasticity. Springer-Verlag (1998)

[214] Simo, J., Ortiz, M.: A unified approach to finite deformation elastoplastic analysis based on the use of hyperelastic consitituve equations. Computer Methods in Applied Mechanics and Engineering **49**, 221–245 (1985)

[215] Simo, J., Taylor, R.: Consistent tangent operators for rate-independent elastoplacticity. Computer Methods in Applied Mechanics and Engineering **48**, 101–118 (1985)

[216] Simo, J.C., Hughes, T.J.R.: Computational Inelasticity, *Interdisciplinary Applied Mathematics*, vol. 7. Springer-Verlag, New York (1998)

[217] Simpson, J.C., Boller, C.: Design and performance of a shape memory alloy-reinforced composite aerodynamic profile. Smart Materials and Structures **17**, 025,028 (2008)

[218] Song, G., Ma, N., Li, H.N.: Applications of shape memory alloys in civil structures. Engineering Structures **28**, 1266–1274 (2006)

[219] Song, G., Sun, Q., Cherkaoui, M.: Role of microstructure in the thermomechanical behavior of sma composites. Journal of Engineering Materials and Technology **121**(1), 86–92 (1999)

[220] Sun, Z.M., Murugaiah, A., Zhen, T., Zhou, A., Barsoum, M.W.: Microstucture and mechanical properties of porous Ti_3SiC_2. Acta Materialia **53**, 4359–4366 (2005)

[221] Tallman, D.J., Naguib, M., Anasori, B., Barsoum, M.W.: Tensile creep of Ti_2AlC in air in the temperature range 1000-1150°c. Scripta Materialia **66**, 805–808 (2012)

[222] Tang, W., Sundman, B., Sandström, R., Qiu, C.: New modelling of the B2 phase and its associated martensitic transformation in the Ti-Ni system. Acta Metallurgica **47**(12), 3457–3468 (1999)

[223] Turner, T.L., Buehrle, R., Cano, R., Fleming, G.: Modeling, fabrication, and testing of a SMA hybrid composite jet engine chevron concept. Journal of Intelligent Material Systems and Structures **17**, 483–497 (2006)

[224] Villanueva, A., Smith, C., Priya, S.: A biomimetic robotic jellyfish (Robojelly) actuated by shape memory alloy composite actuators. Bioinspiration & Biomimetics **6**, 036,004 (2011)

[225] Villanueva, A.A., Joshi, K.B., Blottman, J.B., Priya, S.: A bio-inspired shape memory alloy composite (BISMAC) actuator. Smart Materials and Structures **19**, 025,013 (2010)

[226] Voyiadjis, G.Z., Kattan, P.I.: A comparative study of damage variables in continuum damage mechanics. International Journal of Damage Mechanics **18**, 245–260 (2009)

[227] Voyiadjis, G.Z., Kattan, P.I.: Healing and super healing in continuum damage mechanics. International Journal of Damage Mechanics **23**(2), 245–260 (2013)

[228] Voyiadjis, G.Z., Taqieddin, Z.N., Kattan, P.I.: Anisotropic damage-plasticity model for concrete. International Journal of Plasticity **24**, 1946–1965 (2008)

[229] Wang, W., Lee, J.Y., Rodrigue, H., Song, S.H., Chu, W.S., Ahn, S.H.: Locomotion of inchworm-inspired robot made of smart soft composite (ssc). Bioinspiration & Biomimetics **9**, 046,006 (2014)

[230] Weglewski, W., Basista, M., Chmielewski, M., Pietrzak, K.: Modeling of thermally induced damage in the processing of Cr-Al_2O_3 composites. Composites: Part B **43**, 255–264 (2012)

[231] Wei, Z.G., Sandström, R., Miyazaki, S.: Shape memory materials and hybrid composites for smart systems: Part II shape-memory hybrid composites. Journal of Materials Science **33**, 3763–3783 (1998)

[232] White, S.R., Berman, J.B.: Thermomechanical response of SMA composite beams with embedded nitinol wires in an epoxy matrix. Journal of Intelligent Material Systems and Structures **9**, 391–400 (1998)

[233] Whitten, W., Hartl, D.: Iterative calibration of a shape memory alloy constitutive model from 1d and 2d experimental data using optimization methods. In: SPIE Smart Structures and Materials+ Nondestructive Evaluation and

Health Monitoring, pp. 905,804–905,804. International Society for Optics and Photonics (2014)

[234] Wu, R., Han, M.W., Lee, G.Y., Ahn, S.H.: Woven type smart soft composite beam with in-plane shape retention. Smart Materials and Structures **22**, 125,007 (2013)

[235] Yamada, Y., Taya, M., Watanabe, R.: Strengthening of metal matrix composite by shape memory effect. Materials Transactions, JIM **34**(3), 5083–5091 (1993)

[236] Zhao, Y., Taya, M.: Analytical modeling for stress-strain curve of a porous NiTi. Journal of Applied Mechanics **74**, 291–297 (2007)

[237] Zhen, T., Barsoum, M.W., Kalidindi, S.R.: Effects of temperature, strain rate and grain size on the compressive properties of Ti_3SiC_2. Acta Materialia **53**, 4163–4171 (2005)

[238] Zhou, A.G., Barsoum, M.W., Basu, S., Kalidindi, S.R., El-Raghy, T.: Incipient and regular kink bands in fully dense and 10 vol.% porous Ti_2AlC. Acta Materialia **54**, 1631–1639 (2006)

[239] Zhou, A.G., Basu, S., Friedman, G., Finkel, P., Yeheskel, O., Barsoum, M.W.: Hysteresis in kinking nonlinear elastic solids and the Preisach-Mayergoyz model. Physical Review B **82**, 094,105 (2010)

[240] Zhou, G., Lloyd, P.: Design, manufacture and evaluation of bending behavior of composite beams embedded with SMA wires. Composites Science and Technology **69**, 2034–2041 (2009)

[241] Zhu, Y., Dui, G.: Effect of fiber shape on mechanical behavior of composite with elastoplastic matrix and SMA reinforcement. Journal of the Mechanical Behavior of Biomedical Materials **2**, 454–459 (2009)

APPENDIX A

ISOSTRAIN COMPOSITE MODEL

A simple analytical model of the SMA-MAX phase composites of interest is constructed. Specifically, an isostrain (corresponding to the Voigt bound) approximation is introduced. Such an assumption is introduced as (i) the large contrast in thermoelastic stiffnesses would preclude an isostress assumption and (ii) it roughly approximates a "blocking-force" condition that might be expected. The developed model considers an SMA (denoted by a subscript "1") and MAX (subscript "0") phase. The former is described via a 1D implementation of the constitutive routine in Section 2.1.1 while a 1D isotropic hardening elastic-plastic law is introduced for the MAX phase (note for elastic analysis the yield stress is simply set to infinity).

With the isostrain assumption, the total effective stress, $\bar{\sigma}$, may be written as,

$$\bar{\sigma} = c_0\sigma_0 + c_1\sigma_1, \tag{A.1}$$

or, in an incremental fashion,

$$d\bar{\sigma} = c_0 d\sigma_0 + c_1 d\sigma_1. \tag{A.2}$$

The MAX phase behavior may then be described via the constitutive law,

$$\sigma_0 = E_0\left(\varepsilon_0 - \alpha_0\left(T - T_0\right) - \varepsilon^p\right), \tag{A.3}$$

with E_0, α_0, T, and T_0 being the MAX phase modulus, coefficient of thermal expansion, temperature, and zero-strain reference temperature, respectively. The total

strain of this phase is represented by ε_0 while ε^p is the current total plastic strain. Incrementally, the behavior is described via,

$$d\sigma_0 = E_0 \left(d\varepsilon_0 - \alpha_0 dT \right) - E_0 d\varepsilon^p, \tag{A.4}$$

where the thermoelastic and plastic contributions are separated. Finally, an yield function of the form,

$$\Phi_0 = \frac{\sigma_0}{1-\phi} - K \left(\tilde{\varepsilon}^p \right)^{n_0} - Y_0, \tag{A.5}$$

where K and n_0 are the hardening modulus and exponent, respectively, while Y_0 is the critical thermodynamic value to induce plastic deformation. The $\tilde{\varepsilon}^p$ is used to denote the monotonically increasing plastic strain ($d\tilde{\varepsilon}^p = \sqrt{d\varepsilon^p d\varepsilon^p}$) instead of the current value observed in the constitutive law. As porosity (represented by ϕ) is possible in the MAX phase, its influences are introduced in two ways. First, as shown in the yield expression, Eqn. A.5, it is used in a fashion analogous to an isotropic damage variable so that the continuum damage type "effective" stress is used in considering the onset of yielding. Secondly, porosity is used to determine the value of the current elastic modulus. Specifically, following Hu *et al.* [107], the modulus is assumed to be a function of the porosity and is given by $E_0 = \hat{E}_0 \left(\phi \right) = \tilde{E}_0 e^{-b\phi}$ where $\tilde{E}_0$ is the dense modulus and b is an exponent fit to experimental results.

For the SMA phase, a constitutive law of the form,

$$\sigma_1 = E_1 \left(\xi \right) \left(\varepsilon_1 + \alpha_1 \left(T - T_0 \right) - \varepsilon^{tr} \right), \tag{A.6}$$

or incrementally,

$$d\sigma_1 = E_1 \left(\xi \right) \left(d\varepsilon_1 - d\alpha_1 \left(T - T_0 \right) - \alpha_1 T - d\varepsilon^{tr} \right) + dE_1 \left(\varepsilon_1 - \alpha_1 \left(\xi \right) - \varepsilon^{tr} \right), \tag{A.7}$$

where,

$$dE_1 = \frac{E^M E^A \Delta E}{\left(E^M - \xi \Delta E\right)^2} d\xi, \tag{A.8}$$

and

$$d\alpha_1 = \Delta\alpha d\xi, \tag{A.9}$$

is used. By noting $d\varepsilon^{tr} = H^{cur}\left(\sigma_1\right) \frac{\sigma_1}{|\sigma_1|} d\xi$, the SMA stress increment may be written,

$$\begin{aligned} d\sigma_1 = & E_1\left(\xi\right)\left(d\varepsilon_1 - \alpha_1\left(\xi\right) dT\right) + \\ & \left[\frac{E^M E^A \Delta E}{\left(E^M - \Delta E\right)^2}\left(\varepsilon_1 - \alpha_1\left(\xi\right)\left(T - T_0\right) - \varepsilon^{tr}\right) - E_1\left(\Delta\alpha\left(T - T_0\right) + H^{cur}\left(\sigma_1\right)\frac{\sigma_1}{|\sigma_1|}\right)\right] d\xi. \end{aligned} \tag{A.10}$$

One dimensional forms of the transformation function are given by,

$$\Phi_1^{fwd} = \left(1 - D\right)|\sigma_1| H^{cur}\left(\sigma_1\right) + \frac{1}{2}\Delta S \sigma_1^2 + \sigma_1 \Delta\alpha\left(T - T_0\right) + \rho\Delta s_0 T - \rho\Delta u_0 - f_{fwd}^t\left(\xi\right) - Y_1^t = 0, \tag{A.11}$$

for forward and,

$$\Phi_1^{rvs} = \left(1 + D\right)\sigma_1 \frac{\varepsilon^{tr-rev}}{\xi^{rev}} - \frac{1}{2}\Delta S \sigma_1^2 - \sigma_1 \Delta\alpha\left(T - T_0\right) - \rho\Delta s_0 T + \rho\Delta u_0 + f_{rev}^t\left(\xi\right) - Y_1^t = 0 \tag{A.12}$$

for reverse.

To investigate the response of the composite through an arbitrary loading path, it is assumed that $d\bar{\sigma}$ and dT are known and prescribed by the numerical solver. The isostrain assumption yields $d\bar{\varepsilon} = d\varepsilon_0 = d\varepsilon_1$ and the effective strain may be found (via Eqns. A.2, A.4, and A.10),

$$d\bar{\varepsilon} = \frac{d\bar{\sigma} + \left(c_0 E_0 \alpha_0 + c_1 E_1\left(\xi\right)\alpha_1\left(\xi\right)\right) dT}{c_0 E_0 + c_1 E_1\left(\xi\right)}. \tag{A.13}$$

An elastic predictor-inelastic corrector scheme can be readily adopted. In the latter case, if both mechanisms are active, applying convex-cutting routines to incremental constitutive law and consistency equations produces three equations in terms of three unknowns – the inelastic correction increments of the total effective strain, plastic strain, and martensitic volume fraction denoted respectively by $\Delta\bar{\varepsilon}$, $\Delta\varepsilon^p$, and $\Delta\xi$. These three equations are,

$$\begin{aligned} \left(c_0E_0 + c_1E_1\left(\xi\right)\right)\Delta\bar{\varepsilon} - c_0E_0\Delta\varepsilon^p + c_1\gamma\Delta\xi = 0, \\ \frac{\sigma_0}{|\sigma_0|}\frac{E_0}{1-\phi}\Delta\bar{\varepsilon} - \frac{\sigma_0}{|\sigma_0|}\left(\frac{E_0}{1-\phi} + nK\left(\bar{\varepsilon}^p\right)^{(n-1)}\right)\Delta\varepsilon^p = -\Phi_0, \\ \frac{\partial\Phi_1}{\partial\sigma_1}E_1\left(\xi\right)\Delta\bar{\varepsilon} + \left(\frac{\partial\Phi_1}{\partial\xi} + \frac{\partial\Phi_1}{\partial\sigma_1}\gamma\right)\Delta\xi = -\Phi_1 \end{aligned} \tag{A.14}$$

where,

$$\begin{aligned} \gamma = & \frac{E^M E^A \Delta E}{\left(E^M - \xi\Delta E\right)^2}\left(\bar{\varepsilon} - \alpha_1\left(\xi\right)\left(T - T_0\right) - \varepsilon^{tr}\right) \\ & -E_1\left(\xi\right)\left(\Delta\alpha_1\left(T - T_0\right) + H^{cur}\left(\sigma_1\right)\frac{\sigma_1}{|\sigma_1|}\right), \\ \frac{\partial\Phi_1}{\partial\sigma_1} = & \begin{cases} \left(1-D\right)\frac{\sigma_1}{|\sigma_1|}H^{cur}\left(\sigma_1\right) + \Delta S\sigma_1 + \Delta\alpha_1\left(T - T_0\right); & d\xi > 0 \\ -\left(1+D\right)\frac{\varepsilon^{tr-rev}}{\xi^{rev}} - \Delta S\sigma_1 - \Delta\alpha_1\left(T - T_0\right); & d\xi < 0 \end{cases}, \\ \frac{\partial\Phi_1}{\partial\xi} = & \begin{cases} -\frac{\partial f^t_{fwd}}{\partial\xi}; & d\xi > 0 \\ \frac{\partial f^t_{rev}}{\partial\xi}; & d\xi < 0 \end{cases}. \end{aligned} \tag{A.15}$$

With respect to the smooth hardening function,f^t, special care needs to be taken in evaluating the derivatives. Specifically, due to the selected form, slight numerical adjustments need to be made to avoid expressions that can not be appropriately evaluated. This topic is treated extensively in the work of Lagoudas *et al.* [124] and details will be left to that work. Finally, in the developed model, the cases of just transformation of plasticity may easily be handled by setting $\Delta\varepsilon^p$ or $\Delta\xi$ to zero,

respectively. Finally, as an elastic guess may incorrectly indicated both surfaces are simultaneously active, an additional check is needed following the inelastic corrector to ensure that both surfaces are indeed active.